2001

Superfast Dynamics of Bipyridinium Ions at Interfaces and Polar Solutions.

Yixiang Huang
Louisiana State University and Agricultural & Mechanical College

INFORMATION TO USERS

This manuscript has been reproduced from the microfilm master. UMI films the text directly from the original or copy submitted. Thus, some thesis and dissertation copies are in typewriter face, while others may be from any type of computer printer.

The quality of this reproduction is dependent upon the quality of the copy submitted. Broken or indistinct print, colored or poor quality illustrations and photographs, print bleedthrough, substandard margins, and improper alignment can adversely affect reproduction..

In the unlikely event that the author did not send UMI a complete manuscript and there are missing pages, these will be noted. Also, if unauthorized copyright material had to be removed, a note will indicate the deletion.

Oversize materials (e.g., maps, drawings, charts) are reproduced by sectioning the original, beginning at the upper left-hand corner and continuing from left to right in equal sections with small overlaps.

Photographs included in the original manuscript have been reproduced xerographically in this copy. Higher quality 6" x 9" black and white photographic prints are available for any photographs or illustrations appearing in this copy for an additional charge. Contact UMI directly to order.

ProQuest Information and Learning
300 North Zeeb Road, Ann Arbor, MI 48106-1346 USA
800-521-0600

SUPERFAST DYNAMICS OF BIPYRIDINIUM IONS AT INTERFACES AND POLAR SOLUTIONS

A Dissertation

Submitted to the Graduate Faculty of the
Louisiana State University and
Agricultural and Mechanical College
in partial fulfillment of the
requirements for the degree of
Doctor of Philosophy

In

The Department of Chemistry

by
Yixiang Huang
B. S., Hunan University, 1981
M. S., Hunan University, 1986
M. S. in SySc., Louisiana State University, 1999
May 2001

Bell & Howell Information and Learning Company
300 North Zeeb Road
P.O. Box 1346
Ann Arbor, MI 48106-1346

ACKNOWLEDGEMENTS

I would like to thank Dr. John B. Hopkins, my major professor, for his enthusiastic guidance in science, his patience in teaching femto-second laser spectroscopy technology and computer simulation, his encouragement and help during the entire research work and daily life. I would also like to thank Dr. Robin L. McCarley, also my major professor as the co-chair with Dr. John B. Hopkins in my committee for his guidance in electrochemical methods and help in my research work, especially in the last year of my graduate study.

I thank all my lab partners for their help and friendship. I thank Dr. Junbo Chen for his help in operating the femto-second laser systems and helpful discussions. I would like to thank Dr. Jianzhong Liu for fruitful discussion and help in daily life. Thanks also go to Qiang Liu, Dr. Jianzhong Liu, and Dr. Gales for their help in synthesizing N, N'-ethylene-2, 2'-bipyridinium.

I would like to express my sincere appreciation to Dr. Barry Dellinger, Neil R. Kestner, and Robert F. O'Connell for their time and help as committee members. I would like to thank staffs in the graduate school and chemistry department for her help in my graduate documents. I would like to thank the Department of Chemistry for offering me teaching assistantships during these years of study. I would like to appreciate National Science Foundation Grant No. CHE-9023575 for partially supporting the research in this dissertation.

I would like to thank my wife Donghui Li and boy Xuru Huang for their persistent love, understanding, tolerance and support.

TABLE OF CONTENTS

LIST OF TABLES

LIST OF FIGURES

ABSTRACT

The super-fast dynamics of solutes in polar solvents and at solid-liquid interface is investigated by femtosecond time-resolved Raman scattering (RRS) and computer simulation of molecular dynamics (MD).

Femtosecond RRS is used to investigate four bipyridinium radicals in aqueous solution: methylviologen monocation MV^+, benzylviologen monocation, 4,4'-bipyridinium-N,N'-di(propylsulfonate) monoanion and N,N'-ethylene-2,2'-bipyridinium monocation. Time-resolution of the dynamics of the four radicals is carried out by a pump and probe technique using the time-dependent transient intensity of Stokes and anti-Stokes RRS of C-C stretching mode. It is found that the lifetime of the electronic excited state B_{3u} is less than 350 fs and the vibrational relaxation rates in the electronic ground state are some 2-5 ps. The possible vibrational relaxation mechanisms including the radical structure and charge effect on the vibrational relaxation are discussed.

The photo-induced interfacial electron transfer from colloidal CdS particles to an adsorbed methylviologen is studied by femtosecond RRS. It is found by RRS spectra that part of the electron transfer and the accompanying aromatic-to-quinoid structure change of methylviologen occurs within the laser pulse width 350 fs. Time-resolving the photo-induced MV^+ RRS band by a pump-probe scheme shows that the photo-induced MV^+ dynamics is a double-exponential consisting of two components: 270fs and 6.8ps. The 270fs fast component is assigned to electron transfer from shallow traps and accounts for

the part of MV^+ produced within the pulse width. However the 6.8 ps slow component is assigned to electron transfer from relatively deep traps.

The solvation dynamics upon solute ionization in bulk Stockmayer fluids and at surface is studied using MD simulation. For 20-40 selected thermodynamics states, the non-equilibrium solvation, starting from a neutral polar solute in bulk or adsorbed to a surface is studied by investigating the (complementary) solvent response function, solvent numbers in the first solvent shell, spatial solvent distribution, and pair distribution function. The dependence of the solvation dynamics on solute charge, solvent dipole moment, and surface parameters is studied. A mechanism with two kinds of transient states is proposed to explain the 3-mode dynamics. The computer simulation compliments the solvation dynamics upon electron transfer to a solute.

CHAPTER 1 BACKGROUND

1.1 Introduction

In this dissertation, the spectroscopy and computer simulation techniques are used to investigate the superfast chemical dynamics at solid-liquid interface and in bulk fluids. The femtosecond time-resolved resonance Raman is used to study the four univalent bipyridinium radicals (including methyviologen, benzylviologen, 4,4'-bipyridinium-N, N'-di (propylsulfonate), and N, N'-ethylene-2,2'-bipyridinium monocations); their vibrational relaxation dynamics; and the photo-induced interfacial electron transfer between colloidal CdS(s) and methylviologen (aq.). The molecular dynamics simulation technique is used to study the ion solvation dynamics in Stockmayer fluid and at interface.

The dissertation consists of six chapters. This chapter introduces some theoretical treatment of the Raman scattering and electron transfer. We do not need to use the theoretical treatment because the results obtained in this dissertation are directly based on recent research results. We briefly present this treatment just for reference purposes. The chapter 2 describes the experimental technique. The results are presented in chapter 3 to 5.

Here is a quick summary of the main results to get an overall picture of the dissertation. The results include three parts: (a) femto-second time-resolved RRS investigation of four bipyridinium radicals in aqueous solution, (b) photo-induced interfacial electron transfer from colloidal CdS particles to an adsorbed methylviologen, and (c) the study of solvation dynamics upon solute

ionization in bulk Stockmayer fluids and at surface by molecular dynamics (MD) simulation.

Femtosecond RRS is used to investigate four bipyridinium radicals in aqueous solution: methylviologen monocation MV^+, benzylviologen monocation, 4,4'-bipyridinium-N,N'-di (propylsulfonate) monoanion and N, N'-ethylene-2, 2'-bipyridinium monocation. Time-resolution of the dynamics of the four radicals is carried out by a pump and probe technique using the time-dependent transient intensity of Stokes and anti-Stokes RRS of C-C stretching mode. It is found that the lifetime of the electronic excited state B_{3u} (MO 11, excited) is less than 350 fs and the vibrational relaxation rates in the electronic ground state are some 2-5 ps. The possible vibrational relaxation mechanisms including the radical structure and charge effect on the vibrational relaxation are discussed.

The photo-induced interfacial electron transfer from colloidal CdS particles to an adsorbed methylviologen is studied by femtosecond RRS. It is found by RRS spectra that part of the electron transfer and the accompanying aromatic-to-quinoid structure change of methylviologen occurs within the laser pulse width 350 fs. Time-resolving the photo-induced MV^+ RRS band by a pump-probe scheme shows that the photo-induced MV^+ dynamics is a double-exponential consisting of two components: 270fs and 6.8ps. The 270fs fast component is assigned to electron transfer from shallow traps and accounts for the part of MV^+ produced within the pulse width. However the 6.8 ps slow component is assigned to electron transfer from relatively deep traps.

The computer simulation compliments the solvation dynamics upon electron transfer to a solute. The solvation dynamics upon solute ionization in bulk Stockmayer fluids and at surface is studied using MD simulation. For 20-40 selected thermodynamics states, the non-equilibrium solvation, starting from a neutral polar solute in bulk or adsorbed to a surface is studied by investigating the solvent response function, complementary solvent response function, solvent numbers in the first solvent shell, spatial solvent distribution, and pair distribution function. The dependence of the solvation dynamics on solute charge, solvent dipole moment, and surface parameters is studied. A mechanism with two kinds of transient states is proposed to explain the 3-mode dynamics.

The femto-second Raman spectrometer makes it possible to collect the pump-probe Raman spectra to investigate transient processes and species in femtosecond and picosecond time scale. The investigation of various phenomena in different aqueous solutions and at liquid-solid interfaces by this technique is described here. The transient Raman spectra and the time evolution of the Raman band intensities show features that have never been observed before in historical Raman literature. This is basically due to the unavailability of the Raman spectra on this ultra-fast time scale for the previous researchers. We have completed investigations for several kinds of molecules/ions in aqueous solution and at the liquid-solid interfaces. Some of the following chapters will be devoted to the description of the experimental techniques and the ultrafast Raman spectroscopy of various processes

originating from the relaxation dynamics of bipyridinium ions in aqueous solution and the photo-induced electron transfer dynamics at CdS(s)|methylviologen (aq.) interface. In every case, some first direct observations of a very general type of electron transfer dynamics and condensed phase relaxation phenomena are demonstrated.

Computer simulation techniques are also used to study the ion solvation dynamics immediately following a charge transfer to a neutral molecule around a solid-fluid interface, i.e. a newly created ion at interface. It has been shown that the molecular dynamics (MD) simulation is one of the important computer simulation techniques to compute equilibrium, transport properties as well as non-equilibrium behavior. We have developed software for MD simulation using the object-oriented C++ language according the already existing MD theory, algorithm and source code modules. After serious tests with the present existing criteria, the software is used to simulate a single ion solvation dynamics in Stockmayer fluids at abstract interfaces. The data obtained using the MD simulation study is the first attempt to simulate the dynamic behavior of interfacial charge production and its effect on the ion solvation to our knowledge. Every piece of these data corresponds to the first computer experiment in a very general type of the interfacial ion solvation phenomena. By using very small time resolution and using some simple models to abstract real systems, the computer simulation technique provides us with some data that is useful but may not be obtained by laser

spectroscopy. These simulation results help in understanding the dynamics following the electron transfer at interface.

This chapter is a simple introductory background of both the techniques and the phenomena in the investigation to understand later chapters better. In later chapters, the experimental techniques (Chapter 2) are described and the results (Chapter 3 to 5) and conclusions (Chapter 6) are presented.

1.2 Raman Spectroscopy [1]

When light/radiation is incident on molecules, scattering of light will occur due to electromagnetic radiation interacting with the molecules. If the energy of the scattering radiation is the same as that of the incident radiation, the scattering is called Rayleigh scattering. Otherwise the energy of the scattering radiation is different from that of the incident radiation, the scattering is called Raman scattering. In Raman scattering, the difference in energy between scattering light and incident light does not depend on the incident wavelength. However this energy difference does strictly correspond to the energy gap between two vibrational levels of an oscillator. This is easily illustrated by classical or quantum theory.

1.2.1 Classical Treatment

In classical theory, Raman scattering process is understood by the assumption that electromagnetic radiation will induce a vibrating dipole in the molecule. The electric field **E** of an electromagnetic wave having a periodically varying intensity of frequency ν_0 with time t is expressed as

$$\mathbf{E} = \mathbf{E}_0 \cos(2\pi\nu_0 t) \qquad (1.1)$$

where $\mathbf{E}_0$ is the intensity amplitude of the electric component. Therefore the induced dipole moment is

$$\mu_{ind} = \alpha \mathbf{E} = \alpha \mathbf{E}_0 \cos(2\pi\nu_0 t) \quad (1.2)$$

where α is called polarizability of the molecule. The polarizability α features the size and shape change of the molecule corresponding to the molecular vibrations.

With respect to the normal vibrational coordinate Q, the polarizability tensor α_{ij} may be expanded as following:

$$\alpha_{ij} = (\alpha_{ij})_0 + \left(\frac{\partial \alpha_{ij}}{\partial Q}\right)_0 Q \quad (1.3)$$

The polarizability tensor can be written in matrix form as

$$(\alpha_{ij}) = \alpha \quad (1.4)$$

It is a function of the normal vibrational frequency ν of the molecule as shown in the following equation:

$$\alpha = \alpha_0 + \left(\frac{\partial \alpha}{\partial Q}\right)_0 \mathbf{A}_\nu \cos(2\pi\nu t) \quad (1.5)$$

where $\mathbf{A}_\nu$ is the amplitude of given normal vibration of the molecule frequency ν. The above equation is substituted into the equation (1.2) for μ_{ind}, we have

$$\mu_{ind} = \alpha_0 \mathbf{E}_0 \cos(2\pi\nu_0 t) + \tfrac{1}{2}\left(\frac{\partial \alpha}{\partial Q}\right)_0 \mathbf{A}_\nu \mathbf{E}_0 \{\cos[2\pi(\nu_0 - \nu)t + \cos[2\pi(\nu_0 + \nu)t]\} \quad (1.6)$$

Thus the classical theory indicates that the interaction of light with a vibrating molecule having polarizability α will give scattering of three different frequencies: ν_0, $\nu_0 - \nu$, and $\nu_0 + \nu$. The frequency ν_0 of Rayleigh scattering light

is the same as that of the incident light. The frequency ($\nu_0 \pm \nu$) of the Raman scattering light differs from that ν_0 of the incident light by the frequency ν of the molecular oscillator. There exist two kinds of Raman scattering. In Stokes Raman scattering the light has lower frequency ($\nu_0 - \nu$) or energy than the incident light. In anti-Stokes Raman scattering the light has higher frequency ($\nu_0 + \nu$) or energy than the incident light.

1.2.2 (Semi-) Quantum Mechanical Treatment

The following are some viewpoints of Raman scattering in terms of quantum mechanical treatment. We will use these viewpoints to explain our time-resolved Raman spectroscopy in the chapters that follow (Chapters 3 and 4). Readers who need the detailed knowledge of full treatments of the Raman spectroscopy may refer to the standard books [2-3].

Qualitatively Raman scattering involves a two-photon process in terms of quantum theory as shown in Figure 1.1. This schematic diagram explains both Stokes and anti-Stokes Raman scattering. As shown in this Figure 1.1, in the Raman scattering a molecule will go from an electronic state to an intermediate state, and then return back to the original electronic state of a different vibrational energy level. If the scattering is Stokes, then the molecule will begin with a lower vibrational level (e.g. v =0) and end with a higher vibrational level (e.g. v=1). In contrast if the scattering is anti-Stokes, then the molecule will begin with a higher vibrational level (e.g. v=1) and end with a lower vibrational level (e.g. v=0). Usually more molecules are in the lower vibrational or vibrationless levels compared to higher vibrational levels at

ambient environments. Therefore the intensity of Stokes Raman signal is much stronger than that of the anti-Stokes Raman signal if other conditions are the same.

The selection rule of the Raman scattering depends on the way the vibration of a molecule to be treated: as a harmonic oscillator or an an-harmonic oscillator. Ideally if a molecule is treated as a harmonic oscillator, then only transitions that will have a change in the vibrational quantum numbers by one ($\Delta v = \pm 1$) are permitted. So one will see only the fundamental band in the Raman spectrum. However, in most cases we will see molecules behave as an anharmonic oscillator. In latter case, the selection rule says transitions with $\Delta v = \pm 2, \pm 3, \pm 4, \ldots$ corresponding overtones are also permitted in addition to the transition $\Delta v = \pm 1$ corresponding fundamental band. What is observed in a typical Raman spectrum is a series of bands.

These bands have decreasing vibrational spacing between neighbors of each other, and decreasing intensity as the vibrational frequency increases. By measuring the band positions/frequencies of the overtones, the anharmonicity of the potential and the dissociation energy of the potential can be calculated if the shape of the potential is known. Therefore the overtones will help us to understand the potential well and anharmonicity of the species under study.

However it is difficult to observe the overtones of normal Raman scattering due to the fact their intensities are much weaker than the

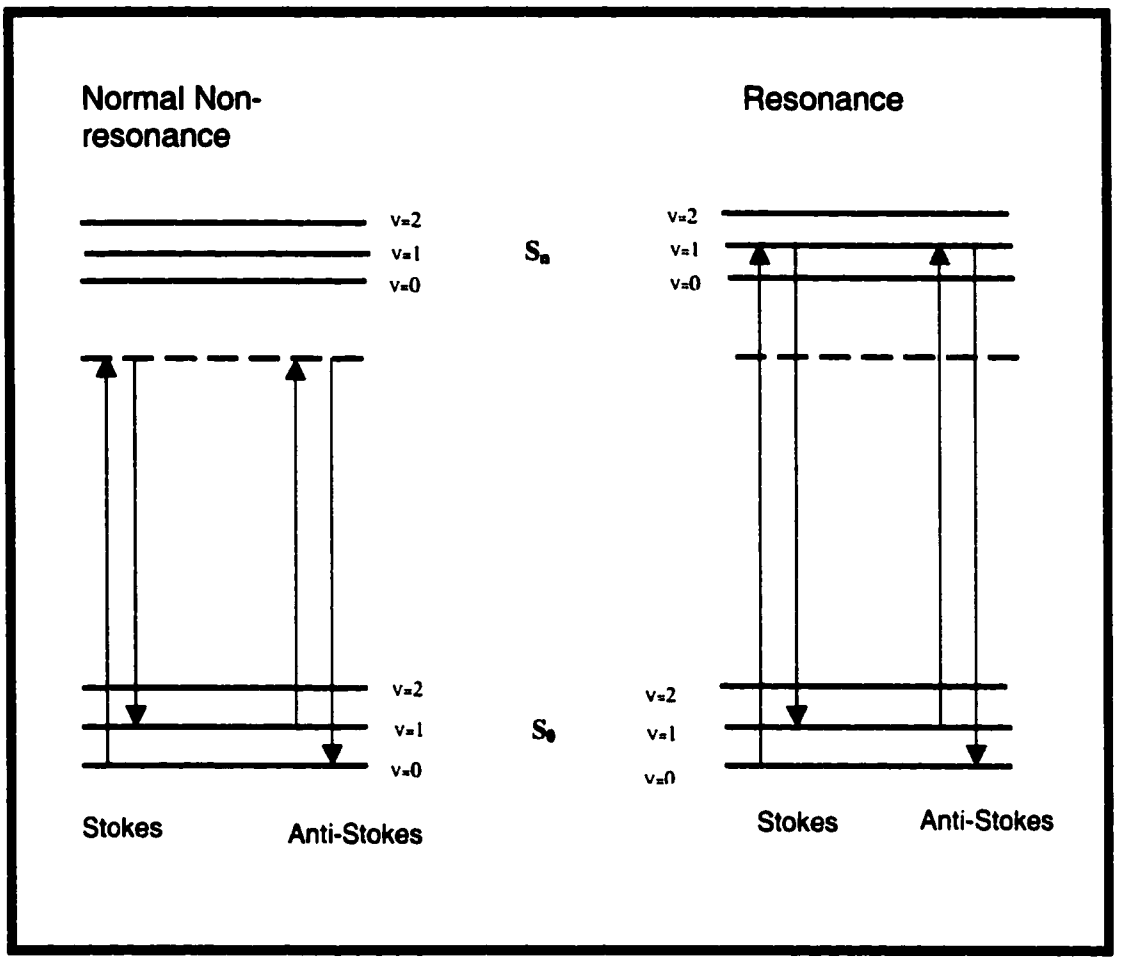

Figure 1.1 Sketch diagram for Raman Scattering: S_0 denotes a ground electronic state, and Sn denotes an excited electronic state. The solid lines for v = 0, v = 1, and v = 2 are the vibrational energy levels of the corresponding electronic states. The dashed line is an intermediate state. The left panel shows non-resonance Raman scattering, and the right panel shows resonance Raman scattering. In the non-resonance Raman the intermediate state is a virtual energy level, but in resonance Raman the intermediate state is a real vibronic level or close to a real energy level.

fundamental band. The intensity of a normal non-resonance band is only about 10^{-6} to 10^{-8} of that of the incident light. So resonance Raman enhancement has been used to achieve a strong Raman signal for bands including fundamental and overtones as the case in our experiments.

In addition to the normal non-resonance Raman scattering, Figure 1.1 also shows the resonance Raman. In normal Raman as shown in the left panel, the incident light excitation will let a molecule go to a virtual energy level (the dashed line). However the incident light excitation will let a molecule go to a real energy level (solid line) or close to a real energy level in resonance Raman as shown in the right panel. That means the resonance Raman scattering results from fact that the excitation light frequency goes toward or falls into the electronic or vibronic absorption band. A detailed treatment of the resonance Raman is described in references [3-6].

The following will focus on the two aspects of the resonance Raman scattering: its intensity and overtones.

The intensity varies with two factors. One factor is the vibrational overlap integral between the initial vibrational state and the upper intermediate vibrational state (in an excited electronic state) and the vibrational overlap integral between the intermediate state and the final vibrational state. This dependence on the vibrational energy levels will greatly influence the Raman intensity as well as the band shape. The other factor is the energy difference or defect between the incident photon and the energy gap of the two real energy levels. The larger the defect, the weaker the Raman intensity. Usually

the intensity of a resonance Raman band is several magnitudes higher than that of a normal Raman band. To achieve high ratio of Raman signal to noise, we have intentionally adjusted our laser light frequency to match or close to the absorption band of the bipyridinium radical species to achieve resonance Raman scattering in the time-resolved experiments (see chapter 3 and 4).

In the resonance Raman, both the fundamental band and overtone bands are enhanced in intensity due to the resonance between the exciting photon and the electronic transition of a molecule. In resonance Raman, the selection rule permits significant intensity in overtones. Thus a series of overtones will be easier to observe compared to normal Raman.

1.3 Molecular Dynamics Simulation

1.3.1 Molecular Dynamics Approach [7-8]

One of the most important computer simulation techniques is molecular dynamics (MD) simulation. In MD classical equations of motions for particles (e.g. atoms, or molecules or ions) are solved. Suppose we have a system consisting of N point-like particles and particle has a mass m_i. The coordinates of particles are $\{\mathbf{r}_i\}_{i=1,...,N}$, and momenta $\{p_i\}_{i=1,...,N}$. The system has a potential of potential energy $V(\mathbf{r}_1, \mathbf{r}_2, ..., \mathbf{r}_N)$. The classical Hamiltonian is

$$H = \sum_i \frac{\boldsymbol{p}_i^2}{2m_i} + V \qquad (1.7)$$

Typically the potential V will be modeled by a simple two-body pair potential $v_{ij}(r_{ij})$ in terms of inter-particle distance, $r_{ij} = |\mathbf{r}_i - \mathbf{r}_j|$ as follows:

$$V = \frac{1}{2}\sum_{i,j} v_{ij}(r_{ij}) \tag{1.8}$$

The application of Hamiltonian equations of motion,

$$\dot{r}_i = \frac{\partial H}{\partial p_i}$$

$$\dot{p}_i = -\frac{\partial H}{\partial r_i} \tag{1.9}$$

to Hamiltonian in equation (1.7) results in Newton's second law,

$$m_i \ddot{r}_i = f_i \tag{1.10}$$

here f_i is the force acting on particle i expressed as:

$$f_i = -\frac{\partial V(r_1, r_2, ..., r_N)}{\partial r_i} \tag{1.11}$$

As long as the potential energy V is known, the equations (1.9) are integrated by numerical methods to produce phase-space trajectories from an initial configuration $\{r_i(0), p_i(0)\}$.

These phase-space trajectories means the positions r_i and momenta p_i of all particles in terms of t:

$$r_i = r_i(t),$$

$$p_i = p_i(t) \tag{1.12}$$

which are used to compute the properties of the system. The equilibrium properties including thermodynamic, structural and dynamic correlation

quantities are computed by taking the averaging over the phase-space trajectories. The non-equilibrium processes such as the ion solvation dynamics can also be studied by MD simulation as shown in chapter 5.

MD simulation uses a MD "box" to simulate the "infinite" system. We need to use periodic boundary conditions (PBC) to reduce the finite-size effect or surface tension. The periodic boundary conditions are applied to the box boundaries as shown in Figure 1.2 using 2-dimensional system as an example. Whenever there is a particle leaving the box on one side, this particle (or equivalently its image) enters immediately from the opposite side (Figure 1.2 left panel). Thus the entire space of the "infinite" system is composed of periodically repeated images of the MD boxes (see Figure 1.2 the right panel). The particles around the boundaries in the MD box will also interact with the particles in the periodic images of this box. Usually by minimum image convention, only the image particles within certain cut off distances are considered in the interaction potential. The PBC allows us to simulate infinite systems without artificial surface effects. This is very useful in simulation of a bulk solution and some interfacial systems in which the systems are infinite in 2-dimension. It is important to note the system is still limited by the periodic boundary conditions, which may introduce some difficulties in simulation processes. Also, the number of particles in the simulation box should be large enough to minimize the finite-size effect. We have checked the effect of number of particles in the MD box in chapter 5 of computer simulation.

The MD technique using equations 1.9 or 1.10 is a scheme to investigate the evolution of a classical N-particle system in volume V. In each time step of the simulations, the total energy E is conserved. Assuming the time averages are equal to the ensemble averages, the averages in the MD simulation is the ensemble averages in the micro-canonical ensemble (NVE). Thus this N-atom system is a micro-canonical ensemble (NVE). We have chosen this system naturally in simulating the non-equilibrium dynamics of ion solvation at interfaces. But before the system is ionized, it is equiliblized using MD at a constant temperature. It is necessary to briefly introduce the techniques to do constant-temperature MD simulations in a canonical ensemble (NVT).

There exist many techniques to simulate the MD at a constant temperature based on the modification of the equations of motion [8-11]. The goal is either to keep the instantaneous temperature T constant

$$T = T_{given} \tag{1.13}$$

or to keep the average temperature <T> constant

$$\langle T \rangle = T_{given} \tag{1.14}$$

at a given interesting value T_{given} . The following are two typical techniques used in our MD simulation to let the system achieve a given temperature. The first one is to enforce equation ($T = T_{given}$) by simply scaling the velocity of the particle using a factor $\sqrt{\frac{T_{given}}{T}}$ as follows:

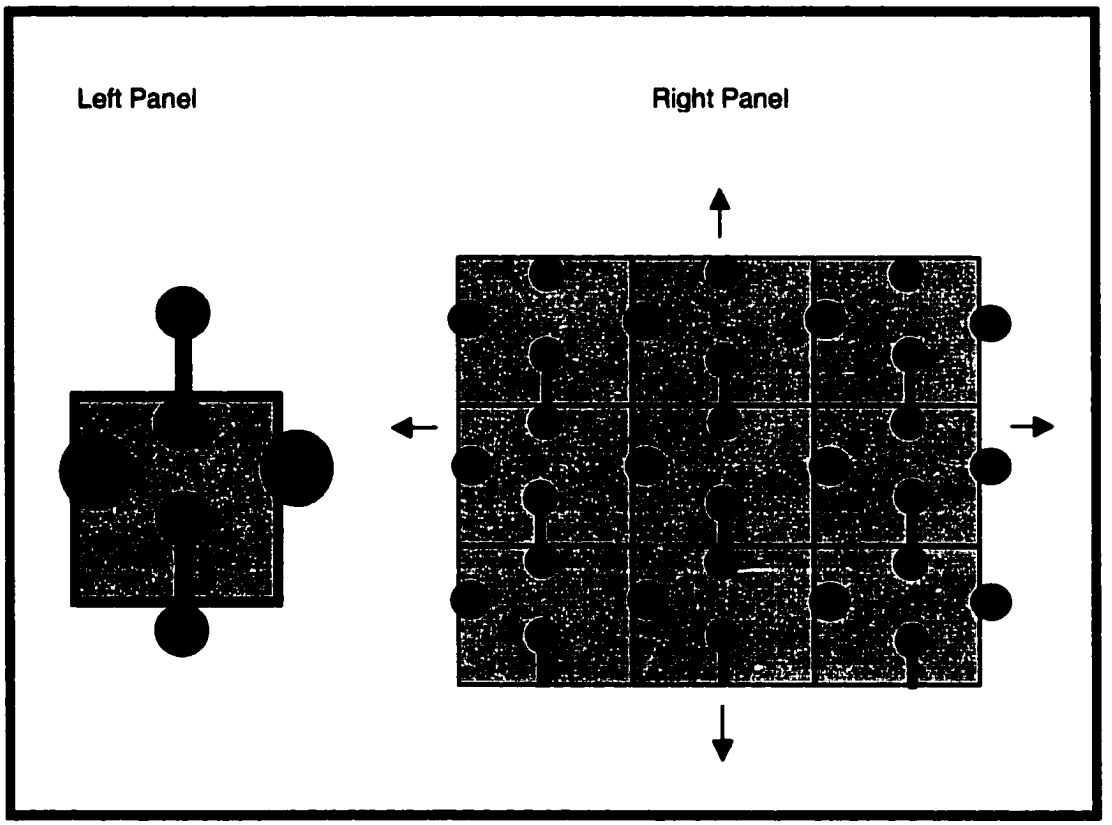

Figure 1.2 The schematic diagram for periodic boundary conditions (PBC) used in molecular dynamics simulations in the case of 2-dimensional periodicity. The left panel is a MD box with PBC, there is large monatomic atom leaving the box and its image entering the box at the same time in the horizontal direction. There is also a diatomic molecule leaving and entering the box simultaneously in the vertical direction. The right panel shows periodically repeated images of an infinite system consisting of these boxes of the left panel in smaller scale.

$$\dot{\mathbf{r}}_i \xleftarrow{\text{assigned-to}} \dot{\mathbf{r}}_i \sqrt{\frac{T_{given}}{T}}, \tag{1.15}$$

as long as the relative error of T is beyond a given tolerance ε. We have chosen the typical value of $\varepsilon = N^{\frac{-1}{2}}$ and the scaling procedure is applied until the system is in thermal equilibrium.

The other approach is to achieve <T> constant at T_{given} as proposed by S. Nose (1.16). This technique uses an extended system, and fictitious degrees of freedom are introduced into Hamiltonian (1.7) to simulate a heat both in contact with the system.

Nose used an extended system having a Hamiltonian

$$H_{ext} = \sum_i \frac{\mathbf{p}_i^2}{2m_i s^2} + V(\mathbf{r}_1, \mathbf{r}_2, ..., \mathbf{r}_n) + \frac{p_s^2}{2Q} + (f+1)k_b T_{given} \ln s \tag{1.16}$$

and the equation of motion as

$$\ddot{\mathbf{r}} = \frac{\mathbf{f}_i}{ms^2} - 2\dot{s}\dot{\mathbf{r}}/s, \tag{1.17}$$

$$Q\ddot{s} = \sum_i m\mathbf{r}_i^2 s - (f+1)k_b T_{given}/s. \tag{1.18}$$

Here the s and p_s are the generalized coordinate and momentum of the heat both; Q is the fictitious mass of the heat both; and f is the number of degrees of freedom (3N-3 if the total momentum is fixed.) Notices that the last two terms in equation (1.16) represent the kinetic and potential energy of the heat

both. It must be noted that there are some differences between the above two approaches. In the simple velocity-scaling scheme the average kinetic energy per particle is rigorously kept constant (iso-kinetic MD scheme), then we do not simulate the true constant-temperature ensemble. The velocity-scaling method yields only the predefined kinetic energy per particle but oppositely do not match any known ensemble. Furthermore this scheme is neither time reversible nor area preserving. It is therefore necessary to stop the velocity-scaling when the system approaches thermal equilibrium.

It is important to note that any kind of constant-temperature schemes may be used when preparing the system at a given temperature before equilibration. The difference between iso-kinetic and canonical schemes is often practically negligible. One of the widely used canonical MD schemes is Nose-Hoover thermostat. For details see reference (7).

1.3.2 Potential Energy Models For The System Of Ion Solvation At Interface

One of the most important issues in MD simulation is the potential-energy model of the system. A generic model is chosen for the interfacial system consisting of two solid surface walls and the liquid solution. The liquid solution is a spherical solute (with or without a point dipole) in a Stockmayer fluid described by a combination of Lennard-Jones (LJ) and dipolar interaction. The solute particle is initially neutral, however carries a point charge since time t=0. This liquid solution is confined between two solid surface walls. The total

configuration potential energy U, of the system is given by the interaction of the following four parts:

U = U(solute-solvent) + U(solvent-solvent)

+ U(solute-surface) +U(solvent-surface)

where

U(solute-solvent) =

U(solute-solvent)(LJ) +U(solute-solvent)(DD)+ U(solute-solvent)(CD) (1.19)

U(solvent-solvent)=U(solvent-solvent)(LJ) +U(solvent-solvent)(DD) (1.20)

In the above equations, the LJ, DD and CD denote the Lennard-Jones, dipole-dipole, and charge-dipole interaction potential energy respectively. It is to be noted that the LJ is short range, while the DD and CD are long-range interactions.

The short-range Lennard-Jones potential u(r) for a pair of particles separated by a distance r is expressed as

$$u(r) = 4\varepsilon[(\sigma/r)^{12} - (\sigma/r)^{6}], \qquad (1.21)$$

where ε and σ are the energy and length parameters respectively. The above LJ equation is used for short-range part of solute-solvent and solvent-solvent interactions.

Though the solute-surface and solvent-surface interactions are also short-range interaction described by the above LJ equation. Some special treatment [12] has been made by taking account the periodic lattice conditions of the solid, thus the expressions for the interaction appears different from

above equation (1.21) due to some mathematical operations such summation and integration made. The following two types of particle-surface interaction potentials are commonly used in computer simulation. The common characteristic of the potentials is that they only depend on the distance z between the particle and the surface in the perpendicular direction to the surface.

(a) The first term of potential between the graphite basal plane surface and a particle is used:

$$U(z^*) = \varepsilon_{gs} \frac{4\pi A^6}{a^*_s}\left(\frac{2A^6}{5z^{*10}} - \frac{1}{z^{*4}} + \frac{A^6}{12.42(z^*+0.994)^9} - \frac{2z^{*2}+9.66z^*+1.33}{8.28(z^*+1.38)^5}\right) \quad (1.22)$$

where $z^*=z/a$, $a^*_s = \sqrt{3}/2$ and $A = \sigma_{gs}/a$. The potential depends on z in addition to the system constants a, ε_{gs} and σ_{gs}. The a =2.46 Å is the length of the lattice-vector for carbon basal plane, the ε_{gs} and σ_{gs} are energy and length parameters of LJ equation between the carbon site and the particle site in the fluids. For nitrogen interacting with the graphite basal plane ε_{gs} /k=31.9K and σ_{gs} =3.36 Å. The above equation is the first dominating term of equation (2.7) of reference [12], the second term of the equation (2.7) in the reference has been ignored to save the computation time for the modified Bessel function.

(b) A more general potential equation[8] is used as

$$U(z) = A\left(\frac{B}{z^{n_B}} - \frac{C}{z^{n_C}}\right), \quad (1.23)$$

where the A, B, C, and n_B, n_C are nonnegative constants. The n_B is larger than n_C and are integers representing expulsing and attracting effects. The values of these constants are chosen reflecting the real surfaces.

The following are the fundamental equations for the dipole-dipole and charge-dipole interaction potential respectively for a pair of particles without consideration of reaction field. The dipole-dipole interaction potential energy u_{ij} for the two particle at $\mathbf{r}_i$ and $\mathbf{r}_j$ with dipoles $\boldsymbol{\mu}_i$ and $\boldsymbol{\mu}_j$ is

$$u_{ij}(\mathbf{r}_{ij}, \boldsymbol{\mu}_i, \boldsymbol{\mu}_j) = \frac{\boldsymbol{\mu}_i \cdot \boldsymbol{\mu}_j}{\mathbf{r}_{ij}^3} - 3\frac{(\mathbf{r}_{ij} \cdot \boldsymbol{\mu}_i)(\mathbf{r}_{ij} \cdot \boldsymbol{\mu}_j)}{\mathbf{r}_{ij}^5}, \tag{1.24}$$

where the $\mathbf{r}_{ij} = \mathbf{r}_i - \mathbf{r}_j$. The charge-dipole interaction potential energy u_{cd} for a particle at $\mathbf{r}_c$ with charge q and a particle at $\mathbf{r}_d$ with dipole $\boldsymbol{\mu}_d$ is:

$$u_{cd}(\mathbf{r}_{cd}, \boldsymbol{\mu}_d) = q\frac{\mathbf{r}_{cd} \cdot \boldsymbol{\mu}_d}{\mathbf{r}_{cd}^3}, \tag{1.25}$$

where the $\mathbf{r}_{cd} = \mathbf{r}_c - \mathbf{r}_d$.

In MD simulation, the most expensive part is to compute the long-range contribution to the potential and force/torque, because significantly much more particles in the simulating image boxes will contribute to the interaction compared to the short-range interaction. Currently there are several approaches such as Ewald summation, multi-pole expansion, Lekner sum, and reaction field, to the problem in 3-D periodic boundary conditions (PCB). For the 2-D periodic boundary conditions in our interfacial system, the computation is more challenging because of the one-dimensional periodicity less than 3-D PCB, and the extension from 2-D to 3-D PCB is not very natural.

In this dissertation, the reaction field method has been chosen to tackle the problem of long-range contribution in the 2-D PCB conditions for the sake of reducing the computation time. The linearly tapered reaction field boundary conditions are described in details in chapter 5 (Table 5.1 (a) to (d)).

Finally it is to be noted that the solute-solvent coupling is described by a short-range (LJ) interaction, dipole-dipole interaction if solute has dipole, and a charge-dipole interaction if the solute is charged. These three contribute to the solvation dynamics through reorganization process.

1.4 Bipyridinium Ions and Relaxation Dynamics

1.4.1 Importance And Applications Of Investigation Of Bipyridinium Ions

Viologens (alkyl derivatives of 4, 4'-bipyridyl or bipyridinium) were first reported as redox indicators in biological investigations by Michaelis in 1933 [13]. Since then the interest in this kind of species has been increasing and many applications have been found. Later they are recognized as the parent compounds for a powerful kind of herbicides, called "paraquats". The herbicidal characteristics of the viologens are contributed by their serving as strong reductants including reducing molecular oxygen particularly [14]. The viologens will change color prominently between the two-oxidation states (e. g. between bivalent and mono-valent bipyridinium ions. Note that the MV^{+2} is colorless but the MV^{+} has strong purple-blue color in aqueous solution.), along with a fast response and good reversibility. Thus viologens are appropriate candidates for electrochemical display devices [15].

Viologens are also well known as mediators (relays) [16,17]. The compounds having no electroactivities, such as biological molecules, can be reduced in a cycle by electrochemically reducing viologen. The viologens in turn chemically reduce the compounds without electroactivities. In addition, viologen-based polymers [18] and viologens at mercury film electrodes [19] have been extensively studied.

1.4.2 Vibrational Relaxation Dynamics [20]

Optical excitations or chemical reactions may cause local excess in vibrational energy of molecules. The vibrational energy redistributes within the molecule and flows to the surrounding subsequently. These processes are called vibrational relaxation that leads to thermal equilibrium within pico-second time scale. It is necessary to use a femto- or pico-second technique to investigate the various relaxation processes.

One of the important vibrational parameters to measure the vibrational relaxation is the population lifetime T_1 of an individual vibrational mode, i.e. the population of the vibrational state changes exponentially with a constant T_1. The population time can be understood only recently using ultrashort pulses. Before the advent of ultrashort laser pulses there is barely knowledge of the population time.

The early researchers use the spectral line-width of the vibrational mode to deduce the "vibrational lifetime". Until 1972 a clear distinction between the "population life time" T_1 and the "vibrational dephasing time" T_2 is not established. The line width of the mode is determined by the vibrational

de-phasing time, in addition to the other line broadening effects including inhomogeneous broadening or isotope multiplicity. It is found in most cases that the energy stays longer in the vibrational mode than the phase of the vibration does in coherently excited medium. That is, the vibrational population lifetime T_1 is longer than the vibrational de-phasing time T_2.

One important contribution to the vibrational relaxation is the intermolecular energy transfer, the vibrational excess energy flow from the molecule to its surrounding. The interesting question is how long the excess energy remains in the molecule in the liquid phase. It is shown by many experiments that the intermolecular energy transfer occurs very rapidly within the order of 10 ps depending on the degree of excitation and the solvent molecule.

The other important contribution to the vibrational relaxation is the vibrational energy redistribution within the molecule or the intramolecular energy redistribution.

For the vibrational energies of more than 1000 cm^{-1} in larger organic molecules, the redistribution over the vibrational manifold of the electronic ground sate occurs very fast, in most cases, within 1ps. The vibrational redistribution in the electronic ground state is proved by many experimental methods. The excess vibrational energy is equivalent to a transient internal temperature of the excited molecule. It is noted that the intramolecular energy redistribution is faster than the intermolecular energy transfer in large molecules such as dyes.

1.5 Interfacial Electron Transfer Dynamics at CdS(s) | Viologen [21]

Recently much attention has been paid to the charge transfer reactions in semiconductor systems (such as CdS and TiO_2) with many applications. In terms of photo-induced charge separation, these systems have many advantages over the molecular assemblies (e.g. micelle or vesicle). First, in the semiconductor systems, the diffusion constant of the electron is at least 10^4 times larger than that of a molecular charge carrier in the molecular assemblies. This is important in the interfacial photo-reduction of MV^{+2} to $MV^{\cdot +}$ in our study, because the electrons produced inside the CdS semiconductor will need to diffuse to its surface as soon as possible to achieve observable amount of $MV^{\cdot +}$. Secondly, the surface of the semiconductor can be modified by suitable functional groups and catalysts to mediate the chemical redox reactions at interfaces. We are going to address the dynamics of light induced redox reactions in the CdS semiconductors in details in later chapter 4. Here is a brief review of the backgrounds related to our investigations including electron-hole carrier recombination dynamics, carrier-trapping dynamics, vibrational relaxation dynamics and electron transfer dynamics at interfaces.

1.5.1 Basic Steps Of Light-Induced Interfacial Electron Transfer Processes

The overall process of the interfacial electron transfer induced by light from a semiconductor quantum particle (Q-particle) to an acceptor consisting of steps (a) to (d) is shown in the Figure 1.3. The two steps, (c) and (d), will determine if the dynamics is diffusion limited or electron transfer limited. By definition if

the diffusion is slower than the interfacial transfer process, the dynamics is limited by the diffusion of the acceptor to the surface of the Q-particle to encounter with the electron to form complex. Therefore the dynamics will be determined by the viscosity of the medium and the radius of the reactants. If the electron transfer is slower than that of diffusion, then the dynamics is electron transfer limited, and dynamics will be characterized by the rate parameter of charge transfer k_{ct} in the unit of cm/s. In our experiment, the electron transfer is sufficient fast that the diffusion of the acceptor will be ignored. If we use normal electrochemical method, the k_{ct} can't be determined because we will measure the diffusion-limited dynamics. Our femtosecond time-resolved resonance Raman (TRRR) is unique in this sense that the electron transfer will still be time-resolved and the k_{ct} will be obtained regardless of the fact that the electron transfer is so fast that the electrochemical dynamics is diffusion limited. This is fundamentally because we are measuring the electron transfer directly by the optical method instead of using the electric current and potential.

However it is still a good idea to correlate the observed rate constant k_{obs} (in the unit of reciprocal of time, e.g. ps $^{-1}$) or the observed time τ_{ct} (in the unit of time, e.g. picoseconds) with the k_{ct} (in the unit of cm/s) defined in the standard electrochemical text book.

According Grätzel [21], if the interfacial electron transfer is rate determining and much slower than the diffusion,

$$k_{obs} = 4\pi R^2 k_{ct} \qquad (1.26)$$

Otherwise if the interfacial electron transfer is faster than diffusion, which controls the overall reaction, we have Smoluchowski expression

$$k_{obs} = 4\pi DR, \qquad (1.27)$$

where the R is the sum of the radii of the Q-particle and the electron acceptor, and D is the respective diffusion coefficient. These two equations do not apply to our experiment where the diffusion effects can be eliminated by adsorption of the acceptors at the semiconductors' surface and by the small time range that does not allow significant diffusion to occur. In our case, a simple expression:

$$k_{ct} = \delta / \tau_{ct} \qquad (1.28)$$

exists, here τ_{ct} is what we observed, the average time needed for the electron to tunnel across the interface, and δ is the thickness of the reaction layer.

1.5.2 Introduction To The Theory Of Electron-Transfer Reactions

The electron-transfer reactions can be classified into adiabatic and non-adiabatic reactions. In adiabatic electron-transfer reactions, there are strong electronic interactions between the reactants. The classical transition theory can be used to treat the electron-transfer reactions. As shown in Figure 1.4, in the initial stage a precursor complex (A ... D) is formed between the electron donor and acceptor. The reaction of the electron transfer goes subsequently along the reaction coordinate from the reactant valley via the transition state (an activated complex formed) to the successor complex (A^-... D^+). The rate constant k_{et} is exponentially related to the free energy of activation ΔG^* by

$$k_{et} = \upsilon_0 \exp(-\Delta G^* / RT) \qquad (1.29)$$

where ν_0 is the frequency for nuclear reorganization to form the activated complex. The simple transition state theory gives that ν_0 = kT/h and k is Boltzman constants.

In a more detailed theory, the formation of activated complex will involve inner sphere organization and outer sphere organization. The inner sphere organization means the change in the nuclear configuration of the reactants that needs an amount of free energy λ_{in}. The outer sphere organization means the rearrangement of the solvation shell that needs an amount of free energy λ_{out}. There are vibrational modes in the formation of activated complexes with frequencies ν_{in} and ν_{out} that correspond to the inner sphere organization and outer sphere organization respectively. The ν_0 will be expressed as

$$\upsilon_0 = \frac{\nu_{out}^2 \lambda_{out} + \nu_{in}^2 \lambda_{in}}{4\Delta G^*} \qquad (1.30)$$

The central concept is the activated complex and its configuration with coordinates at the intersection of the two free energy curve in the Figure 1.4, where the free energy of the precursor equals that of the successor. The electron transfer occurs in this configuration that will not violate the Frank-Condon principle.

The Figure 1.4 is also a good way to distinguish the adiabatic and non-adiabatic electron transfer reaction. The potential will split at the intersection

Figure 1.3 The basic steps of interfacial light-induced electron transfer from a semiconductor Q-particle to an acceptor such as MV^{+2} adsorbed. It will compete with carrier trapping and recombination.

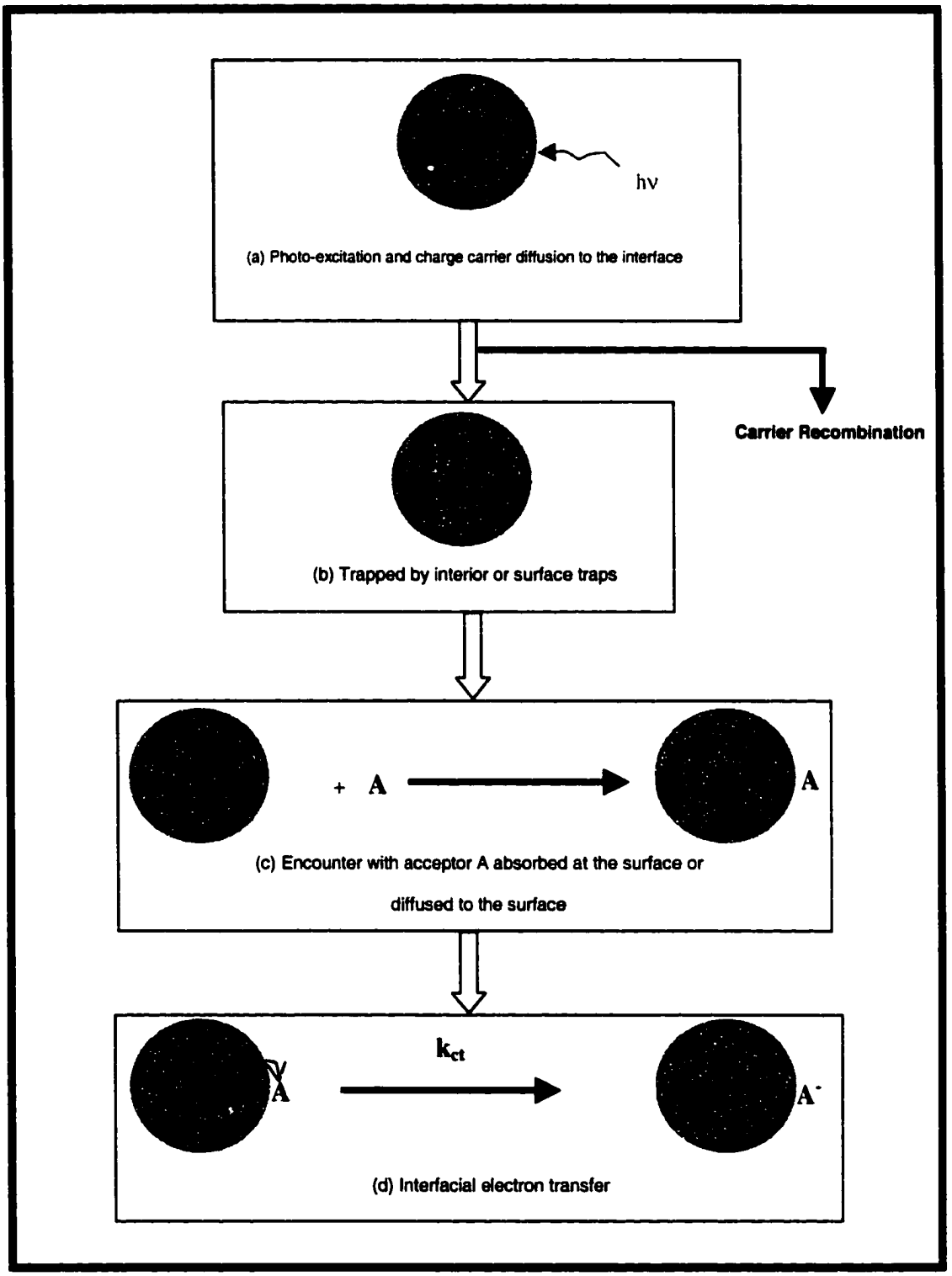

into lower and upper part. The separation is described by the electronic matrix element H_{SR} that couples the reactant and product state. The splitting will increase as the electronic interaction in the activated complex increase. The terminology "adiabatic" means that the system has such a large H_{SR} that system will remain on the lower free energy surface during the electron transfer. That is to say, that the system remains in the same energy surface during the conversion from precursor to successor complex (see the lower curve in Figure 1.4). One typical value of H_{SR} is at least 0.025eV as the criterion for adiabatic reaction at room temperature. As long as the transition state is reached, the passage into the product valley occurs with 100% probability. On the other hand, in "non-adiabatic" reaction, the interaction energy is smaller. Therefore it is possible for the system to cross from the lower to the upper potential curve, which will reduce the reaction probability.

1.5.3 Adiabatic Electron-Transfer Reaction: Marcus Theory

Marcus theory [22] is usually used to describe the outer sphere electron-transfer by statistical treatment of the nuclear arrangement required for the producing activated complex. The activation free energy ΔG^* is expressed as

$$\Delta G^* = (\Delta G^0_{et} + \lambda)^2 / (4\lambda) \qquad (1.31)$$

in terms of the reorganization free energy λ, and standard free energy ΔG^0_{et} of the electron transfer process from the precursor to successor state. This ΔG^0_{et} is different from the overall free energy ΔG^0_{et} (overall) for the reaction from

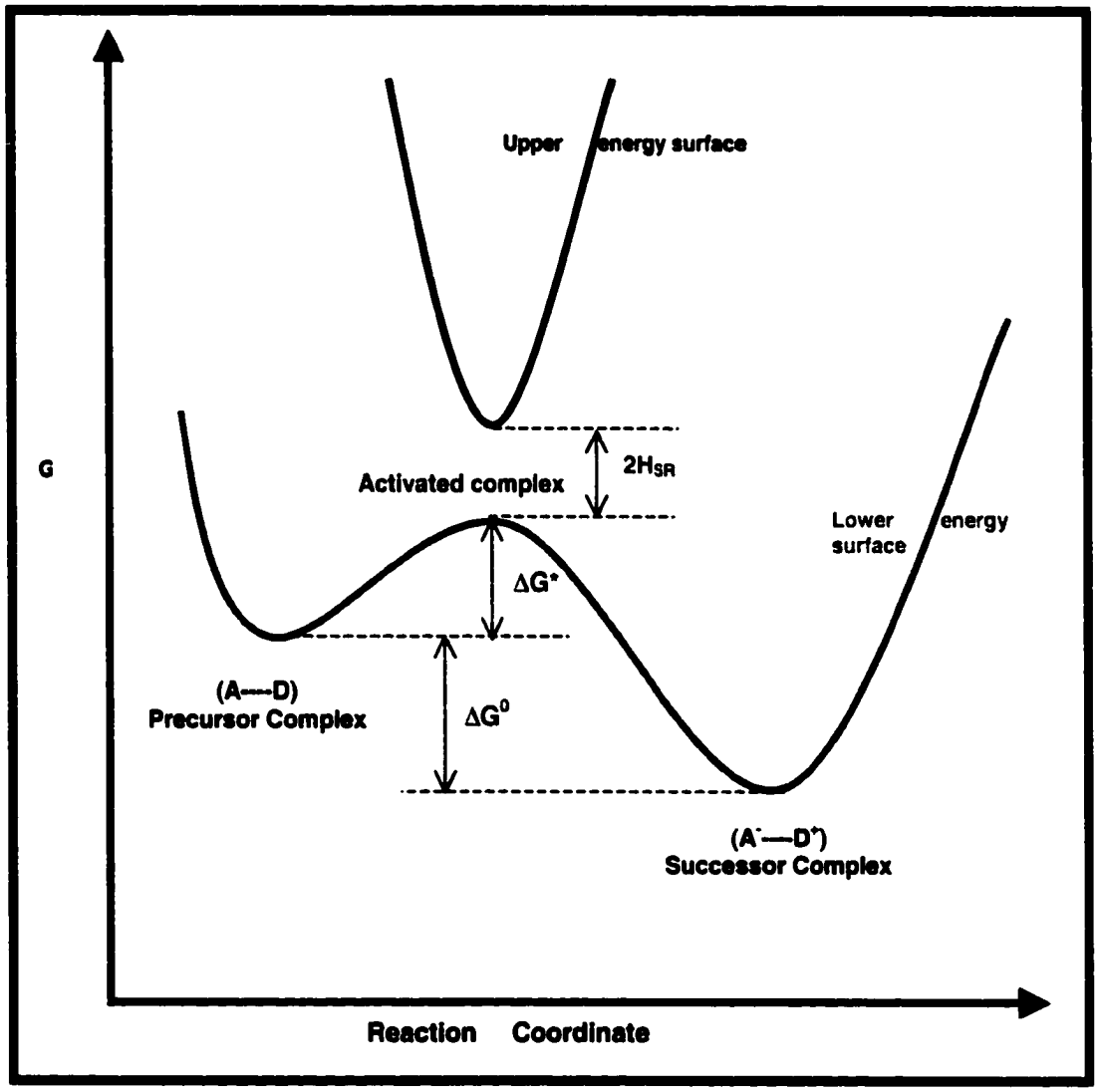

Figure 1.4 Diagram for free energy (G) in electron transfer reaction from a donor D to an acceptor A. The (A----D) and (A^-----D^+) are the nuclear configuration (reaction coordinate) for the precursor and successor complexes respectively. The ΔG_0 and ΔG^* are standard and activation free energy respectively. The H_{SR} is the electronic matrix element used to identify adiabicity of the reaction. If the system remains on the lower energy surface during the electron transfer it is adiabatic, otherwise it is non-adiabatic.

reactant to product by the work terms, W_p and W_s as follows:

$$\Delta G^0_{et}(\text{overall}) = \Delta G^0_{et} + W_p - W_s \qquad (1.32)$$

where the W_p and Ws are the work necessary to form the precursor state from reactant and to form successor state from product respectively.

The critical term is the above equation (1.31) is the reorganization free energy λ . It is defined as the free energy that would have been required to change the equilibrium configuration of the precursor complex and its surrounding solvents to the equilibrium configuration of the successor complex without the electron transfer. This λ consists of the inner sphere term λ_{in} and outer sphere term λ_{out}, and

$$\lambda = \lambda_{in} + \lambda_{out} \qquad (1.33)$$

The λ_{in} is the contribution from the changes from precursor to successor complex by the activation modes

$$\lambda_{in} = \frac{1}{2}\sum_i k_i (d_s - d_p)_i^2 \qquad (1.34)$$

Here the d_s and d_p are the equilibrium bond lengths of the ith vibrational mode in the successor and precursor complex respectively. The k_i is the average force constant of the ith mode. The summation includes all the vibration modes of the complex.

The λ_{out} is the contribution form outside the complex, or from the changes in the configuration of the solvent molecules. It is derived from the polarizability of the solvent assumed as a continuous polar medium as follows:

$$\lambda_{out} = (\Delta e)^2 (\frac{1}{2r_D} + \frac{1}{2r_A} - \frac{1}{r})(\frac{1}{D_{op}} - \frac{1}{D_s}) \quad (1.35)$$

Here the D_{op} is the square of the refractive index of the medium, and D_s is the static dielectric constant. The r is the distance between the reactant centers in the transition state, and the r_D and r_A are the radii of the reactants. The Δe is the charge transferred from donor to the acceptor.

Substituting equation $\Delta G^* = (\Delta G_{et}^0 + \lambda)^2 / (4\lambda)$ into equation (1.29), we have the equation for the adiabatic electron transfer:

$$k_{et} = \upsilon_0 \exp(-(\Delta G^0{}_{et} + \lambda)^2 / 4\lambda RT) \quad (1.36)$$

It is obvious that the rate constant is maximum when the $-\Delta G^0_{et} = \lambda$.

1.5.4 Non-adiabatic Electron-Transfer Reaction

In nonadiabatic electron-transfer reaction the coupling between the electron donor and acceptor is weak. There are many nonadiabatic electron-transfer reactions in chemistry and biology. For example, the interfacial electron transfer is usually nonadiabatic because the donor and acceptor are separated by the interface such as CdS(s)|MV^{2+}(aq) in our study. The model for adiabatic electron-transfer is not appropriate for nonadiabatic electron-transfer reaction. The rate constant k_{et} of the nonadiabatic electron-transfer is expressed as:

$$k_{et} = \frac{2\Pi}{\hbar} | H_{DA} |^2 (FC) \quad (1.37)$$

This equation uses Born-Oppenheimer approximation assumption that the motion of the electron is not dependent on that of the nucleus. The (FC) term is the Frank-Condon factor denoting the contribution to the probability of electron transfer by the nuclear reorganization. It represents the effect of thermal activation of nuclear vibrations on the electron transfer probability.

The term $|H_{DA}|$ is the absolute value of the electron exchange element, and includes the electron tunneling rate depending on the distance. The H_{AD} is a measurement of the interaction energy between the tails of the wave function of the electron on the donor and the acceptor site. $|H_{DA}|$ decreases exponentially with d, the distance between the donor and acceptor, beyond the contact distance d^0, that is

$$|H_{DA}|^2 = |H_{DA}|^2 (d = d^0) \exp(-\beta(d - d^0)) \qquad (1.38)$$

where β is the damping coefficient.

There exists three approaches to the non-adiabatic electron transfer: the classical, semi-classical and quantum mechanical theories.

In the classical description of the nonadiabatic electron-transfer reactions, the nonadiabacity is explained by a correction factor called electronic transmission coefficient κ, under the framework of Marcus theory as follows:

$$k_{et} = \upsilon_0 \kappa \exp(-(\Delta G^0_{et} + \lambda)^2 / 4\lambda RT) \qquad (1.39)$$

Here the κ is the probability of electron transfer at the configuration of the transition state. There is a difference between adiabatic and nonadiabatic

reactions in κ. For adiabatic reaction the κ is 1, while for nonadiabatic reaction it is less than 1. The equation for κ is derived under quantum mechanical formalism on the basis of Landau [23] as follows:

$$\nu_0 \kappa = \frac{2\pi}{\hbar} | H_{DA} |^2 (4\pi\lambda kT)^{-1/2} \qquad (1.40)$$

Using equations (1.39) and (1.40), we have the following equations for the rate constant of electron transfer (the subscript "et" for ΔG^0_{et} has been dropped there after as ΔG^0).

$$\begin{aligned} k_{et} &= (\frac{\pi}{\lambda kT})^{1/2} \frac{1}{\hbar} | H_{DA} |^2 (d = d^0) \exp[-\beta(d - d^0)] \exp(-(\Delta G^0 + \lambda)^2 / 4\lambda RT) \\ \nu_0 &= (\frac{\pi}{\lambda kT})^{1/2} \frac{1}{\hbar} | H_{DA} |^2 (d = d^0) \\ \kappa &= \exp[-\beta(d - d^0)] \\ (FC) &= (\frac{\pi}{\lambda kT})^{-1/2} \exp(-(\Delta G^0 + \lambda)^2 / 4\lambda RT) \end{aligned} \qquad (1.41)$$

Thus the transmission coefficient κ explains the distance dependence of the k_{et}, while the (FC) still remains obtained by the Marcus theory to account for the temperature dependence.

The classical theory will give lower estimate of the k_{et} at low temperature using (FC). The semiclassical and quantum theories use different approaches to calculate the (FC) factor. The quantum theory successfully explain the fact that the k_{et} is independent of temperature at low temperature, while the semiclassical theory gives a k_{et} in between classical and quantum theory. Both semiclassical and quantum theory approach the same result as

classical theory at high temperature. A detailed description of these theories is given in reference (21) if readers are interested. The semiclassical theory [24-26] of nonadiabtic electron transfer is developed by Hopefield on the basis of Förster and Dexter's interpretation of non-radiative transfer of electronic excitation energy. The donor is considered as a electronic subsystem independent of the acceptor. The electron transfer involves tunneling from an occupied level of the donor into an unoccupied state of the acceptor system. If only one frequency ν is involved in the reorganization and λ (D/D^+) = λ (A/A^-). The FC expression is derived as follows

$$(FC) = (2\pi\hbar\nu\lambda\coth(h\nu/2kT))^{-1/2}\exp[-(\frac{(\Delta E^0+\lambda)^2}{2h\nu\lambda\coth(h\nu/2kT)})] \quad (1.42)$$

It will reduce to the classical (FC) at high temperature limit.

The calculation of the (FC) quantum theory has been reviewed by De Vault [27]. The quantum mechanical treatment is required in the case of the donor and acceptor coherently coupled to the same vibrational modes of surroundings.

1.5.5 Interfacial Electron-Transfer Reaction

The interfacial electron transfer occurs within a system of at least two different phases. It has some unique properties that will affect the electron transfer, such as the electrical field present at the phase boundary and the colloidal dimensions of the dispersed phase that reduces the dimensionality of the reaction space.

The heterogeneous electron-transfer reaction is assumed as the first order with respect the concentration of the electro-active species. The net current i (in A/cm^2) represents the rate of the electron transfer reaction. It consists of cathodic i_- and anodic i_+ contribution

$$i = i_+ + i_- \tag{1.43}$$

The corresponding heterogeneous rate constant k_+ and k_- (in cm/s)are expressed as

$$i_+ = nFk_+c_R^{\sigma} \tag{1.44}$$

$$i_- = nFk_-c_O^{\sigma} \tag{1.45}$$

Here the σ indicates surface concentration, the k_+ and k_- are the heterogeneous rate constants.

Depending on the electrode material, the interfacial electron-transfer kinetics shows different potential dependence behavior. For conducting electrode such as a metal, the electron-transfer process follows Butler-Volmer equation:

$$i=i^0\{\exp[(1-\alpha)n\eta F/RT]-\exp[-\alpha n\eta F/RT)]\} \tag{1.46}$$

It is apparent that the net current i varies with the overvoltage η applied. The electronic-transfer process at a conducting electrode is fully characterized by two kinetic parameters: the transfer coefficient α and the rate parameter i_0 or k^0 (Note i_0 is proportional to the rate constant k^0 at standard potential).

Comparing the Butler-Volmer equation with the Marcus equation for the classical treatment of nonadiabatic electron transfer reaction obtained above, one obtain that

$$\alpha = 0.5 + \Delta G^0/2\lambda \quad (1.47)$$

In the case of semiconductor electrode, there exists space charge layer. If the capacity of this layer is smaller than that of the adjacent double layer in the electrolyte, any variation in the externally applied voltage often changes only the potential drop within the semiconductor while the potential difference η between semiconductor and solution is not affected. So the electron transfer kinetics is different from that of the conducting electrode in that the rate constant k_+ or k_- does not depend on the applied voltage in the semiconductor case.

For cathodic process, the concentration of electrons in the semiconductor bulk differs from that present at the surface due to band bending, we have

$$i_- = -nFc_O^\sigma k_- \exp((\phi_{surface} - \phi_{bulk})F/RT) \quad (1.48)$$

Where k_- is independent of the applied potential in contrast to the metal electrode. Thus for electron transfer from the conduction band of an n-type semiconductor to an acceptor in solution, the transfer coefficient is 1.0 and the Tafel slope, is 59mV at room temperature.

It should be noted that the rate constant k in the study of interfacial charge transfer has a unit of centimeter per second. However the rate constant k_{et} from the theory of electron-transfer process is expressed in second. It is worth mentioning that relationships between k_{et} and k is

$$k_{et} = (dR)k \quad (1.49)$$

where the dR is the thickness the reaction layer.

1.5.6 Quantum Size Confinement Effect

The system used in Chapter 4 is colloid having size less than 10^3 Å and forming clear solution. In the colloid solution, quantum size effects may occur if the radius of the semiconductor particle is equal or less than that of the Bohr radius of the first exciton in the semiconductor, and the particle is called Q-particle. These will result in a blue shift of the fundamental absorption edge and of the luminescence maximum with decreasing particle size.

As shown in Figure 1.5, the charge carriers in the colloidal solution are locally confined in the Q-particle of a small radius. These produce discrete electronic states in the valence and conduction bands, resulting in an increase in the effective band gap. The energy of the quantized levels becomes inversely proportional to the effective mass and the square of the particle diameter to the first approximation. This quantum size effect causes dramatic change in the absorption spectra. The colloidal solution of CdS can be yellow to colorless as the size of the CdS-Q-particle decreases in our experiment. To correlate the electronic energy levels with the size of the Q-particles, several models have been proposed by Brus [28], and Foitik and Weller [29]. In Brus' exciton model [28], an electron-hole pair confined in the spherical Q-particle semiconductor crystallite is considered. By approximating the exciton wave function as one or few configurations of the particle-in-a-box orbitals, the energy of the first excitonic state of the Q-particle can be expressed as the following equation:

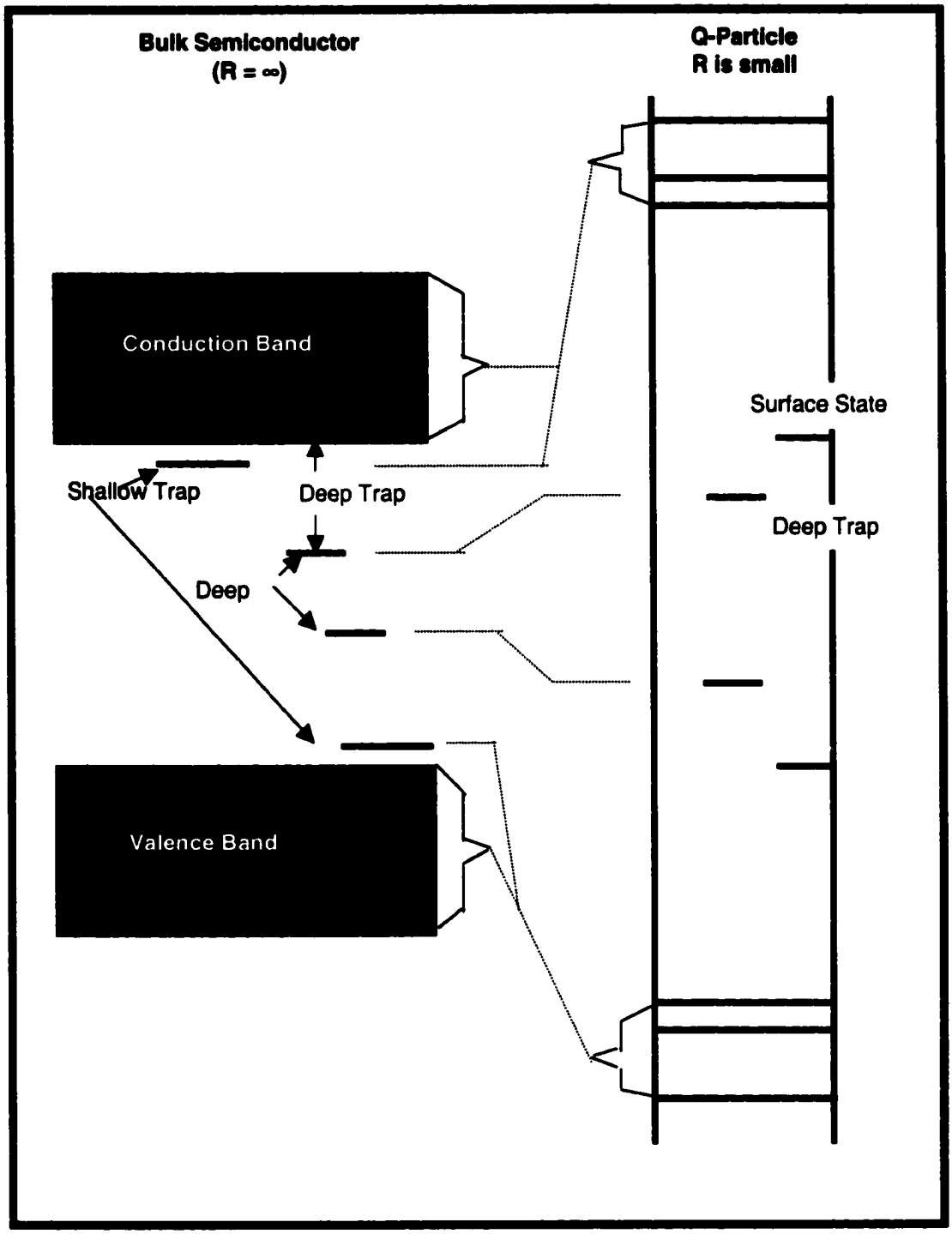

Figure 1.5 The carrier confinement effect: from bulk semiconductor (radius R = ∞) to nano-clusters Q-particle [28]

$$E_g(R) = E_g(R=\infty) + \frac{h^2\pi^2}{2R^2}\left[\frac{1}{m_{e^-}} + \frac{1}{m_{h^+}}\right] - \frac{1.8e^2}{\varepsilon R}$$

(1.50)

where R is the radius of the Q-particle, and m_{e^-} and m_{h+} are the mass of the electron and hole respectively. In the above equation, the first term expresses the band gap of the bulk semiconductor, the second term expresses the energies due to confinement of the electron and holes, and the third term is the coulombic interaction energy between the electron and the hole. Clearly we can see the blue shift of the absorption band (i.e. the $E_g(R)$-$E_g(R=\infty)$) is due to the second spatial confinement term out-weighting the third electrostatic term. For a given semiconductor, the blue shift solely depends on the radius of the particle and the confinement term shifts $E_g(R)$ to higher energy in R^2 as R decreases. This is in turn very important in our experiment, we used the absorption spectra's edge and its first excitonic band of CdS colloid to determine the radius of the colloidal Q-particle as shown in later chapter.

Usually the Brus' model will predict larger shifts in band gap with decreasing particle radius compared to experimental results. So Foitik and Weller et. al. proposed another model [29]. In their model the confined exciton is considered as an electron of reduced mass ($1/m_{e^-} + 1/m_{h+}$) moving in the

field of the potential energy walls, and the hole sits still in the center of the Q-particle. They get better agreement with experimental results.

1.5.7 Distribution Of Trapping Depths

The photochemical charge transfer reactions are often carried out in polycrystalline semiconductors such as CdS that contains trap sites inside the bulk or at its surface. We are interested in the distribution of the charge carriers between the conduction band (or valence band) and the trapping states, particularly the distribution of electron between the conduction band (or discrete states for Q-dots CdS) and its trapping states. Later we will show this distribution will have great impact to the electron transfer dynamics and actually is the origin of multi-exponential behavior of the observed time–resolved dynamics.

First let us define the trap depth of an electron trap as the energy difference between the bottom of the conduction band and the trapping level, one example is shown in Figure 1.5 for the depth of a deep trap. Though we may think that the deeper the depth is, the more effective the electron trapping is. However the entropy effect still need to be considered. Based on the concept of trap depth, several models have been proposed to describe the distribution of the electrons.

A simple approach is introduced by Grätzel [21]. It is assumed that the n_t trapping sites in the small semiconductor particle of volume V all have the same trap depth, or the same internal energy E_t. At electronic equilibrium, the chemical potential of the trapped electrons is equal to that of the free electrons

corresponding to the Fermi level of the semiconductor particle. Using this equilibrium condition, the distribution of electrons between the trapping sites and the conduction band is obtained as following equation:

$$\frac{N_{cb}}{N_t} = \frac{n_{cb}}{2(n_t - N_t)} \exp(-\frac{E_t}{kT}) \qquad (1.51)$$

or equivalently

$$N_t = \frac{\frac{2n_t}{n_{cb}} e^{\frac{E_t}{kT}}}{\frac{1}{N_{cb}} + \frac{2}{n_{cb}} e^{\frac{E_t}{kT}}} \qquad (1.52)$$

where n_{cb} is the number of accessible conduction band states, and n_t is the number of accessible electron traps. The N_{cb} and N_t correspond to the number of electron at the conduction band and at the trap states respectively. This equation shows, the number of trapped electrons goes up approximately exponentially with the trap depth. A typical case is as follows: If 50% of the electrons are trapped at 298 °K, and the n_{cb} =3600 and (n_t-N_t) = 100, the trap depth is evaluated as 0.072 eV.

This model gives an analytical equation about the electron distribution and is easy to understand. This gives a very good picture in concept about the distribution of conduction band electron and the trapped electron varies with the trap depth. The approach over-simplifies the matter by assuming all the trap sites have the same energy. In fact the trap sites may be in different

energy state, though they can be classified basically into two kinds: shallow and deep traps by later researchers. Later Mitchell [30] has done some detailed calculations.

1.6 Ion Solvation Dynamics At Interface Between Solid And Stockmayer Fluids

Stockmayer characterized the polar molecule by a Lennard-Jones particle with an embedded point dipole (Stockmayer model) in 1941 [31] to describe the thermodynamic properties of the fluid consisting of the polar molecules. Since then it has been an interesting topic in many areas, especially in theoretical studies due to the simplicity of this model.

One important issue of great recent interest is the solvation dynamics of a newly created ion in polar solvents. The dynamics is simplified theoretically as shown in Figure 1.6 using Stockmayer model to model the solvent and solute particles. Figure 1.6 (a) shows an individual neutral solute is initially in equilibrium with its surrounding Stockmayer solvents. Figure 1.6 (b) shows that at time t = 0, some charge q is suddenly produced on the solute, such as by electron transfer. The solute becomes an ion, and the system is not in equilibrium at this time. The system will evolve by reorganization of the solute and its surrounding solvent shell as time goes. Finally the system approaches a new equilibrium as shown in Figure 1.6 (c). The solvation dynamics under study is how the system evolves from Figure 1.6 (b) to (c). In other words, the process of suddenly creating a new charge on a individual neutral solute in the Stockmayer fluid solvents and then monitoring how the system evolves to

equilibrium. Usually this involves the reorganization by translational and rotational motion of the solute and solvents in the order of fs to ps time scale. Recent research on solvation dynamics of a newly created ion in polar solvent [32-35] is carried out by the investigation of the system response to a sudden change in the charge distribution of the solute or solute point charge. These studies includes theoretical and computer simulation [36-38] and some experiments [39-40]. However these approaches have only focused on the solute in bulk solvents.

In this dissertation, we extend the previous computer-simulation work of the solvation in the bulk Stockmayer fluids to the interfacial solvation between solid surface and Stockmayer fluids. We also extend the solute with no dipole to one with dipole. To our knowledge, this is the first attempt to study how the interface affects the solvation dynamics under different charges and dipole moments of the solute. The results obtained are significant in understanding the reorganization process for the solute and its surrounding solvation shell after the interfacial electron transfer. Thus the computer-simulation results compliment the experimental results in understanding the ion solvation after the electron transfer. However compared to experiments, the computer simulation offers some advantages in: (a) more flexibility in changing the parameters of the system and (b) smaller time scale that is not possible by current laser pulses.

Figure 1.6 The schematic diagram of solvation for a newly created ion: (a) an individual neutral solute in equilibrium with the surrounding solvents, (b) at time t=0, some charge q is suddenly created on the solute, (c) system approaches an new equilibrium after reorganization

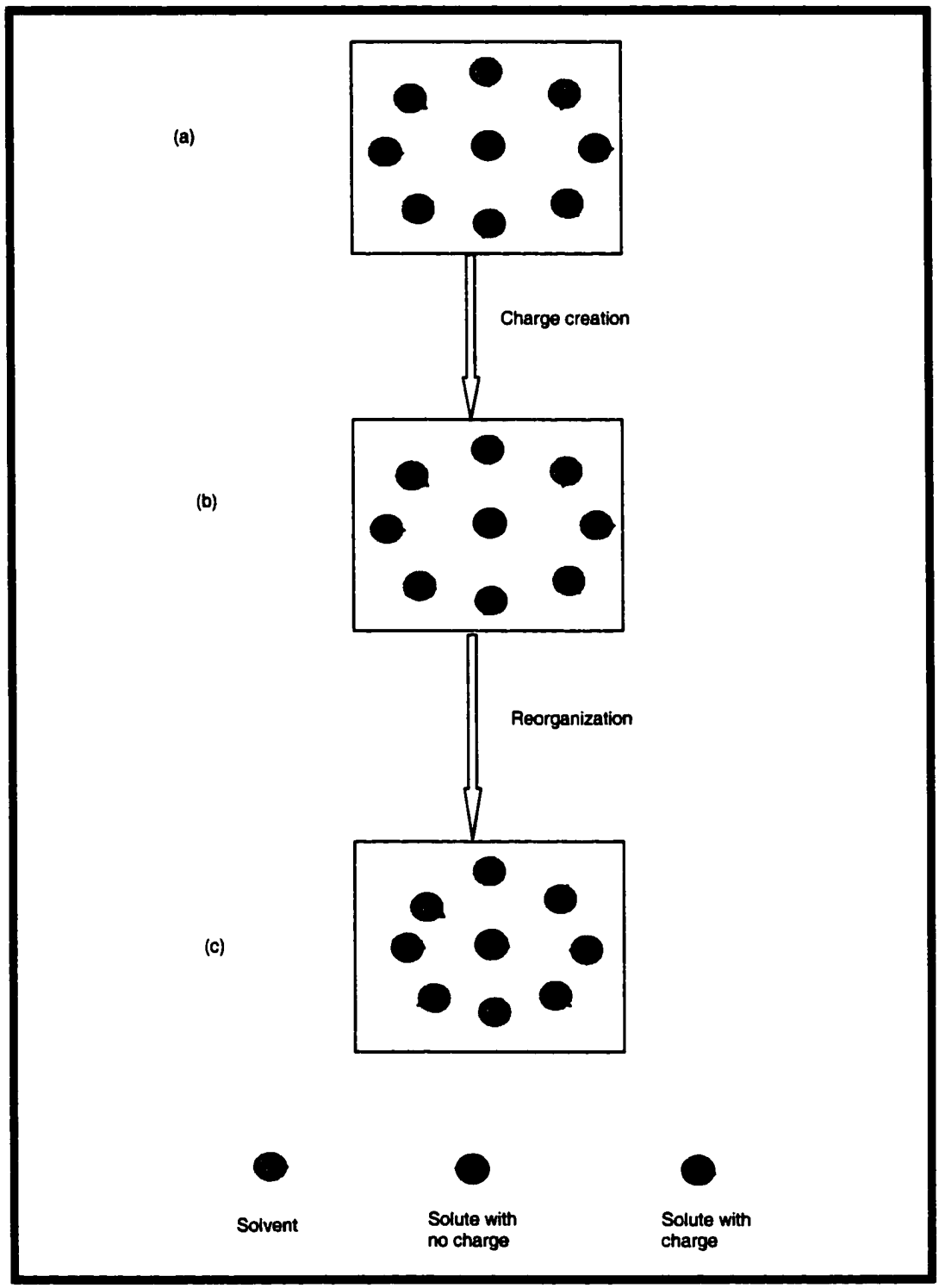

1.7 Organization of the Dissertation

After introducing the background of the methods and systems in this chapter 1, the experimental techniques used in time-resolved resonance Raman are described in chapter 2. The results and discussions are presented in three chapters: 3, 4, and 5, followed by a conclusion chapter 6. The femtosecond resonance Raman investigation of four univalent bipyridinium radicals is described in chapter 3. The femtosecond resonance Raman study of photo-induced interfacial electron transfer between colloidal CdS and methylviologen is presented in chapter 4. Molecular dynamics simulation of ion solvation dynamics at solid-Sotckmayer liquid interface is presented in chapter 5.

1.8 References

(1) Ferraro, J. R., Nakamoto, K. Introductory Raman Spectroscopy, Academic Press, Inc.: New York, 1994

(2) Struve, W. S. Fundamentals of Molecular Spectroscopy, Wiley and Sons: New York, 1989

(3) Long, D. A. Raman Spectroscopy, McGraw-Hill: New York, 1977

(4) Sension, R. J., Strauss, H. L., J. Chem. Phys. 1986, 85, 3791

(5) Mukamel, S., J. Chem. Phys.1985, 82, 5398

(6) Strommen, D. P., Nakamoto, K., J. Chem. Education 1977, 54, 474

(7) Frenkel, D. Smit, B., Understanding Molecular Simulation, from algorithms to applications, Academic Press, Inc: San Diego/NewYork: 1996; pp125-147

(8) (a) Allen, M. P., Tildesley, D. J., Computer simulation of Liquids Clarendon Press:Oxford; 1987; (b) Tironi, I. G.; Luty, B. A.; van Gunsteren, W. F. J. Chem. Phys.; 1997, 106, 6068-6075

(9) (a) Nosé, S. J. Chem. Phys., 1984. 81(1), 511. (b) Nosé, S. Molecular Physics, 1984, 52(2), 255

(10) Hoover, W. G., Ladd, A. J. C., Moran, B. Phys. Rev. Lett., 1982, 48, 1818

(11) Anderson, H. C. J. Chem. Phys., 1980. 72(4), 279

(12) (a) Steele, W. A.; Surface Science, 1973, 36, 317-352; (b) Steele, W. A.; Vernov, A. V.; Tildesley, D. J. Carbon, 1987, 25, 7

(13) Michaelis, L.; Hill, E. S. J. Gen. Physiol. 1933, 16, 859

(14) Pospisil, L.; Kuta, J.; Volke, J. J. Electroanal. Chem. 1975, 58, 217

(15) Van dam, H. T.; Ponjee, J. J. J. Electrochem. Soc. 1974, 121, 1555

(16) Bewick, A.; Lowe, A. C.; Wederell, C. W. Electrochim. Acta 1983, 12, 1899

(17) Bird, C. L.; Kuhn, A. T. Chem. Soc. Rev. 1981, 10, 49

(18) Bookbinder, D. C.; Wrighton, M. J. Electrochem. Soc. 1983, 130, 1080

(19) Lezna, R. O., Centeno, S. A. Langmuir 1996, 12, 591

(20) Seilmeier, A.; and Kaiser, W. In Topics in Applied Physics: Ultrashort Laser Pulses and Applications, Edited by Kaiser, W., Springer-Verlag Berlin Heidelberg, 1988, pp279-318

(21) Grätzel, M.; Heterogeneous Photochemical Electron Transfer, Chapter 3, CRC Press. Inc.: Boca Raton, Florida, 1989

(22) Marcus, R. A., Annu. Rev. Phys. Chem. 1964, 15, 155

(23) Landau, L., Phys. Z. Sowjetunion, 1932, 1, 88

(24) Förster, T., Naturwissenschaften, 1946, 33, 166

(25) Dexter, D. C., J. Chem. Phys., 1953, 21, 836

(26) Hopefield, J. J., Biophys. J., 1977, 18, 311

(27) De Vault, D., Rev. Biophys. 1980, 13, 387

(28) (a) Brus, L. E., J. Chem. Phys., 1984, 80, 4403; (b) J. Chem. Phys., 1983, 79, 5566

(29) (a) Foitik, A., Weller, H., Koch, U., and Henglein, A., Ber. Bunsenges. Phys. Chem. 1984, 88, 969 (b) Weller, H., Schmidt, H. M., Koch, U., Foitik, A., Baral, S., Henglein, A., Kunath, W., Weiss, K., and Diekmann, E. Chem. Phys. Lett. 1986, 124, 557

(30) Mitchell, J. W., Photo. Sci. Eng. 1983, 27, 3

(31) Stockmayer, W. H. J. Chem. Phys., 1941, 9, 398-402

(32) Maroncelli, M;. J. Mol. Liq. 1993, 57, 1

(33) Ultrafast reaction dynamics and solvent effects, AIP Conference Proceedings, Edited by Gauduel, Y.; Rossky, P. J.; vol. 298, AIP, New York, 1994

(34) Structure fluctuation, and relaxation in solutions, Thematic issue of J. Mol. Liq.; 1995, vol. 65-66

(35) Stratt, R. M.; Maroncelli, M;. J. Phys. Chem. 1996, 100, 12981

(36) Day, T. J. F.; Patey, G. N.; J. Chem. Phys. 1997, 106, 2782

(37) Graf, P.; Nitzan, A.; Chem. Phys.1998, 235, 297

(38) Neria, E; Nitzan, A.; J. Chem. Phys. 1992, 96, 5433

(39) Horng, M. L.; Gardecki, J. A.; Papazyan, A.; Maroncelli, M.; J. Phys. Chem. 1995, 99, 17311

(40) Cho, M.; Rosenthal, S. J.; Scherer, N. F.; Ziegler, L. D.; Fleming, G. R.; J. Chem. Phys. 1992, 96, 5033

CHAPTER 2 EXPERIMENTAL TECHNIQUES

2.1 Experimental Transient Raman Spectroscopy at Interfaces and Solutions: The Problems And Solutions

Normally we want to obtain observable and discernable signals in experiments. For example in our Raman spectra, an observable spectral intensity and discernable Raman band in wavelength are required. However, there are some problems the experimental scientists will encounter in running experiments to investigate ultra-fast phenomena in liquid solutions compared to gaseous phase, and these problems becomes more prominent at interfaces. The following describes the problems that add some difficulties in our experiments.

1) To start with, it is not so easy to generate an experimental observable amount of the species in transient state. Compared to bulk liquid study, even species in ground state is not so easy to achieve at interfacial study. In our example of studying the interfacial electron transfer between CdS(s)||methylviologen (aq, polymer), the methylviologen mono-ion (MV^+) is the radical species produced by the electron transfer. It is used in return to trace the dynamics of this electron transfer process. In principle, we would like to generate large ensemble of these MV^+ to increase signal. But in practice, its amount is very small since only the methylviologen (MV^{2+}) adsorbed on the interface is ready to be converted to MV^+ and the adsorbed MV^{2+} is only a small part of the very diluted MV^{2+} solutes in bulk solution. The MV^{2+} in solution has to be very diluted to keep the CdS colloidal particles from

aggregation. This drives us to seek higher power of laser pulse by using femto-second laser and to adjust laser wavelength to get more enhancements in Raman spectroscopy as shown later (see chapter 4). Even so for some species with structure similar to the MV^{2+} it is not possible to achieve similar studies as we have done for MV^{2+} limited to the adjustability of the wavelength and other experimental conditions, even though we tried hard. This shows the study of the interfacial transient phenomena is more challenging than that in bulk liquids.

2) The second difficulty in studying the energy transfer between molecules in liquid lies in that the basic steps of energy transfer is very difficult to observe, because the relaxation processes appears very fast in solution. The typical collision frequency in a liquid [1] is 100fs. The solute carrying excess energy has a lot of chances to transfer energy at every 100fs. So many interesting processes in liquid phase occur on the sub-picosecond time scale.

3) There exists the third difficulty in studying relaxation processes in the condensed phase results from the various broadening mechanisms, which causes broader transitions than these in gaseous phase. The range of static microscopic solvent configurations of the molecule in solution [2] is one effect of line broadening, because the gap between the potential energy surfaces of the ground and excited electronic state differs for each microscopic solvent configuration. This type of broadening is not directly related to dynamical processes, however the other effect of line broadening induced by collision is important in solution. Collision will cause shorter lifetime of the molecular

state and therefore broaden the transitions by uncertainty principle $\Delta E\ \Delta\tau \sim h$. In inelastic collisions in solution the molecular quantum state denoted by quantum number changes. The inelastic energy transfer causes population relaxation processes with an exponential lifetime of T_1 of the quantum state, which is an important quantity in our TRRR experiments. T_1 frequently denoted as vibrational energy relaxation (VER in the dissertation), is smaller in solution compared to gaseous phases, because the collision is more frequent in condensed phase.

The other contribution to the collision-induced line broadening is from quasi-elastic collisions. In quasi-elastic collisions, only the phase of the molecular wave functions is disturbed, which is also called T_2 de-phasing process. (Note: T_1 frequently denoted as vibrational energy relaxation (VER in the dissertation). T_2 means de-phasing process. In the early literature, the term, vibrational relaxation, is used to denote both processes.) The de-phasing processes caused by the very fast environmental fluctuations will broaden the energy levels of each molecule [2], and thus referred as homogeneous broadening.

Both inelastic and elastic collisions will reduce the lifetime of the molecular quantum states, however the homogeneous collisions due to the rapid solvent fluctuations are frequently the most detrimental broadening mechanism to spectroscopist.

For example the 100fs collision interval in a liquid solution will cause a homogeneous broadening of 50 cm^{-1}. The spacing between the vibrational

transitions of some molecules is less than 50 cm^{-1} .It is obvious that this add difficulties for vibrationally resolving absorption or fluorescence spectroscopy.

2.2 Femto-second Laser System and Time-resolved Raman Spectrometer

As shown the diagram [3] for the femto-second laser system in Figure 2.1. The system is composed of a synchronously mode-locked femto-second dye laser pumped by the second harmonic generation of compressed mode-locked YAG pulse train and a Ti:sapphire amplifier using chirped-pulse-amplification technique. It will output laser beam of typically 0.2mJ pulse energy with 350fs-time duration, at 760nm (typically tunable) for a repetition rate of 1kHz. It has the advantages of relatively high repetition rate, high pulse energy, relatively tunable and stable.

The train of laser pulses from the mode-locked Nd:YAG laser is frequency-doubled to get its second harmonic of the laser pulses. These laser pulses are then used as the pump for the femto-second dye laser system. The output pulses from the dye laser is then amplified by Ti:sapphire amplifier using chirped-pulse-amplification technique. These are described in more detail as follows.

The Quantronix 416 ML YAG laser generates train (repetition rate 100MHz) of 80ps pulses with a power of 5W at wavelength 1064nm that are compressed by a fiber-grating compressor to 5ps with a power up to 2.2W. After the second harmonic generation from the KTP a green beam at wavelength 532nm of up to 800mW with 3-4ps pulses is obtained. Typically

Figure 2.1 Femto-second laser system used in our experiment

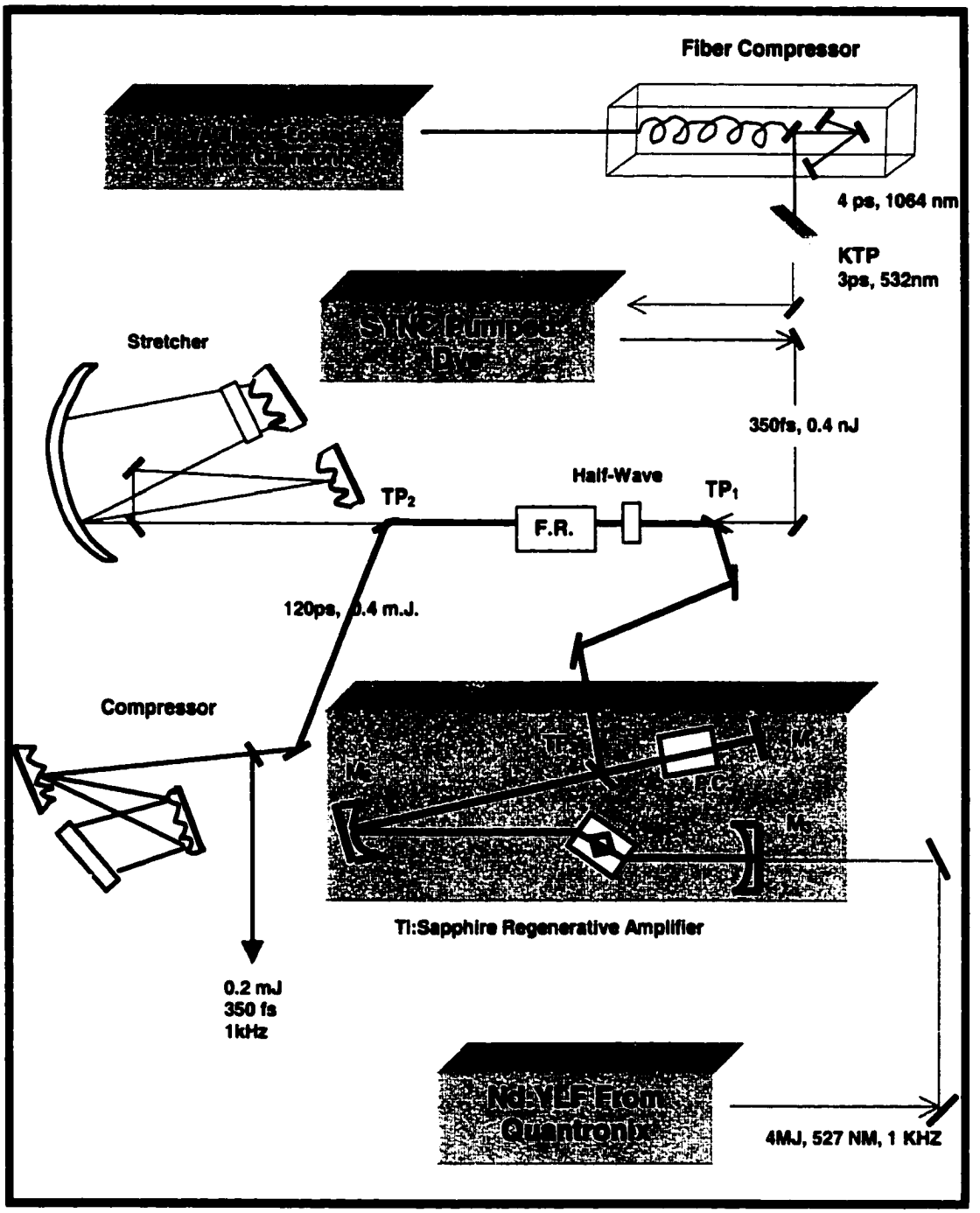

600mW of this green at 100MHz repetition rate serves as a pump beam for the styryl-8- dye laser that is home-made in our lab. The dye laser absorbs 85% of the green pump power (by choosing the dye concentration) and produce 80mW output power at 760nm wavelength of pulses of 350fs duration, when the output coupler has 17% transmission. The dye laser wavelength is adjustable from 720nm to 780nm.

The chirped-pulse-amplification is accomplished by first stretching the pulse width by a pulse stretcher. The pulse then goes through the cavity of a regenerative amplifier that is pumped by a Quantronix 527 Nd:YLF Q-switched laser to amplify the pulse energy. Finally the width of the amplified pulse is compressed back to its original width using a pulse compressor. In addition a half-wave plate and a 45-degree Faraday rotator (F.R.) in tandem with two thin-film polarizers (TP_1 and TP_2) are used to adjust the pulse destination by changing the pulse polarization.

The regeneration amplifier cavity consists of a three mirror (M_1, M_2, M_3) folded resonator with folding angle of 6 degree.

The focus length of M_1 is 25cm, and that of M_2 is 75, and M_3 is flat. In the cavity of the regeneration amplifier, there is a combination of Pockels cell (P.C.) with a thin-film polarizer (TP_3) used to switch the pulse in and out of the cavity through the change in birefringence property of the Pockels cell. The Ti:Sapphire crystal in the cavity absorbs 80% of the pumping light of 527nm wavelength from a Quantronix 527 Q-switched YLF laser. When 2.8 W of green power (527nm) is absorbed by the crystal at 1KHz pumping rate, the

regeneration amplifier will output red power (760nm) of 350mW. After the red light going through the compressor, 230mW of red light at a repetition rate of 1kHz with pulses of 350fs duration is available. It should be noted the red output depends on the wavelength, at 820 nm, up to 400mW of red is achieved. This femto-second red light is then frequency doubled to be used in the Raman experiments after second harmonic generation (see Figure 2.2 for pump-probe technique).

The time-resolved resonance Raman experiment is carried out by a pump and probe technique through the optical configuration illustrated in Figure 2.2. As shown in the Figure 2.2 the red 759 nm ultrashort (350fs) laser pulse from our femto-second laser system (Figure 2.2) is first converted by a BBO crystal partially into violet light with double frequency (379.6nm). A beam splitter then separates the mixture of the red and violet, and the red is dumped and the violet is used. A very small part of this violet is reflected to a diode by a thin plate of nearly transparent organic glass. Through the diode the fluctuation in this laser intensity is picked up and sensed by the computer. If the intensity of the laser intensity or the pulse energy is below a previously given value, the data resulting from this pulse is discarded and not counted in the Raman signal obtained in the following to achieve a much higher signal to noise ratio.

Most of the violet (typically with a pulse energy of 20 μJ) passing through the glass and is splitted into two beams, namely pump and probe beams, by a beam splitter (B. S.). Both the pump and probe beams are of the

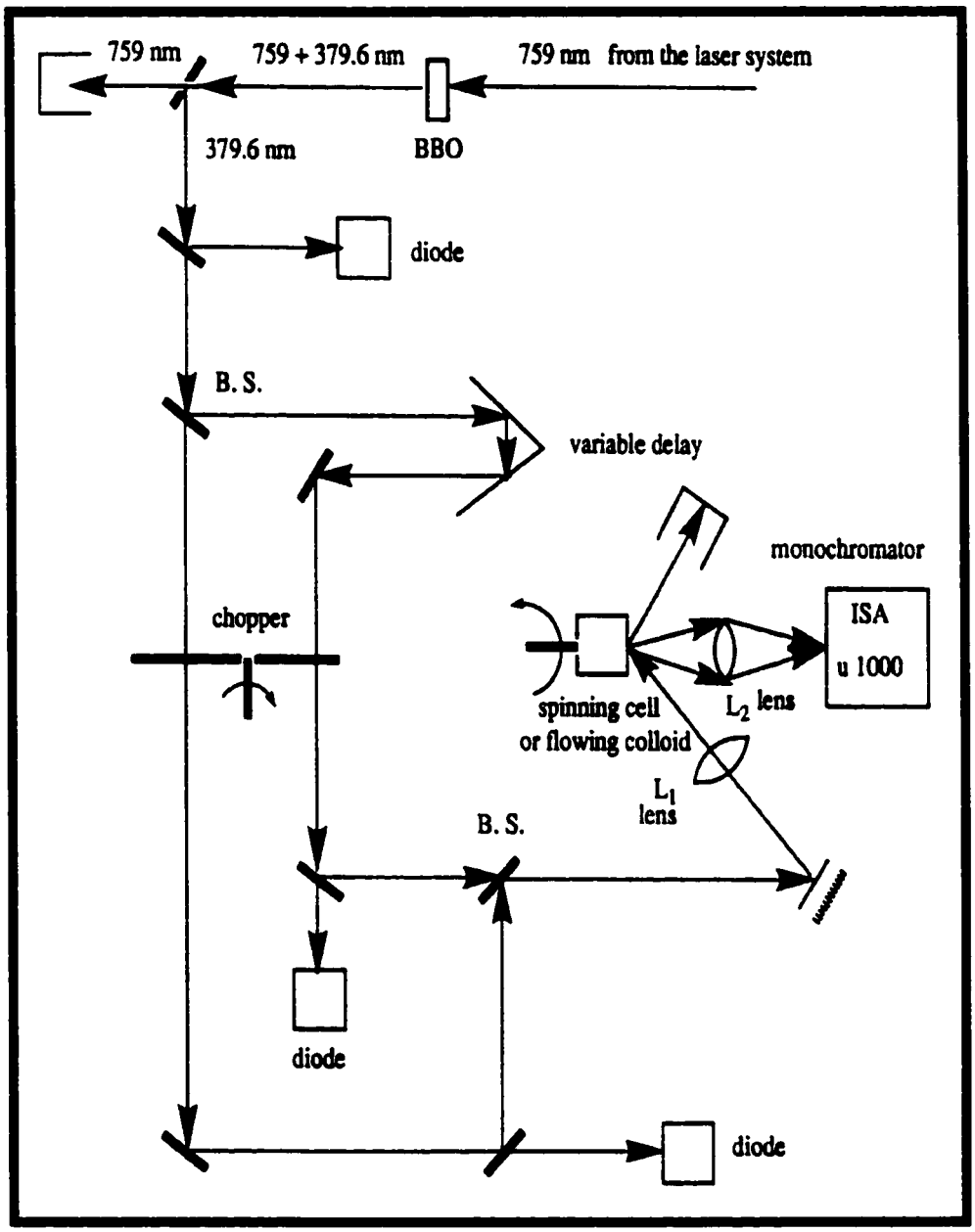

Figure 2.2 Experimental setup for pump-probe TRRR

same color (379.6nm). The wavelength is chosen so that the bipyridinium ion (radicals) will have resonance enhancement as shown later in the study of both interfacial electron transfer between CdS(S, colloid)||methyl viologen and the study of relaxation dynamics for bipyridinium radical ions in aqueous solutions.

After a beam splitter, each beam will travel different distance by letting a beam travel a fixed distance while another beam travel a variable distance by a variable delay line. The delay line consists of a stepper motor to drive the lead screw on which a reflector is assembled. The computer controls the motor to let the reflector to go successive distances. The optical reflector will bounce the beam left to right and then back over the distances carefully determined by the computer. Since a travel time of 1ps is 0.3 mm distance, this simple method controls the distances traveled by the two pulses, thus implements the delay time range of femtoseconds to picoseconds for the two pulses. Scanning the variable delay to change the distance one beam needs to travel is equivalent to scanning (changing) the delay time, thus different delay time is achieved.

After the mechanical chopper, the two beams (pump and probe) are then recombined by a beam splitter and then focused to the sample by a 15 cm focusing lens to obtain Raman scattering at different time delay. The beam hits the sample in the cell at an angle of 70 degrees to the vertical direction of the optical cell, i.e. the collecting direction.

The Raman scattering signal is collected by a f /1.0 lens at the wavelength. We use a dispersive monochromator (ISA μ1000) of 1-meter and double gratings to select the wavelength of the scattering light. A cooled photomultiplier tube (PMT; RCA C31034A) is used to image the dispersed light at the exit slit. The resulting PMT signal is treated by a gated integrator (Lecroy 229SG converter) and then kept in the computer. The computer also controls the movement of a stepper motor controller (Daedal PC-400-1F), which drives both the monochromator scan to obtain the Raman spectra and the translation stage controlling the time delay between pulses to obtain the time-resolution of dynamics.

The signal obtained by gated integration contains the contribution from the transient species, as well as that from the ground-state equilibrium species. If there is no multi-photon effects, the data signal point collected consists of three origins: Raman scattering, fluorescent background, and electronic background from PMT and other related electronics. When pump beam and probe beam illuminate together in combination on the sample, the data points collected may be contributed by the following six parts, depending on the molecular states (excited or ground state) and the kinds of laser pulses (pump or probe) as shown in Table 2.1.

Contributions from the ground equilibrium species must be subtracted to obtain the pure transient spectrum. To achieve this goal, the chopper shown in Figure 2.2 and subtraction method are used.

Table 2.1 Molecular states and data signals collected

Data Signals Collected	From states	Produced (generated and probed) by laser pulse
Weak Raman scattering	Excited states	Pump pulses
Weak Raman scattering	Excited states	Probe pulses
Strong Raman scattering	Ground states of solutes and solvents	Probe pulses
Fluorescent background		Probe pulses
Fluorescent background		Pump pulses
Electronic background noise		

As shown in the Figure 2.2, each of the pump and probe beams can be chopped mechanically by a chopper at 1KHz. Since the chopper is designed to synchronize with the repetition rate (1kHz) of the laser pulses, it has the advantage of no pulses will be partially blocked. The chopper controls which beam can incident on the samples: that is, pump and probe combined, pump only, probe only, and no beam (both beams chopped). So at one scan of the monochromator or the translational delay stage we collect four wave number-

resolved spectra or time re-solved dynamics respectively for the cases: pump-probe, pump only, probe only and background (no pulses). Two photo-diodes are used to sense the on or off of the beam by passing the very small piece of the pump or probe beam to it. The computer uses this information to classify the data from each pulse into one of the four bins corresponding to four beam combinations for the pump and probe as above and following. The pump-probe beam combined incident on the sample will be sorted to produce pump-probe spectrum. The pump beam only incident on the sample will be sorted to produce pump-only spectrum. The probe beam only incident on the sample will be sorted to produce probe-only spectrum. The no beam incident on the sample (all blocked) will be sorted to produce background spectrum. So by chopping the beams, we are able to separate the Raman scattering signals from pump-probe beam, pump beam only, probe beam only and background. Subtraction the pump-beam signal and the probe-beam only signal from the pump-probe beam signal, the Raman signals from the excited states at various relaxation times are isolated.

Using this subtraction or the difference spectrum technique (pump and probe – pump only – probe only) allows us to get a pure transient Raman. This technique features our experiment in isolating the transient spectrum or dynamics from the data originating from unexcited species or dynamics within the pump or probe width. Therefore any characteristic emerging outside the noise level in this data is contributed by the transient species or dynamics produced by the pump pulses and is characterized by the time delay. The

bleaching of ground states by photoexcitation will result in a negative transient band. On the other hand, the creation of a new band by the excitation pump will produce a positive transient band. The description of a transient band in terms of its magnitude relative to the magnitude of the corresponding pump-only and probe-only band has been proven very useful in later chapters and also as in many experiments in this group.

It is worth mentioning that the time resolution is determined by the delay time and limited to the smallest scale of laser pulse duration (350fs). At best we can get a dynamics of around ~350 fs of our laser time duration, otherwise the two pulses begin to overlap in time if the delay time is less than 350 fs. Furthermore, we don't need electronics with femtosecond or pico-second responses to do the time-resolution experiment. At a delay time of 1ps, we mean the arrival of the probe pulse is delayed by 1ps to pump pulse caused by the mechanical translational stage (notice light speed in vacuum is 0.3 mm per pico-second, a mechanical translation of 0.3 mm will cause 1 time delay of 1 ps.). So the data point of Raman scattering corresponds to the molecule that has relaxed for 1 ps. after pump excitation. Do successive scan of the time delays, we get the time-dependence of the Raman scattering.

The signals resulting from different pulses (that is either pump or probe pulse) illuminating on the sample are classified to corresponding data by the computer using the methods described previously. Each wave number - resolved data (spectrum) or time-resolved data (dynamics) normally needs about five minute's scans in wave number or delay time respectively. Typically

we do twenty of scans and then add the data of each scan together to average out the pulse to pulse fluctuation in the signal by the computer. Thus the total time to get one spectrum or time-resolved dynamics needs order of hours. Remember that pulses with energy beyond the given range (typically smaller than 20% or larger than 80%) are discarded, so if the laser pulses are unstable in power, it will take more time to get a spectrum. Each data point thus obtained in the spectrum or time-resolved dynamics is the result of 4000 to 6000 (note each spectrum contains many data points) laser pulses illumination.

The control of pump-probe delay and mono-chromator scanning, the sensing whether it is pump pulse or probe pulse or pump-probe pulse incident on the sample for a given laser shot, and the collection of data are completed by a computer (PDP 11/03L). The software to collect data, to control experiment, and to analyze data was previously written by Dr. J. B. Hopkins in Fortran and assembler and has been proved functionally well by the previous experiments in this group [3]. We have also used some recent commercial software (Microsoft Excel and DataFit from OakDale Engineering) to analyze data by PC.

To achieve best Raman spectra and the dynamics diagram for Raman intensity as a function of time, the following experimental details are experienced.

First, to achieve the highest Raman signal of transient state or species, the pump and probe beams must have an excellent overlap in space so that

the probe will be exactly travel the space the pump travels. It takes a lot of time for us to get experienced in overlapping (or combining) the two beams into spatially one beam. The trick is using two pinholes of certain distances and let each of the beam goes through the straight line defined by the two pinholes. Then let the "overlapped" beam hits a name card (a paper that will emit fluorescent upon laser illumination.) that is located in a comparable distance as the cell containing the sample. Check the sizes of the beam on the name card produced by the beams of pump, probe and pump-probe. If the sizes of the beams are the same and are located at the same center, a good spatial overlap is achieved.

Next to get the precise time-resolved dynamics, it is necessary to determine the accurate time delay between pulses for calibration of the optical delay. We first use fishing line to measure the optical path of the two beams, which gives us a delay of the order of hundred pico-seconds. Then we adjust the translational stage used for mechanical delay to find the zero of delay time. That is when the two overlapped beam having a delay time zero, a coherent interference phenomena that gives a picture of alternate light and dark stripes, will be shown on the spot of the name card above. As long as we see this phenomenon, we know we get the time zero. The symmetry of our one color pump and probe method described previously verifies this zero of time also. That is to say, the transient dynamics is symmetry with respect to the time zero.

Third, it is very important to focus the beam as tight as possible to get enough transient state or species. But too tight beam focusing will result in plasma (very bright strong light emission of a mixture of different wavelength) that will prevent us from obtaining useful Raman signal. Typically a beam size of around ~0.5 mm is appropriate in diameter at the sample.

Finally, to reduce the false dynamics caused by the multi-photon effect in the transient dynamics experiment. We have collected the data points by fixing mono-chromator at a wave number of the center of the strongest Raman band and at another wave number near by of no Raman band. It is expected the false dynamics produced by the multi-photon production will be similar at both wave-numbers. So a subtraction of the no-Raman-band data from the center-of-Raman-band data reduces or even eliminates the false dynamic. This way we are convinced that the transient dynamics obtained is free of the false dynamic caused by the multi-photon effect.

2.3 General Methods in Experiments and Result Analysis

When an ultra-short laser pulse is applied to Raman spectroscopy, we have ultra-fast time-resolved Raman spectroscopy. The normal Raman signal is intrinsically weak, thus resonance enhance is required to increase the signal to noise ratio for the purpose of studying species of low concentration. This time-resolved resonance Raman is usually called TRRR or TR^3. TRRR has been proven to be one of the useful methods to characterize the structural information of molecules, especially transient reaction intermediates [4].

2.3.1 Methods For Production Of Bipyridinium Monovalent Radicals

The bipyridinium radical ions are very sensitive toward O_2 oxidation in the air. The preparation and use of the radicals must be accomplished under strictly observed anaerobic conditions. In our experiment of studying the vibrational relaxation of the bipyridinium radicals, the preparation is carried under a N_2 box and then transferred to a cylindrical optical cell. The cell is sealed tightly to prevent O_2 contact as described in chapter 3. On the other hand, to oxidize the monovalent radicals back to the corresponding bivalent viologen ions, an optical cell that allows the radicals open to O_2 in the air is used in the study of the interfacial electron transfer in chapter 4.

Current procedures to prepare the mono-valent radical include (a) chemical reduction of the viologens (bivalent ions) by strong chemical reductants such as $Na_2S_2O_4$ and Zn [5]; (b) photoreduction such as reducing MV^{+2} byproflavin and excess EDTA [6]; (c) electrochemical preparation [7]. Here only the methods used in this dissertation are mentioned, for detailed information about the preparation see reference (8).

2.3.1.1 Chemical Reduction

The chemical reduction procedures are effective, but have some limitations. First, the reagents/reductants are strong enough to produce irreversible reduction [9] to neutral species of viologens beyond their redox-active, free-radical (semi-quinone) state. For example, excess Zn may produce neutral MV by the following equation:

$$MV^{+2} + Zn \rightarrow MV + Zn^{+2} \quad (2.1)$$

instead of radical $MV^{+\cdot}$ by

$$2MV^{+2} + Zn \rightarrow 2MV^{+\cdot} + Zn^{+2} \quad (2.2)$$

It is noted that there is a reaction

$$MV^{+2} + MV = 2MV^{+\cdot} \quad (2.3)$$

Care must be taken in using the amount of the strong reductants according to ratio of the viologen bivalent ions to the reductants in the above equation. Too little amount of the reductants will leave unreacted, oxidized viologen present, however excess generates the irreversibly reduced dihydroviologens.

Second, the chemical reduction will produce by-products due to the viologen reduction reactions. In the case of the use of Zn and $Na_2S_2O_4$, the possible by-products include Zn^{+2}, $Zn(OH)_2$, SO_3^{2-}, SO_4^{-2}, $S_2O_3^{2-}$, S^{2-} etc depending on the pH and other conditions. In our experiments, we start with neutral (pH=7) solution, the possible by-products such as SO_4^{-2} does not show significant effects in the Raman spectroscopy mainly because their intensity is not resonance enhanced.

2.3.1.2 Photo-Reduction

Even though the radicals can be prepared by photo-reduction in bulk solution solution [10]. Our interest also includes the photo-production of $MV^{+\cdot}$ at semiconductor CdS(s) and aqueous solution interface [11]. The laser pulse excites the electrons in the valence band to the conduction band of CdS. The MV^{+2} is then reduced to $MV^{+\cdot}$ by the conduction band electron as shown in the following Figure 2.3. One of the purposes of the dissertation is to study the

interfacial electron transfer dynamics. Unlike the electron transfer from TiO_4 to MV^{+2}, which is relatively slow, the electron transfer from CdS to MV^{+2} is very fast and the dynamics has not been resolved yet. This is possibly due to the conduction band electrons of CdS has higher energy than that of TiO_4. Therefore the over-potential is greater to drive the reduction of MV^{+2} and the electron transfer is faster. As shown later in chapter 4, it is very harder to produce significant amount of the transient $MV^{+\cdot}$ by the photo-induced electron transfer. The laser wavelength and the sample have been carefully chosen to maximize the measured dynamics signal.

2.3.2 Methods For Producing Ground And Photo-Excited Bipyridinium Radicals In Solution

The methods to prepare the photo-excited vibronic states of bipyridinium radicals is based on the electron energy levels, which is revealed theoretically by HMO and experimentally by the absorption spectra. The MV^+ and other bipyridinium mono-valent ion solution absorb in red region resulting in blue-violet color. Their corresponding neutral species shows pale yellow color due to the absorption of short wavelength at the end of the visible region. Use MV^+ radical as an example, the absorption spectra of the MV^+ radical [12] and the absorption spectra of electrochemically generated $MV^{\cdot+}$ in acetonitrile solution [13] exhibit two important characteristics. First, there is a relatively weak visible absorption[12] (λ_{max} = 605nm, ε_{max} = 10060) that produces the blue-violet color of the solution. Second, there are three additional strong absorption bands overlapped occurring

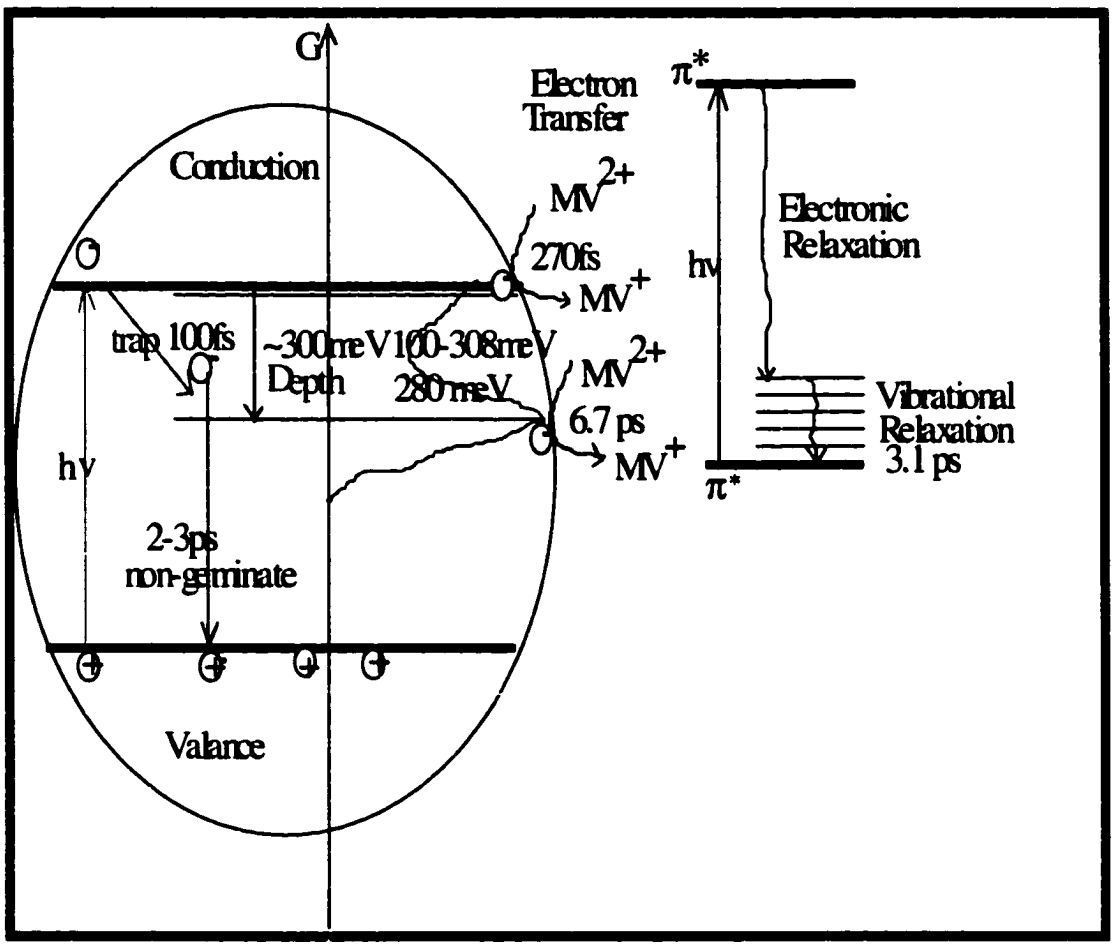

Figure 2.3 Photo-reduction of MV^{+2} to $MV^{+\cdot}$ at interface

between 360-400nm consisting of absorption bands centered at 399nm, 385nm and 368nm at the end of visible range. However unfortunately, no consistent assignments of the absorption bands to the electron energy levels exist yet to our knowledge. Basically there are two different approaches to the energy level diagram as represented by the Kosower and Cotter's papers [12,14] and Zahradnik, Carsky & Hünig's papers [15, 16]. In Zahradnik, Carsky & Hünig's papers the HMO scheme of electron energy levels of biphenyl radical anions ($BP^{\cdot-}$) is introduced. The absorption spectra of the $BP^{\cdot-}$ are very similar to those of 4, 4'-bipyridyl radical ions ($BPy^{\cdot-}$) or bipyridiniums. It is expected that the MO energy level diagram of bipyridinium are similar to that of the $BP^{\cdot-}$ because they all have the same ioselectronic π–system. Figure 2.4 shows the π-orbital energy diagram and the corresponding transitions in the visible, ultraviolet and infrared ranges.

According to Zahradnik, Carsky & Hünig's papers as shown in Figure 2.4, both 610 nm band and the 399 nm bands are contributed by $\pi^* \rightarrow \pi^*$ transitions. The absorption band at 610 nm is assigned to the transition from MO 7 with B_{3u} symmetry to MO 10 of B_{2g} symmetry. The absorption at 399 nm having fine structures at 385 nm and 368 nm is assigned to the transition from MO 7 (B_{3u} , π^*) to MO 11 (B_{3u} , π^*), which is used in our experiment to prepare the photo-excited states in the vibrational relaxation study and to achieve Raman enhancement (See Figure 2.4). The fine structure maybe due to different vibrational states. The energy gap between 399 nm and 385 nm is about 910 cm^{-1} and that between 385 nm and 368 nm is about 1200 cm^{-1}. It is possible that

the two wave numbers correspond to bipyridinium ions' vibration at 1214 cm^{-1} and 816 cm^{-1}. Both vibrations have something to do with the stretching mode between the nitrogen and its substitution groups. In addition to the two main bands (610 nm and 399 nm) in the visible range, the other transitions will result in bands either in near infrared or in ultraviolet range as shown in the table at the bottom of Figure 2.4.

Table 2.2 The transitions for $BP^{\cdot-}$ and bipyridinium radical ions ($BPy^{\cdot}$) having D_{2h} symmetry according to Zahradnik, Carsky & Hünig's papers.

Transitions		Transition energy and wave-number (cm^{-1})	Corresponding absorption band (nm)
From orbital number (symmetry)	To orbital (symmetry)		
7 (B_{3u} , π^*)	10 (B_{2g}, π^*)	0.6 and 15250	610
7 (B_{3u} , π^*)	11 (B_{3u} , π^*)	1.2 and 30500	399, 385, 368
7 (B_{3u} , π^*)	8(B_{1g} , π^*) or 9 (A1u , π^*)	0.3 and 7600	Near IR range
6 (B_{2g} , π)	7 (B_{3u} , π^*)	1.4 and 35600	(~250nm) ultraviolet

On the other hand, according to Kosower and Cotter's papers [14,15] these features in the absorption spectra can be explained in a semi-quantitative way in terms of the molecular orbital theory, by considering how the insertion of the nitrogen into a ring position of the benzene will affect the disposition of the energy levels. The approximate electronic energy levels of the MV^+ radical are shown in the following (Figure 2.5). Of the six π-levels of benzene illustrated on the left there are two pairs of degenerate levels. Inserting the nitrogen "splits" these levels, resulting in the potentiality of two transitions in the energy range for which there is only one for benzene. The combination of the energy levels for the two pyridinyl groups give rise to these for MV^+ radicals illustrated on the right hand

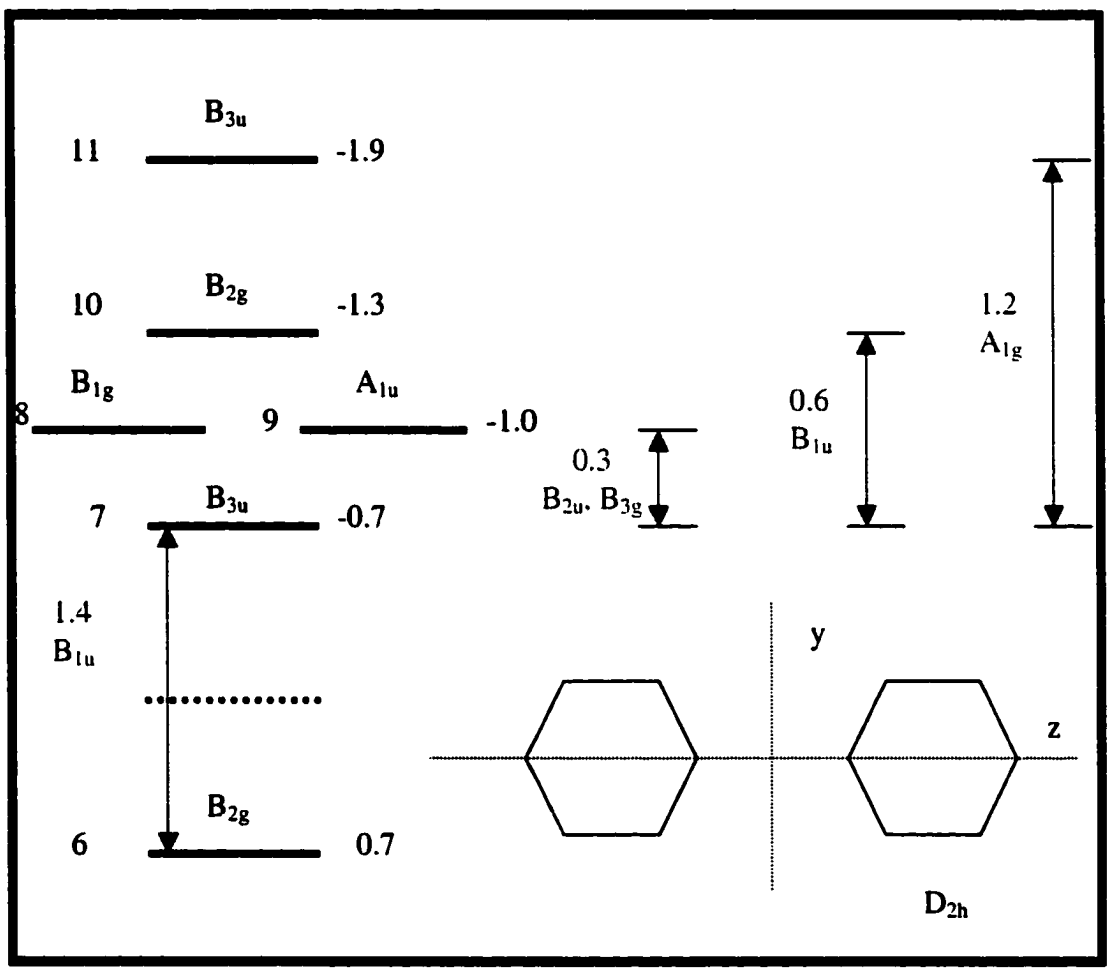

Figure 2.4 The electron energy levels for $BP^{\cdot-}$ and bipyridinium radical ions ($BPy^{\cdot+}$) having D_{2h} symmetry according to Zahradnik, Carsky & Hünig's papers.

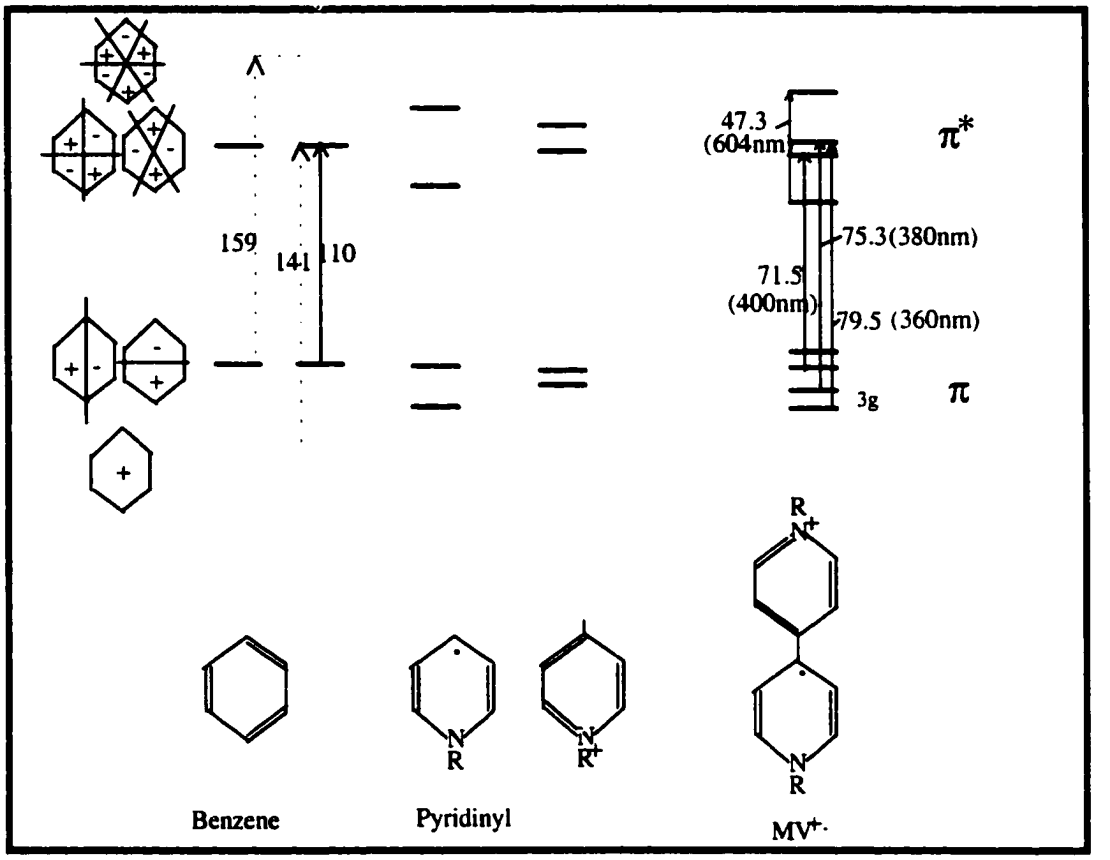

Figure 2.5 Electronic level diagram for MV^+ based on the data in the experimental absorption spectra and the provisional energy levels for benzene and pyridinyl radicals(Values are given in kcal/mole and nm, and 1 kcal/mole = 3.498×10^{-5} $(nm)^{-1}$, R = CH_3) [14]. On the left are the diagrams showing the molecular orbitals for the six π levels of benzene. There are two pairs of degenerate (equal energy) levels for benzene, which become split on N-insertion to form pyridinyl radicals. The combination of the two pyridinyl groups gives the energy levels for MV^+ radicals. This level scheme is qualitative, however gives a good understanding of the spectra and behavior of the MV^+ radical. The lower part lists from benzene, pyridinyl radicals to $MV^{+\cdot}$ radicals.

side of the Figure 2.5. Thus there are three strong absorption bands in the range of 360-400nm due to π to π^* transition. Furthermore, the highest occupied level of the MV^+ radical contains a single unpaired electron which results in the low energy weak π^* to π^* transition of 604nm.

From the above review, though both research groups agree that band at 604-610 nm is ascribed to the $\pi^* \rightarrow \pi^*$ transition of the free electron, they disagree the assignments to the band around 399 nm with shoulders at 385 and 368nm. Kosower and Cotter's papers assign it to the $\pi \rightarrow \pi^*$ transition, but Zahradnik, Carsky & Hünig's papers assign it to the $\pi^* \rightarrow \pi^*$ transition that is used by Feng [13]. Of course, it is necessary to do further work to identify the electronic transitions corresponding to the absorption bands to resolve the confliction.

The above is the basic background we have in our mind for the diagram of the energy levels of bipyridinium radical ions. In our experiment, we use the laser pulses of 379.5 nm, that is a very close match to absorption band at 390 nm to excite the species from electronic ground state to an electronic excited state (see Figure 2.6). The species are excited electronically from ground state of 7 (B_{3u} , π^*) to excited state 11 (B_{3u} , π^*) using Zahradnik, Carsky & Hünig's terminology, or from a π ground state to a π^* excited state using Koswer's terminology. Regardless of the different assignments of the electronic ground and excited states, the electronic excited state relaxes quickly (not observable) to the electronic ground state (see the following Figure 2.6). It is this electronic

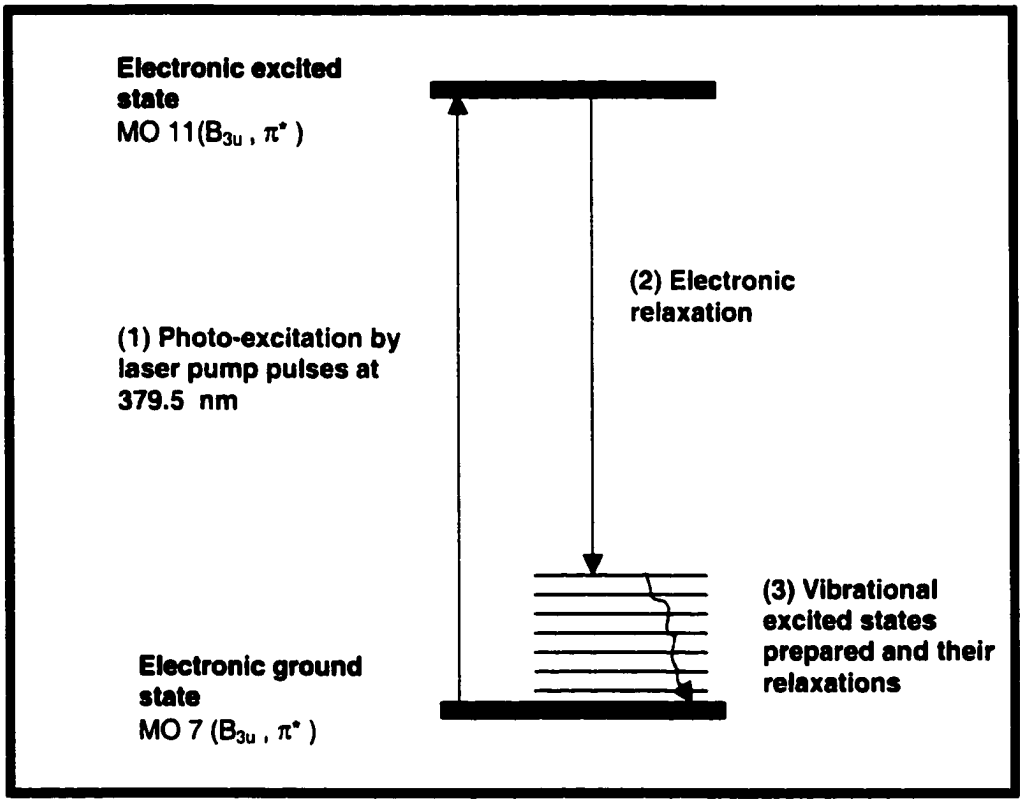

Figure 2.6 Schematical diagram for preparation of the vibrationally excited state at the electronic ground state. First the transition from electronic ground state MO 7 (B_{3u}, π^*) to excited state MO 11(B_{3u}, π^*) is induced by a laser pump pulse. Second the excited state MO 11(B_{3u}, π^*) rapidly relaxes back to ground state MO 7 (B_{3u}, π^*) producing highly excited vibrational levels in the electronic ground state. Finally the excited vibrational levels in the MO 7 (B_{3u}, π^*) electronic ground state are probed using a probe pulse to obtain the resonance Raman spectrum, which reflects the vibrational relaxation dynamics.

relaxation that produces the populations having different vibrationally excited states at the electronic ground state. The femto-second time-resolved Raman is then used to observe the vibrational population relaxation at the electronic ground state.

2.3.3 Techniques To Study Vibrational Population Relaxations Using Stokes And Anti-Stokes Raman In Tandem[17]

As stated above, the intramolecular and intermolecular vibrational relaxation processes of polyatomic molecules in liquid phase are ultrafast in the order of 1 and 10ps respectively. The photocells or photodiodes are not fast enough to measure these processes. It is necessary to have ultrashort pulses to directly observe the time constants.

Usually, the pump-probe technique is used. A first ultrashort light pulse excites the molecule. A second, delayed pulse probes the momentary population of the vibrational states. For different problems and molecules, there exist different excitation and probing methods or processes.

2.3.3.1 Excitation Methods

Three excitation methods are shown in Figure 2.7 including stimulated Raman excitation, Infrared absorption and internal conversion. One way to produce an excess population in a vibrational state is by stimulated Raman excitation. In the simple case only one laser pulse of a fixed frequency smaller than the electronic transition frequencies (non-resonance Raman) is needed to excite the defined vibrational mode (Figure 2.7(a)). This is appropriate to study the

specific mode, the mode with the largest Raman scattering section. In very concentrated system, excess populations in the order of 10^{-3} are achieved. The excess populations up to 3×10^{-2} may be obtained by using two ultrashort pulses excitation at frequencies υ_L and υ_S, where is the Stokes frequency $\upsilon_S = \upsilon_L - \upsilon_{vib}$.

The second way to produce vibrational excess energies by large excitation of several 10^4 cm^{-1} in a molecule is to use internal conversion of electronic energy. As shown in Figure 2.7 (b), a first visible or UV pulse excites the molecule to the first excited state S_1. If the molecule possesses fast internal conversion or radiationless transitions, the electronic energy is transferred to the vibrational manifold of the ground state. Thus large excess vibrational populations may be produced.

Finally the vibrational excitation is directly provided by infrared absorption technique as shown in Figure 2.7 (c). The infrared pulse having frequency υ_1 will resonantly excite the vibrational mode of the molecule in the electronic ground state. As long as the mode is infrared –active, the excess population is achieved by using the corresponding infrared pulses. It has been reported that the population number is as high as 10^{-1} for transitions with large absorption cross-sections.

The energy transferred to the vibrations of the electronic ground state by internal conversion will be redistributed within the molecule. The excess population obtained by stimulated Raman and infrared absorption will relax or depopulate to the lower lying states which are populated simultaneously. In

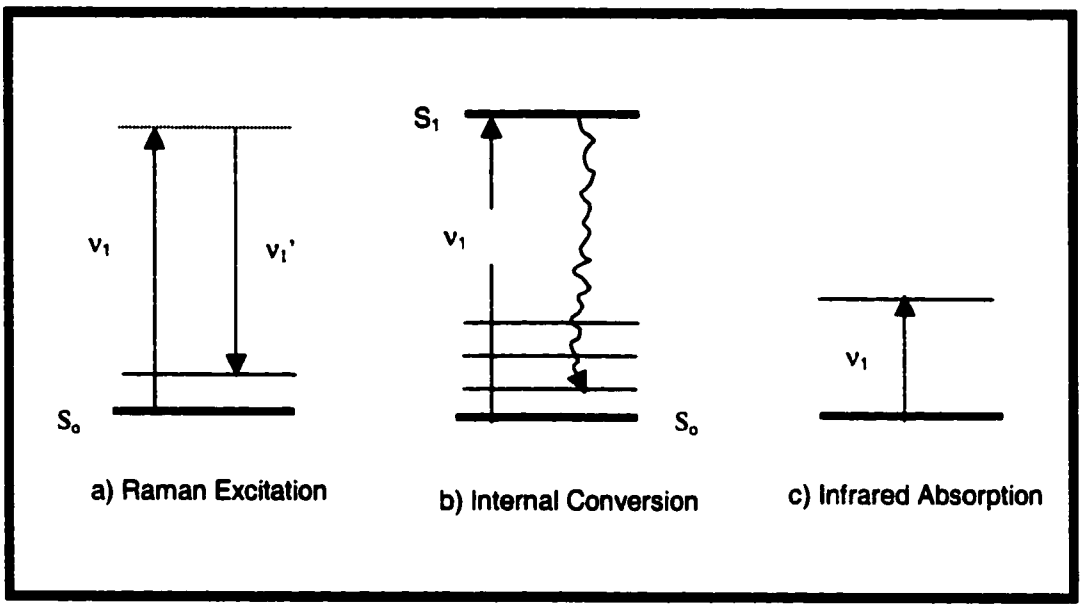

Figure 2.7 The vibrational excitation in the electronic ground state S_o by three methods. The vibrational level is populated through (a) Raman excitation, (b) a larger amount of energy is supplied to the vibrational manifold via electronic excitation and subsequent rapid internal conversion, and (c) resonant infrared absorption.

our experiment, the resonance Raman is used, so the excess population is achieved through the first two method, stimulated Raman excitation and internal conversion of electronic energy. The corresponding relaxation includes the intramolecular redistribution and intermolecular energy transfer.

2.3.3.2 Probing Methods

Different probing techniques have been developed recently. Figure 2.8 focuses the anti-Stokes probing. It is assumed in the figure that the molecules are excited at frequency υ_1.

As shown in Figure 2.8, the transient population of the vibrational mode υ_i is proportional to the magnitude of the spontaneous anti-Stokes Raman signal at the frequency $\upsilon_{AS} = \upsilon_2 + \upsilon_i$ generated by the probe pulse of frequency υ_2. By varying the time delay of the probing pulse relative to the excitation or pump pulse, the time-resolved data are obtained.

The anti-Stokes technique is powerful in obtaining detailed information about the degree of population, on the lifetimes of the different vibrational states and on the energy flow among the different levels. However the technique is subject to some experimental difficulties since the normal Raman scattering sections of vibrational modes are small. Using higher intensities of the probing pulse will give higher signal but there are also upper limits to it. Under very high intensities spurious signals are also generated by various nonlinear optical processes including dielectric breakdown, multi-photon transitions or self-phase modulation. We used resonance Raman to enhance

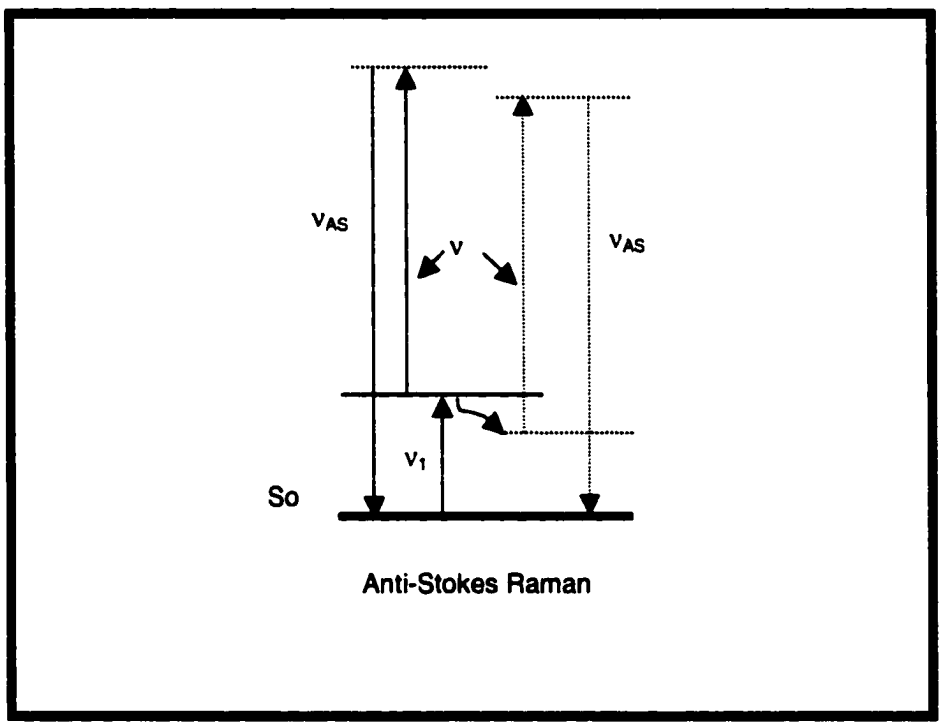

Figure 2.8 Techniques to probe the instantaneous population of vibrational state. The populations of a vibrational level are observed by spontaneous anti-Stokes Raman scattering.

the signal, and the background subtraction methods to reduce the possible nonlinear optical effect to obtain reliable data in our experiments as shown in chapter 3 and 4 later.

2.4 Advantages Of Our Time-Resolved Raman Technique

Transient Raman experiments has been well accepted as an important tool to investigate the ultra-fast phenomena by many researchers. Compared to others our transient Raman experiments possess many distinguished features.

First, two separate laser beams instead just one beam are used to do separate jobs. One called pump pulse or beam will first prepare the species in a given electronic state, after a delay time the other one called probe pulse will then probe the species. With the help of this pump-probe method, one spectrum with both pump and probe pulses and two background spectra with pump pulse alone and probe pulse alone can be gathered. Subtraction the two background spectra from the one spectrum above gives us a transient spectrum that represents the transient features as a function of the delay time between the pump and probe pulse. Our technique guarantees a direct measurement of the transient spectrum and has many advantages over the one beam method used by many other researchers. Using the latter method, the Raman spectroscopy experiment is carried out at some laser powers between low-power and high-power. The Raman bands resulting from different molecular states behave differently with the laser power. The Raman band of ground species changes linearly with power, while the Raman band of excited states changes approximately quadratically with power. In this one beam

method, the Raman probe light is reabsorbed by the excited states existing on different time scales due to the transient absorption effects, which in return complicate the one beam Raman method. Our pump-probe method does not have this complication. Further it is more sensitive to some weak features because the subtraction will eliminate the intense background bands.

The next distinguished feature in our transient Raman spectroscopy experiment is that the dynamics spectra, where the transient signal is plotted as a function of time delay between pump and probe pulses, are symmetric in time. This is because the pump and probe pulses used here are of the same wavelength of 379.5nm, so that each pulse can act as pump if reaches the species earlier or probe if it reaches the species later. This helps us recognize the actual time zero (i.e. at which the delay time is zero) and find out any artificial facts that will cause the dynamics spectra distorted from symmetry in time easily. The work in this dissertation as well as other works of this laboratory [18] reflects the development of this method.

Finally we are able to measure the stokes Raman signal correlated with anti-stokes Raman signal as a function of time. This femtosecond stokes/anti-stokes technique allows us to resolve some controversies existing in the vibrational relaxation dynamics study. Chapter 3 shows some examples of using this techniques to monitor the evolution of vibrational populations of four kinds of bipyridinium ions in the study of dynamics of vibrational relaxation of molecules. The reason for using this stokes/anti-stokes technique to observe the vibrational population distribution via vibrational energy levels or vibrational

quantum number v is obvious as following. The stokes Raman scattering originates from the lower levels, but the anti-stokes Raman scattering originates from the higher energy levels. The Stokes Raman signal will shine light on the information of lower vibrational energy levels such as v=0, 1. On the other hand the anti-stokes Raman signal will shine light on the information of higher vibrational energy levels such as $v \geq 1$. So combining the Stokes and anti-Stokes Raman signal in tandem as a function of delay time provide the time evolution of the vibrational population distribution.

2.5 References

(1) Campbell, T. D.; Dwek, R. A.; Biology spectroscopy, Benjamin/Cummings, Menlo Park, 1984

(2) Mukamel, Shauel; J. Chem. Phys., 1985, 82, 5398

(3) (a) Chen, J. Development of a Femtosecond Time-resolved Raman Spectrometer for Hemoglobin Studies, Ph. D. Dissertation, Fall, 1994; (b) Lingle, Jr. R. Picosecond pump-probe Raman spectroscopy of excited states and relaxation phenomena in the condensed phase, Ph.D. Dissertation, Louisiana State University, 1991

(4) Hopkins, J. B; Chen, J.; in Ultra-fast Dynamics of Chemical Systems, J. D. Simon, ed.; Kluwer Academic Publishers, 1994

(5) Forster, M.; Girling, R. B.; Hester, R. E. J. Raman Spectrosc. 1982, 12, 36

(6) Mahew, S. G.; Abels, R., Platenkamp, R. Biochem. Biophys. Res. Commun. 1977, 77, 1397-1403

(7) Thorneley, R. N. F. Biochim. Biophys. Acta 1974, 33, 487-496

(8) Corbin, J. L.; Watt, G. D. Anal. Biochem. 1990, 186, 86-89

(9) Carey, J. G.; Cairns, J. F.; Colchestu, J. E. Chem. Commun., 1969, 1280-1281

(10) Mahew, S. G., Abels, R., Platenkamp, R. Biochem. Biophys. Res. Commun. 1977, 77, 1397

(11) Rossetti, R.; Brus, L. E. J. Phys. Chem. 1986, 90, 558

(12) Kosower, E. M.; Cotter, J. L. J. Am. Chem. Soc. 1964, 86, 5524

(13) Feng, Q; Surface-enhanced Raman Scattering of MethylViologen at Silver Electrodes and its Application to Study of Charge Transfer at the Semconductor/Electrolyte Interface, A Dissertation, University of Nebraska, Lincoln, Nebraska, August, 1987

(14) Kosower, E. M. In Free Radicals in Biology, Pryor, W. A. Ed; 1976, 2, Chapter 1, pp1-54

(15) Zahradnik, R.; Cársky, P. J. Phys. Chem. 1970, 74, 1240

(16) Hünig, S.; Scheutzow, D.; Carsky, P.; Zahradnik, R. J. Phys. Chem. 1971, 75, 335

(17) Seilmeier, A.; Kaiser, W. In Topics in Applied Physics: Ultrashort Laser Pulses and Applications, Edited by Kaiser, W., Springer-Verlag Berlin Heidelberg, 1988, pp279-318

(18) Chen, J. Development of a Femtosecond Time-resolved Raman Spectrometer for Hemoglobin Studies, Ph. D. Dissertation: Fall, 1994

CHAPTER 3 FEMTOSECOND RESONANCE RAMAN INVESTIGATION OF FOUR UNIVALENT BIPYRIDINIUM RADICALS

3.1 Introduction

Vibrational and electronic relaxation and related energy redistribution are very important in photo-induced processes[1,2]. Of particular value is the population time of individual vibrational modes which is of paramount importance for the understanding of state-selective chemistry, and the biochemical function of some bio-chemicals[3-7] and the interaction between solutes and solvents in chemical dynamics[8,9]. Since this time scale is in the order of several tens of femtoseconds to 100ps in liquid phases, various spectroscopes with ultrashort laser pulses have been used to elucidate the dynamics and physical mechanisms of intramolecular energy redistribution and intermolecular energy transfer.

One of the more powerful techniques is time-resolved Raman spectroscopy[10] including normal Raman scattering (NRS)[11] and resonance Raman scattering (RRS)[12]. The anti-Stokes Raman intensity directly depends on the relative populations of vibrationally-excited levels, thus the anti-Stokes technique[1] can be used to obtain detailed information on relative populations and lifetimes of different vibrational states. For example, spontaneous anti-Stokes NRS has been used to probe the vibrational relaxation and population lifetimes of small neutral molecules (less than 10 atoms)[13,14], large neutral

molecules[15-17] and small aqueous ions[8]. Time-resolved anti-Stokes RRS has also been used to observe the vibrational relaxation in the X state of I_2[18a] and recently to characterize vibrationally excited ground-state populations in biomolecules such as deoxyhemoglobin[18b,c], carotenoids[4,5] and the retinal chromophore[7].

However, apparently no direct information on vibrational energy transfer rates in large radical ionic species in solution exists. Hence we have undertaken a study to directly measure the vibrational energy relaxation of radical ion species by femtosecond resonance Raman spectroscopy. The goal of this study is to determine how population lifetimes of the large radical ions are different from those of the neutral large molecules, and if their different structures and charges will affect the vibrational relaxation dynamics. Four bipyridinium univalent radical ions: MV^+, BV^+, $BPDPS^-$ and EB^+, which consist of 28 or more atoms, shown in the Figure 3.1, have been chosen for this study.

Bipyridinium ions (e.g. Methylviologen dication MV^{+2} and its reduced radical MV^+) are of considerable interest in their use as potent herbicides[19] and recently as electron relays in various schemes for hydrogen generation through the photochemical splitting of water[20]. In many applications the optical characteristics of the bipyridinium radicals are critical, consequently they have received much attention. In the case of MV^{+2} and MV^+, the electronic absorption (EA) spectrum[21-25], NRS of the dication[23,24,26,27], RRS of MV^+[23-26,28-30] and surface-enhanced Raman scattering and surface-

enhanced resonance Raman scattering spectroscopy[26,28-32],have been investigated extensively. Tentative vibrational assignments such as normal-coordinate analysis of the in-plane vibrational modes of MV^{+2} and the totally symmetric vibrations of MV^{+} have been obtained[33,34]. Deuteration of MV^{+2} has also been used to confirm some assignments[35,36]. The previous work on MV^{+2} and its reduction radicals is helpful in establishing assignments of other bipyridinium radicals discussed in this paper due to the similarity of their main molecular skeletons.

Compared with MV^{+2} and MV^{+}, much less Raman data exists on other bipyridinium species. The NRS of solid $BVCl_2$ (900 to 1700 cm^{-1})[34] and BV^{+2} in CH_3CN (1500 to 1850cm^{-1})[37] has been reported. RRS (1500 to 1850 cm^{-1}) of BV^{+} in acetonitrile solution[37] has also been used to detect excited- state electron transfer in porphyrin viologen systems without mentioning the assignments. NRS of EB^{+2} (in the form of the bromide salt $EBBr_2$), and RRS as well as some excitation profiles of radical EB^{+}[38] have also been reported. However, much remains unknown. To our knowledge, Stokes RRS of $BPDPS^{-}$ and anti-Stokes RRS spectra of the four bipyridinium radicals has never been reported.

This chapter is organized as following: we first report the RRS spectra of the radical mono-ions MV^{+}, BV^{+} and $BPDPS^{-}$, and extend the assignments of the bands of BV^{+} and $BPDPS^{-}$ to corresponding vibrational modes by comparison with the known assignments for similar bands of MV^{+2}, MV^{+} and BV^{+2}. Next the anti-Stokes RRS spectra and assignments of the bands of MV^{+},

Figure 3.1 Structures of the four bipyridinium radical ions i.e. methylviologen MV^+, where the superscript dot standing for the free electron has been omitted for simplicity; benzylviologen BV^+; 4,4'-bipyridinium -N,N'-di(propylsulfonate) $BPDPS^-$ and N,N'-ethylene - 2,2'-bipyridinium EB^+ radicals. The structural differences between the 4,4'-bipyridinium radicals and 2,2'-bipyridinium radicals can be easily seen in this figure. The systematic names for the radicals in CA are: MV^+: 1,1'-dimethyl,4,4'-bipyridinium radical ion(1+); BV^+: 1,1'-bis(phenylmethyl),4,4'-bipyridinium radical ion(1+); $BPDPS^-$: 1,1'-bis(3-sulfopropyl)dihydroxide,4,4'-bipyridinium bis (innersalt) radical ion (1-); EB^+: 6,7-dihydrodipyridio (1,2-a:2',1'-c) pyrazinediium radical ion(1+)

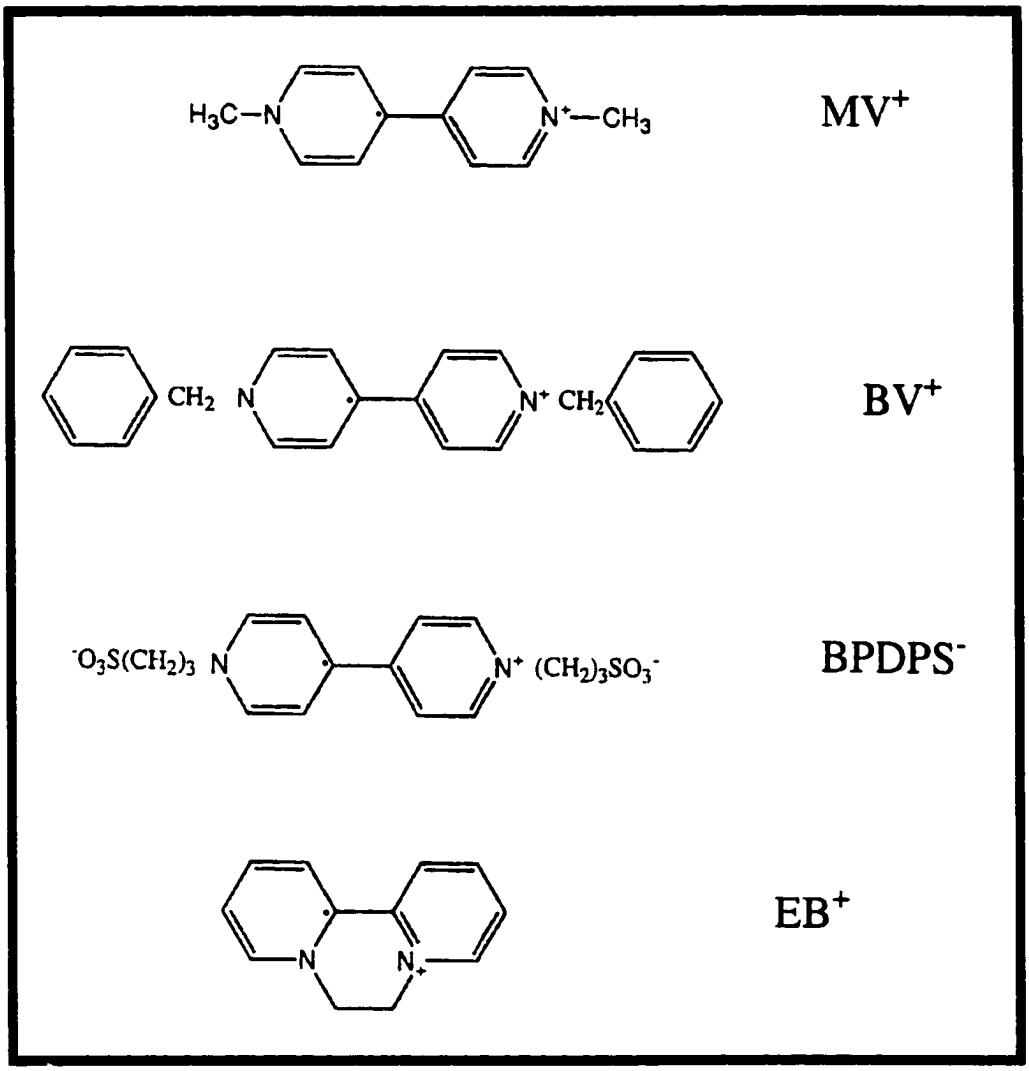

$BPDPS^-$ and EB^+ are discussed. Finally the vibrational cooling dynamics of the C-C stretching mode is time-resolved, by pump and probe technique. The data are interpreted based on the time evolution of both the Stokes and anti-Stokes intensities. The radical structure and charge effects on the vibrational cooling dynamics are discussed. In addition this work develops some insight into the relationship between the RRS and molecular structures of the radical ions.

3.2 Experimental

Methylviologen dichloride hydrate ($MVCl_2$), benzyl viologen dichloride ($BVCl_2$) (Aldrich Chemical Co., Milwaukee, WI) and 4,4'-bipyridinium -N, N'-di (propylsulfonate) (BPDPS (Sigma Chemical Co., ST. Louis, MO) are used without further purification. N,N'-ethylene-2,2'-bipyridinium dibromide hydrate ($EBBr_2 \cdot H_2O$) is synthesized following the standard procedures in the literature[39] and is verified by ultraviolet EA spectroscopy and mass spectroscopy[40]. The monovalent bipyridinium radicals are produced by reduction of the corresponding bipyridinium salts with sodium dithionite (Eastman Kodak Co.) or zinc metal dust (Mallinckrodt, A. R.)[24, 41] and then they are loaded in a closed cell after the zinc dust (if any) is filtered out. All the operations are conducted in a nitrogen box to avoid oxidation of the radicals by air. Distilled, deionized water is used to make the solution. The concentrations of the bipyridinium radicals are chosen at about 2×10^{-4} mol/dm^3 to avoid possible dimerization of the radicals[42].

The time-resolved Resonance Raman experiment[43] is carried by pump-probe technique through the optical configuration illustrated in Figure

3.2. The 759 nm pulse with a pulse width of 350 fs and repetition rate of 1 kHz produced from our femtosecond laser system[43] are frequency-doubled by a BBO crystal. The second harmonic of a pulse energy typically 20 microjoules is then separated by a beam splitter (B. S.) into two beams, one pump beam goes through a fixed delay, and the other probe beam goes through a variable delay. The pump and probe beams are then recombined by another beam splitter and focused by a 15cm focusing lens L_1 into the sample. A spinning cell is used so that each laser shot would hit a fresh region of the liquid sample. The laser beam geometry is set about 70 degrees away from the spinning cell normal direction i.e. the signal collecting direction. The Raman signal is collected by a f/1.0 lens. An ISA m1000 double-grating monochromator selects the desired wavelength and the signal is detected by a cooled photomultiplier tube (PMT, RCA C31034A). The signal from the photomultipler is sampled by a gated-integrator (Lecroy 2249SG converter) and then processed by a computer. The computer also controls the movement of a Daedal PC-400-1F stepper motor controller, which drives both the monochromator to scan the wavelength or the translation stage to scan the time delay.

The signal obtained by gated-integration contains the contribution from the transient species as well as that from the ground state equilibrium species. Contribution from the ground state equilibrium species must be subtracted to obtain the pure transient spectrum. A chopper synchronized to the laser pulse is used to chop both the pump pulses and the probe pulses. Two diodes are

Figure 3.2 Time-resolved RRS optical setup by pump and probe technique

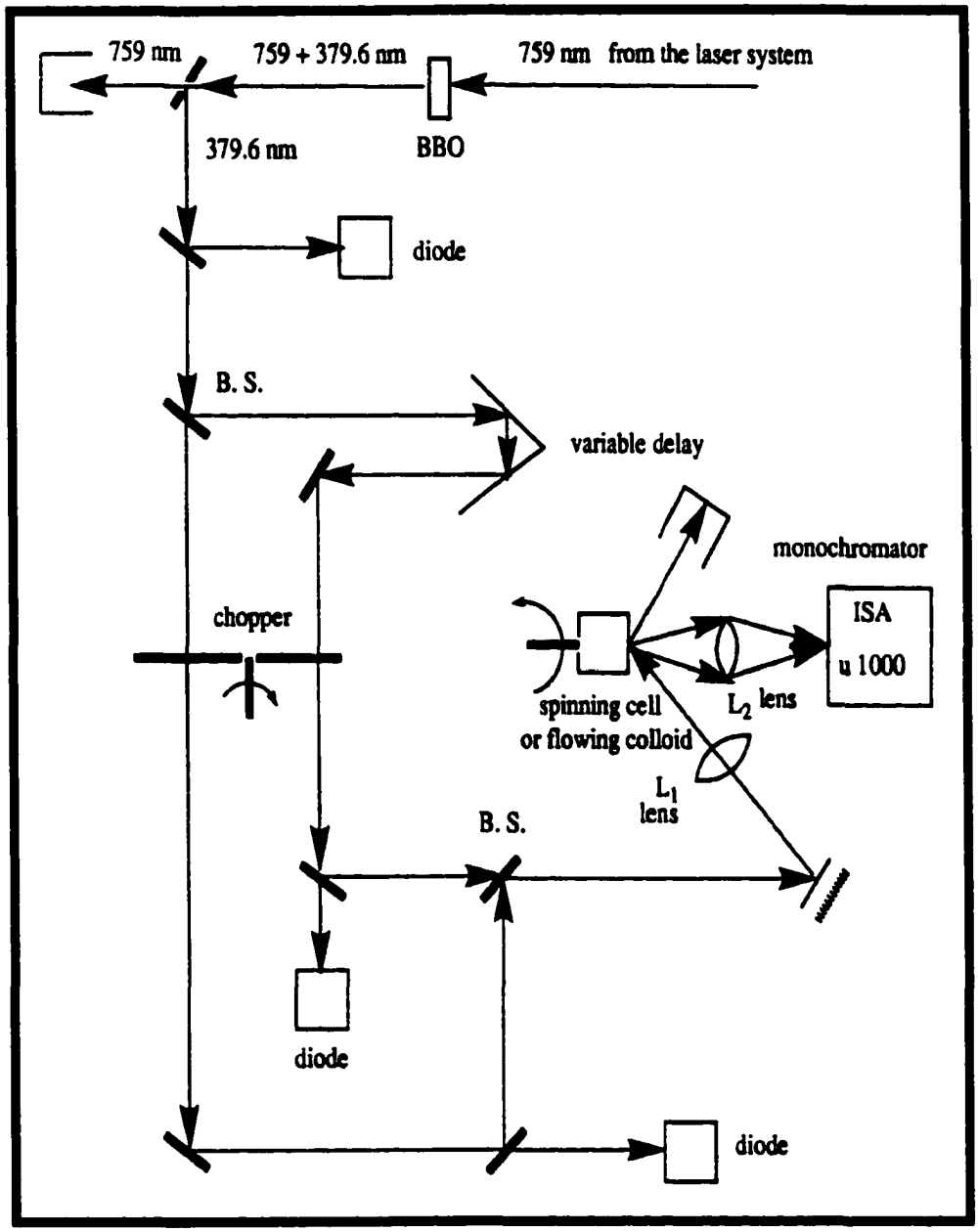

used to monitor the passage of each beam. The two diode signals are then used to direct the computer to sort the data from the PMT into different channels, which represent the pump pulse and probe pulse signal, pump pulse only signal, and probe pulse only signal, respectively. Thus in one scan all the three spectra (i.e. one spectrum with pump and probe pulses, one spectrum with pump pulses only, and another spectrum with probe pulses only) can be obtained to fulfill the subtraction. To minimize the noise caused by shot to shot fluctuation, another diode picks up a small fraction of the laser beam before it is split. The PMT signal is normalized by taking the ratio of PMT output with respect to the photodiode output. Considering the different linearity between the PMT and photodiode, a software window discards laser pulses whose intensity falls outside of a predetermined energy range, resulting in much better signal-to-noise ratio.

The stationary Raman spectra are obtained when the delay is set at time zero and the chopper is not used.

3.3 Results and Discussion

3.3.1 Stationary Stokes RRS Measurements And Assignments

Figure 3.3 (a to c) shows the RRS spectra of MV^+, BV^+, and $BPDPS^-$ respectively. Several bands ranging from 600 to 1750 cm^{-1} are observed for MV^+, which are consistent with the reported spectra[24]. Table 3.1 lists the wavenumbers, relative intensities and tentative assignments for the strong bands of Figure 3.3. Only strong bands are selectively collected in table 3.1.

The assignments of the bands for BV^+ and $BPDPS^-$ are tentative, and they are based on the following reasoning: (a) the similarity in molecular skeleton of these species to MV^{+2} and MV^+, (b) the fact that the substituents do not markedly affect the overall D_{2h} symmetry of the MV^{+2} and MV^+ or 4,4'-bipyridiniums and (c) the fact that the N,N'-substituted groups can be considered as point masses[34].

Table 3.1 Wavenumbers (n/ cm^{-1}), relative intensities (I) and assignments of the five strong Stokes bands of 4,4'-bipyridinium radicals in Figure 3.3. (a) Wavenumbers from Ref. (34); (b) Solid $BVCl_2$ from Ref. (34), BV^+ in CH_3CN from Ref.(37); (c) Assignments based on similar assignments for MV^{+2}, MV^+, and BV^+ of Ref.(34); ir = inter-ring; R = Methyl/ CH_3, Benzyl / C_7H_7 or Propylsulfonate /$C_3H_6SO_3$ for MV^+, BV^+ or $BPDPS^-$ respectively. Only main contribution is denoted. All modes are in-plane stretching vibration. The intensities I are normalized to the most intense band.

MV^{+2}	n[a]	841		1193	1301	1538	1654
MV^+	n[a]	818		1212	1358	1536	1663
	n	816		1214	1354	1525	1658
	I	9.24		33.9	29.3	28.7	100
BV^{+2}	n[b]		1001	1158	1296	1545	1644
BV^+	n[b]					1525	1664
	n	831	1031	1183	1352	1525	1651
	I	32.6	2.7	27.4	46.5	44.7	100
$BPDPS^-$	n	808	1035	1198	1353	1527	1652
	I	11.0		43.4	41.7	37.5	100
Assignments[c]		C-N C-C		N-R	$(C\text{-}C)_{ir}$	C-N	C-C

Figure 3.3 Stokes RRS of bipyridinium radicals (A) 2.08×10^{-4} mol/dm^3 MV^+ (zinc powder reduction) (B) 2.11×10^{-4} mol/dm^3 BV^+ (sodium dithionite reduction) (C) 2.46×10^{-4} mol/dm^3 $BPDPS^-$ (sodium dithionite reduction). The wavenumbers, relative intensities and tentative assignments of the strong bands are listed in table 3.1. The wavenumber shifts primarily contributed to the N-R mode is clearly shown.

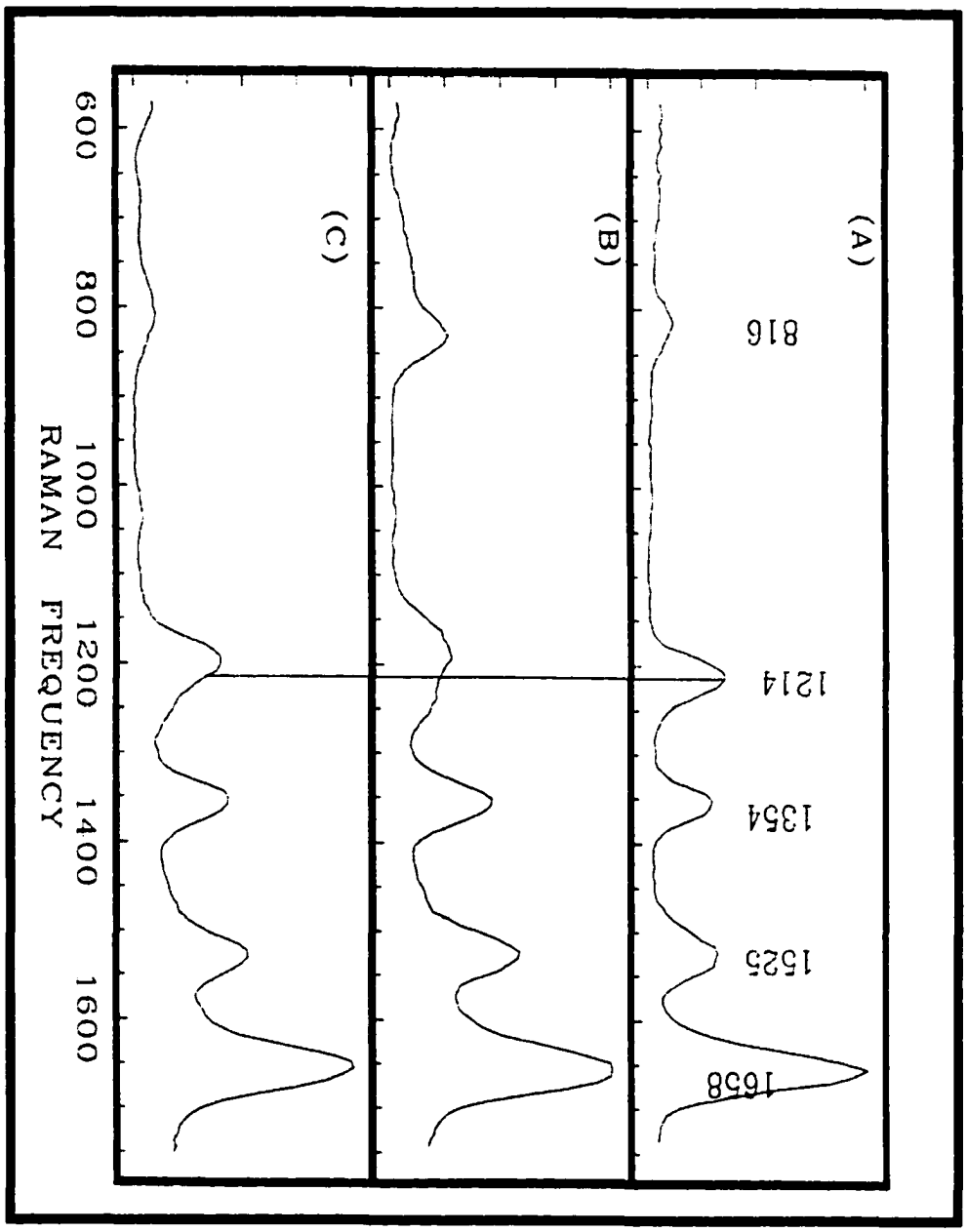

The band assignments for BV^+ and $BPDPS^-$ appear quite reasonable and consistent with experimental results. For instance, comparing the RRS spectrum of MV^+ with that of BV^+, and $BPDPS^-$ (Figure 3.3), it may be seen that the band assigned as N-R stretching is very sensitive to the nitrogen substituents (denoted by R). This band is at 1214 for MV^+, 1183 for BV^+ and 1198 cm^{-1} for $BPDPS^-$ (table 3.1). These wavenumber shifts of N-R mode can be explained by the different point masses and charges of the substitution group R. Increasing the mass of R causes a down-shift of the wavenumber. However negatively charged R will result in coulombic attraction to the positively charged N in the bipyridinium skeleton, therefore the bond force constant of N-R increases, though the fact that the charge is delocalized over the two rings of the radical skeleton will attenuate this attraction. The mass of the methyl group (15g/mole) is less than that of benzyl group (91g/mole), and neither methyl group nor benzyl group is charged, thus the wavenumber ($1214cm^{-1}$) of MV^+ is larger than that ($1183cm^{-1}$) of BV^+. Ghoshal et al[34] discovered a similar fact that the 1193 band in MV^{+2} shifts to $1158cm^{-1}$ in $BVCl_2$ (see data in Table 3.1 quoted from ref 34), and they reasoned the shift to lower frequency in $BVCl_2$ is caused by the larger mass of the benzyl group compared to the methyl group in MV^{+2}. Their explanation for dications supports ours for monocations. It must be noted that in $BPDPS^-$ the R is mono-anionic propylsulfonate group of molar mass 122g/mol. As compared with MV^+, the negatively charged propylsulfonate group of $BPDPS^-$ will increase its frequency; but the larger mass of propylsulfonate group will

decrease its frequency; and the net effect is that the frequency (1198cm^{-1}) of BPDPS$^{\cdot}$ is less than that (1214cm^{-1}) of MV^{+} as a result that the mass effect wins against the charge effect. From BV^{+} to BPDPS$^{\cdot}$, the negative charge effect of R is relatively more important, and it overcomes the mass effect due to a relatively small mass change of R from 91 for BV^{+} to 122 g/ mol for BPDPS$^{\cdot}$, therefore the wavenumber shifts up 15cm^{-1} (from 1183 to 1198 cm^{-1}). Thus the experimental results verify our assignment that this band should be attributed primarily to the N-R stretching vibration.

As shown in table 3.1, a significant change in wavenumber (1296 to 1352 cm^{-1}) of the inter-ring C-C stretching mode can be observed upon reducing BV^{+2} to BV^{+}. This change can also be explained by comparing these results with those of Ghoshal et al[34] for MV^{+2} and MV^{+}. These researchers observed that upon reduction of MV^{+2} to MV^{+} , the structure changes from a largely delocalized aromatic-type of MV^{+2} to a more delocalized quininoid-type of MV^{+}, the bond stretching force constant increases from 4.1 to 5.4 mdyn A^{-1}[33], and considerable electron density is added to this bond so that its wavenumber shifts from some 1300 to about 1350 cm^{-1}[23-26,29,31,33,34]. A similar argument can be used for the change in the vibrational frequency due to inter-ring C-C stretching for BV^{+2} and BV^{+}. It may be possible that upon reduction from BV^{+2} to BV^{+}, the conformation of the species changes from aromatic-type for BV^{+2} to quinonoid-type for BV^{+} to gain the delocalization energy for the unpaired electron. Thus the bond order between the inter-ring C-C increases.

3.3.2 Stationary Anti-Stokes RRS Measurements And Assignments

Figure 3.4 (a, b, c) shows the anti-stokes RRS spectra of MV^+, $BPDPS^-$ and EB^+ respectively. The tentative assignments of the bands of EB^+ are marked in Figure 3.4c according to the assignments of the corresponding Stokes band regions[38]. The wavenumbers, relative intensities and tentative assignments of the bands in Figure 3.4 for MV^+ and $BPDPS^-$ are shown in table 3.2. The assignments are made by comparision of the anti-Stokes RRS (Figure 3.4)

Table 3.2 Wavenumbers (n/cm^{-1}), relative intensities (I) and assignments of the anti-Stokes bands of 4, 4'-bipyridinium radicals MV^+ and $BPDPS^-$ in Figure 3.4. Only main modes contributed to the band are assigned, ir = inter-ring, all modes are in-plane stretching vibration, R the same as table 3.1. The intensities are normalized to the most intense band.

MV^+	n	780	1027	1193	1339	1478	1635
	I				48.0		100
$BPDPS^-$	n	796	1027	1165	1330	1505	1628
	I	46	40	27	29	29	100
As-signm-ents		C-N C-C		N-R	$(C-C)_{ir}$	C-N	C-C

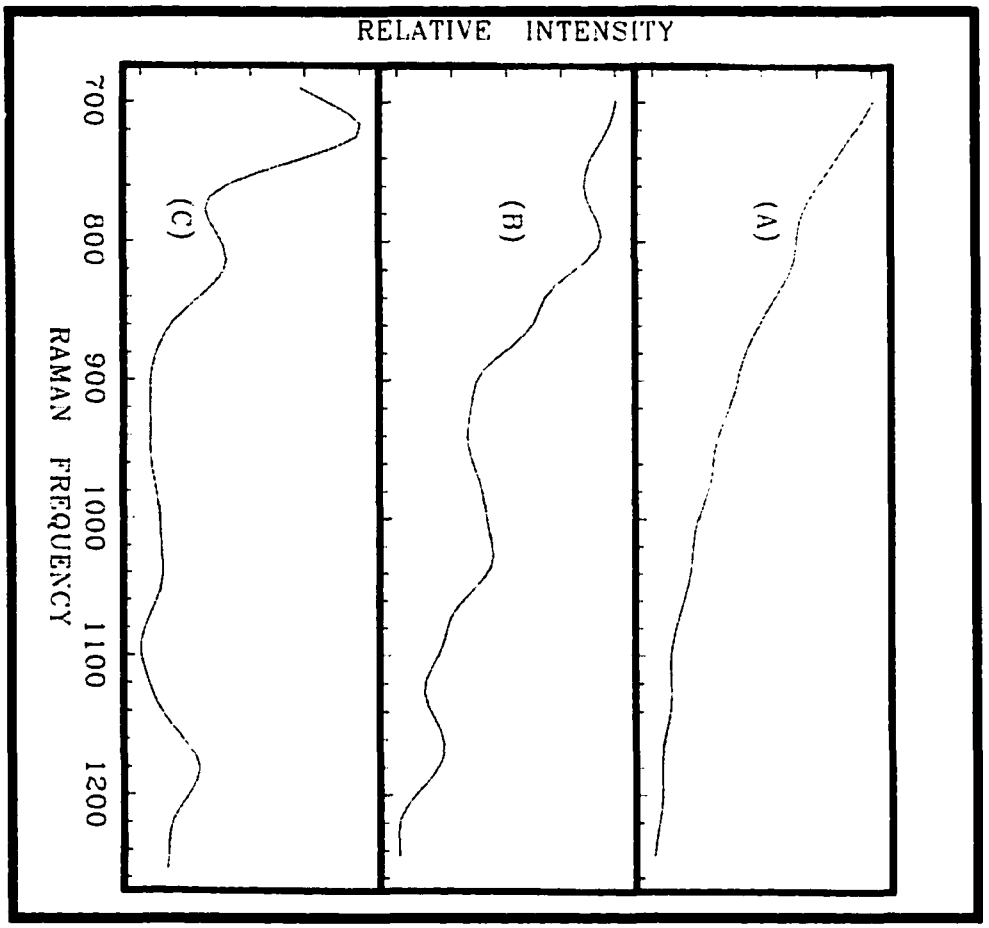

Figure 3.4 (a) Lower wavenumber part of Antistokes RRS of bipyridinium radicals (A) MV+ (B) BPDPS- (C) 2.08x10-4 mol/dm3 EB+ (zinc dust reduction). The concentrations and reduction conditions of MV+ and BPDPS- are the same as those in Figure 3.3. The wavenumbers, relative intensities and tentative assignments of MV+ and BPDPS- are listed in table 3.2. The tentative assignments of EB+ are marked in frame (C) according to the Stokes assignments in reference 38, i. e. 1300-1400 cm-1 as inter-ring stretching, 1500 -1600cm -1 as ring stretching vibration.

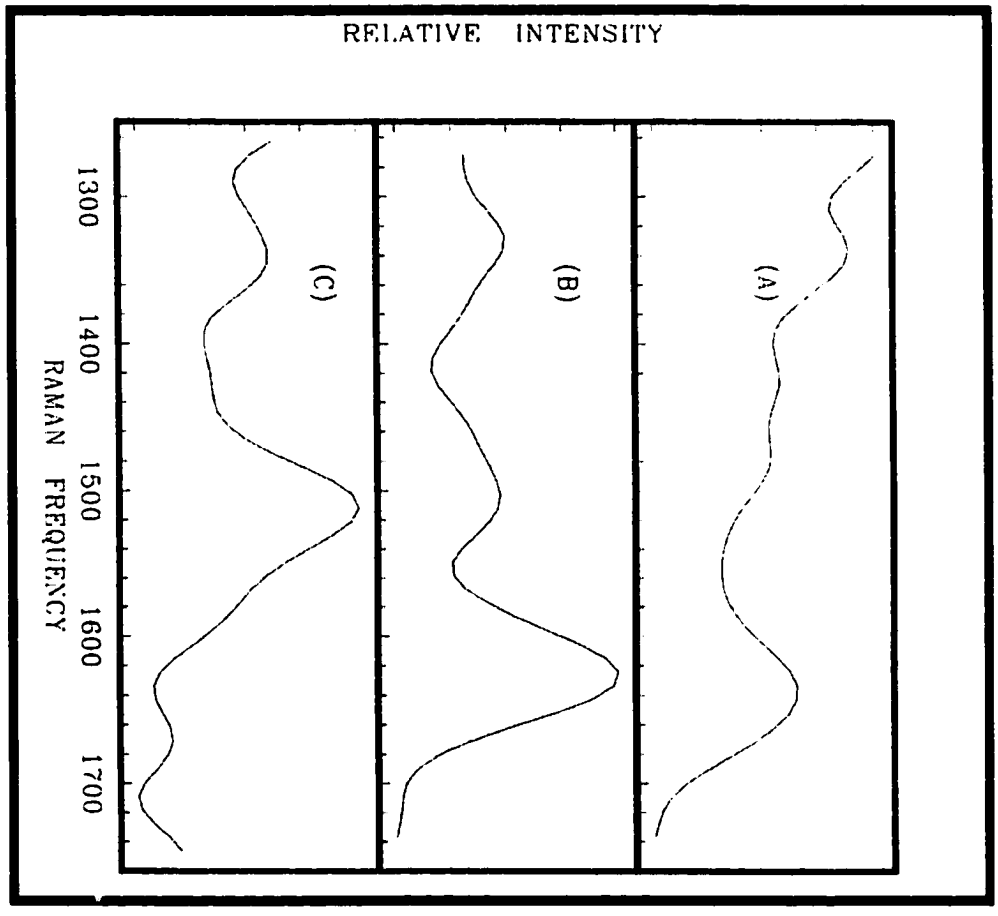

Figure 3.4 (b) Higher wavenumber part of Antistokes RRS of bipyridinium radicals (A) MV^+ (B) $BPDPS^-$ (C) $2.08x10^{-4}$ mol/dm^3 EB^+ (zinc dust reduction). The concentrations and reduction conditions of MV^+ and $BPDPS^-$ are the same as those in Figure 3.3. The wavenumbers, relative intensities and tentative assignments of MV^+ and $BPDPS^-$ are listed in table 3.2. The tentative assignments of EB^+ are marked in frame (C) according to the Stokes assignments in reference 38, i. e. 1300-1400 cm^{-1} as inter-ring stretching, 1500 -1600cm $^{-1}$ as ring stretching vibration.

spectra with the Stokes RRS spectra (Figure 3.3). The main conclusion of this data is that the resonance enhancement in these molecules is such that the same bands observed in the Stokes spectrum are also observed in the anti-Stokes spectrum.

3.3.3 Time-Resolved RRS ---- Dynamics Of Vibrational Relaxation For C-C Stretching Mode By Time-Resolved RRS

The dynamics data are obtained by using one pulse to excite the B_{3u} (MO 7, ground) to B_{3u} (MO 11, excited) electronic transition[32,44]. As described below our results indicate that the latter state rapidly relaxes back to the B_{3u} (MO 7, ground) state producing highly excited vibrational levels. The excited vibrational levels in the B_{3u} (MO 7, ground) state are probed using a second pulse to obtain the resonance Raman spectrum.

Based on the above assignments of the bands, time-resolution of any specific mode in the spectral region of Figure 3.3 can be made. We will concentrate on the band mainly contributed by C-C stretching vibration. The wavenumber of the monochromator is fixed at the band center and the pump and probe dynamics of the band is obtained by sweeping the time delay between pulses. Figure 3.5 (a to f) shows how the transient Stokes and anti-Stokes RRS intensities of the C-C band changes with delay time for MV^+, for $BPDPS^-$, and for EB^+. The transient Stokes RRS intensity has a negative maximum depletion at time zero, and then recovers with delay time. However the transient anti-Stokes intensity has a positive maximum, then decrease with delay time. It is important to note that these dynamics scans are symmetrical

with increasing time delay in both directions from time zero, because the two pulses used in the experiment are of the same wavelength. Table 3.3 shows the population time constants for the dynamics obtained by deconvolution of the data shown in Figure 3.5.

Table 3.3 Time constants (ps) of stokes (S) dynamics and anti-stokes (AS) dynamics of Figure 3.5

Radicals	MV^+	BV^+	$BPDPS^-$	EB^+
Time constants AS	2.0	------	2.0	1.8
Time constants S	2.5-3.7	1.8	1.7	5.0

The mechanistic interpretation of the observation shown in Figure 3.5 and table 3.3 involves the formation of the vibrationally excited populations of lower electronic state B_{3u} (MO 7, ground) by the electronic relaxation of the excited electronic state B_{3u} populated by the 379.6 nm optical excitation and the vibrational cooling of the lower electronic state. As shown in Figure 3.5, the anti-stokes signal has a maximum at time zero, which means that the dynamics of formation of the vibrationally excited ground-state B_{3u} (MO 7, ground) is not time-resolved even by a femtosecond laser of pulse duration 350 fs. The fact that the Stokes band depletes while the anti-Stokes band increases in intensity at time zero convinces us that we are only monitoring the ground electronic state and not Raman scattering from the excited electronic state. Thus it is reasonable to assume that the electronic relaxation of B_{3u} (MO 11, excited) is faster than 350 fs. The same general kinetic and spectroscopic results characterizing vibrationally excited ground-state populations in the retinal chromophore of bacteriorhodopsin[7] has

Figure 3.5 Stokes and anti-stokes transient RRS intensities as a function of delay time. (A) Stokes band 1652 cm^{-1} of MV^{+}, (B) anti-Stokes band 1632 cm^{-1} of MV^{+}, (C) Stokes band 1652cm^{-1} of $BPDPS^{-}$, (D) anti-Stokes band 1615 cm^{-1} of $BPDPS^{-}$, (E) Stokes band 1585cm^{-1} of EB^{+}, and (F) anti-Stokes band 1511cm^{-1} of EB^{+}. The spectrum in each frame is independently scaled to fill the available space. The circles are the experimental data points. The solid line is the fit to the dynamics. This fit includes a single- exponential decay time constant, and convolution with the laser pulse. The Stokes is shown recovering with delay time, however the anti-Stokes dynamics decreasing with delay time. The deconvolved decay time constants are shown in table 3.3.

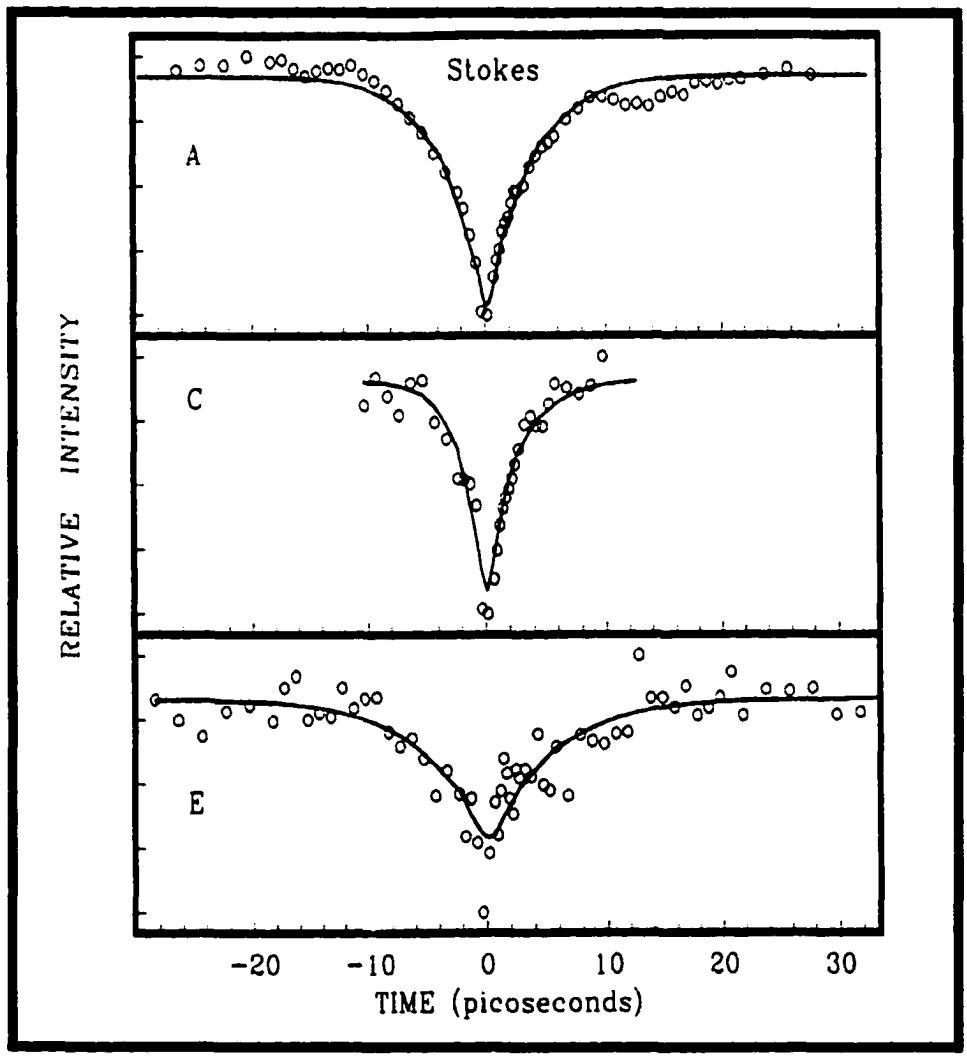

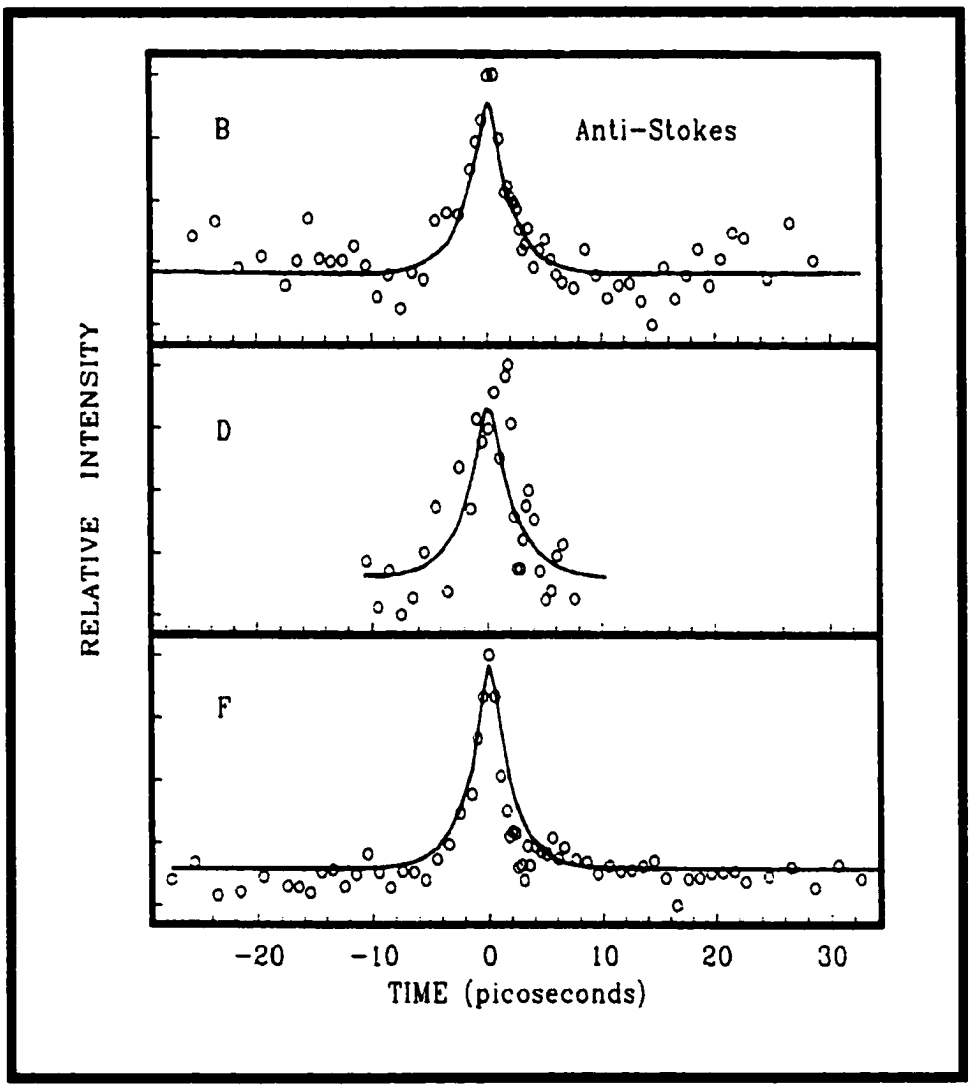

also been found by picosecond time-resolved anti-Stokes Raman scattering by previous researchers such as Brack and Atkinson.

On the other hand, the anti-Stokes signals of the pump and probe experiments can be easily used to monitor the decay of the vibrationally excited B_{3u} (MO 7, ground) populations prepared by the electronic relaxation. The data (Figure 3.5) are explained by assuming that the anti-Stokes signal largely depends on the vibrationally-excited B_{3u} (MO 7, ground) populations. Thus the dynamics of the anti-Stokes spectrum is interpreted as the dynamics of the population in the vibrationally excited levels of C-C stretching mode in the B_{3u} (MO 7, ground) electronic ground state.

The Stokes dynamics in Figure 3.5 has a depletion at time zero which recovers with a time constant of 1.7-5 ps (table 3.3). The maximum Stokes depletion is interpreted as population depletion in the vibrational ground levels of the B_{3u} (MO 7, ground) electronic ground state caused by the excitation of 379.6nm laser pulse. The fact that the Stokes intensity increases with time reflects the increasing RRS cross section as the result of increasing the population in the lower vibrational levels by means of vibrational relaxation, which is confirmed by the anti-Stokes dynamics.

The complementary negative Stokes transient intensities recovering with time and positive anti-Stokes transient intensities decreasing with time of Figure 3.5 are the predicted dynamics of vibrational relaxation of hot B_{3u} (MO 7, ground) population for bipyridinium radicals. The same type of the Stokes and anti-Stokes transient intensity as a function of delay time between pump and probe pulses has been found for deoxyhemoglobin at 1563 cm^{-1} band[18,c].

The population lifetime constants of the anti-Stokes dynamics (Table 3.3) are 2.0 ps for MV^+, 2.0 for $BPDPS^-$ and 1.8 ps for EB^+. The same anti-Stokes dynamics for different radicals indicates that the N,N'- substituents in the viologen skeleton do not play an important part in vibrational relaxation. This is likely a consequence of two factors: (a) the vibrational mode detected is C-C stretching not N-R stretching, and the former is only related to inter-ring and intra-ring C-C stretching[24,32,33,34] which is apparently not affected by the different N,N'- substitution groups, (b) the large radicals here have large mode density, the energy supplied to some specific vibrational states coupled with the electronic transition in large radicals may flow very rapidly to numerous isoenergetic overtones and combination modes (intramolecular vibrational redistribution IVR). In this way, the excess energy is quickly redistributed over the vibrational manifold of the molecule. Therefore the population life time constant is not radical structure-specific since all the radicals have very large numbers of mode density and therefore similar IVR times.

Unlike the anti-Stokes dynamics where the time constants are the same for radicals of different structures, the time constants of Stokes dynamics (Table 3.3) are somewhat different with different radicals, they are 2.5 -3.7 ps for MV^+, 1.8ps for BV^+, 1.7 ps for $BPDPS^-$ and 5.0ps for EB^+. The three 4,4'-bipyridinium radicals (MV^+,$BPDPS^-$ and BV^+) have time constants very close to each other, however the EB^+ radical has a slower constant as compared with that of each 4,4'-bipyridinium radical.

The EB^+ is known to have the unique "locking effect "[39] exerted by the 2,2'-ethylene bridging group (Figure 3.1) which limits the out-of-plane twisting or slight rotating of the rings relative to each other. The two rings in a 4,4'-bipyridinium radical are not locked (Figure 3.1), therefore it appears relatively easier for the two rings to twist or rotate as compared with EB^+. The twisting or rotating of the two rings in 4,4'-bipyridiniums represents vibration of very low frequency modes. These low frequency modes are apparently very important in accelerating the transfer of the vibrational energy because they add more vibrational state density to the radical in the low frequency region. This provides an efficient means for coupling the radical vibration to the solvent accepting modes.

It might at first seem curious that the Stokes and anti-Stokes dynamics of the C-C stretch exhibit different dynamics. This difference results from the transient vibrational population. Anti-Stokes scattering originates from all vibrations, which contain at least one quantum of C-C stretch. Stokes scattering can originate from all vibrations although with different resonance enhancements.

Our interpretation of the dynamics observed here is that the anti-Stokes spectra measure the loss of population from all vibrations containing excitation in the C-C modes, while the Stokes dynamics measures the final steps in the cooling process as all of the lower frequency modes relax toward equilibrium values. Since the twisting of the two rings in $EB^{+\cdot}$ limited by the ethylene bridge represents lower frequency, so the above structural effect is expected.

3.3.4 Discussion Of The Vibrational Relaxation Mechanism And Charge Effect

The mechanism of vibrational relaxation in the radical cations cannot be completely determined from these experiments. What is clear from the anti-Stokes dynamics is that the C-C stretching vibration relaxes in 2 ps. Since this experiment cannot distinguish between intramolecular vibrational redistribution (IVR) and intermolecular vibrational energy relaxation (VER) all that can be definitively stated is that the 2ps time represents the sum of all processes, which result in loss of quanta of vibration in this vibrational mode. In principle this involves both IVR and VER.

In most molecules VER slows down as the vibrational populations shifts to lower energy vibrations. This is the result of two factors; (1) a lower state density which causes larger increments of energy to be accepted by the solvent leading to poorer overlap with the solvent accepting modes and (2) for a given mode, lower quantum number vibrations relax more slowly compared to higher quantum number vibrations[45]. As a result, the last stages of VER are usually the slowest.

For the radicals discussed in this paper the dynamics of the Stokes spectrum are interpreted to measure the last stages of VER from lower energy vibrations. Even here the relaxation rate is found to be similar to the higher frequency C-C mode as a result of the existence of a large density of extremely low frequency modes, which efficiently coupled the vibrational energy to the solvent accepting modes. The exception is EB^+ which had a

slightly slower relaxation time (5ps) as a result of the locking effect exerted by its N,N'-ethylene group as shown by the radical structures.

The explanation of the vibrational relaxation processes in the electronic ground state can be expanded by comparing with analogous data reported for polyatomic large molecules in room temperature solutions. For large organic molecules, the rate of both intramolecular vibrational redistribution and intermolecular energy transfer from the absorbing solute to its surrounding solvent have been shown to vary greatly, dependent on the specific molecular interaction involved[1,2,46-47]. For example, large dye molecules have been reported to undergo intramolecular vibrational relaxation in both S_0 and S_1 states in less than 1 ps[46]. Presumably, the large density of states available as accepting modes in these dye molecules dominates mode-specific channels. Intramolecular redistribution in the electronic ground state occurs within 1, 2, and 5 ps for azulene[48] , Coumarin6[49], and naphthalene[16] respectively. Intermolecular energy transfer between the excited solute and its solvent can exhibit similar variations. For instance, azulene in room temperature solvents, the intermolecular energy transfer takes place on a time scale of 7 to 50 ps , depending on specific solute-solvent interaction[48].

Based on the above comparison with literature, further discussion can be made on the charge effect or the long-range solvent-solute coulombic interaction. The radicals studied here have relaxation times close to these of the neutral molecules of the similar size in room temperature solution. For example, the intramolecular redistribution of the excess vibrational energy in less than 2 ps

for anthracene (24 atoms) in Ar-saturated C_2Cl_4 solution[17] has been determined. This comparison may indicate that the charge of the radicals does not play an important role in the vibrational relaxation rate. However, theoretical considerations[2] such as molecular dynamics simulations of CH_3Cl vibrational relaxation in water solvent[50] show that the charge can accelerate the vibrational relaxation, and that the charge magnitude (Z) dependence of this acceleration is approximately proportional to Z^2. The radicals have two kinds of charges (Figure 3.1): (a) the charge from quaternary N^+ (Z=1), (b) the charge localized in the substitution groups e. g. group $(CH_2)_3SO_3^-$ (Z=-1). Why do these charges for the radicals discussed in this paper not accelerate the vibrational relaxation significantly as compared to similar neutral molecules such as anthracene? The answer is obvious after consideration of the charge distribution in the radicals. Actually the coulombic part of the relaxation rate depends on the product of Z^2 and the probability that the atom on which the charge is located moves during the internal motion[2]. With the charge localized in the substitution groups, this probability is very small since only the C-C stretching vibration of the rings is probed, though these charges might distort slightly the charge distribution on the atoms of the rings by long-range coulombic interaction or by nucleophilic and/or electrophilic effects. Only the charge in quaternary N^+ is directly involved in the vibrations of concern here, since it is delocalized over the two rings of 12 atoms[33]. Assuming this unit charge is distributed more or less uniformly over the 12 ring atoms, each atom only has 1/12 unit charge (Z=1/12). Based on this estimation of Z and the Z^2 dependence, the effect of delocalized charge on the

vibrational relaxation rate is therefore very small, approximately only $(1/12)^2$ = 1/144 of that of the charge localized in one atom. This rough estimation is consistent with the molecular dynamics simulation which does predict delocalization will slow down the vibrational relaxation rate, because the interaction between a solvent and a solute is weaker the more delocalized the charge distribution on the solute. For instance simulation of the vibration of the mythical molecule I-I$^-$ in water gives a vibrational relaxation time of 300 fs which is twice as fast as for the symmetric charge distribution of the I_2^-[51]. Therefore our results are significant in confirmation of the theoretical prediction, it is the delocalization charge distribution that makes the charge have minor effect in the vibration relaxation dynamics.

3.4 Conclusion

1. The measurement of stokes RRS spectra for MV^+, BV^+, and $BPDPS^-$ (Figure 3.3), and the first measurement of anti-stokes RRS spectra for MV^+, $BPDPS^-$ and EB^+ (Figure 3.4) are obtained. The tentative assignments of some bands are made (Table 3.1 and 3.2). The wavenumber of the N-R vibration mode for the radicals changing with different R from methyl group, benzyl group to propylsulfonate group are discussed in terms of the mass and charge effect of the substituent groups. It is also found that the increase in wavenumber of the inter-ring C-C mode upon reduction of BV^{+2} to BV^+ is due to more electron density added to the bond.

2. It is shown that the electronic relaxation from B_{3u} (MO 11, excited) to B_{3u} (MO 7, ground) is much faster than the 350 fs. The subsequent vibrational

relaxation dynamics of the vibrationally-excited B_{3u} (MO 7, ground) population for the C-C stretching mode is found to take place in 2 to 5 ps.

3. The 2 ps anti -Stokes dynamics is found not to be affected by the N, N'-substituents for the radicals; however the Stokes dynamics does reveal some radical structure affect on the rate of vibrational relaxation (Table 3.3). The 5 ps Stokes dynamics of EB^+ is discussed as the result of the "locking effect" exerted by its 2,2'-ethylene bridge, which limits the twisting of the two rings, decreases the channels to transfer vibrational energy through low frequency modes, and consequently reduces the rate of vibrational relaxation.

4. The charge of the quartnary N^+ structure in the radical has been shown to have little effect on the rate of the vibrational relaxation rate by comparison with neutral molecules of similar size in solution; which is discussed in terms of the delocalization charge density over the 12 ring atoms and confirms the prediction of molecular dynamics simulation.

5. The vibrational energy of the C-C stretching mode may decay via inter- and/or intra-molecular routes, which are not identified at present time due to the limited data. Further work is being done in our laboratory to time-resolve the dynamics of the other modes to determine possible intramolecular decay routes via energy redistribution among the different modes.

Registry No. $MVCl_2$, 1910-42-5; MV^{+2},4685-14-7; MV^+, 78991-90-9; $BVCl_2$, 1102-19-8; BV^{+2}, 13096-46-3; BV^+, 127338-04-9; BPDPS, 77951-49-6; $BPDPS^-$, 79008-86-9; $EBBr_2$, 85-00-7; EB^{+2}, 2764-72-9; EB^+, 59079-66-2.

3.5 References

(1) (a) Seilmeier, A.; Kaiser, W. In Ultrashort Laser Pulses and Applications; Kaiser, W. Ed; Springer-Verlag: Berlin Heidelberg, 1988; pp279-317. (b) Elsaesser,T.; Kaiser,W. Annu. Rev. Phys. Chem. 1991, 42, 83

(2) Owrutsky, J. C.; Raftery, D.; Hochstrasser, R. M. Annu. Rev. Phys. Chem. 1994, 45, 519

(3) Hayashi, H.; Kolaczkowski, S. V.; Noguchi, T.; Blanchard, D.; Atkinson, G. H. J. Am. Chem. Soc. 1990, 112, 4664

(4) Hayashi, H.; Tasumi, M.; Atkinson, G. H. Chem. Phys. Lett. 1991, 178(4), 388

(5) Hayashi, H; Brack, T. L.; Noguchi, T.; Tasumi, M.; Atkinson, G. H. J. Phys. Chem., 1991, 95, 6797

(6) Hayashi, H.; Noguchi, T.; Tasumi, M.; Atkinson, G. H. Biophysical Journal 1991, 60, 252

(7) Brack, T. L.; Atkinson, G. H. J Phys. Chem., 1991, 95, 2351

(8) Heilweil, E. J.; Doany, F. E.; Moore, R.; Hochstrasser, R. M. J. Chem. Phys. 1982, 76, 5632

(9) Li, M.; Owrutsky, J.; Sarisky, M.; Culver, J. P.; Yodh, A.; Hochstrasser, R. M. J. Chem. Phys. 1993,98, 5499

(10) Anfinrud, P. A.; Johnson, C. K.; Sension, R.; Hochstrasser, R. M. in Applied Laser Spectroscopy: Techniques, Instrumentation, And Applications; Andrews, D. L., Ed.; VCH Publishers, Inc.:New York, 1992; pp401-460

(11) Laubereau, A.; Kaiser, W. Rev. Mod. Phys. 1978, 50, 607

(12) Schomacher, K. T.; Bangcharoenpaurpong, O.; Champion, P. M. J. Chem. Phys. 1984, 80, 4701

(13) Graener, H; Laubereau, A. Appl. Phys. B 1982, 29, 213

(14) Kolmeder, C.; Zinth, W.; Kaiser, W. Chem. Phys. Lett. 1982, 91, 323

(15) Sverdlov, L. M.; Korvner, M. A. ; Krainov, E. P. Vibrational Spectra of Polyatomic Molecules ; Wiley: New York, 1974

(16) Gottfried, N. H.; Kaiser, W. Chem. Phys. Lett. 1983, 101,331. and refs there in

(17) Gottfried,N. H.; Seilmeier,A., Kaiser, W. Chem. Phys. Lett. 1984, 111, 326

(18) (a) Xu, X.; Lingle, Jr. R.; Yu, S. C.; Chang, Y. J.; Hopkins, J. B. J. Chem. Phys. 1990, 92, 2106. and references there in. (b) Lingle, Jr. R.; Xu, X. ; Zhu, H.; Yu, S. C. ; Hopkins, J. B. J. Am. Chem. Soc. 1991, 113, 3992. (c) Lingle, Jr. R.; Xu, X.; Zhu, H.; Yu, S. C.; Hopkins, J. B. J. Phys. Chem. 1991, 95, 9320

(19) (a) Kosower, F. M. In Free Radicals in Biology; Vol.2; Pryor,W. A., Ed.; Academic Press: New York,1976;p1 (b) Calderbank, A. In Advances in Pest Control Research; Vol. 8; Metcalf, R. L. , Ed.; Jonh Wiley & Sons Inc. : New York, 1968; p127

(20) Kiwi,J.; Kalyanasundaram,K.; Grätzel,M. In Structure and Bonding, Vol. 49; Clarke, M. J. et al., Eds; Springer Verlag: Berlin ,1982; p 37

(21) Kosower, E. M.; Cotter, J. L. J. Am. Chem. Soc. 1964, 86, 5524

(22) Landrum, H. L.; Salmon, R. T.; Hawkridge, F. M. J. Am. Chem. Soc. 1977, 99, 3154

(23) Lee, P. C.; Schmidt, K.; Gorden, S.; Meisel, D. Chem. Phys. Lett., 1981, 80, 242

(24) Forster, M.; Girling, R. B.; Hester, R. E. J. Raman Spectrosc. 1982, 12, 36

(25) Datta, M.; Jansson, R. E.; Freeman, J. J. Appl. Spectrosc. 1986, 40, 251

(26) Regis, A.; Corset, J. J. Chim. Phys. 1981, 78, 687

(27) Benchenane, A.; Bernard,L.; Théophanides, T. J. Raman Spectrosc. 1974, 2, 543

(28) Melendres, C. A.; Lee,P. C.; Meisel, D. J. Electrochem. Soc. 1983, 130, 1523

(29) Lu, T.; Birk, R. L.; Lombardi, J. R. Langmuir 1986, 2, 305

(30) Ohsawa, M.; Nishijima, K.; Suëtaka, W. Surf. Sci. 1981, 104, 270

(31) Feng, Q.; Cotton, T. M. J. Phys. Chem. 1986, 90, 983

(32) Feng, Q.; Yue, W.; Cotton, T. M. J. Phys. Chem. 1990, 94,2082

(33) (a) Hester, R. E.; Suzuki, S. J. Phys. Chem. 1982, 86, 4626. (b) Hester, D. E. in Time-Resolved Vibrational Spectroscopy; Atkison, G. H., Ed.; Academic Press: New York, 1983; p177

(34) Ghoshal, S.; Lu, T.; Feng, Q.; Cotton, T. M. Spectrochim. Acta 1988, 44A, 651

(35) Poizat, O.; Sourisseau, C.; Mathy, Y. J. Chem. Soc., Faraday Trans.,1984, 80, 3257

(36) Poizat, O.; Sourisseau, C.; Corset, J. J. Mol. Struct. 1986, 143, 203

(37) Force, R. K.; McMahon, R. J.; Yu, J.; Wrighton, M. S. Spectrochimica Acta, 1989, 45(1), 23

(38) Barker, D. J.; Cooney, R. P.; Summers, L. A. J. Raman Spectrosc. 1985, 16(4), 265

(39) Homer, R. F.; Tomlinson, T. E. J. Chem. Soc. 1960, 2498

(40) EA is carried out by AVIV Model 14DS Spectrophotometer.It shows an absorption maximum at 308 nm for EB^{+2}, which agrees well with the literature 308-311nm[39]. Mass spectroscopy is obtained by TSQ 70 mass spectrometer. The fast atom bombardment (FAB) is used as the ionization source with glycerol as the matrix and Cs^+ as bombardment atoms. Since $EBBr_2$ dissolves in glycerol to form EB^{+2} dication of calculated mass 184 g/ mole, mass spectroscopy reveals the characteristic mass 183.0 for ($EBBr_2.H_2O$ - $Br_2.H_3O$). This results strongly support that the ethylene group in the parent ethylene dibromide (1,2-dibromoethane) has been bonded to N, N' atoms of parent bipyridine

(41) (a) Corbin, J. L.; Watt, G. D. Anal. Biochem. 1990, 186, 86. (b) Mahew, S. G.; Abels, R.; Platenkamp, R. Biochem. Biophys. Res. Commun. 1977, 77, 1397

(42) MV^+ has been reported to undergo a monomer-dimer equilibrium, and the equilibrium constant of dissociation of $(MV^+)_2$ to $2MV^+$ at 1 M salt concentration is 2.6×10^{-3} M[24]. However our spectra (Figure 3.3 A) at the chosen concentration showed no bands that can be attributed to MV^+ dimmers, which are likely to be formed with increasing MV^+ concentrations. Therefore the dimerization effect can be neglected.

(43) Chen, J. Development of a Femtosecond Time-resolved Raman Spectrometer for Hemoglobin Studies, Ph. D. Dissertation: Fall, 1994

(44) Zahradnik, R.; Cársky, P. J. Phys. Chem. 1970, 74, 1240

(45) (a) Nesbitt,D.J.; Hynes,J.T. J. Chem. Phys. 1982, 76, 6002. (b)Nesbitt, D. J.; Hynes, J. T. J. Chem. Phys. 1982, 77, 2130

(46) Wild, W.; Seilmeier, A.; Gottfried, N. H.; Kaiser, W. Chem. Phys. Lett. 1985, 119, 259

(47) Hippler, H.; Lindemann, L.; Troe, T. J. Chem. Phys. 1985, 83, 3906

(48) Amirav, A.;Jortner, J.; J. Chem. Phys. 1984, 81, 4200

(49) Kaiser, W.; Bäuerle,R. J.;Elsaesser, T.; Hübner, H. J.; Seilmeier, A. In Ultrafast Phenomena VI, Yajima, T.; Yoshihara, K.; Harris, C. B.; Shinoya, S. Eds. ; Springer: Berlin, 1988; p. 453

(50) Whitnell, R. M.; Wilson, K. R.; Hynes, J. T. J. Phys. Chem. 1990, 94, 8625

(51) Benjamin, I.; Whitnell, R. M. Chem. Phys. Lett. 1993, 204, 45

CHAPTER 4 FEMTOSECOND RESONANCE RAMAN STUDY OF PHOTO-INDUCED INTERFACIAL ELECTRON TRANSFER BETWEEN COLLOIDAL CDS AND METHYLVIOLOGEN

4.1 Introduction

The field of photoredox reactions sensitized by colloidal semiconductors such as CdS has attracted a great deal of attention over the past decades. Semiconductors are used as photo-sensitizers in converting solar light energy to chemical energy including water splitting [1(b), 2(b)], in photocatalysis[3,4], in carbon dioxide fixation[5], in organic photosynthesis[4], in water purification[6], and in photo-imaging processes such as xerography, photography[7]. Photo-induced interfacial electron transfer processes between colloidal CdS and acceptors such as methylviologen play an important part in understanding those applications [1(b), 2(b), 8-10], due to the well-characterized carrier dynamics [11-30(a), 31-34] and electronic or optical properties [4,10,19,35-39(a),40-45] of quantum-sized CdS colloids.

The interfacial electron transfer from the CdS to viologens has been studied by various static and/or time-resolved spectroscopic methods such as fluorescence[46-54], absorption or pulsed laser photolysis[1(b),47-51,54-66], and resonance Raman scattering (RRS)[53,67,68]. The time scales investigated vary from minutes to milliseconds[48,59,56,66], microsecond to nanosecond[1(b),52,54,61,63,65,66,68], and picoseconds[51,62-64,67,69]. Several schemes of the sequential charge transfer have been proposed[48,51,55,56,60,61,63,66,70].

However, no exact value[71] of the interfacial electron transfer rate constants are available, only the upper limits of the rate constants are determined. For example, the rate constants of electron transfer from colloidal CdS to MV^{+2} have been reported as diffusion-controlled in low time-resolution experiments[59,61], or as laser pulse width-limited from less than 15ms to less than 3.3ps[1(b),8,51,52,54,63,64,66,67].

In this research a femtosecond laser pulse is used to excite the aqueous CdS colloid to generate electron-hole pairs. The electron transfer from CdS to MV^{+2} to form MV^{+} is probed by the RRS signal of the MV^{+} using a second time delayed femtosecond pulse. The probe pulse cannot excite MV^{+2} but is in resonance with electron transition in the electron transfer product MV^{+}. The time evolution of MV^{+} RRS monitors the electron transfer process directly, and the rate constant and dynamics are obtained in addition to the structural information of the transient species.

This chapter is organized as following: After the experimental section the femto-second RRS spectrum of MV^{+} photo-induced in CdS colloid is reported. The results from the absorption spectroscopy and time resolved resonance Raman spectroscopy are presented and discussed for different laser wavelengths and optical cells. The discussions are made according to the vibrational relaxation theory and electron transfer theory. Finally a conclusion is made. In the following we will begin with the experimental methods including the preparation of the CdS colloid and aqueous $MV^{+\cdot}$ solution and RRS measurements by our femtosecond laser.

4.2 Experimental

4.2.1 Preparation Of The CdS Colloid And Aqueous MV^+ Solution

Colloidal particles of CdS are produced by rapid mixing of Na_2S (Aldrich Chem. Co.) and $CdCl_2$ (Aldrich Chem. Co.) solutions following the principle in the literature[33] with slightly different procedures.

First 11cm^3 of 9x10^{-3}mol/dm^3 $CdCl_2$ solution, 25cm^3 of 1.157% (g/cm^3) HMP (hexametaphosphate, Malinckrodt OR) stabilizer stock solution, and 25cm^3 of deionized H_2O are mixed. Next while the mixture is stirred vigorously, 1cm^3 of 0.1mol/dm^3 fresh Na_2S solution is rapidly injected with a volumetric pipette and a transparent yellow CdS colloid is immediately formed. Finally 7cm^3 of 1.04x10^{-2} mol/dm^3 $MVCl_2$ (methylviologen dichloride hydrate, Aldrich Chem. Co.) are rapidly injected into the colloid while it is being stirred. The above preparation will give 69cm^3 of the colloid.

In this typical preparation, the number of moles for Cd^{+2} is equal to that for S^{-2}, the colloid is composed of 1.43x10^{-3}mol/dm^3 CdS monomer, 1.06x10^{-3}mol/dm^3 $MVCl_2$, 0.416% (g/cm^3) HMP, and 2.86x10^{-3} mol/dm^3 NaCl. The colloid has a pH = 7.07. The average diameter of the CdS particle is determined as 60Å by the onset of the absorption of the colloid (see results and discussion) using an AVIV Model 14DS spectrophotometer (AVIV Associate, Inc. N. J.). The aqueous MV^+ solution is produced by reducing $MVCl_2$ with Zn dust (Mallinckrodt, A. R.).

4.2.2 Femtosecond Laser System And Transient RRS Measurements

The time-resolved resonance Raman experiment[72] is performed by a pump-probe technique through the optical configuration (Figure 2.2) and laser system (Figure 2.1) illustrated in chapter 2. The laser system is first tuned to wavelength 819.2 nm (see section 4.3.2 to 4.3.5 later), then to wavelength 759.6nm. The colloidal sample is either contained in a sealed spinning cell as described in chapter 3 or recirculating in the open optical cell. We use the 759.6nm laser and recirculating colloid in the cell as an example for the transient RRS measurement in the following.

The 759 nm pulses with a pulse width of 350 fs and repetition rate of 1 kHz produced from our femtosecond laser system[72] are frequency-doubled by a BBO crystal. A dichroic mirror separates the harmonic from the fundamental by selectively transmitting the red component (759 nm) and reflecting the violet (379.6 nm). The violet pulse energy is typically 20 micro joules and is then split by a beam splitter into two beams, The pump beam goes through a fixed delay, and the probe beam goes through a variable delay. The pump and probe beams are then recombined so that they are collinear and focused by a 15cm lens into the sample. A volume of c.a. 250 cm^3 colloid solution is recirculating in an optical cell so that each laser shot hits a fresh region of the liquid sample. The laser beam geometry is set about 70 degrees away from the signal collecting direction. The Raman signal is collected by an F/1.0 lens to collect the maximum amount of scattering signal. An ISA U1000 double-grating

monochromator selects the desired wavelength and the signal is detected by a cooled RCA C31034A photomultiplier tube (PMT). The signal from the photomultipler is sampled by a gated integrator (Lecroy 2249SG converter) and then processed by a computer. The computer also controls the movement of a Daedal PC-400-1F stepper motor, which drives either the monochromator to scan the wavelength or the optical delay. Raman spectra are obtained at fixed time delays and dynamics are carried out by measuring the Raman signal at one fixed frequency while scanning the optical delay.

To minimize the noise caused by shot to shot fluctuation, a diode picks up a small fraction of the laser beam. The PMT signal is normalized by taking the ratio of PMT output with respect to the photodiode output. Because of the slightly different signal responses between the PMT and photodiode, a software window discards laser pulses whose intensity falls outside of a predetermined energy range resulting in a much better signal-to-noise ratio.

For general description of the laser system and experimental method, see chapter 2.

4.3 Results and Discussion

4.3.1 Absorption Spectra And Size Of CdS Colloid

The absorption from different preparations of the CdS colloid is shown in Figure 4.1. The absorption diagram shows different features with different preparations. It takes some practice to get good colloid solution each time for the experiment. The onset of the absorption (Figure 4.1 a) is used to characterize the size of the colloid particles through the quantum size

confinement effects. For colloid with too smaller particles (Figure 4.1 b), the colloid is nearly transparent, and it is not appropriate to our experiment because there not much laser light is absorbed by the CdS to get enough light excitation of the electrons from the valence band to the conduction band. In fact, we have optimized our laser wavelength so that it gets good resonance with the $MV^{+\cdot}$ absorption band and the nearly all of the light is absorbed by the colloid after it passes through it.

Smaller CdS particles have quantum size-confinement, resulting in a blue shift of the absorption spectrum[30,39,50,73-79] from that of the bulk crystal, which has an onset of the absorption at about 500nm (2.53 eV). The onset of the absorption and the position of the excitonic peak are strongly correlated to the sizes of the colloidal particles[39(a),50,76,78,80-82]. This has been verified both experimentally[30,39b-c,79] and theoretically[73,75]. As a result, the electronic absorption spectrum of the colloid[12,39,73,82] can be used to deduce the colloid particle sizes (see Chapter 1.5.6). The absorption spectrum (Figure 4.1 (a)) of the colloidal CdS particles in our typical preparation has an excitonic shoulder at 446 nm and absorption onset around 474nm, corresponding to an average particle diameter of 60Å[24,50,39(a), 76,82].

4.3.2 Raman Bands Of $MV^{+\cdot}$ And Cds Phonon At Different Laser Wavelengths

Different enhancement of the Raman bands' intensity depends on the laser wavelength as shown in Figure 4.2. The intensity of phonon band decreases

Figure 4.1 The absorption spectra for CdS colloids for colloidal CdS (1.43 mM), HMP (0.416% w/v) (a) Typical preparation (b) Colloids with smaller particles

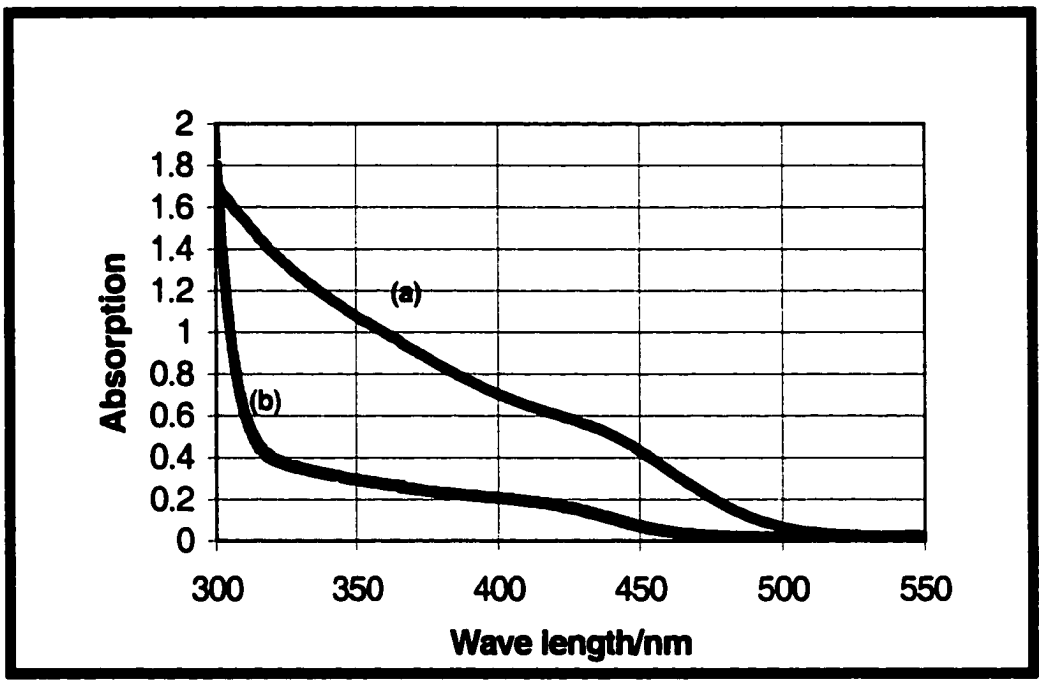

from obvious band to a shoulder when the laser wavelength changes from 409.6nm to 379.6nm. The relative intensity of $MV^{+\cdot}$ bands also changes with different laser excitation wavelength. The following table 4.1 shows the relative intensity of bands in each excitation wavelength in Figure 4.2 using the 816 cm^{-1} band intensity as the criteria for comparison with a relative intensity of 1.0. Though the relative intensity of 1658 cm^{-1} band is always enhanced the most of the five bands at both wavelengths, the relative intensity at 379.6 nm excitation is larger than that at 409.6nm. This serves as one of the basis of using 379.6 nm laser excitation to study the interfacial electron transfer.

Table 4.1 The relative intensity of Raman bands in different excitation wavelengths

Bands cm^{-1}	816	1214	1354	1525	1658
Relative Intensity at 379.6 nm	1.00	3.8	2.6	2.4	8.1
Relative Intensity at 409.6 nm	1.00	0.91	0.82	0.92	2.5

As shown in Figure 4.2, the spectrum in dashed line (a) is Resonance Raman Spectrum at 379.6nm laser excitation for CdS phonon and $MV^{+\cdot}$ bands using spinning cell containing sample of CdS colloid (1.43 mM monomer) , $MVCl_2$(1.06 mM), and hexametaphosphate (HMP) stablizer(0.446% w/v). The sample has been pre-irradiated for more than 3 hours and has a visible blue circle region of $MV^{+\cdot}$. The spectrum in solid line (b) is Resonance Raman

Figure 4.2 Comparison of RRS Raman bands of $MV^{+\cdot}$ and CdS phonon at (a) 379.6nm and (b) 409.6nm laser excitation. For CdS phonon band, the intensities of the two spectra are compared since the CdS concentration is the same in the two spectra. It is obvious that intensity of phonon band at 305 cm^{-1} is larger at 409.6 nm laser excitation that at 379.6 nm laser excitation. It is to be noted that the two spectra are independently measured without knowing the concentration of $MV^{+\cdot}$, so only relative intensity in the same spectroscopy is significant in the comparison of $MV^{+\cdot}$bands.

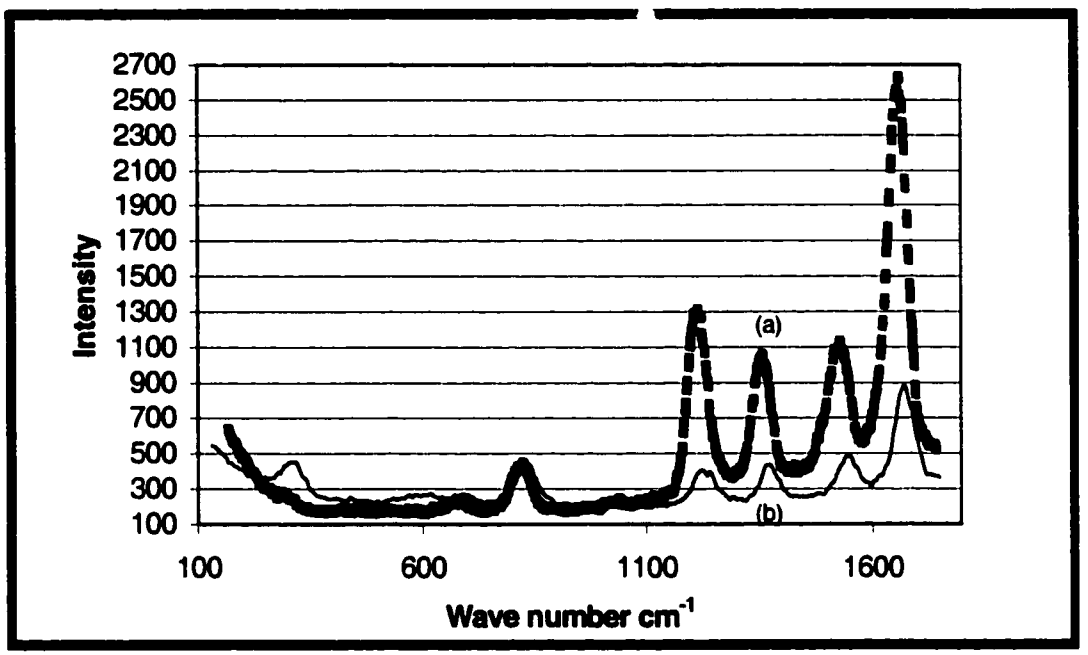

spectrum at 409.6nm laser excitation for CdS phonon and $MV^{+\cdot}$ bands using spinning cell containing sample of CdS colloid (1.43 mM monomer), $MVCl_2$ (1.06 mM), and hexametaphosphate (HMP) stablizer(0.446% w/v). But the sample has been pre-irradiated for more than 7 hours and has a visible blue circle region of $MV^{+\cdot}$.

4.3.3 Phonon Band Of CdS Colloid And Its Relaxation Dynamics

The CdS is also characterized by its characteristic LO phonon band at ~305 cm^{-1}. It has been previously reported that the LO phonon mode for CdS at 40-45 Å size is sensitive to the crystallite size (smaller size may have broader Raman line) by Rossetti et al[68]. It is found in our experiment (see above Figure4.2 in comparison of Raman bands of $MV^{+\cdot}$ and CdS phonon at 409.6nm and 379.6nm.) that the Raman band of phonon 305 cm^{-1} is obvious by laser excitation at wavelength at 409.6nm, however it becomes very weak (only a shoulder seen) at wavelength of 379.6nm. The second harmonic band of phonon band at ~610 cm^{-1} is visible at 409.6 nm, but it is nearly invisible at 379.6 nm laser excitation. This indicates that the resonance enhancement of phonon band is wavelength dependent and the enhancement is higher at 409.6 excitation wavelength than at 379.6 nm.

At 409.6 nm laser excitation, the phonon's relaxation dynamics is time-resolved using our femtosecond laser. In Figure 4.3 we see the vibrational relaxation occurs within ~2 ps before de-convolution with the laser pulse width assuming the dynamics is exponentially decreasing with time. It is shown later

the coupling the phonon modes of CdS with the vibrational modes of the adsorbate $MV^{+\cdot}$ provides very important channels for relaxation of $MV^{+\cdot}$. It helps us to identify the vibrational relaxation of the $MV^{+\cdot}$ adsorbed on CdS(s) colloid and the electron transfer dynamics from CdS colloid to MV^{+2} (see 4.3.8)

4.3.4 Raman Spectra Of $MV^{+\cdot}$ In Aqueous And Colloidal Solution

The Raman spectra of $MV^{+\cdot}$ by 379.6 nm laser excitation in a spinning cell containing $MV^{+\cdot}$ sample from different mediums are compared in the Figure 4.4. Spectrum (a) results from the $MV^{+\cdot}$ solution obtained from reduction of MV^{+2} in aqueous solution by Zn dust by reaction: $Zn + 2MV^{+2} \rightarrow Zn^{+2} + 2MV^{+\cdot}$. Spectrum (b) results from the $MV^{+\cdot}$ prepared by the same chemical method as (a) , and then added to CdS colloid solution. Spectrum (c) results from the $MV^{+\cdot}$ obtained from electron transfer from CdS to MV^{+2} by laser irradiation of the solution of CdS colloid and MV^{+2} in a sealed cylindrical spinning cell for Some time to form the blue solution. All these solutions of $MV^{+\cdot}$ are at concentrations low enough so that the dimer of $MV^{+\cdot}$ will not form and the colloid will not coagulate.

The Raman spectra of the $MV^{+\cdot}$ of these different media are the same in band wave number and shape. It is concluded that the presence of the CdS has not changed the characteristics of $MV^{+\cdot}$ significantly. We can use its wave number to characterize the $MV^{+\cdot}$ produced in colloid solution safely in the study of electron transfer from CdS to MV^{+2} later.

Figure 4.3 Dynamics at 305 cm^{-1} for CdS Phonon. Time resolution of the Raman band at 305cm^{-1} for phonon using laser of 409.6 nm wavelength and a spinning cell. The cell contains sample of colloidal CdS (1.43 mM monomer) and HMP stablizer (0.416 %w/v). The time dependence is obtained by subtraction of the background dynamics at 409 cm^{-1} dynamics from that at phonon band center 305 cm^{-1} for an average of 12-14 scans.

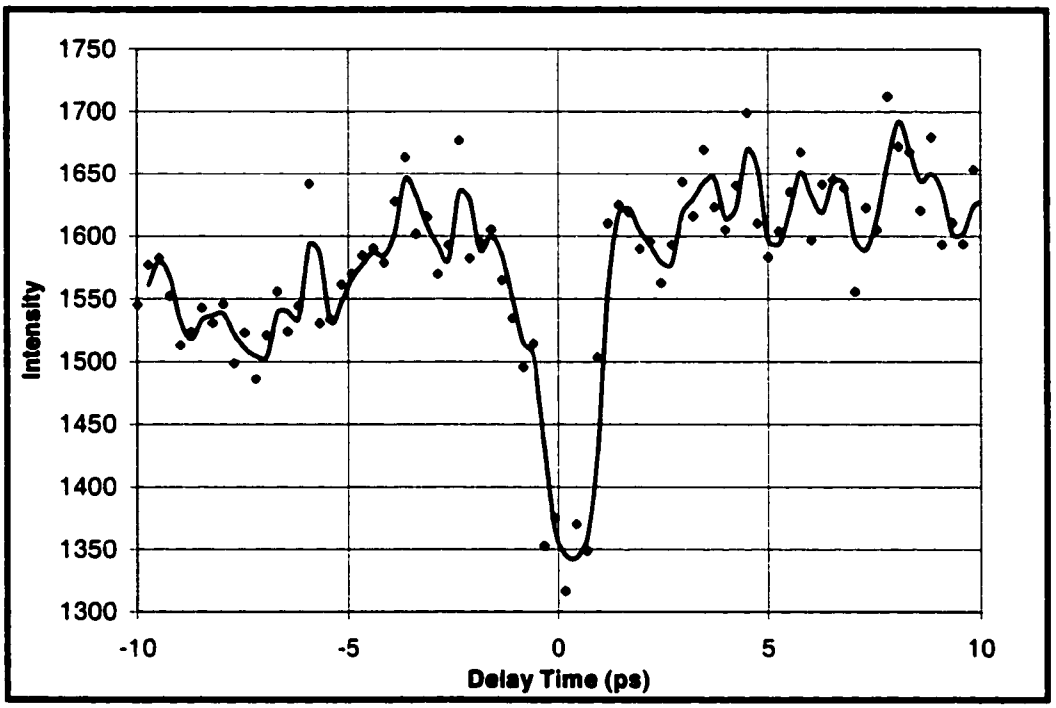

4.3.5 Accumulation Of Photo-Induced $MV^{+\cdot}$ And Its Dynamics In Cds Colloid

At the laser wavelength of 409.6 nm, the time-resolved dynamics is not so obvious. Because the $MV^{+\cdot}$ produced in such a small time range (fs to ps) is hard to observe. That is, at the wavelength, very little photons are absorbed by CdS, so not many electrons are excited to the conduction band. Therefore small amount of $MV^{+\cdot}$ is produced to be observed by RRS. And on the other hand, the resonance enhancement of $MV^{+\cdot}$ is not large. Only after we adjust the laser wavelength to 379.6 nm, it is possible to observe the dynamics.

But the $MV^{+\cdot}$ is actually produced as indicated by the accumulation of the $MV^{+\cdot}$ after laser irradiation for some time. It is shown in the Figure 4.5, the intensities of Raman bands of $MV^{+\cdot}$ increases gradually for successive measurements due to the irradiation time increase. After ~6.5 hr irradiation by laser at 409.6 nm, the relative intensity of $MV^{+\cdot}$ band at 816 cm^{-1} to phonon band has doubled.

The above experiments in the air-tightened spinning cell prove that the $MV^{+\cdot}$ produced by photo-reducing MV^{+2} partially remains in the cell during the time range of shot to shot (1 ms) of lasers and even lasts for the entire experiment. This is quite possibly caused by the fact the hole will not oxidize all the $MV^{+\cdot}$, and after a millisecond time range some of the $MV^{+\cdot}$ diffuse off the surface of the CdS into the bulk of the solution and last forever without the present of some other oxidants such as O_2. It is believed that the $MV^{+\cdot}$ concentration will reach a stationary state where rate of the production of $MV^{+\cdot}$

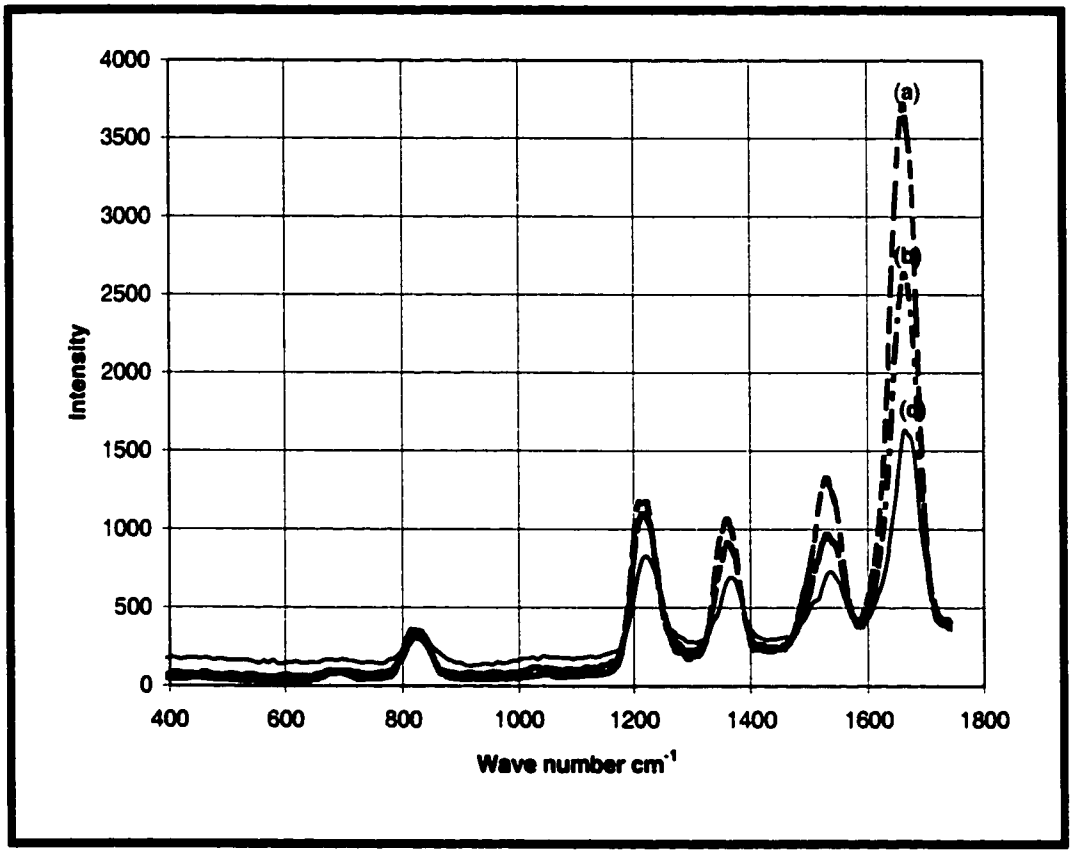

Figure 4.4 Comparison of Raman bands of MV^{+}. The Raman spectra of $MV^{+\cdot}$ by 379.6 nm laser excitation in a spinning cell containing $MV^{+\cdot}$ sample from different mediums.(a) In aqueous solution, $MV^{+\cdot}$ (1.04 mM) from reducing MV^{+2} by Zn powder. (b) in CdS, $MV^{+\cdot}$ (0.151 mM) from reducing MV^{+2} mixed with colloidal CdS (1.43mM monmer, HMP 0.416% w/v) (c) in CdS|MV^{+2} , MV^{+} blue circle: Raman bands of $MV^{+\cdot}$ from blue circle region in CdS(1.43 mM monomer), HMP(0.426% w/v), and $MVCl_2$ (0.151 mM) after ~2.5 hours laser irradiation.

by photo-reduction of MV^{+2} equal to the rate of consumption of $MV^{+\cdot}$ by hole oxidization of MV^{+} to MV^{+2}. The concentration of $MV^{+\cdot}$ will remain at a maximum constant as the laser irradiation time increases to some value.

The dynamics for the $MV^{+\cdot}$ from sample in a sealed spinning cell containing colloid CdS and MV^{+2} irradiated for the hours is time-resolved by measuring the time dependant of band at 816 cm^{-1} for $MV^{+\cdot}$ using 409.6nm laser (see Figure 4.6 (a) to (d)). Under the experimental condition the successive laser shot chain will hit the region where there is already $MV^{+\cdot}$ present. The dynamics will be a combination of the electron transfer dynamics with the dynamics of some transient processes of the previously produced $MV^{+\cdot}$ including the vibrational relaxation of $MV^{+\cdot}$. Certainly the higher the concentration of initially present $MV^{+\cdot}$ is, the larger the effect of its dynamics is. This is shown in the difference between the dynamics using fresh sample and the sample already irradiated by laser (Figure 4.6 (a) or (c) compared to (b)). Certainly the dynamics obtained using the sample of ~7hr laser irradiation mainly consists of the dynamics of the $MV^{+\cdot}$ Previously accumulated in the solution. The shorter wavelength of 379.6 nm laser excites more electrons to conduction band, thus give higher accumulation rate of $MV^{+\cdot}$ (see Figure 4.6 (c)). This is obvious by comparing dynamics the Figure 4.6 (a) excited by 409.6nm laser with Figure 4.6 (c) excited by 379.6 nm laser. The later dynamics has a very un-symmetric dynamics due to the accumulation of $MV^{+\cdot}$ as time increases. To get rid of this $MV^{+\cdot}$ accumulation and therefore its dynamics the cell inside which colloidal solution is re-circulating is used.

Figure 4.5 The Raman bands of $MV^{+\cdot}$ to show the accumulation of the MV^{+} varying with different laser irradiation time at 409.6nm laser wavelength. The spinning cell contains colloidal sample of CdS colloid (1.43 mM monomer), $MVCl_2$(1.06 mM), and hexametaphosphate (HMP) stablizer(0.446% w/v). It is shown that after ~6.5 hr laser irradiation, the band intensity of $MV^{+\cdot}$ is significantly increased. This 6.5 hr aged and irradiated sample (a) has doubled the relative intensity to phonon compared to the fresh sample (b).

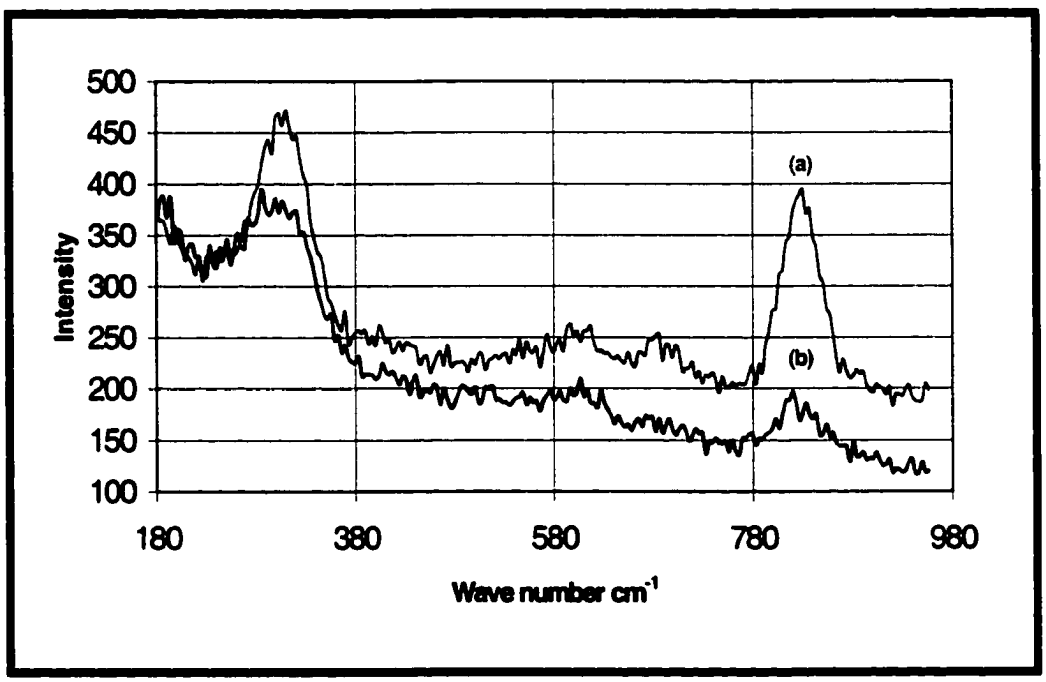

Figure 4.6 Dynamics of $MV^{+\cdot}$ bands consists of electron transfer, $MV^{+\cdot}$ relaxation and $MV^{+\cdot}$ accumulations in a spinning cell containing sample of colloidal CdS (1.43 mM), HMP(0.416% w/v), and $MVCl_2$ (1.06 mM). Measuring Raman intensity of band at 816 cm^{-1} at laser excitation of 409.6 nm is done for (a) and (b). Measuring Raman intensity of band at 1658 cm^{-1} of laser excitation at 379.6 nm is done for (c) and (d). (a) Using fresh sample, no obvious dynamics is shown due to very small amount of $MV^{+\cdot}$ produced by electron transfer. (b) The sample is already irradiated by laser beam for ~7hr. There are obvious dynamics and slightly un-symmetry of the dynamics due to the aqueous $MV^{+\cdot}$relaxation previously present and $MV^{+\cdot}$ accumulation from electron transfer. (c) Using a fresh sample, there exists a band intensity linear increase with time due to $MV^{+\cdot}$ accumulation in the cell, with slight dynamics of $MV^{+\cdot}$ relaxation and $MV^{+\cdot}$ from electron transfer.(d) Using aqueous $MV^{+\cdot}$ sample (1.04 mM MVCl prepared by Zn dust reduction.), there is an obvious relaxation dynamics of $MV^{+\cdot}$

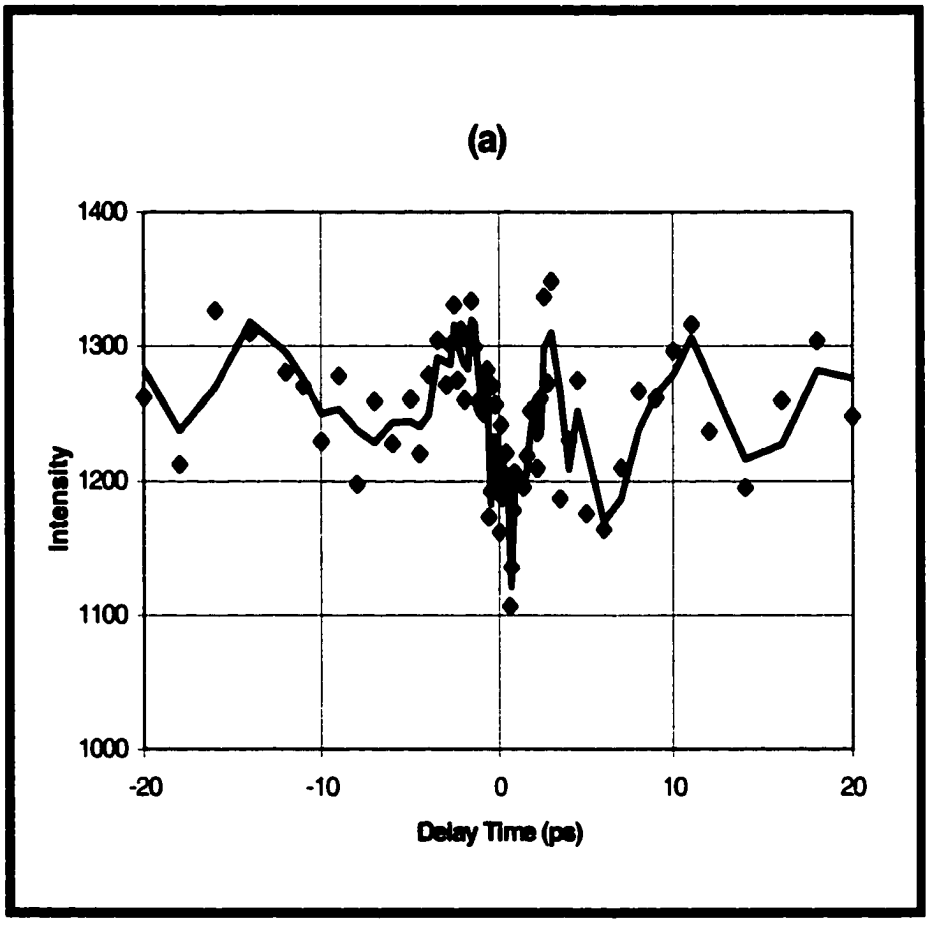

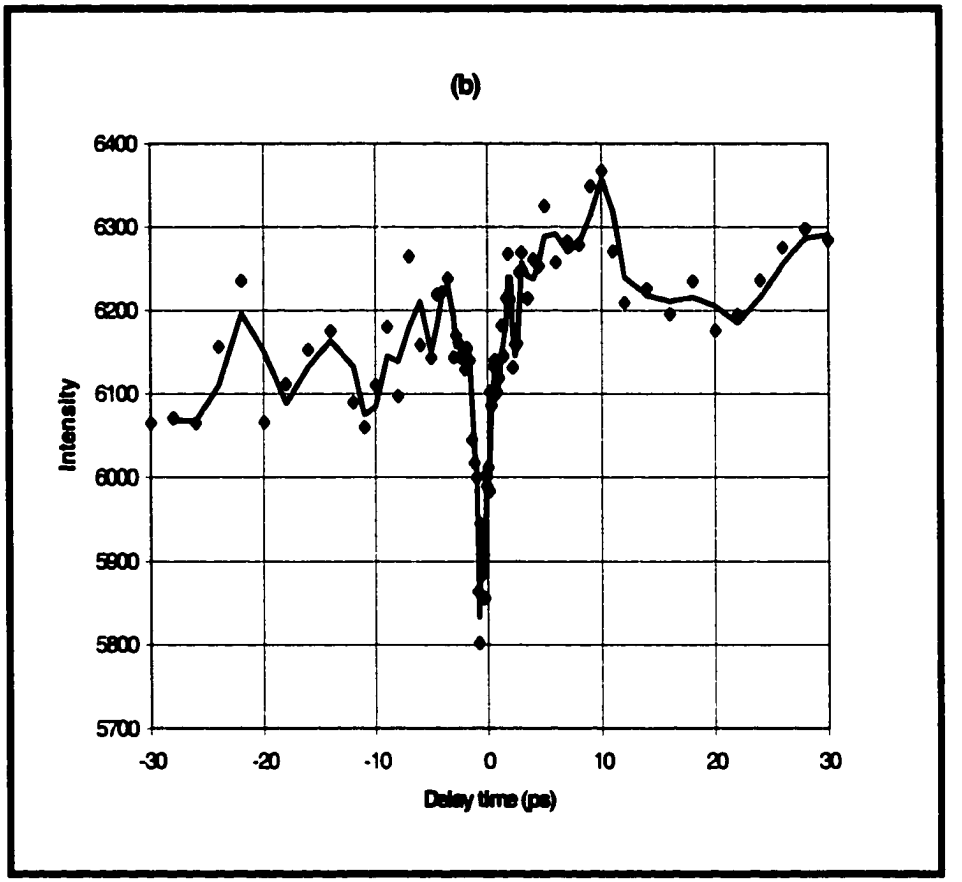

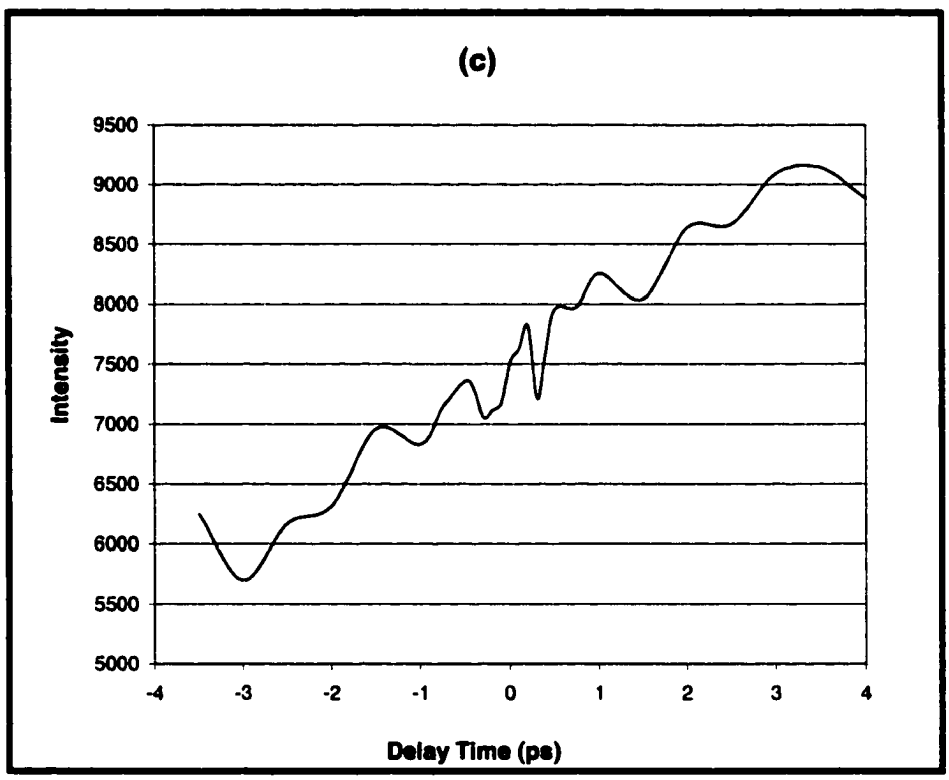

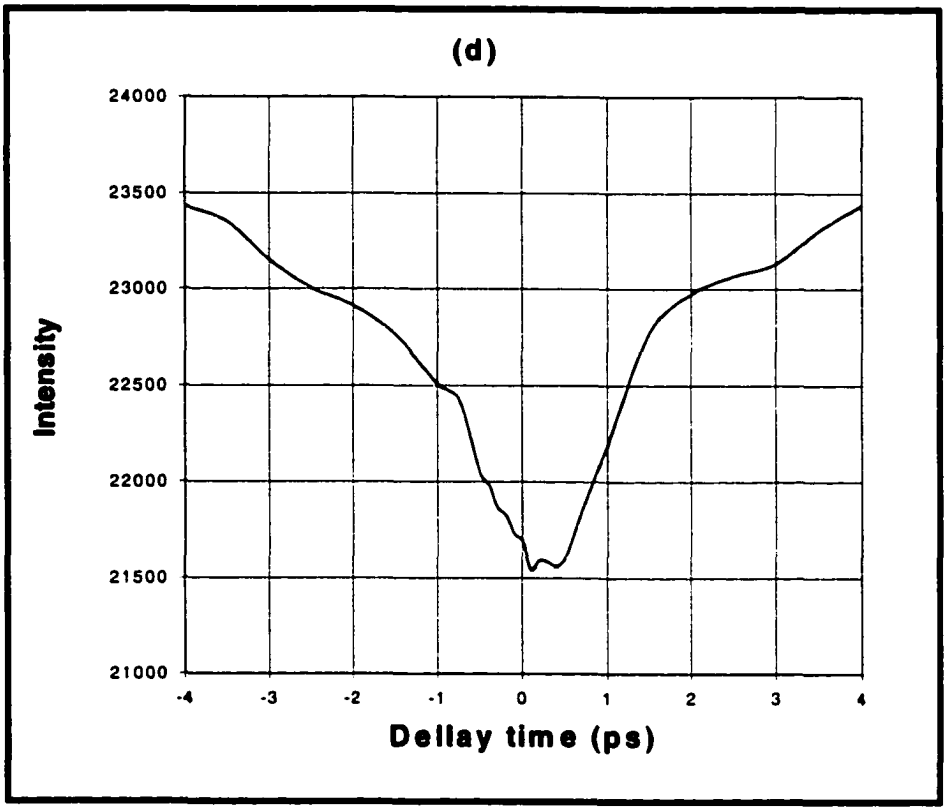

4.3.6 Significance Of Change In Laser Wavelength And Optical Cell

Even though the wavelength at 409.6nm is good for the study of phonon band of CdS, it does not give significant $MV^{+\cdot}$ signal in the study of electron transfer. Change wavelength from 409.6 to 379.6nm will increase the $MV^{+\cdot}$ signal for two main reasons. Firstly shifting the laser wavelength to more violet will increase the absorbance of the laser light by CdS colloid (see CdS absorption Figure 4.1), so electrons with higher energy and larger amount are excited to the conduction band, and in turn the more MV^{+2} is reduced to form $MV^{+\cdot}$ by electron transfer. Secondly the Raman resonance enhancement still occurs due to good match of the wave length of the laser with the absorption of $MV^{+\cdot}$'s B_{3u} (MO 7, ground) to B_{3u} (MO 11, excited) electronic transition (Note the $MV^{+\cdot}$ has a broad absorption peak of 399nm with fine structure at 385 and 368 nm, the 379.6nm of our laser wavelength matches this absorption band.) The wavelength 397.6nm is chosen in most of our experiments, after carefully comparing the characteristics of the Raman bands for $MV^{+\cdot}$ and CdS phonons using these two wavelengths.

The rotating/spinning cell in which the sample is sealed is appropriate for study the relaxation dynamics of $MV^{+\cdot}$ in aqueous solution because every alternative millisecond there is a laser shot, and the relaxation $MV^{+\cdot}$ completes within this time. This is basically no new substance is produced by the laser excitation except new states are produced. In our study of interfacial electron transfer experiments, the production of $MV^{+\cdot}$ will add more challenging to

resolve the electron dynamics due to the accumulation of the $MV^{+\cdot}$ produced in the cell. The laser will cause electron transfer to reduce MV^{+2} to $MV^{+\cdot}$. The $MV^{+\cdot}$ accumulates within the sealed rotating cell in the laser irradiation regions. After irradiating for a time long enough, a visible blue region (circle) is formed in the cylindrical cell. Thus in one scan to measure dynamics of the Raman band intensity of $MV^{+\cdot}$ as delay time using the pump and probe technique described earlier, it will include the following three dynamics. (a) The dynamics for electron transfer from CdS particulate to the MV^{+2} occurs with a range of 270 fs to 6.7 ps as shown later. (b) The accumulation dynamics of the $MV^{+\cdot}$ produced by the previous laser irradiation occurs within ms to hours during the entire experimental time. That is, the $MV^{+\cdot}$ produced is only partly oxidized by the holes to give back to MV^{+2}, and some $MV^{+\cdot}$ still remains in the solution. As the experiments proceed, the $MV^{+\cdot}$ concentration increases in the solution, particularly in the early stage of the laser irradiation. After laser irradiation for some time, a stationary state may be reached between the accumulations of $MV^{+\cdot}$ by laser irradiation and the hole oxidization of it, since the accumulation of $MV^{+\cdot}$ will increase the probability of hole oxidation. Thus, this part contributes the dynamics at the first several scans most, and gradually has less effect. (c) The vibrational relaxation dynamics of the accumulated $MV^{+\cdot}$ present in the solution occurs in ~ 2ps as determined in chapter 2. The more $MV^{+\cdot}$ accumulated, the more dominate the effect is. So it is expected this will have the most effect after a stationary state is reached, and the accumulated $MV^{+\cdot}$ concentration reaches its maximum. We have

measured the dynamics of the $MV^{+\cdot}$ accumulated in the rotating cell (The blue circle is formed because the cell is spinning). The dynamics measured using the sealed rotating cell is complicated by the above processes.

To simplify the theoretical analysis of the problem, an optical cell with sample re-circulating in it is used, in which large amount of colloid sample in contact with oxygen in the air is re-circulating through the optical cell with high speed. This eliminates the $MV^{+\cdot}$ accumulation effect and the resulting $MV^{+\cdot}$ vibrational relaxation dynamics (later in details). This is because (a) the re-circulation of high speed will mix the $MV^{+\cdot}$ produced by laser irradiation homogeneously in the solution in ms scale, and the oxygen in the solution will oxidize the $MV^{+\cdot}$ produced immediately to MV^{+2}, (b) the hole will also oxidized part of the $MV^{+\cdot}$ produced, and (c) the large amount of re-circulating colloid enables each laser shot will encounter a fresh sample. Thus the accumulation of $MV^{+\cdot}$ is eliminated using this fast recirculating colloid in contact with air method. The following sections describe the results using 379.6nm laser and recirculating colloid.

4.3.7 MV^{+} Partly Produced Within The Pulse Width ---- RRS Spectra Of Both MV^{+} Photo-Induced In CdS And MV^{+} Chemically Produced In Solution

The RRS spectra of both MV^{+} photo-induced in the aerated colloidal CdS excited by a femtosecond laser pulse and MV^{+} produced in the aqueous solution by Zn dust reduction are shown in Figure 4.7. Both spectra show four strong bands in the range of 1100 to 1740cm^{-1}: namely 1214, 1354, 1525, and 1658 cm^{-1}. These modes are primarily stretching vibration modes: N-R (R is the

substituent in the N atom of MV^+), interring C-C, C-N, and C-C correspondingly [83]. There exist only slight spectral differences between solution MV^+ and photogenerated MV^+ produced on the colloid. There is a slight down shift of the frequency and broadening of the bands for MV^+ adsorbed on the colloid. This result is consistent with the picosecond RRS results of Brus et al., and may be due to the formation of MV^+-S^{-2} complex[67].

The RRS signal of MV^+ on the CdS colloid is laser fluence-dependent as shown by keeping the laser power constant but changing the area of focus of the laser beam. In loose focus, no MV^+ signal can be observed, only the very weak non-resonance MV^{+2} signal exists. The spectrum of Figure 4.7 for the colloid system is obtained only with a tighter focus. This observation is expected if one photon is used to photo-induce the MV^+ and another photon is used to probe the photo-induced MV^+. As expected the photo-induced MV^+ concentration is found to be proportional to the square of the laser flux. Furthermore the photo-induced MV^+ is back-oxidized to MV^{+2} during the cycle time in the recirculated aerated colloidal system. Oxidation occurs partly by reacting with oxygen and partly by reaction with holes on the colloidal surface. Therefore the MV^+ signal observed in the colloidal system is assigned to the photo-induced MV^+ and cannot result from the accumulated MV^+. These results convince us that the MV^+ is being produced by electron transfer from the photo-induced electrons in the conduction band of CdS. With the pump and probe pulses overlapped in time all of the MV^+ signal must be produced within our

Figure 4.7 RRS spectra for $MV^{+\cdot}$ (A) MV^{+} produced by laser-induced photo-electron transfer from CdS to $MVCl_2$ in the recirculated colloidal system of CdS (1.43mM), $MVCl_2$ (1.06mM), and HMP stabilizer (0.416% w/v). (B) 2.08×10^{-4} M MVCl in solution (no colloid) obtained by Zn dust reduction in a spinning cell.

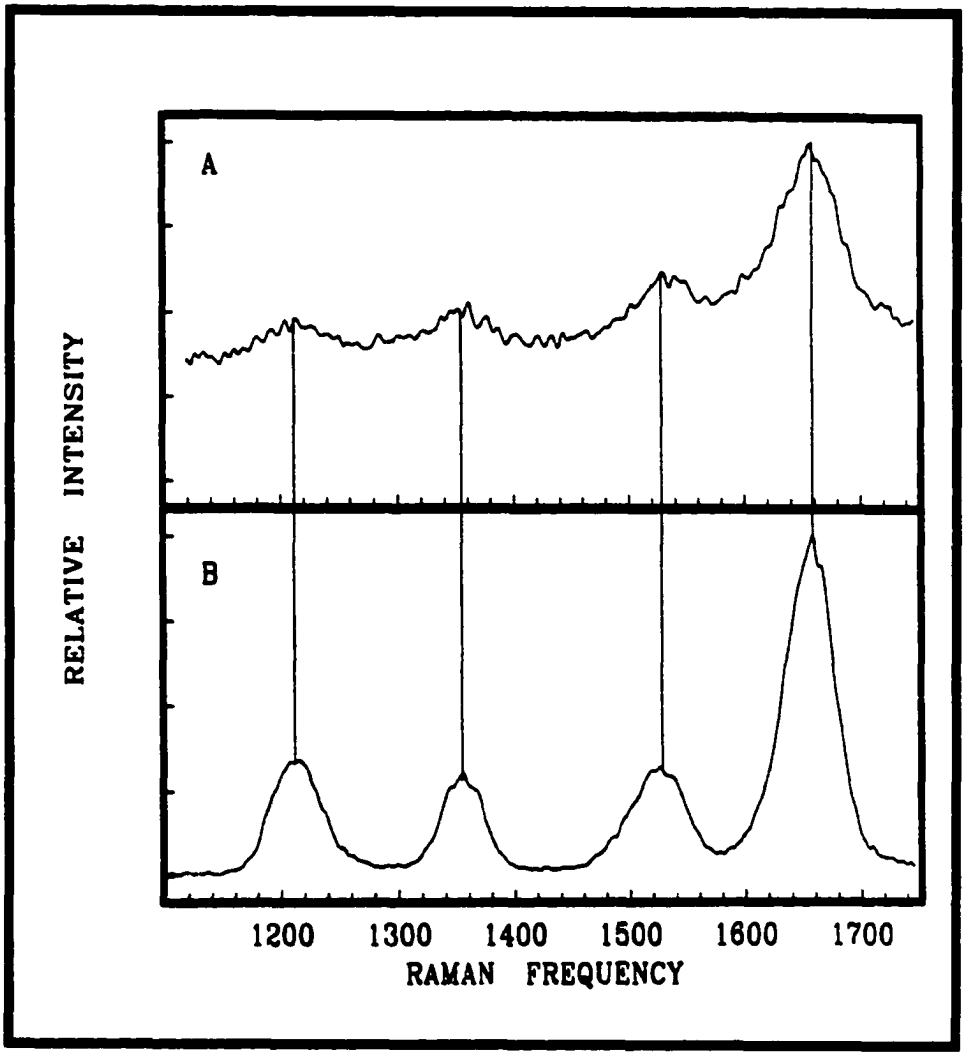

laser pulse width of 350fs. This is consistent with previous results that suggests the MV^{+2} is adsorbed on the surface of CdS particles[52-55,63,64,67,68,84], since it is impossible for the bulk MV^{+2} to diffuse through the solution to the colloidal particles within such a short time[85].

Further discussion of the change in molecular structure upon reduction from MV^{+2} to MV^{+} can be made by considering the above results and the different structures between MV^{+2} and MV^{+}. The molecular ring-structure of MV^{+2} is a delocalized aromatic-type, however that of MV^{+} is a more delocalized quinoid-type. A significant change in wavenumber of $53cm^{-1}$ (from 1301 to $1354cm^{-1}$) for the inter-ring C-C stretching mode is observed in the RRS spectra upon reducing MV^{+2} to MV^{+}[83].

In this experiment, the pump pulse virtually initiates the structure change. Therefore in principle the transition state from MV^{2+} to MV^{+} would have been reflected by the wavenumber change in the interring C-C mode if the structure change has a time scale comparable to the pulse width, and if the Raman scattering cross section is enhanced with the structure change to allow a detectable Raman signal of the transition state from MV^{2+} to MV^{+}. However, the RRS spectra in Figure 4.7 shows that there is no observable difference in the wavenumber between aqueous MV^{+} prepared by zinc reduction of MV^{+2} and MV^{+} produced by photo-reduction of MV^{+2} in the CdS colloid within the pulse width. Thus it is concluded that this structure change is almost complete within the pulse width 350fs[86] and that is whythere is no observable difference in the wavenumber between aqueous MV^{+} and that obtained from electron transfer.

4.3.8 Time-Resolution Of The Dynamics Of Photoinduced MV^+ --- Multi-Exponential Behavior Consisting Of Two Major Components

The photoinduced MV^+ dynamics can be monitored by the intensity of any of the RRS bands for MV^+ as a function of delay time. The $1658cm^{-1}$ band is preferred in this study to maximize the signal. First a pump pulse is used to initiate the electron transfer from CdS to the adsorbed MV^{+2} to form MV^+. At the probe wavelength of 379.6nm, the MV^+ gives very strong RRS, however MV^{+2} only has weak normal Raman scattering. A second time-delayed probe pulse is used to determine the RRS intensity of the photo-generated MV^+ at various delay times, by scanning the delay from 0 to 30 ps and fixing the monochromator at the center position of the $1658cm^{-1}$ band. The RRS intensity determined in this way is shown as a function of delay time in Figure 4.8. It can be seen that the rate of change in the RRS intensity has two time components (Figure 4.8). It is important to note that these dynamics scans are symmetrical with increasing time delay in both directions from time zero, because the two pulses used in the experiment are of the same wavelength.

The observed transient RRS in Figure 4.8 is the convolution of the photoinduced MV^+ dynamics with the instrument response function. The latter is related to the pump or probe pulse profile, which is determined by an autocorrelation method. The photoinduced MV^+ dynamics are modeled by an empirical multi-exponential formula: $a_1 + a_2\exp(-a_3t) + a_4\exp(-a_5t) + \ldots$, where t is the delay time, a_i (i=1,2,3,4,5,...) is the parameter. This function is convoluted with the laser pulse profile and is used to fit the observed transient RRS data of

Figure 4.8. A best fit is obtained by a double-exponential decay $a_1 + a_2\exp(-a_3t)$ + $a_4\exp(-a_5t)$ with time constants $1/a_3$= 270±30 fs, and $1/a_5$= (6.7±1.9) ps as shown in Figure 4.8. The validity of the double exponential fit is demonstrated in Figure 4.9 where a single exponential fit is attempted which clearly does not fit the early time dynamics.

The above results show that the photoinduced MV^+ dynamics consist of two primary components. The fast component of time constant 270fs confirms that the electron transfer takes place, at least in part, within the laser pulse width, which is quite consistent with our earlier conclusion made from the time zero RRS spectra in Figure 4.7. However, the slow component with time constant 6.7ps may have two origins. First it may be primarily ascribed to a slow component of electron transfer. Second it may result from processes associated to the electron transfer such as the vibrational & electronic relaxation of MV^+.

4.3.9 MV^+ Vibrational Relaxation Interference --- Dynamics Of Aqueous MV^+

Vibrational relaxation in the ground electronic state of MV^+ following its formation on the colloid can cause a dynamic change in the RRS scattering cross section of MV^+. In a previous paper[87(a)], aqueous (no colloid present) MV^+ produced by chemical reduction was used to study the vibrational relaxation dynamics, using the same pump-probe scheme as above. The dynamics of both Stokes and anti-Stokes bands were measured and it was found that vibrational relaxation is not double-exponential, but a single-

Figure 4.8 The RRS intensity determined by fixing the monochromator at 1658cm^{-1} is shown as a function of delay time between the pump and probe pulses, for the recirculated colloidal system CdS (1.43mM), $MVCl_2$ (1.06mM), and HMP stabilizer (0.416%w/v). The circles are experimental data, and the solid line is the multi-exponential fit described in the text. The best fit is obtained by a double-exponential decay with rate constants of 1/270fs and 1/6.7ps.

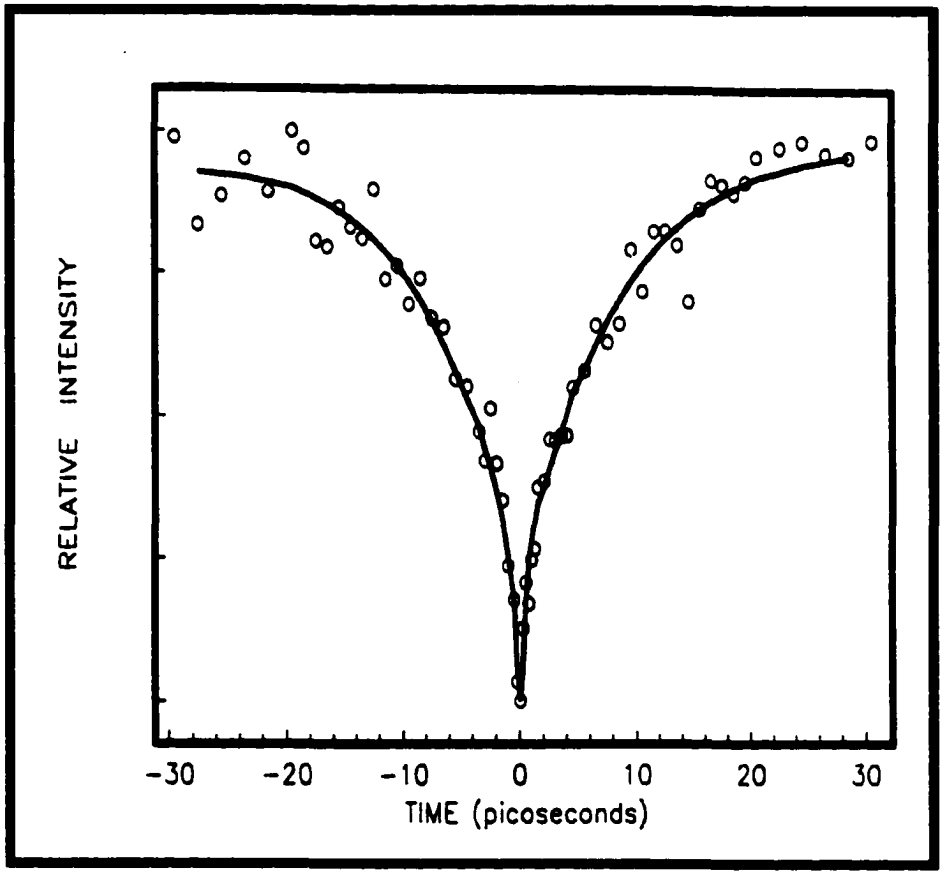

exponential decay with a time constant of 3.1ps (see Figure 4.10). The fact that this relaxation time constant is significantly different from the slow component of the photo-induced MV^+ on the colloid suggests that the vibrational relaxation dynamics plays a minor part in the MV^+/colloid dynamics. Our following interpretation of this result favors that the slow component 6.7 ps is unlikely originated from the vibrational relaxation of MV^+/colloid.

As compared to the aqueous MV^+, the MV^+ adsorbed on the CdS colloid might have some new mechanism[87(b)] to transfer vibrational energy. That is the adsorbed MV^+ relaxes through the CdS substrate via coupling the phonon modes (multiphonon damping) & creation of electron-hole (e^- -h^+) pair in the substrate. In metal substrates the creation of e^- -h^+ pair has been considered as one of the effective ways to transfer vibrational energy from adsorbate to the substrate since the band gap of metal is zero. However our CdS is a semiconductor with bandgap much larger than the vibrational energy, so the creation of e^- -h^+ pair in CdS by the vibrational energy is impossible. The other possible mechanism, which has been common in the dielectric substrate, is by multi-phonon damping[87(b)]. If this latter case would be possible, then the vibrational population lifetime of the adsorbed MV^+ should have been slow, typically in the time range 10^{-10} - 10^{-9} s[87(b)]. This is primarily due to the energy mismatch: the vibrational wavenumber of the C-C stretching mode of the MV^+ is 1658cm^{-1}, however the wavenumber of the LO phonon mode of CdS is 305 cm^{-1}[68].The five-phonon damping occurs only at low rate.

Figure 4.9 This fit obtained by the single-exponential decay is very poor, which proves the multi-exponential identity of the photo-induced dynamics. The circles are the same experimental data as Figure 4.8, but the solid line is the single-exponential fit.

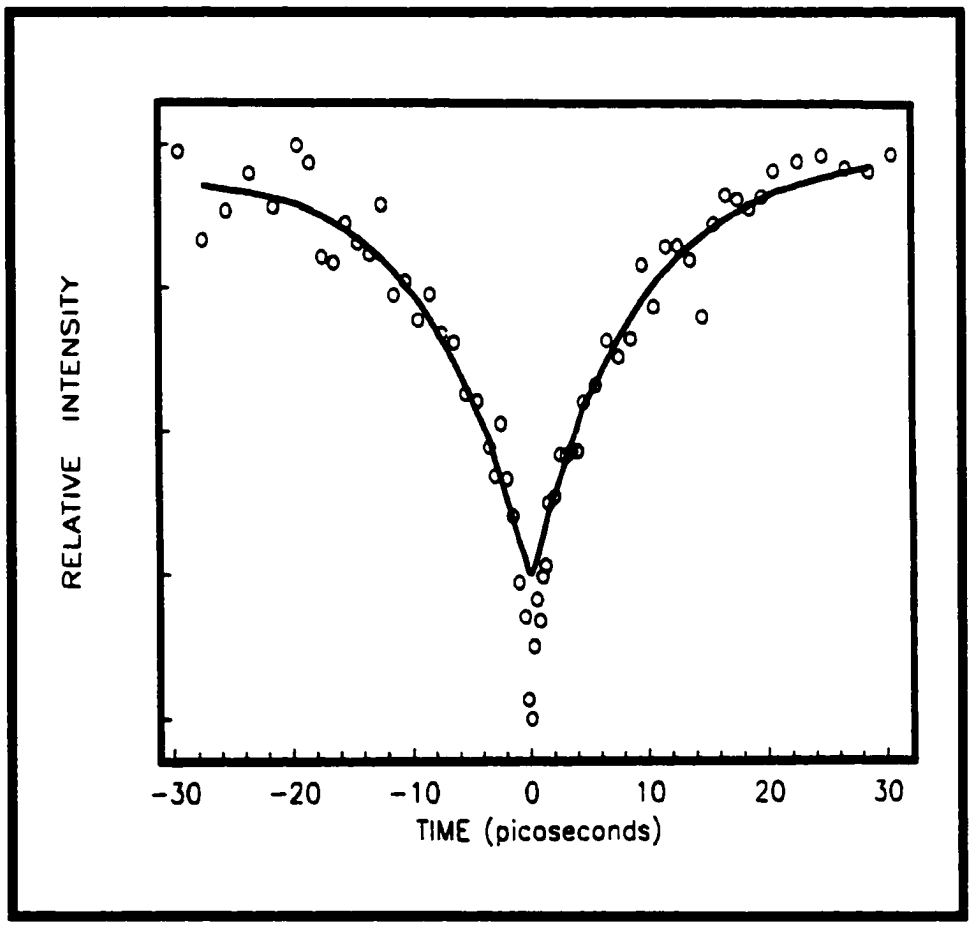

Furthermore the vibrational population decay time of the adsorbed MV^+ should have been shorter than that of the MV^+ in solution by analogy to the other similar system. For example upon adsorption on semiconductor SiO_2 the population lifetimes of C=O stretching mode for series of compound $Rh_2(CO)_4Cl_2$, $Co_4(CO)_{12}$, and $Rh_6(CO)_{16}$ are 4 times shorter than those in solution [87(c)]. However our experiment shows that the 6.7ps slow component is neither in the expected 10^{-10} - 10^{-9} s time range nor shorter than the 3.1ps of the corresponding mode of MV^+ in aqueous solution. Therefore it is obvious that the 6.7ps slow component is unlikely from the vibrational relaxation of the adsorbed MV^+.

4.3.10 Assignment Of The Two Components --- Discussion Of The Electron Transfer Mechanism

The relaxation of the MV^+ has been excluded in the above control experiment, but other processes may still affect the interfacial electron transfer from CdS to the MV^{2+}. Upon laser irradiation above the band gap of CdS, the generated electrons are trapped subsequently in the time range of 10^{-13} to 10^{-14}s[23,24]. More precisely the electron trapping has been time-resolved recently to occur in 90 fs in CdS dispersed in acetonitrile[11(a)] or within 100fs in aqueous colloidal CdS[12,13] by transient absorption of trapped electrons. In view of the time range, the 270fs fast component in the photoinduced MV^+ dynamics may be influenced by both free electrons and trapped electrons, especially very shallowly trapped; however the 6.7ps slow component is completely contributed by the trapped electrons.

Figure 4.10 The RRS intensity determined by fixing the monochromator at the center position of the 1658cm^{-1} is shown as a function of delay time between the pump and probe pulses, for the 2.08 x 10^{-4} M MVCl solution obtained by Zn dust reduction in a spin cell.

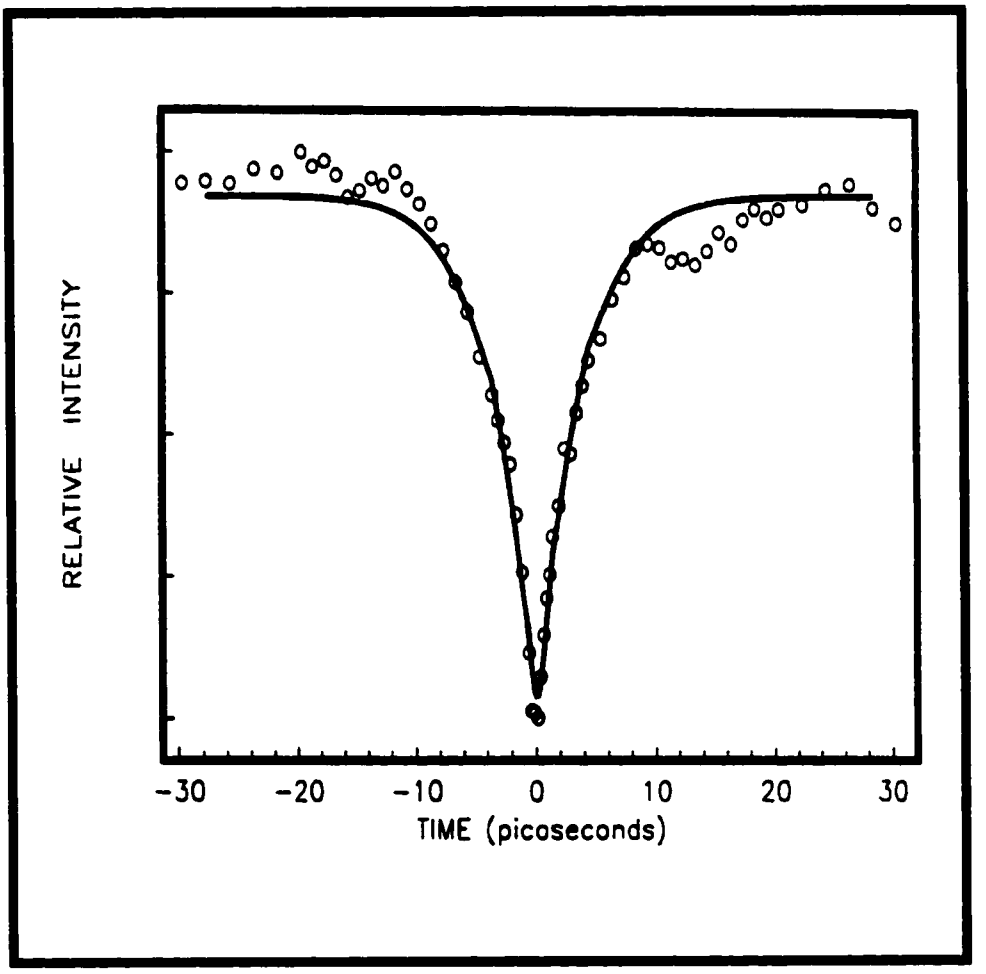

The trapped electrons then undergo electron-hole recombination[88] in diverse time ranges, according to which the trapped electrons are divided into two types. One recombines with holes in the time range of nanoseconds and microseconds[11(a),30(a),69]. The other recombines with holes in the time range of picoseconds having time constants of 50ps for geminate recombination and a 2-3ps for nongeminate recombination[11(a)-13,23,30(a),69]. It is obvious that only the non-geminate recombination may compete with the 6.8ps slow component of the photoinduced MV^+ dynamics. However the non-geminate recombination is very sensitive to the laser fluence and is only observed at high pump intensities[12-13] or at high concentration of trapped electrons. In our experiment, the laser flux (1.0 photons/$Å^2$) is typically comparable to the literature[12-13], however no difference in the photo-induced dynamics is observed by decreasing the laser flux by a factor of two within our experimental error. Thus there is a difference in the flux dependence between our electron-transfer dynamics in MV^{2+}/CdS colloid and the electron-hole recombination dynamics in CdS colloid of the literature[12-13]. Evidently, the contribution of the non-germinate recombination to the slow component of the photoinduced MV^+ dynamics is small. The reason may be that part of the electrons in our system has already been transferred to MV^{+2} to produce MV^+ through the 270fs fast component prior to the non-geminate recombination, or equivalently the concentration of trapped electrons has been reduced in the presence of MV^{+2}. Consequently the contribution of the non-germinate recombination to the slow component of the photoinduced MV^+ dynamics has been attenuated greatly.

Based on the above discussion, the fast 270fs component of the photoinduced MV^+ dynamics is assigned to the transfer of very shallowly trapped electrons including a small part of free electrons. The slow 6.8ps component is primarily contributed by the transfer of trapped electrons that are relatively deeply trapped. As shown in the further discussion in the following (4.3.11 and 4.3.12), the reason for the multiple components may be very complicated by the distribution of traps and electron tunneling distance.

4.3.11 Discussion Of The Double-Exponential Electron Transfer And Trap Depth

The multi-exponential behavior has been very common in the fluorescence decay[19,30(a),32,89(b),27(b)] and in absorption bleaching decay[23] studies of electron-hole recombination. In principle, electron-hole recombination could be understood as an electron transfer process in which the electron is transferred to a spatially separated hole. Thus, one of the straight forward explanation of the multi-exponential behavior of the above electron transfer from CdS to MV^{2+} is to use similar explanations to the multi-exponential recombination, i.e., the distribution in electron trap depths [16,19,22,23] being the main contributions.

The distribution in the electron-trap depths[16,19,22,23,90] at the CdS surface is shown schematically in Figure 4.11 (a), which indicates that some electrons are shallowly trapped, while the others are relatively deeply trapped[19,22]. This difference in electron trap depth means difference in electron free energy. So the trap sites on CdS surface apply the trap depths to shift the free energy of the electrons to be transferred. This is similar to the case where the applying

different external potentials across the electrode-solution interface shift the free energy of the electrons to be transferred. The electron goes from shallow trap to deep trap has the similar effect on its free energy to applying a potential from cathodic toward anodic one. By interfacial electrochemical theory, this shift in free energy of the electrons due to potential or here due to trap depth is well expressed by a diagram as shown in Figure 4.11 (b). It is shown in this Figure, the more shallow the trap, the less the activated energy $\Delta G^{\dagger}$ of the electron transfer (Figure 4.11(b)), therefore the faster the rate constant according to electron transfer theories [1(a),7]. Thus the distribution in the trap depths will give the multi-exponential dynamics, though only two components are resolved corresponding to the two peaks in the distribution.

Moreover, the trap depth difference ΔD between the shallow and deep traps in the distribution shown in Figure 4.11(a) can be correlated to the activated energy difference $\Delta G^{\dagger}_{ds}$ between the fast and slow components by the electron transfer coefficient α through $\Delta D = \Delta G^{\dagger}_{ds} / \alpha$ (Figure 4.11(b)). The $\Delta G^{\dagger}_{ds}$ can be evaluated as 3.2RT or 77meV at room temperature by the rate constants (a_3, a_5 from section 3) through equation, $\exp(-\Delta G_{ds}/RT) = a_5/a_3 = 0.27/6.7=0.042$. Therefore the $\Delta D = \Delta G_{ds}/\alpha$, is 100 to 308meV, since α is less then 1 (ca 0.25 to 0.75 is assumed.). This ΔD, 100-308meV varying with different α, actually represents the typical deep trap depth, because the fast component a_3 corresponds to the shallowly trapped & free.

Figure 4.11 Schematic diagrams for free energy G difference caused by trap depth D difference (A) The population distribution of shallowly and relatively deeply trapped electrons[19,22]. The $\Delta D > 0$ is the free energy G difference or trap depth D difference between the shallowly and relatively deeply trapped electrons. (B) The ΔD causes a difference in the activated energy between the shallowly trapped electrons and relatively deeply trapped electrons in the electron transfer process according to the interfacial electron transfer theory[1(a),7]. The activated energy for relatively deeply trapped electrons (ΔG_d) is larger than that for shallowly trapped electrons (ΔG_s) by $\alpha\Delta D > 0$, where the α is the electron transfer coefficient. This is obvious in the figure, because $\Delta G_d + (1-\alpha)\Delta D = \Delta G_s + \Delta D$ resulting in $\Delta G_{ds} = \Delta G_d - \Delta G_s = \alpha\Delta D > 0$. Note the free energy G in (A) and (B) parts of the figure is independently scaled.

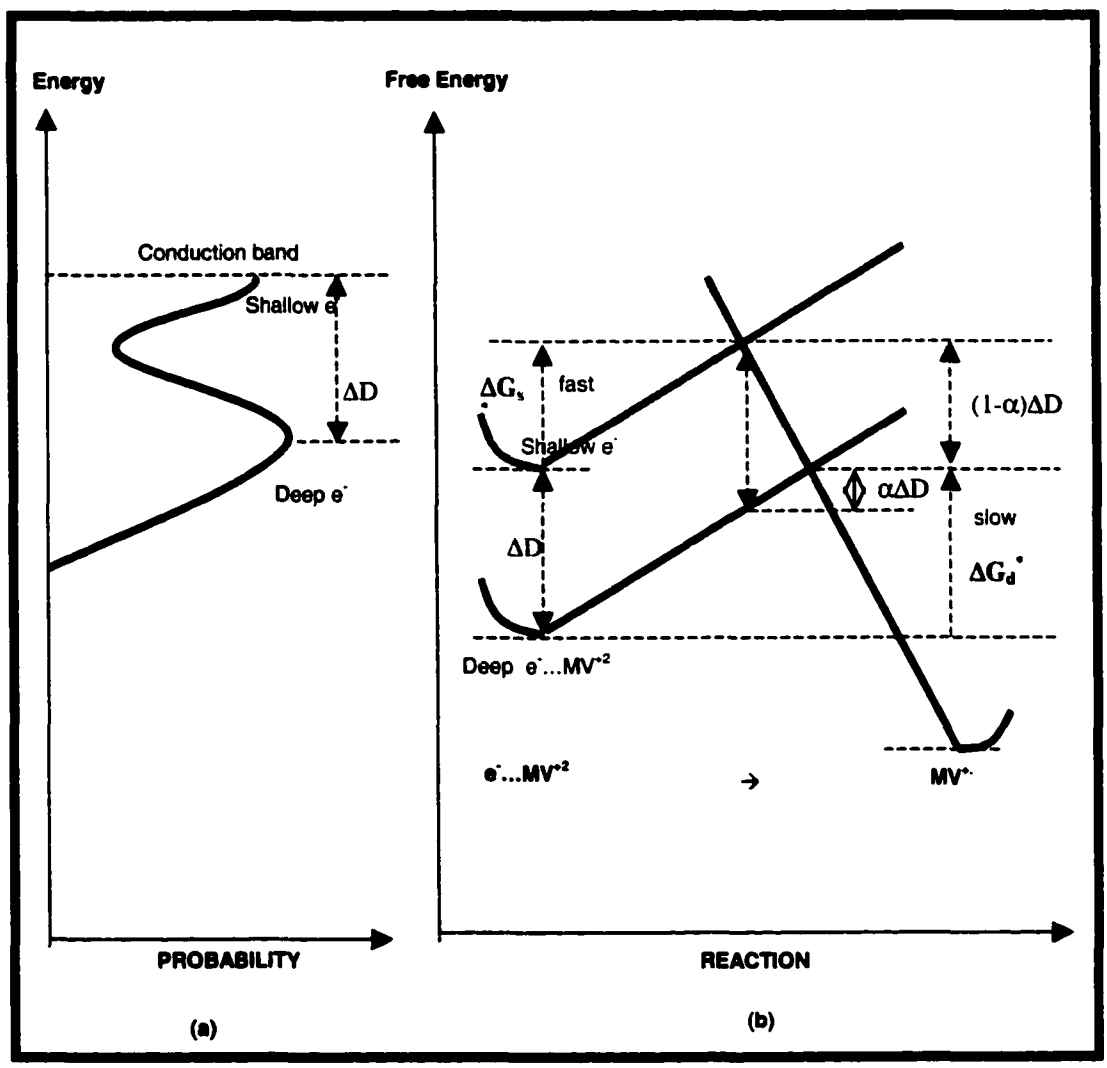

If the above explanation by the distribution in the electron trap depths (Figure 4.11) is correct, then the deep trap depth range 100-308mV obtained from the fast and slow components a_3 and a_5 of electron transfer should be comparable to that obtained by other methods by studying the electron trapping and detrapping rates in the colloid. A thermodynamic calculation based on the combined data of Bowman's group[11(a)], Zhang's group[12,13], and Weller's group[22] is then carried out and gives the typical relatively deep trap depth of ca 280 meV (see the reference part[91]). Also Weller et al[19,22] obtained a deep trap depth, ca 300meV by measuring the excitonic fluorescence decay time resulted from the electron detrapping process. Thus there is agreement in the relatively deep trap depth among the above three methods.

4.3.12 Further Discussion Of The Electron Transfer Dynamics

We have discussed multi-exponential behavior of the electron transfer using interfacial electron transfer theory in the above section. The classical treatment of the electron-transfer theory within the Marcus framework is used in the following section to give more insight to the electron transfer dynamics.

According to the classical treatment of the electron-transfer theory, the fast component τ =270fs and slow component τ = 6.8ps can be explained using the following equation:

$$\tau^{-1} = \nu_0 \exp[-\beta(d-d_0)]\exp\{-(\Delta G^0+\lambda)^2/(4\lambda kT)\} \qquad (4.1)$$

Here ν_0 is $10^{13.3}$ s^{-1} at room temperature[92]. At very optimal condition $\Delta G^0 = -\lambda$, and $d = d_0$ (adiabatic reaction, the species are in contact). The time constant τ can be as small as $1/10^{13.3}$ s^{-1} = 50.1 fs.

We have not observed such a fast time constant, this could be due to the electron-transfer reaction is not at optimal: either the d not equal to d_0 or the $\Delta G^0 \neq -\lambda$, or both. We are unable to distinguish which case it is from our limited data at present time, however the following analysis helps us to understand the origins of the multiple or two components further.

4.3.12.1 Contribution Of Electron-Transfer Distances – Effect Of Electron Tunneling

Suppose the standard free energy is at optimal where $\Delta G^0 = -\lambda$ but the electron transfer is not in the closest contact, i.e. it is non-adiabatic as most of the interfacial electron-transfer reaction is. The 270fs and the 6.7ps components result from that the electron transfer occurs over different *distances* $d-d_0$ = 1.40 and 4.0 angstroms respectively when $\beta = 1.2$ $Å^{-1}$ (see Ref (1)). Thus the two components mean some electrons on the CdS(s) conduction band will tunnel longer the distances than others to reach the MV^{+2} around the CdS(s) surface. The longer is the distance, the slower the electron-transfer rate constant. The distance distribution of electrons in CdS(s) and MV^{+2} in solution causes multiple component behaviors of the electron-rate constants, though only two components are observed in average. Some cases that could cause the different distances between the electron and MV^{+2} are cited as follows (see Figure 4.12): (a) The electrons may be

distributed either at the surface sites or at interior sites some distance away from the CdS(s) surface. (b) The MV^{+2} ions are distributed at the surface or at some distance away from the surface in the solution.

As shown in Figure 4.12, the upper panel shows the schematic diagram for different tunneling distances of electrons from CdS(s) to the MV^{+2} in solution. The distance distribution of electrons in CdS(s) and MV^{+2} in solution causes multiple components in the electron-transfer rate constants. Here two typical tunneling distances are shown, one corresponds to the fast component, the other corresponds to a lower component. The difference in distances between the fast and slower components is 2.6 angstroms, either because the electron is at the sites inside the CdS(s) or because the MV^{+2} is at the sites inside the solution (or absorbed MV^{+2} with difference layers) around the interface.

The lower panel shows schematic diagram of electron tunneling through the barrier of a different width d_{slow}, or d_{fast}. E denotes the total energy of the electron impinging the barrier from the left such as in CdS(s). V is the potential energy of the top of the barrier. Inside the barrier the electron has negative energy. Gamov [93] derived the expression for the average transition time for the electron with energy E to tunnel across a potential barrier with shape V(x) as

$$\tau^{-1} = V_0 \exp(-\beta d) \qquad (4.2)$$

$$\beta = \frac{(8m_e)^{1/2}}{\hbar} \int_0^d (V(x) - E)^{1/2} dx \qquad (4.3)$$

where V_0 is the frequency factor and d is the barrier width and β is damping factor related to the shape and height of the barrier. This Gamov's equation only strictly applies to isolated particles in free space whose energy level distribution is continuous, but it is very similar to the equation (4.1) for electron transfer as shown above when $\Delta G^0 = -\lambda$. We adopt it here as an over simplified picture to describe the electron transfer. It is used here to qualitatively explain the multiple component of rate constant of electron transfer due to the exponential dependence of the reaction rate on distance between the donor (electron at CdS(s)) and the acceptor (MV^{+2}). It is obvious that different $d = d_{slow}$, or d_{fast} will cause different transition time or time constants for electron transfer.

4.3.12.2 Contribution Of The Electron-Transfer Activation Energy ----Effect Of Trap Depth Distribution

From the above analysis, the fact that electron transfer occurs over different distances is one of the contributions to the multiple component behavior of the electron-transfer dynamics, assuming an optimal standard energy $\Delta G^0 = -\lambda$. On the other hand, the standard free energy may not be at optimal either. The term $\exp\{-(\Delta G^0 + \lambda)^2/(4\lambda kT)\}$ according the Marcus theory may also contribute to the multiple components at given electron transfer distances in $d\text{-}d_0$. This is basically due to electrons in the CdS(s) may be trapped in different trap sites, some trapped at shallow sites with higher energy, and the others trapped at deeper trap sites with lower energy. The standard free energy ΔG^0 for the electron-transfer reactions denoted in the

Figure 4.12 Contribution of Electron-transfer distances. The upper panel shows the schematic diagram for different tunneling distances of electrons from CdS(s) to the MV^{+2} in solution. The lower panel shows schematic diagram of electron tunneling through the barrier of a different width d_{slow}, or d_{fast}.

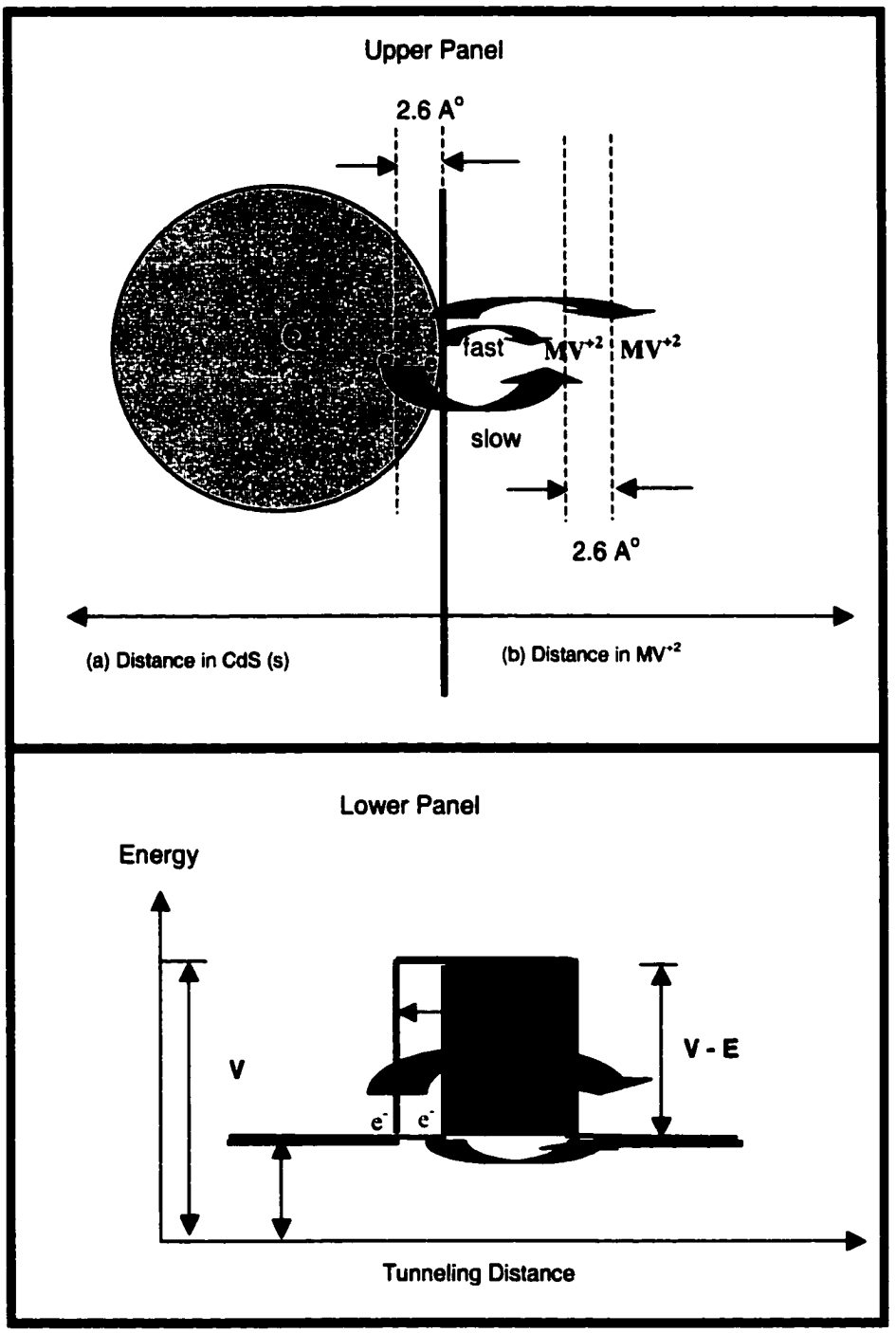

Table 4.2 The notations for standard free energy for the electron-transfer reactions from different traps

Precursor → Successor	Standard free energy (change) ΔG^0
e^- (at shallow trap) + MV^{+2} → $MV^{+\cdot}$	ΔG^0_s
e^- (at deep trap) + MV^{+2} → $MV^{+\cdot}$	ΔG^0_d

Tables 4.2 is different for electrons trapped at different sites. $\Delta G^0 = \Delta G^0_s$ for shallowly trapped electron transfer reaction and $\Delta G^0 = \Delta G^0_d$ for deeply trapped electron transfer reaction. If the entropy of the shallowly trapped electron – MV^{+2} precursor is the same as that of the deeply trapped electron –MV^{+2} precursor, then the difference in ΔG^0 between the deeply trapped electron and shallowly trapped electron transfer reactions, $\Delta G^0_d - \Delta G^0_s$ is the same as the difference in the energy or the trap depth , $D_d - D_s = \Delta D$ as shown in Figure 4.13.

Using this and following some simple algebraic calculation via equation (4.1), the relationship between electron-transfer time constant τ_d of deeply trapped electron and that τ_s of the shallowly trapped electron can be derived .

When the electron transfer occurs at the same distance ($d-d_0$) for all electrons, the expression for relationship of time constants, τ_s and τ_d between shallow and deep electron transfer respectively can be obtained as follows.

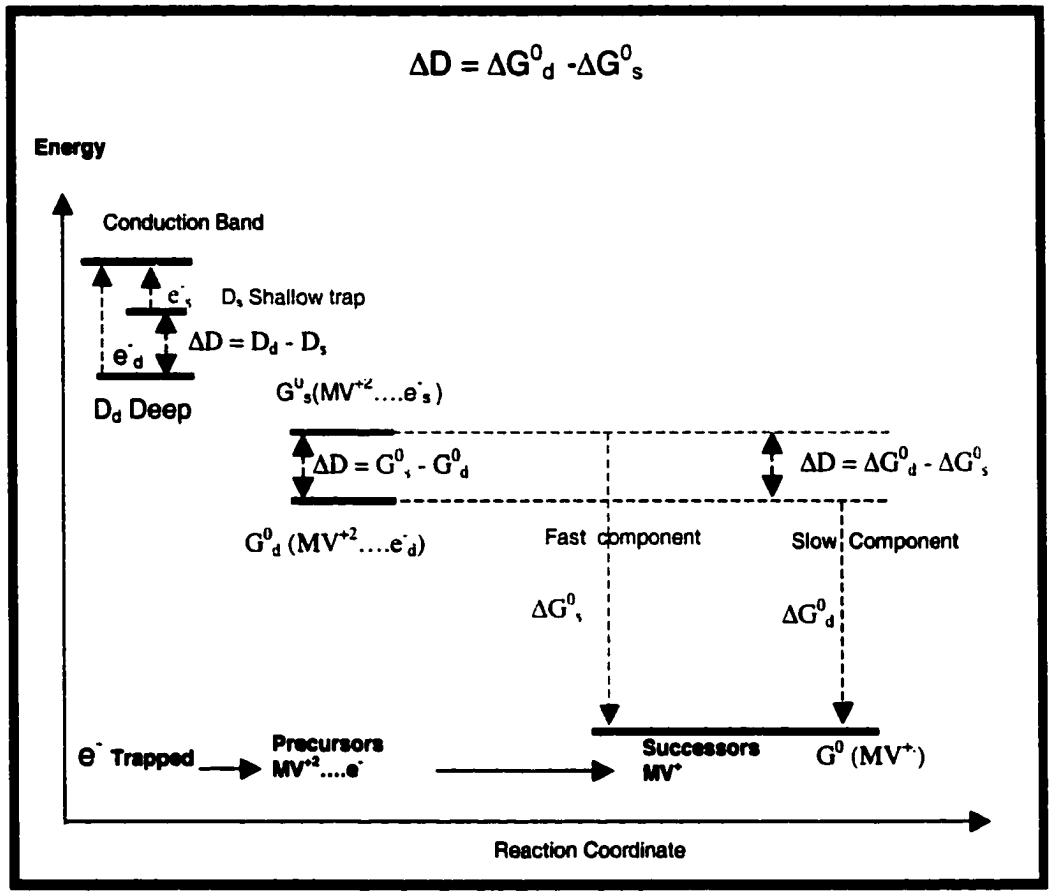

Figure 4.13 Schematic diagram to show that the difference in trap depths between shallow (subscript s) and deep (subscript d) traps $\Delta D = D_d - D_s > 0$ is equal to the difference in standard free energy ($\Delta G^0_d - \Delta G^0_s$). Here the ΔG^0_s is the standard free energy for electron-transfer reaction from the precursor ($MV^{+2}....e^-_s$) to $MV^{+\cdot}$, however the ΔG^0_d is that from the precursor ($MV^{+2}....e^-_d$) to $MV^{+\cdot}$. The e^-_s and e^-_d represents electrons at shallow and deep traps respectively. It is assumed that the energy difference between ($MV^{+2}....e^-_s$) and ($MV^{+2}....e^-_d$) precursors is ΔD. This ΔD becomes the standard free energy difference between the $G^0_s(MV^{+2}....e^-_s)$ and $G^0_d (MV^{+2}....e^-_d)$ at standard temperature T and pressure P, ignoring the volume difference (ΔV) and entropy difference (ΔS) between the two kinds of precursors. This is because $G^0_d(MV^{+2}....e^-_s) - G^0_s (MV^{+2}....e^-_d) = \Delta D + P\Delta V - T\Delta S = \Delta D$ if ΔV and ΔS are zero (see middle of the Figure). The $\Delta D = (\Delta G^0_d - \Delta G^0_s)$ is shown on the right of the Figure.

Assuming the reorganization free energy λ for the electron transfer reaction is the same for all electron-transfers. From the classical electron transfer theory

$$\tau^{-1} = \nu_0 \exp[-\beta(d-d_0)]\exp\{-(\Delta G^0+\lambda)^2/(4\lambda kT)\} \quad (4.4)$$

Apply the above equation for electrons at shallow and deep traps to get τ_d , τ_s respectively and then the ratio can be obtained:

$$\tau_d / \tau_s = \exp\{-[(\Delta G_s^0+\lambda)^2 - (\Delta G_d^0+\lambda)^2]/(4\lambda kT)\}$$

$$= \exp\{-[(\Delta G_s^0-\Delta G_d^0)/kT] [(\Delta G_s^0+ \Delta G_d^0+ 2\lambda)/4\lambda]\} \quad (4.5)$$

Since the electron transfer coefficient

$$\alpha = \frac{1}{2} + \Delta G^0/2\lambda \quad (4.6)$$

by using it, the shallow and deep electron transfer coefficients α_s and α_d are as follows,

$$\alpha_s = \frac{1}{2} + \Delta G_s^0/2\lambda \qquad \alpha_d = \frac{1}{2} + \Delta G_d^0/2\lambda \quad (4.7)$$

Therefore the average electron transfer coefficient α_{avg} is

$$\alpha_{avg} = (\alpha_s + \alpha_d)/2 = (\Delta G_s^0+ \Delta G_d^0+ 2\lambda)/4\lambda \quad (4.8)$$

Substitute the above equation into the equation for τ_d / τ_s, we have

$$\tau_d / \tau_s = \exp\{-[(\Delta G_s^0-\Delta G_d^0)/kT] \alpha_{avg} \}$$

Drop the subscript avg in α_{avg} and use $(\Delta G^0_d - \Delta G^0_s) = \Delta D$ from Figure 4.13, we finally have:

$$\tau_d/\tau_s = \exp[-(\Delta G^0_s - \Delta G^0_d)\alpha/kT] = \exp[-(D_s - D_d)\ \alpha/kT] = \exp[\Delta D\alpha/kT] \quad (4.9)$$

Remember the α in the above equation is the (average) electron transfer coefficient for shallow and deep electron transfers. This equation is very useful in explaining the multiple components of the electron transfer dynamics. Note

ΔD is positive, the larger it is, the deeper the deep traps relative to the shallow trap, the slower the electron transfer from the deep trap. From this equation above, it is obvious that multiple trap depths D will cause multiple trap depth difference ΔD, which in turn causes multiple time constants τ for the electron transfer. The deeper the electron trap depth, the slower (or larger) of the time constant for the electron transfer. To cause the 270fs fast component and 6.7ps slow components we need a difference in the trap depth ΔD as shown in the equation (4.10) and the equation is obtained from a simple thermodynamic and kinetic theory:

$$\Delta D = (kT/\alpha)\ln(\tau_d / \tau_s) = (kT/\alpha)\ln(6.7/ 0.27) = 3.21(kT/\alpha) \qquad (4.10)$$

Assuming the electron transfer coefficient α is 0.5, the ΔD is 6.42kT or 0.154 eV at room temperature. That means to activate the electron in the deep trap to the shallow trap, and thus eliminate the slow component, 6.42 times of the average thermal energy (kT) is required. We have failed to perform an experiment at a temperature of more than six times higher than the standard one, because the colloid CdS(s) will coagulate to form larger particles and settle down into large lump at the bottom of the container.

In deduction of the above equation we have assumed that the reorganization free energy λ of the electron transfer is the same for electrons, regardless of it is deeply trapped or shallowly trapped. This assumption is very reasonable because the reorganization free energy is defined as the free energy that would have been required to change the equilibrium state of the precursor $e^-...MV^{+2}$ to the equilibrium sate of the successor $CdS...MV^{+\cdot}$ if the

electron transfer did not occur. As we know the λ consists of λ_{in} and λ_{out}. The inner reorganization energy part λ_{in} is solely related to the nuclear configuration of methylviogen cations, it is the free energy needed to change from the delocalized aromatic-type structure of MV^{+2} to its corresponding more delocalized quinoid-type structure of $MV^{+\cdot}$. To this point, this part is not related to the trapped electron. The outer sphere reorganization free energy λ_{out} is the free energy needed for the change in the solvent environments around the reaction complexes. It is expected that this part is only slightly depending on the trapped electron.

It should be noted that the electron transfer coefficient appearing in the above equation is actually the *average* electron transfer coefficient of the electrons at different traps. We used $\alpha_{avg} = (\alpha_s + \alpha_d)/2$ to derive the above equation. This is not obvious using the Figure 4.11 from the interfacial electron transfer theory (see 4.3.10 above), but it is apparently required using Marcus theory.

Comparing the explanation using equations from Marcus theory and that using the diagram from interfacial theory (see 4.3.10), though we reach the same conclusion, the graphical of the interfacial theory is much more simpler than the algebraic expression. It is easy to see intuitively from the Figure 4.11 that the activation energy difference $\Delta G^*_d - \Delta G^*_s = \alpha\Delta D = \alpha(\Delta G^0_d - \Delta G^0_s)$, is always nonnegative, and is only a part of the trap depth difference ΔD or standard free energy difference $(\Delta G^0_d - \Delta G^0_s)$ (That is because the value of

the electron transfer coefficient falls between 0 and 1, so only an α proportion of the ΔD or (ΔG^0_d - ΔG^0_s), contributes to the activation energy difference.). The physical meaning underlying this is given in the classical electron transfer theory from Marcus related to the reorganization process of the electron transfer. In the derivation above we have the following equation

$$\alpha = \frac{1}{2} + \Delta G^0/2\lambda = 0.5(1 + \Delta G^0/\lambda) \qquad (4.11)$$

We can see how the reorganization energy adjusts the portion that contributes to the activation energy difference, which in turn will adjust the contributions to the multiple component dynamics by the distribution of trap depths. If the $\Delta G^0 = -\lambda$ at optimal condition, then the electron coefficient α is zero, the trap depth difference plays no part in the multiple components behavior of the electron transfer. If the reorganization energy λ is much larger than that of the standard free energy ΔG^0, then the average electron transfer coefficient is close to 0.5. So only half of the standard free energy or trap depth difference used as the activation energy difference will affect the multiple component dynamics. If the $\Delta G^0 = \lambda$, then the electron transfer coefficient is 1, and all of the trap depth difference is used in the activation energy, and in this last case the trap depth has the largest effect of the multiple component behavior of the electron transfer.

In the above discussions we have isolated two ideal cases to simply the analysis, one case is at optimal standard free energy $\Delta G^0 = -\lambda$, another one is electron-transfer occurring at the same distance $d-d_0$. In either case, the

multiple-component characteristic of electron transfer is qualitatively explained according to both the classical electron transfer theory within Marcus framework and the interfacial electron transfer theory. The actual process for the electron transfer is complicated by the combination the above two cases. For example, the electrons trapped at trap sites with different trap depths and different distances from the CdS surface may be transferred to MV^{+2} at different distances around the interface. We are only able to resolve two main components limited to the accuracy of the experimental data. Our conclusion here is the electron transfer occurs with main components of electron-transfer time constant 270fs and 6.7 ps. They are possibly contributed by the distance distribution of electron in CdS Q-dots and MV^{+2} in solution and trap depth distribution of trapped electrons. We have discussed the behavior of the electron-transfer dynamics contributed by electron tunneling distance distribution and trap depth distribution including the reorganization free energy adjustments. However it is apparent further work is needed to identify which contributes the most.

4.4 Conclusion

(a) The first direct femtosecond measurements of the RRS spectrum of photo-induced MV^{+} and the dynamics of the photo-induced electron transfer from aqueous colloidal CdS to the adsorbed MV^{+2} have been performed.

(b) The CdS colloidal particles are characterized by electronic absorption spectroscopy and Raman phonon bands. The dynamics of CdS phonon relaxation is time resolved to recover within 2 ps.

(c) Different laser wavelengths and optical cell arrangements are used to study the electron transfer dynamics. The experiment shows that it is easier to get more observable photo-induced $MV^{+\cdot}$ signal using 379.6nm than 409.6 nm laser excitation. It is also found that using an optical cell inside which the colloidal sample is recirculating open to air will get rid of the accumulation of photo-induced $MV^{+\cdot}$. However using a sealed spinning cell will cause the $MV^{+\cdot}$ accumulated in the cell, and thus interfere with the measured electron transfer dynamics.

(d) The RRS spectrum reveals that the part of the electron transfer accompanied by the structure change from aromatic MV^{+2} to a quinoid MV^{+} occurs within 350 fs (the pulse width).

(e) Time-resolving the dynamics by monitoring the RRS intensity of MV^{+} as a function of delay time has been carried out. The photo-induced MV^{+} dynamics in the CdS colloid are quite different from that of the chemically prepared MV^{+}, the latter is a single-exponential of time constant 3.1ps, however the former is a double-exponential or two components of time constants 270fs and 6.7ps.

(f) The fast component 270fs accounts for the part of MV^{+} produced within the pulse width by the transfer of very shallowly trapped electrons, and the slow component 6.8ps is assigned as the transfer of relatively deeply

trapped electrons. The slower 6.8ps component does not represent the pure electron transfer rate constant because electron hole pair recombination is known to compete on this time scale.

(g) This double-exponential behavior for the electron transfer is discussed as the contribution mainly from the distributions in electron trap depths following the interfacial electron transfer theory. The calculated relatively deep trap depth 100-300meV is consistent with that given by Weller's group[19,22].

(h) The dynamics is also discussed in terms of the classical treatment of the electron transfer theory within Marcus's framework. The two main components of electron-transfer time constant 270fs and 6.7 ps are possibly contributed by the combination of the distance distribution of electron in CdS Q-dots and MV^{+2} in solution with trap depth distribution of trapped electrons. We have discussed the behavior of the electron-transfer dynamics contributed by electron tunneling distance distribution and trap depth distribution including the reorganization free energy adjustments. However it is apparent further work is needed to identify which contributes the most.

4.5 References

(1) (a) Grätzel, M. Heterogeneous Photochemical Electron transfer; CRC Press, Inc.: Boca Raton, Florida, 1989. (b) Grätzel, M. Acc. Chem. Res. 1981, 14, 376

(2) (a) Kalyanasundaram, K.; Borgarello, E.; Douonghong, D.; Grätzel, M. Angew. Chem. Int. Ed. Engl. 1981, 20, 987. (b) Kalyanasundaram, K.; Grätzel, M.; Pelizzetti, E. Coordination Chem. Rev. 1986, 69, 57

(3) Linsebigler, A. L.; Lu, Guangquan; Yates, Jr., J. T. Chem. Rev. 1995, 95, 735

(4) Fox, M. A.; Dulay, M. T. Chem. Rev. 1993, 93, 341

(5) Halmann, M. In Energy Resources Through Photochemistry and Catalysis; Grätzel, M., Ed.; Academic Press: New York, 1983; 507-534

(6) Matthews, R. W. Pure Appl. Chem. 1992, 64, 1285

(7) Kavarnos, G. J. Fundamentals of Photoinduced Electron Transfer, VCH Pub. Inc: New York; 1993

(8) Kamat, P. V. Chem. Rev. 1993, 93, 267

(9) Mills, A.; Doulas, P.; Green, A.; Williams, G. In Electrochemistry in Colloids and Dispersions; Mackay, R. A., Texter, J. Eds; VCH PUB. Inc.: New York, 1992; 385

(10) Henglein, A. Topics in Current Chem. 1988, 143, 113

(11) (a) Skinner, D. E.; Colombo, D. P.; Cavaleri, J. J.; Bowman, R. M. J. Phys. Chem. 1995, 99, 7853 (b) Klimov, V.; Bolivar, P. H.; Kurz, H. Phys. Rev. B. 1996, 53, 1463

(12) Zhang, J. Z.; O'Neil, R. H.; Roberti, T. W. J. Phys. Chem. 1994, 98, 3859

(13) Zhang, J. Z.; O'Neil, R. H.; Roberti, T. W.; McGowen, J. L.; Evans, J. Ev. Chem. Phys. Lett. 1994, 218, 479

(14) Tian, Y.; Wu, C.; Fendler, J. H. J. Phys. Chem. 1994, 98, 4913

(15) Kamat, P. V.; Wijngaarden, M. de L. van; Hotchandani, S. Israel J. Chem. 1993, 33, 47

(16) Hässelbarth, A.; Eychmüller, A.; Weller, H. Chem. Phys. 1993, 203, 271

(17) Hässelbarth, A.; Eychmüller, A.; Eichberger, R.; Giersig, M.; Mews, A.; Weller, H. J. Phys. Chem. 1993, 97, 5333

(18) Barzykin, A. V.; Fox, M. A. Israel J. Chem. 1993, 33, 21

(19) Weller, H.; Eychmüller, A.; Vogel, R.; Katsikas, L.; Hässelbarth, A.; Giersig, M. Israel J. Chem. 1993, 33, 107

(20) Rajh, T.; Micic, O. I.; Lawless, D.; Serpone, N. J. Phys. Chem. 1992, 96, 4633

(21) Eychmüller, A.; Katsikas, L.; Weller, H. Langmuir, 1990, 6, 1605

(22) (a) Eychmüller, A.; Hässelbarth, A.; Katsikas, L.; Weller, H. J. Luminescence 1991, 48/49, 745. (b) Eychmüller, A.; Hässelbarth, A.; Katsikas, I.; Weller, H. Ber. Bunsenges. Phys. Chem. 1991, 95, 79

(23) Ernsting, N. P.; Kaschke, M.; Weller, H.; Katsikas, L. J. Opt. Soc. Am. B 1990, 7, 1630

(24) Kaschke, M.; Ernsting, N. P.; Muller, U.; Weller, H. Chem. Phys. Lett. 1990, 168, 543

(25) Wang, Y.; Suna, A.; McHugh, J.; Hilinski, E. F.; Lucas, P. A., Johnson, R. D. J. Chem. Phys. 1990, 92, 6927

(26) Bawendi, M. G.; Wilson, W. L.; Rothberg, L.; Carl, P. J.; Jedju, T. M.; Stegerwald, M. L.; Brus, L. E. Phys. Rev. Lett. 1990, 65, 1623

(27) (a) O'neil, M.; Marohn, J.; McLendon, G. Chem. Phys. Lett. 1990, 168, 208 (b) O'neil, M.; Marohn, J.; McLendon, G. J. Phys. Chem. 1990, 94, 4356

(28) Kamat, P., V.; Dimitrijevic, N. M.; Nozik, A. J. J. Phys. Chem. 1989, 93, 2873

(29) Hilinski, E. F.; Lucas, P. A.; Wang, Y. J. Chem. Phys. 1988, 89, 3435

(30) (a) Chestnoy, N.; Harris, T. D.; Hull, R.; Brus, L. E. J. Phys. Chem. 1986, 90, 3393. (b) Alivisatos, A. P.; Harris, A. L.; Levinos. N. J.; Steigerwald, M. L.; Brus, L. E. J. Chem. Phys. 1988, 89, 4001. (c) Rossetti, R.; Ellison, J. L.; Gibson, J. M.; Brus, L. E. J. Chem. Phys. 1984, 80, 4464. (d) Shiang, J. J.; Risbud, S. H.; Alivisatos, A. P. J. Chem. Phys. 1993, 98, 8432

(31) (a) Henglein, A.; Kumar, A.; Janata, E.; Weller, H. Chem. Phys. Lett. 1986, 132, 133. (b) Henglein, A.; Fojtik, A.; Weller, H. Ber. Bunsenges. Physik. Chem. 1987, 91, 441

(32) Weller, H.; Koch, U.; Gutiérrez, M.; Henglein, A. Ber. Bunsenges. Physik. Chem. 1984, 88, 649

(33) Ramsden, J. J.; Grätzel, M. J. Chem. Soc., Faraday Trans. 1, 1984, 80, 919. (b) Ramsden J. J.; Webber, S. E.; Grätzel, M. J. Phys. Chem. 1985, 89, 2740

(34) Lambe, J. J.; Klick, C. C.; Dexter, D. L. Phys. Rev. 1956, 103, 1715.
(35) Weller, H. Adv. Mater. 1993, 5, 88

(36) (a) Weller, H. Angew. Chem. 1993, 105, 43. (b)Weller, H. Angew. Chem., Int. Ed. Engl. 1993, 32, 41

(37) Persans, P. D.; Silvestri, M.; Mei, G.; Lu, E.; Yukselici, H.; Schroeder, J. Brazilian Journal of Physics 1993, 23, 144

(38) Türk, T.; Vogler, A.; Fox, M. A. In Photosensitive Metal-Organic Systems: Mechanistic Principles and Applications (Advances in Chemistry Series 238) Kutal, C.; Serpone, N. Eds; Am. Chem. Soc: Washington, DC, 1993; 233

(39) (a) Wang, Y.; Herron, N. J. Phys. Chem. 1991, 95, 525. (b) Wang, Y.; Herron, N. Phys. Rev. B 1990, 42, 7253. (c) Wang, Y. J. Phys. Chem. 1991, 95, 1119

(40) Wang, Y. Acc. Chem. Res. 1991, 24, 133

(41) Bawendi, M. G.; Steigerwald, M. L.; Brus, L. E. Annu. Rev. Chem. 1990, 41, 477

(42) Henglein, A. Chem. Rev. 1989, 89, 1861

(43) Brus, L. E. J. Phys. Chem. 1986, 86, 2555

(44) Brus, L. E. IEEE J. Quantum Electron. 1986, QE-22, 1909

(45) Henglein, A. Pure Appl. Chem. 1984, 56, 1215

(46) Chandler, R. R.; Coffer, J. L. J. Phys. Chem. 1993, 97, 9767

(47) Pileni, M. P.; Mott, L.; Petit, C. Chem. Mater. 1992, 4, 338

(48) Yuan, Y,; Fendler, J. H.; Cabasso, I. Chem. Mater. 1992, 4, 312

(49) Petit, C.; Pileni, M. P.; J. Phys. Chem. 1988, 92, 2282

(50) Spanhel, L.; Weller, H.; Henglein, A. J. Am. Chem. Soc. 1987, 109, 6632.

(51) Serpone, N.; Sharma, D. K.; Jamieson, M. A.; Grätzel, M.; Ramsden, J. J. Chem. Phys. Lett. 1985,115,473

(52) Kuczynski, J.; Thomas, J. K. J. Phys. Chem. 1983, 87, 5498

(53) Metcalfe, K.; Hester, R. E. J. Chem. Soc., Chem Commun.,1983, 133

(54) Duanghong, D.; Ramsden, J.; Grätzel, M. J. Am. Chem. Soc. 1982, 104, 2977-2985

(55) Nosaka, Y.; Nakaoka, Y. Langmuir, 1995, 11, 1170

(56) Torimoto, T.; Maeda, K.; Maenaka, J.; Yoneyama, H. J. Phys. Chem. 1994, 98, 13658

(57) Peral, J.; Mills, A. J. Photochem. Photobiol. A: Chem., 1993, 73, 47

(58) Nosaka, Y.; Ohta, N.; Fukuyama, T.; Fujii, N. J. Colloid and Interface Science 1993, 155, 23

(59) Green, A.; 9, A. J. Photochem. Phtobiol. A: Chem., 1992,64, 211(58) Nosaka, Y.; Ohta, N.; Fukuyama, T.; Fujii, N. J. Colloid and Interface Science 1993, 155, 23

(60) Nosaka, Y; Ohta, N.; Miyama, H. J. Phys. Chem. 1990, 94, 3752

(61) Mills, A.; Douglas, P.; Williams, G. J. Photochem. Photobiol A: Chem., 1989, 48, 397

(62) Kamat, P. V.; Ebbesen, T. W.; Dimitrijevic, N. M.; Nozik, A. J. Chem. Phys. Lett. 1989, 157, 384

(63) Nosaka, Y.; Fox, M. A.; J. Phys. Chem. 1988, 92, 1893

(64) Nosaka, Y.; Miyama, H.; Terauchi, M.; Kobayashi, T. J. Phys. Chem. 1988, 92, 255

(65) (a) Ramsden, J. J.; Grätzel, M. Chem. Phys. Lett. 1986, 132, 269

(66) Kuczynski, J.; Thomas, J. K. Chem. Phys. Lett. 1982, 88, 445

(67) Rossetti, R; Brus, L. E. J. Phys. Chem. 1986, 90, 558

(68) Rossetti, R.; Beck, S. M.; Brus, L. E. J. Am. Chem. Soc. 1984, 106, 980

(69) Rothenberger, G.; Moser, J.; Grätzel, M.; Serpone, N.; Sharma, D. K. J. Am. Chem. Soc. 1985, 107, 8054

(70) Mills, A.; Douglas, P.; Green, A.; Williams, G. In Electrochemistry in Colloids and Dispersions; Mackay, R. A., Texter, J. Eds.; VCH PUB. Inc.: New York, 1992; 385

(71) Serpone et al. once reported that the rate constant was about 1ns[51] which is significantly slower than that reported by others. However their conclusion was mainly made from the change in the absorbance at 530nm of the dimer of MV^+, therefore it is conceivable that their rate constant reflects primarily the conversion of MV^+ already formed previously by photo-reduced electron transfer to its dimmer.

(72) Chen, J. Ph. D. Dissertation, Louisiana State University, 1994

(73) Lippens, P. E.; Lannoo, M. Phys. Rev. B 1989, 39, 10935

(74) Fischer, C.-H; Henglein, A. J. Phys. Chem. 1989, 93, 5578

(75) (a) Brus, L. E. J. Chem. Phys., 1983, 79, 5566. (b) Brus, L. E. J. Chem. Phys. 1984, 80, 4403

(76) Choi, K. M.; Shea, K. J. J. Phys. Chem. 1994, 98, 3207

(77) Rossetti, R.; Hull, R.; Gibson, J. M.; Brus, L. E. J. Chem. Phys. 1985, 82, 552

(78) Fojtik, A.; Weller, H.; Koch, U.; Henglein, A. Ber. Bunsenges. Physik. Chem. 1984, 88, 969

(79) (a) Henglein, A. Ber. Bunsen-Ges. Phys. Chem. 1982, 86, 301. (b) Gutierrez, M.; Henglein, A. Ber. Bensen-Ges. Phys. Chem. 1983, 87, 474

(80) Nosoka, Y.; Shigeno, H.; Ikeuchi, T. J. Phys. Chem. 1995, 99, 8317

(81) Ogawa, S.; Fan, Fu-Ren F,; Bard, A. J. J. Phys. Chem. 1995, 99, 11182

(82) Nedeljkovic, J. M.; Patel, R. C.; Kaufman, P.; Joyce-Pruden, C.; O'leary, N. J. Chem. Edu. 1993, 70, 342

(83) Ghoshal, S.; Lu, T.; Feng, Q.; Cotton, T. M. Spectrochim. Acta 1988, 44A, 651

(84) Nosaka, Y.; Fox, M. A. Langmuir 1987, 3, 1147-1150

(85) The diffusion distance can be evaluated by $2.0(Dt)^{1/2}$=1.8Å, for MV^{+2} with diffusion coefficient $D=8.9x10^{-10}$ m^2/s[64] and a typical time scale t=10ps. The distance is so small that the MV^{+2} is essentially not mobile.

(86) A significant wavenumber change would have been observed if the structure change occurs slower than the pulse width, supposing the RRS enhancement for the structures intermediate between the aromatic and quinoid are high enough.

(87) (87) (a) Huang, Y.; Hopkins, J. B. J. Phys. Chem. 1996, 100, 9585; Here suppose the aqueous MV^+ has roughly the same relaxation dynamics as MV^+ adsorbed on CdS colloid. (b) Cavanagh, R. R.; King, D. S.; Stephenson, J. C.; Heinz, T. F.. J. Phys. Chem. 1993, 97, 786; Heilweil, E. J.; Casassa, M.P.; Cavanagh, R. R.; Stephenson, J. C. Annu. Rev.Phys. Chem. 1989, 40, 143.(c) Heilweil, E. J.; Stephenson, J. C.; Cavanagh, R. R. J. Phys. Chem. 1988, 92, 6099

(88) In addition to the electron trapping, other possible processes are the detrapping of electrons[22], the MV^+ back-reacting with holes to form MV^{+2}[68], dimerization of MV^+[65], hole scavenging[62,63], and the trapped electron-hole recombination[11(a)-13,23,30(a),69]. However those processes, except electron-hole recombination, are unlikely to contributed to the photoinduced MV^+ dynamics and are therefore neglected because they take place in the order of microseconds to nanosecond.

(89) (a) Wang, Y.; Herron, N. J. Phys. Chem. 1987, 91, 257. (b) Wang, Y.; Herron, N. J. Phys. Chem. 1988, 92, 4988

(90) (a)Barral, S.; Fojtik, A.; Weller, H.; Henglein, A. J. Am. Chem. Soc. 1986, 108, 375; (b) The detailed chemical identities of the distribution in the trap depths have not been identified yet, though crystal defects and ad-atoms at the surface are normally thought to serve as electron traps[1,23,24,30(a),31,32,90(a)]. For example, sulfur vacancies V_s^{+1} and Cd^{+2} ad-atoms or edge atoms can trap electrons in the form of V_s^0 and Cd[30(a)]. Electrons can also be trapped in the form of e- associated with Cd^{+2} [23,24,31(a),90]. Lacking in detailed information about the trap distribution as a function of chemical identities makes it hard to relate the components of rate constants to specific traps at present time.

(91) Combination of the published data about the trapping rate constant k_t (ca. 90-100fs, in ref.11 (a)-13) with the detrapping rate constant k_d (20ns at 270K,ref22) enable us to make an first evaluation of the average trap

free energy ΔG_t thermodynamically. $-\Delta G_t = RT\ln K_{eq}$ $= 12RT = 27kj/mol = 280meV$, where K_{eq}, the trapping equilibrium constant, and it is evaluated by the ratio of k_t= ca $1.x10^{13}s^{-1}$ to $k_d = 5x10^7 s^{-1}$. This ΔG_t is essentially the a typical relative deep trap depth ΔD. Our thermodynamically evaluated ΔD agrees very well with the value ca 300meV evaluated kinetically by Weller et al[19,22].

(92) Miller, J. R., Beitz, J. V., and Huddeston, R. K., J. Am. Chem. Soc., 106, 5057, 1984

(93) Gamov, G. Z., Physik, 51, 205, 1928

CHAPTER 5 MOLECULAR DYNAMICS SIMULATION OF ION SOLVATION IN STOCKMAYER FLUID-SOLID INTERFACE SYSTEM

5.1 Introduction

5.1.1 Previous Research On Solvation

One important issue of great recent interest is the solvation[Note 1] dynamics of a newly created ion in polar solvents. Recent research on solvation dynamics of a newly created ion in polar solvent [1-6] is carried out by the investigation of the system response to a sudden change in the charge distribution of the solute or solute point charge. These studies include theoretical and computer simulation [1, 2] and some experiments [7-9]. However these approaches have only focused on the solute in bulk solvents.

For the mechanism involved in bulk solvents, significant information has been obtained by using theoretical and computer simulation results for pure one-component solvent [1, 3, 10-19] and binary component solvent [2]. It is shown by the investigations in bulk one-component solvent that the solvent relaxation happens in two distinct steps including a fast step, followed by a slower step. This global picture is also observed by the experiments [20, 21] done in the pure one component solvent. For the bulk binary two-component solvent mixture,

---

(Note 1): Here the term "solvation", "solvent relaxation", and "reorganization" will share the same meaning according to different theory. For example, in terms of Marcus electron transfer theory, the solvation of a newly created ion is the ion's out-sphere reorganization process.

some experiments [7-9] as well as theoretical calculations and computational simulations [2, 22] of solvation dynamics in mixtures have also been published.

Of the theoretical research, the Stockmayer Model is commonly used to characterize the bulk fluid particles. This is dated back to 1941 when Stockmayer characterized the polar molecule by a Lennard-Jones particle with an embedded point dipole (Stockmayer model) in 1941[23, 24] to describe the thermodynamic properties of the fluid consisting of the polar molecules. Since then it has been used in many areas, especially in theoretical studies due to the simplicity of this model. We also adopted this model in our computer simulation.

5.1.2 Problems Remaining And Expected Results

In contrast to the effort which bulk solvent systems have received, relatively little attention has been paid to the problem of ion solvation at interfacial system such as at solid and solvent fluid interface. In addition previous research is restricted to a given dipole moment and charge. The effect of charge and dipole moment on the solvation dynamics remains unknown. Certainly there are a lot of questions left with respect to solvation dynamics at interfacial systems and bulk fluids. We are especially interested in the unexplained oscillation behavior in the solvation dynamics between the fast and slower component of S(t) observed both in bulk fluids by the previous researchers and in interfacial systems of our study. Meanwhile we have focused ourselves to the charged solute translational motion and the

redistribution of the solvent shell, with comparison to the results in bulk system obtained in this research and in the previous research by others.

The solvation dynamics at interface upon solute ionization is of interest because of the importance of the interfacial electron transfer and in view of the recent experimental and numerical studies. It is expected that the solvation environment at interface is different from the corresponding process in bulk for the following reasons: (a) At the interface, the solvents and solute can be adsorbed; the adsorption layer may confine the solute and solvents close to surface. (b) The local density of the solvents in the adsorption layer will be higher than that in bulk, and the density will affect the dynamics as shown in the previous study [1]. It is expected that the adsorption layer will also affect the dynamics through density. (c) At the surface, the solvent shell of the adsorbed solute can only be formed in half sphere on the fluid side if the solute is tightly adsorbed to the surface, while the solvent shell of the solute in bulk can be formed in an entire sphere.

In both bulk and surface systems, the effect of a broad range of charges and dipole moments are conducted instead of just using one charge and dipole moment.

The dipole moment effect discovered in this paper is comparable to the effect of composition with weak and strong dipoles in mixed fluids by previous researchers [2]. So our results on dipole moment effect give new explanations to previous results on component effect.

The charge of the solute after ionization is the main factor coupling the solute and its solvent shell. Changing the solute charge will allow us to see the roles played by the solute, the solvent shell, and the solute/solvent shell mixed together.

The solute particle upon ionization will prefer a more polar environment compared to a neutral particle. At equilibrium in solid-fluid interfacial system, it is expected that the ionized solute initially adsorbed on the solid would likely have high number of polar solvents in its vicinity. On the other hand, a neutral solute particle would have less preference over polar solvent particles and but more preference over the solid (a collection of particles arranged in some crystal lattice.). Thus following the ionization, a definite redistribution of the solvent particle relative to the solute particle, i.e. the redistribution of the solvent shell must occur. In addition a translational motion of solute particle relative to the solid must occur by the competition between the solid phase and the solvent fluid phase to attract the solute particle. The rates of these processes might depend on various factors. The most obvious ones will be the charge of the solute, the solid –solute interaction potential parameters and the relative strength of the dipoles.

To our knowledge our study of the ion solvation dynamics at interface by computer simulation is unique as stated above, although there have been some theoretical calculation and computer simulation to study the adsorption [25-31] of solute from fluids to the surface such as graphite.

5.1.3 How To Solve The Problems

5.1.3.1 S(t) and CS(t)

In the solvation dynamics reflected by S(t), the oscillation behavior is commonly observed in the previous studies, but its explanation remains unknown. A new function called complementary solvent response function CS(t), is introduced for this purposes. The S(t) traces the solute-solvent interaction, while CS(t) traces all other interaction except the solute-solvent interaction; therefore they are complementary to each other. By comparing the S(t) and CS(t), a mechanism having two kinds of transient states is newly proposed, which shines lights on the origin of the oscillation behavior.

Suppose the solute is charged at t=0, the progress to equilibrium can be monitored via the solvation response function [2]

$$S(t) = \frac{U_{ss}(t) - U_{ss}(\infty)}{U_{ss}(0) - U_{ss}(\infty)} \qquad (5.1)$$

where $U_{ss}(t)$ is the total solute-solvent (ss) interaction energy at time t, including short-range contribution. In addition, it can also be monitored by the complementary solvation response function CS(t):

$$CS(t) = \frac{U_{other}(t) - U_{other}(0)}{U_{other}(\infty) - U_{other}(0)} \qquad (5.2)$$

where the $U_{other}(t)$ is the average interaction potential of each solvent with other solvents and surface, excluding the solute-solvent interaction: i.e.

$$U_{Other}(t) = \frac{\text{Total potential of all the particles - } U_{ss}(t)}{\text{Number of solvents}} \qquad (5.3)$$

5.1.3.2 r_{sz}(t) and N1Shell(t)

To study how the solute will move by translation, we introduced function r_{sz} that is the distance of solute from the surface in the direction perpendicular to the surface. The

$$r_{sz}(t) = z_s(t) \qquad (5.4)$$

reflects the dynamics of translational motion of solute in z direction, where z is the coordinate of the solute.

The spatial redistribution of the first solvent shell is studied by introducing another new function N1Shell(t) that is the number of solvents within certain distance from the solute in the first shell. The N1Shell(t) reflects the time dependents of the solvent number in different parts of the shell, and therefore the redistribution dynamics of the solvents in the shell.

By comparing the time dependence of r_{sz} and N1Shell to the S(t) and CS(t), the solute translation and the spatial redistribution of the solvents during the solvation are elucidated clearly.

5.1.4 Layout Of The Chapter

In the present chapter, the dynamics of reorganization or solvation of selective ion in modeled solid-fluid interfacial systems is studied. Computer simulation of this process by molecular dynamics (MD) methods is carried out and the mechanism of the solvation is explored and discussed in details. The effect of parameters including dipole moment strength, charge amount, and solid-particle interaction constants are examined. In addition to the usual solvation response functions, S(t), which is very important in bulk solvents [1, 2], the

present chapter also introduces some additional response functions such as CS(t), $r_{sz}(t)$, and N1Shell(t) to demonstrate the solvation dynamics including solute translation and solvent shell redistribution to achieve a new equilibrium. As mentioned before, this study provides more physical insight to the out-sphere reorganization dynamics in an interfacial transfer process (see chapter 1 for reorganization process).

We extend the previous computer-simulation work of the solvation in the bulk Stockmayer fluids to the interfacial solvation between solid surface and Stockmayer fluids. We also extend the solute with no dipole to one with dipole. Our study is also unique in the effects of more extensive charges and dipole moments on the solvation dynamics. The results obtained are significant in understanding the reorganization process for the solute and its surrounding solvation shell after the interfacial electron transfer. Thus the computer-simulation results compliment the experimental results in understanding the ion solvation after the electron transfer. However compared to experiments, the computer simulation offers some advantages in: (a) more flexibility in changing the parameters of the system and (b) smaller time scale that is not possible by current laser pulses in our laser system.

This chapter is organized as follows. After the introduction to the previous study, remaining problems, and proposed solution, the computer simulation procedure by MD is presented. Then the results from the original MD simulation and by fitting the data are presented with discussions, and finally conclusions are made.

5.2 Procedures In MD Simulation

The simple picture of the solvation of a newly created ion is already described in Chapter 1.6. The equations of potentials including LJ, dipole-dipole, charge-dipole, and particle-surface interaction have already been described in Chapter 1.3.2.

5.2.1 Systems Under Study

5.2.1.1 Abstract Surface

A general potential equation for particle-surface interaction [32, 33] is used as

$$U(z) = A\left(\frac{B}{z^{n_B}} - \frac{C}{z^{n_C}}\right) \qquad (5.5)$$

where the A, B, C, and n_B, n_C are nonnegative constants. The n_B is larger than n_C and are integers representing repulsing and attracting effects. The values of these constants are chosen reflecting the real surfaces. We have used n_B=9 and n_C=3, and called abstract surface (AS).

The general equation (5.5) is an extension to the specific particle-graphite basal plane potential [28, 34, 35] as shown in the following equation (5.55) in Table 5.1(d). The advantage to do this is the parameters A, B, C is able to be changed to reflect the various surfaces, while the graphite basal plane has some fixed parameters' values instead.

5.2.1.2 Bulk fluids

A Stockmayer particle[24] is a Lennard-Jones particle with an embedded point dipole. The bulk fluid used here consists of Stockmayer particles. There are 256 particles in our simulation box with no differences between solute and

solvents to start with in the neutral solution. Upon equilibrium at a given temperature, one of the particles adsorbed to/closest to the surface is selected as solute to give charge Q at t=0. The dynamics of solvation (t>0) is studied by monitoring the S(t), CS(t), $r_{sz}(t)$, and N1Shell(t) averaged over 20 to 40 initial equilibrium systems.

5.2.2 Lagrangian Equation For The Fluid-Interface System

5.2.2.1 Lagrangian

The motion of the particles can also be expressed in terms of Lagrangian equations

$$\Lambda_i L = 0 \tag{5.6}$$

$$\Lambda_i = \frac{d}{dt}\frac{\partial}{\partial \dot{q}_i} - \frac{\partial}{\partial q_i} \tag{5.7}$$

where q_i and $\dot{q}_i$ (the corresponding derivative of q_i with respect to time t) are the generalized coordinates. The generalized coordinates for particle i could be Cartesian coordinate vector

$$\mathbf{r}_i = \{x_i, y_i, z_i\} \tag{5.8}$$

and velocity

$$\mathbf{v}_i = \dot{\boldsymbol{r}}_i \tag{5.9}$$

for translation and unit vector

$$e_i = \{e_{x_i}, e_{x_y}, e_{z_i}\} \tag{5.10}$$

and $\dot{e}_i$ for rotation. For particles of mass m and moment of inertia i with dipole moments μ (our model assumes all particles have the same m, I, and μ.), the Lagrangian is

$$L = \sum_i \frac{1}{2} m \mathbf{V}_i^2 + \sum_i \frac{1}{2} I \dot{e}_i^2 - \frac{1}{2} \sum_{i \neq j} \sum_j U_{ij}^{LJ}(r_i, r_j) - \frac{1}{2} \sum_{i \neq j} \sum_j U_{ij}^{DD}(r_i, r_j, e_i, e_j)$$
$$- \sum_{i \neq c} U_{ci}^{CD}(r_c, r_i, e_i) - \sum_i U_i^{SP}(r_i) + \sum_i \lambda_i (e_i^2 - 1) \qquad (5.11)$$

Here the first and second terms are the translational and rotational kinetic energies respectively. The third term is the short-range LJ potential. The forth term is the dipole-dipole (DD) long-range interaction potential. The fifth term (CD) is the potential due to charge on a solute c interacting with the dipoles of the solvent i. The sixth term (SP) is the potential of particles interacting with the surfaces. The last term is the constraint [36] that will keep the magnitude μ of the dipole moment constant or the magnitude of the unit vector being 1, though the vector may rotate by changing its orientation. The λ_i is the Lagrange multiplier. Similar Lagrangian [37] can be found for the MD simulation of bulk Stockmayer fluid.

5.2.2.2 Translational Motion

Applying the equation (5.6), we have

$$\frac{d}{dt} \frac{\partial}{\partial \dot{q}_i} L = \frac{\partial}{\partial q_i} L \qquad (5.12)$$

considering translational coordinates $\mathbf{r}_i = \{x_i, y_i, z_i\}$, and $v_i = \{\dot{x}_i, \dot{y}_i, \dot{z}_i\}$, the above equation becomes

$$m\ddot{r}_i = -\sum_{i\neq j}\left(\frac{\partial U_{ij}^{LJ}}{\partial r_i} + \frac{\partial U_{ij}^{DD}}{\partial r_i}\right) - \frac{\partial \sum_{i\neq c} U_{ci}^{CD}}{\partial r_i} - \frac{\partial U_i^{SP}}{\partial r_i} \quad . \qquad (5.13)$$
$$= -\sum_{i\neq j}[\nabla_{r_i}(U_{ij}^{LJ} + U_{ij}^{DD})] - \nabla_{r_i}\sum_{i\neq c} U_{ci}^{CD} - \nabla_{r_i} U_i^{SP}$$

This equation is similar to the Newton's second law. Thus the translation of the particles is governed by the combination of forces as shown on the right side, due to LJ, dipole-dipole, charge-dipole and surface-particle interactions respectively.

In the above equation, it is necessary to distinguish the solvent and solute for charge-dipole interaction. It is noted that the only one solute c interacts with solvent i, so

$$-\nabla_{r_i}\sum_{i\neq c} U_{ci}^{CD} = -\nabla_{r_i} U_{ci}^{CD} \qquad (5.14)$$

for a solvent particle i≠c; However every solvent i interact with the solute c, so

$$-\nabla_{r_i}\sum_{i\neq c} U_{ci}^{CD} = -\sum_{i\neq c}\nabla_{r_c} U_{ci}^{CD} \qquad (5.15)$$

for a solute i=c. Also notice there is a difference in the expression between the operator $\nabla_{r_i} = \nabla_{r_\kappa}$ and $\nabla_{r_c} = \nabla_{r_{ci}}$ that are useful to save computation time.

5.2.2.3 Rotational Motion

On the other hand, considering rotational coordinates $\mathbf{e}_i = \{e_{xi}, e_{yi}, e_{zi}\}$ and $\dot{e}_i$, the equation (5.12) becomes the following:

$$I\ddot{e}_i = -\sum_{i\neq j}\nabla_{e_i}U_{ij}^{DD} - \nabla_{e_i}\sum_{i\neq c}U_{ci}^{CD} + 2\lambda_i e_i \qquad (5.16)$$

Thus the rotational motion of the particle i involves three terms of the generalized force on the right hand side, corresponding to the dipole-dipole, charge-dipole interaction, and the unit vector constraint. It is to be noted in the above equation the

$$-\nabla_{e_i}\sum_{i\neq c}U_{ci}^{CD} = -\nabla_{e_i}U_{ci}^{CD} \qquad (5.17)$$

for solvent i, however $-\nabla_{e_i}\sum_{i\neq c}U_{ci}^{CD}$ disappears for solute i=c because the term $\sum_{i\neq c}U_{ci}^{CD}$ is independent of $\mathbf{e}_c$. In other words, the orientations of the solvent particles are affected by the creation of the charge on the solute particle. However the orientation of the solute itself is affected by the solvent particle, therefore indirectly affected by the creation of the charge.

5.2.2.4 Differential Equations Used In MD

Our purpose is to solve the differential equations:

$$m\ddot{r}_i = -\sum_{i\neq j}[\nabla_{r_i}(U_{ij}^{LJ} + U_{ij}^{DD})] - \nabla_{r_i}\sum_{i\neq c}U_{ci}^{CD} - \nabla_{r_i}U_i^{SP}$$

$$I\ddot{e}_i = -\sum_{i\neq j}\nabla_{e_i}U_{ij}^{DD} - \nabla_{e_i}\sum_{i\neq c}U_{ci}^{CD} + 2\lambda_i e_i \qquad (5.18)$$

to obtain the configuration $r_i = \{x_i, y_i, z_i\}$, $V_i = \{\dot{x}_i, \dot{y}_i, \dot{z}_i\}$, $e_i = \{e_{x_i}, e_{x_y}, e_{z_i}\}$ and $\dot{e}_i$ at time t using some integration method by plugging in the expressions for the

potentials according different models. The key issues are to obtain the gradients (generalized force) on the right hand side of the above equations under different potential model.

5.2.3 Potential And Gradient Of Potential With Reaction Field

5.2.3.1 Example

In the case of no linearly tapered reaction field (NoRFT) boundary condition [1], the dipole-dipole potential for particle i and j is [33]

$$(U_{ij}^{DD})_{NoRFT} = \frac{\mu^2}{r_{ij}^3}[e_i.e_j - 3\frac{(e_i.r_{ij})(e_j.r_{ij})}{r_{ij}^2}] \tag{5.19}$$

We have the following gradients for the above equations.

For translational motion:

$$-\nabla_{r_i}(U_{ij}^{DD})_{NoRFT} = \frac{3\mu^2}{r_{ij}^5}\{[\mathbf{e}_i.\mathbf{e}_j - 5\frac{(\mathbf{e}_i.\mathbf{r}_{ij})(\mathbf{e}_j.\mathbf{r}_{ij})}{r_{ij}^2}]\mathbf{r}_{ij} + (\mathbf{e}_j.\mathbf{r}_{ij})\mathbf{e}_i + (\mathbf{e}_i.\mathbf{r}_{ij})\mathbf{e}_j\} \tag{5.20}$$

$$-\nabla_{r_j}(U_{ij}^{DD})_{NoRFT} = \nabla_{r_i}(U_{ij}^{DD})_{NoRFT} \tag{5.21}$$

For rotational motion:

$$-\nabla_{e_i}(U_{ij}^{DD})_{NoRFT} = \frac{\mu^2}{r_{ij}^3}[3\frac{r_{ij}(e_j.r_{ij})}{r_{ij}^2} - e_j] \tag{5.22}$$

$$-\nabla_{e_j}(U_{ij}^{DD})_{NoRFT} = \frac{\mu^2}{r_{ij}^3}[3\frac{r_{ij}(e_i.r_{ij})}{r_{ij}^2} - e_i] \tag{5.23}$$

For computation purposes, the equations for i and j are listed together. It is noted that the i and j are not always symmetric for some gradient operations (see Table 5.1).

If the above dipole-dipole potential model were used, all the particle pairs inside the simulation box and the particles in the image boxes would have been required in the computation. This is very expensive in computation time, because significantly much more particles in the simulating image boxes will contribute to the interaction compared to the short-range interaction.

Currently there are several approaches such as Ewald summation [38-44], multi-pole expansion [45-49], and reaction field [1], to the problem in 3-D periodic boundary conditions (PCB). For the 2-D periodic boundary conditions in our interfacial system, the computation is more challenging as by Ewald sum [50-54)].

In this dissertation, the reaction field method [1], has been chosen to tackle the problem of long-range contribution in the 2-D PCB conditions for the sake of reducing the computation time.

The table 5.1 summarizes the expressions of potentials and the corresponding gradients used in this computer simulation. These include LJ potential energy and its gradient, dipole-dipole potential energy and its gradient under reaction field and linear tapering, charge-dipole potential energy and its gradient under reaction field and linear tapering, and particle-surface potential energy and its gradient. The equations for surface include abstract surface and graphite basal plane, though the latter is not used in this research. It is listed here for reference purposes if any researcher is interested in it later.

5.2.3.2 LJ Potential And Gradient

Table 5.1 (a) LJ Potential and Gradient, the sphere cut off with linear taper is used

Potentials and Model	Gradients in Lagrangian Equations
(a) LJ potential for particle i and j (sphere cut off)[1, 33] $U_{ij}^{LJ}(r_{ij}) = 4\varepsilon[(\frac{\sigma}{r_{ij}})^{12} - (\frac{\sigma}{r_{ij}})^{6}]\Theta(R_C - r_{ij})$ (5.24) where R_C is the cut off distance, and $\Theta(x) = 1 \quad x>0$ $= 0 \quad x \le 0$ (5.25)	$-\nabla_{r_{ij}} U_{ij}^{LJ} = \frac{24\varepsilon}{r_{ij}^2}[2(\frac{\sigma}{r_{ij}})^{12} - (\frac{\sigma}{r_{ij}})^{6}\mathbf{r}_{ij}]$ (5.26) $-\nabla_{r_{ji}} U_{ij}^{LJ} = \nabla_{r_{ij}} U_{ij}^{LJ}$ (5.27)
(b) Shifted force-potential [33, p145] $U_{ij}^{SF}(r_{ij}) = U_{ij}^{LJ}(r_{ij}) - U_{ij}^{LJ}(R_C) - (\frac{dU_{ij}^{LJ}(r_{ij})}{dr_{ij}})_{r_{ij}=r_C}(r_{ij} - R_C)$ (5.28)	$-\nabla_{r_{ij}} U_{ij}^{SF} = -\nabla_{r_{ij}} U_{ij}^{LJ} + (\frac{dU_{ij}^{LJ}(r_{ij})}{dr_{ij}})_{r_{ij}=R_C}\frac{r_{ij}}{r_{ij}}$ (5.29) $-\nabla_{r_{ji}} U_{ij}^{SF} = \nabla_{r_{ij}} U_{ij}^{SF}$ (5.30)

5.2.3.3 Dipole-Dipole Potential And Gradients With Reaction Field And Linear Tapering

Table 5.1 (b) Dipole-Dipole Potential and Gradients With Reaction Field and Linear Tapering

Potentials and Model	Gradients in Lagrangian Equations
Dipole-dipole potential for particle i and j with linearly tapered reaction field boundary [1]. Note the subscripts in the equations are defined as follows: NoRFT =no tapered reaction field RFNoT =With reaction field, but without tapering Otherwise = $r_{ij} > R_c$ or $r_{ij} < R_s$ $U_{ij}^{DD}(\mathbf{r}_{ij},\mathbf{e}_i,\mathbf{e}_j) = \mu^2[(\frac{1}{r_{ij}^3} - \frac{2(\varepsilon - 1)}{(2\varepsilon + 1)R_{rf}^3})(\mathbf{e}_i.\mathbf{e}_j - 3\frac{(\mathbf{r}_{ij}.\mathbf{e}_i)(\mathbf{r}_{ij}.\mathbf{e}_j)}{r_{ij}^5})]\chi(r_{ij}) = (U_{ij}^{DD})_{RFNoT}\chi(r_{ij})$ (5.31)	If $R_s <= r_{ij} <= R_c$: $(-\nabla_{\mathbf{r}_i} U_{ij}^{DD})_{R_s \le r_{ij} \le R_c} =$ $\frac{R_C - r_{ij}}{R_C - R_s}[-\nabla_{\mathbf{r}_i}(U_{ij}^{DD})_{NoRFT}] + \frac{(U_{ij}^{DD})_{RFNoT}}{R_C - R_s}\frac{\mathbf{r}_{ij}}{r_{ij}}$ (5.35) Otherwise: $(-\nabla_{\mathbf{r}_i} U_{ij}^{DD})_{otherwise} = (-\nabla_{\mathbf{r}_i} U_{ij}^{DD})_{NoRFT}$ (5.36) $-\nabla_{\mathbf{r}_j} U_{ij}^{DD} = \nabla_{\mathbf{r}_i} U_{ij}^{DD}$ (5.37) Where $-\nabla_{\mathbf{r}_i}(U_{ij}^{DD})_{NoRFT} = \frac{3\mu^2}{r_{ij}^5}\{[\mathbf{e}_i.\mathbf{e}_j - 5\frac{(\mathbf{e}_i.\mathbf{r}_{ij})(\mathbf{e}_j.\mathbf{r}_{ij})}{r_{ij}^2}]\mathbf{r}_{ij} + (\mathbf{e}_j.\mathbf{r}_{ij})\mathbf{e}_i + (\mathbf{e}_i.\mathbf{r}_{ij})\mathbf{e}_j\}$ (5.38)

Table 5.1(b) continued

Where

$$U_{ij}^{DD}(\mathbf{r}_{ij},\mathbf{e}_i,\mathbf{e}_j)_{RFNoT} = \mu^2[(\frac{1}{r_{ij}^3}-\frac{2(\varepsilon'-1)}{(2\varepsilon'+1)R_{eff}^3})(\mathbf{e}_i.\mathbf{e}_j) - 3\frac{(\mathbf{r}_{ij}.\mathbf{e}_i)(\mathbf{r}_{ij}.\mathbf{e}_j)}{r_{ij}^5}] = (U_{ij}^{DD})_{NoRFT} + RFMag\ (\mathbf{e}_i.\mathbf{e}_j)$$

(5.32)

$$RFMag=-\frac{2(\varepsilon'-1)}{(2\varepsilon'+1)R_{eff}^3}\mu^2$$

(5.33)

And the tapering function is

t(r) = 1, $r \le R_s$
=1-(r-R_s)/(R_c-R_s), $R_s<r<R_c$
=0. $R_c \le r$,

(5.34)

If $R_s <= r_{ij} <= R_c$:

$$-\nabla_{e_i}U_{ij}^{DD}=\frac{R_C-r_{ij}}{R_C-R_s}[-\nabla_{e_i}(U_{ij}^{DD})_{NoRFT} - RFMag\mathbf{e}_j]$$

(5.39)

$$-\nabla_{e_j}U_{ij}^{DD}=\frac{R_C-r_{ij}}{R_C-R_s}[-\nabla_{e_j}(U_{ij}^{DD})_{NoRFT} - RFMag\mathbf{e}_i]$$

(5.40)

Otherwise

$$-\nabla_{e_i}U_{ij}^{DD}=[-\nabla_{e_i}(U_{ij}^{DD})_{NoRFT} - RFMag\mathbf{e}_j]$$

(5.41)

$$-\nabla_{e_j}U_{ij}^{DD}=[-\nabla_{e_j}(U_{ij}^{DD})_{NoRFT} - RFMag\mathbf{e}_i]$$

(5.42)

Where

$$-\nabla_{e_i}(U_{ij}^{DD})_{NoRFT}=\frac{\mu^2}{r_{ij}^3}[3\frac{\mathbf{r}_{ij}(\mathbf{e}_j.\mathbf{r}_{ij})}{r_{ij}^2}-\mathbf{e}_j]$$

(5.43)

$$-\nabla_{e_j}(U_{ij}^{DD})_{NoRFT}=\frac{\mu^2}{r_{ij}^3}[3\frac{\mathbf{r}_{ij}(\mathbf{e}_i.\mathbf{r}_{ij})}{r_{ij}^2}-\mathbf{e}_i]$$

(5.44)

5.2.3.4 Charge-Dipole Potential And Gradients

Table 5.1 (c) Charge-Dipole Potential and Gradients

Potentials and Model	Gradients in Lagrangian Equations
Charge-dipole potential for particle i[1]	$-\nabla_{r_{ci}} U_{ci}^{CD} = q\mu\{[\frac{3(r_{ci}.e_i)r_{ci}}{r_{ci}^5} - RFA.e_i]t(r_{ci}) + \frac{RFA.(r_{ci}.e_i)}{R_C - R_S}\frac{r_{ci}}{r_{ci}}\Theta(r_{ci} - R_S)\Theta(R_C - r_{ci})\}$ (5.48)
$U_n^{CD}(r_n, e_i) = q(\frac{1}{r_n^3} - \frac{2(\varepsilon' - 1)}{(2\varepsilon' + 1)R_{eff}^3})(r_n.\mu_i)t(r_n)$ (5.45)	$-\nabla_{r_{ic}} U_{ci}^{CD} = \nabla_{r_{ci}} U_{ci}^{CD}$ (5.49)
$U_{ci}^{CD}(\mathbf{r}_{ci}.\mathbf{e}_i) = q\mu RFA(\mathbf{r}_{ci}.\mathbf{e}_i)t(r_{ci})$ (5.46)	$-\nabla_{e_i} U_{ci}^{CD} = -q\mu RFA r_{ci} t(r_{ci})$ (5.50)
Where $RFA = \frac{1}{r_{ci}^3} - \frac{2(\varepsilon' - 1)}{(2\varepsilon' + 1)R_{eff}^3}$ (5.47)	$-\nabla_{e_c} U_{ci}^{CD} = 0$ (5.51)

5.2.3.5 Particle-Surface Potential And Gradients

Table 5.1 (d) Particle-Surface Potential and Gradients. The Abstract Surfaces are used; the Graphite Surface is prepared as a comparison

Potentials and Model	Gradients in Lagrangian Equations
(a) Abstract Surface $U_i^{SP}(z_i) = A(\frac{B}{z_i^{n_B}} - \frac{C}{z_i^{n_C}})$ (5.52) Potential due to the left and right surfaces separated by L in z direction: $U_i^{SP}(z_i) = A\{B(\frac{1}{z_i^{n_B}} + \frac{1}{(L-z_i)^{n_B}}) - C(\frac{1}{z_i^{n_C}} + \frac{1}{(L-z_i)^{n_C}})\}$ (5.53)	For left and right surfaces: $-\nabla_{r_i} U_i^{SP} = A\{Bn_B[\frac{1}{z_i^{n_B+1}} - \frac{1}{(L-z_i)^{n_B+1}}] - Cn_C[\frac{1}{z_i^{n_C+1}} - \frac{1}{(L-z_i)^{n_C+1}}]\}\hat{k}$ (5.54) where $\hat{k}$ is the unit vector in z direction.

Table 5.1 (d) continued

(b) Surface-particle potential for particle i for graphite basal plane [28]

$$\frac{U_i^{SP}(z_i^*)}{\varepsilon_{fs}} = \frac{4\pi A^6}{a^*_s}\left(\frac{2A^6}{5z_i^{*10}} - \frac{1}{z_i^{*4}} + \frac{A^6}{12.42(z_i^*+0.994)^9} - \frac{2z_i^{*2}+9.66z_i^*+1.33}{8.28(z_i^*+1.38)^5}\right) \quad (5.55)$$

where $A = \frac{\sigma_{fs}}{a}$; $z_i^* = \frac{z_i}{a}$; and $a_s^* = \frac{\sqrt{3}}{2}$.

Potential for the left and right surfaces separated by L in z direction:

$$\frac{U_i^{SP}(z_i^*)}{\varepsilon_{fs}} = \frac{4\pi A^6}{a^*_s}\{0.4[\frac{A^6}{z_i^{*10}} + \frac{A^6}{z_{iR}^{*10}}] - [\frac{1}{z_i^{*4}} + \frac{1}{z_{iR}^{*4}}] + [\frac{A^6}{12.42(z_i^*+0.994)^9} + \frac{A^6}{12.42(z_{iR}^*+0.994)^9}] - [\frac{2z_i^{*2}+9.66z_i^*+1.33}{8.28(z_i^*+1.38)^5} + \frac{2z_{iR}^{*2}+9.66z_{iR}^*+1.33}{8.28(z_{iR}^*+1.38)^5}]\} \quad (5.56)$$

where $z^*_{iR} = \frac{L - z_i}{a}$ (5.57)

For the left and right surfaces:

$$-\nabla_{r_i} U_i^{SP} = \frac{\varepsilon_{fs}}{a}\frac{4\pi A^6}{a_s^*}\{4A^6[\frac{1}{z_i^{*11}} - \frac{1}{z_{iR}^{*11}}] - 4[\frac{1}{z_i^{*5}} - \frac{1}{z_{iR}^{*5}}] + 0.7246376A^6[\frac{1}{(z_i^*+0.994)^{10}} - \frac{1}{(z_{iR}^*+0.994)^{10}}] + [\frac{4z_i^*+9.66}{8.28(z_i^*+1.38)^5} - \frac{4z_{iR}^*+9.66}{8.28(z_{iR}^*+1.38)^5}] - 0.6038647[\frac{2z_i^{*2}+9.66z_i^*+13.33}{(z_i^*+1.38)^6} - \frac{2z_{iR}^{*2}+9.66z_{iR}^*+13.33}{(z_{iR}^*+1.38)^6}]\}\hat{k} \quad (5.58)$$

where $\hat{k}$ is the unit vector in z direction

5.2.4 Simulation Details

In the simulation, the reduced unit system is used to save redundant computations for essentially duplicate systems and the time for some computation. The reduced unit is based on mass m of the particles, LJ energy ε and length σ parameters for particle-particle interaction including solvent-solvent as well as solvent-solute interactions. In our model it is assumed that the solvent and solute particles all have the same m, and ε, σ. The following table 5.2 summarizes the reduced unit system applied to our simulation. It is noted that the charge q is in the unit of $mN^{1/2}$ instead of Coulomb C, because the charge in C is divided by factor $(4\pi\varepsilon_0)^{1/2}$, and this gives the charge the unit of $mN^{1/2}$.

5.2.5 Simulation Procedures

The Lagrangian equations of motion for the Stockmayer solvent and solute are used so the rotational motion is represented using unit vector of the dipole. The rotational coordinator enters the equation the same as translational motion coordinators without special treatment like quaternion.

In our simulation, all the systems are investigated at ρ^*=0.8, T^*=1.35. The moment of inertia for solvents and solutes are fixed at I^* =0.025. The charge q^* (around 6 to 81) and dipole moment μ^* (0.25 to 1.75) of the solvents and solutes are varied to study the charge and dipole moment effect. The typical values of the parameters are shown in Table 5.3.

Table 5.2 Reduced unit systems in MD simulation. The reduced unit is based on mass m, LJ energy ε and length σ parameters for particle-particle interaction including solvent-solvent as well as solvent-solute interactions. The parameters with the superscript * is the one in reduced unit. So $m^* = 1$, $\varepsilon^* = 1$, and $\sigma^* = 1$ for interaction among solvents and solutes.

Physical Quantities	Relationships between the quantities in reduced and non-reduced units	
Density	$\rho^* = \rho\sigma^3$	(5.59)
Temperature	$T^* = k_b T/\varepsilon^3$	(5.60)
Energy	$E^* = E/\varepsilon^3$	(5.61)
Time	$t^* = (\varepsilon/m\sigma^2)^{1/2} t^3$	(5.62)
Force	$f^* = f\sigma/\varepsilon^3$	(5.63)
Charge	$q^* = q/(\sigma\varepsilon)^{1/2}$	(5.64)
Dipole	$\mu^* = \mu/(\sigma^3\varepsilon)^{1/2}$	(5.65)
Moment of inertia	$I^* = I/(m\sigma^2)$	(5.66)

The system can be characterized by parameters μ and Q for bulk fluids (solute and solvents); and A, B, and C for abstract surface. The systems with the following variations of the parameters are studied to see the dipole, charge and surface effects: Fluids (μ =0.25, 0.5, 1.0, 1.4, 1.75; Q=6, 12, 20, 36, 81) and surface (A=11.53, 36; B=0.01, 0.03, 0.06, 0.133, 0.5; C=1, 2, 4, 6).

The time integration are carried out via Verlet algorithm using a reduced unit of time step of $\Delta t^* = 0.0025$ (This is 5.4 fs for Argon, and 6.5 fs for CHF_3, usually it is in the order of femtoseconds depending on the m, ε and σ of the particles studied since $t^* = (\varepsilon/m\sigma^2)^{1/2}t$. see below[(Note 2)].

The rotational motion is accomplished by introducing the unit vector representing the orientation of the dipole moment in Lagrangian equations (see section 5.2.2.3), which avoids the complication of introducing torques and the related quaternion.

The system are initially equilibrated at a constant temperature for more than 150000 time steps, with averages accumulated for a further 50000 time steps. For the uncharged solute, a total of 20 to 40 configurations are isolated from the equilibrium trajectory generated. These configurations are afterward used as initial configurations for the non-equilibrium simulations.

(Note 2): (1) For argon (ε=119.8K and σ =0.341nm), the time step is 5.4 fs. That is to say each time step $t^*=(\varepsilon/m\sigma 2)t=0.0025$ that is 5.4 fs. Or the unit of time is 5.4fs/0.0025=2.16 ps. (2) For CHF_3 tri-fluoromethane, ε =199.6 K, σ = 4.007 Å, M =70.01 a.m.u.; then each time step is 6.5 fs and the unit of Time ($m\sigma^2/\varepsilon$) is 2.6 ps. (3) In the following, all the values of quantities are in reduced units except explicitly denoted in fs for time constants. For example, t=1 means t=2.16 ps if the particle is Ar, or t=2.6 ps if the particle is CHF_3.

All the MD computations upon the ionization at t=0 are carried out at constant energy. The data for dynamics of S(t), CS(t), $r_{sz}(t)$, and N1Shell(r,t) are averaged dynamics from the different initial 20 to 40 configurations.

Table 5.3 Potential parameters and their values. The values in reduced units are used in the actual simulation. But the ones in the example are just used for reference.

Parameters	Values in Non-Reduced Unit	Values in Reduced Unit
LJ particle-particle potential		
ε: energy σ: distance R_C: cutoff distance Others: ρ: fluid density	For example: ε/k_b =120K (Ar) σ = 0.34nm (Ar) R_c=2.5σ	ε^*=1 σ^*=1 R_c^*=2.5 ρ^*=0.8
Dipole-dipole potential		
μ: dipole moment ε' : reaction field dielectric constant f: tapering factor =0.95 Others: I: moment of inertia Deduced parameters: Switching Radius $R_S = f R_C$ (5.67) $R_{eff}^3 = \frac{(1+f+f^2+f^3)}{4} R_C^4$ (5.68)	$\varepsilon'(y) = 1 + 2.932\, y + 4.210\, y^2 - 1.323\, y^3 + 0.6115\, y^4$ $For\ 0 \le y \le 3.31$ $y = \frac{4\pi\rho\mu^2}{9k_BT}$ (5.69) f: tapering factor =0.95	μ^* =0.25 to 1.75 ε'^*=82.23 using $y = \frac{4\pi\rho^*\mu^{*2}}{9T^*}$ =3.309661396 (when μ^*=2, T^*=1.35, and ρ^*=0.8) f=0.95 I^*=0.025 R_s^*=2.375 R_{eff}^*=2.438034071
Charge-dipole potential		
q: charge		q^*=2 to 81
Surface-particle potential		
Abstract: A B C n_B n_C		A=11.53 to 36 B=0.01, 0.133 to 0.5 C=1.0 to 6 n_B=9 n_C=3
Graphite: σ_{fs}: LJ length ε_{fs}/k : LJ energy parameters a : lattice vector a_S^* : constant for certain plane	Graphite: $\sigma_{fs} = 3.36\,\text{Å}$ $\varepsilon_{fs}/k = 31.9K$ $a = 2.46\,\text{Å}$ $a_S^* = \frac{\sqrt{3}}{2}$	$\sigma^*_{fs} = 0.988$ $\varepsilon^*_{fs} = .2658$ $a^* = 0.723$ $a_S^* = 0.866025403$

5.2.6 Fitting Data

The data obtained from computer simulation are fitted to the seven models in Table 5.4 to get the time constants and amplitudes.

The first equation $Y_2(t)$ is used to fit N1Shell(outer)=N1Shell(r/σ<=1.3)-N1Shell(r/σ<=1.0)}, N1Shell(outer)/N1Shell(inner)={N1Shell(r/σ<=1.3)-N1Shell(r/σ<=1.0)}/N1Shell(r/σ<=1.0), the second equation $Y_1(t)$ is used to fit the N1Shell(inner)=N1Shell(r/σ<=1.0), and N1Shell(inner+outer)= N1Shell(r/σ<=1.3). The third $Y_3(t)$ and fourth $Y_4(t)$ equations are used to fit the S(t) and CS(t) respectively. The fifth $Y_5(t)$ equation is used to fit the $r_{sz}(t)$ at large Q and N1Shell(r/σ<=1.3), while the sixth equation $Y_6(t)$ is used to fit $r_{sz}(t)$ when Q is small. The seventh equation $Y_7(t)$ is used to fit N1Shell(outer) when Q small.

In these equations, $Y_1(t)$ models the increase with time, while $Y_2(t)$ models the decrease with time with two components. The parameter a is the amplitude of the Gaussian component with time constant τ_G, and parameter b is the amplitude of the exponential component with time constant τ_E. The parameter c is equilibrium value at large t.

The other equations ($Y_3(t)$ to $Y_7(t)$) are derived from the first two equations by noticing the relationships among the equations. If a+b=1 (normalized data) in the first equation $Y_1(t)$, it reduces to the third one $Y_3(t)$. If c=a+b=1, the $Y_2(t)$ equation reduces to the fourth one $Y_4(t)$. If the data in dynamics have been normalized to 1 like S(t), CS(t), then $Y_3(t)$, or $Y_4(t)$ is used, otherwise $Y_1(t)$, or $Y_2(t)$ is used. The $Y_1(t)$ and $Y_2(t)$ are complementary

to each other as $Y_3(t)$ and $Y_4(t)$ do in their time dependency opposite to each other. The $Y_2(t)$ reduces to $Y_5(t)$ if a=0, which means there is no Gaussian component. The $Y_2(t)$ reduces to $Y_6(t)$ if b=0, which means there is no exponential component. The $Y_1(t)$ reduces to $Y_7(t)$ if b=0, which means there is no exponential component.

Table 5.4 The models used to fit the data.

Model	Data
$Y_1(t) = a\exp(-\frac{1}{2}(\frac{t}{\tau_G})^2) + b\exp(-\frac{t}{\tau_e})$ (5.70)	N1Shell(r/σ<=1.3)-N1Shell(r/σ<=1.0)}, $\frac{\{\text{N1Shell}(r/\sigma <= 1.3) - \text{N1Shell}(r/\sigma <= 1}{\text{N1Shell}(r/\sigma <= 1.0)}$
$Y_2(t) = c - a\exp(-\frac{1}{2}(\frac{t}{\tau_G})^2) - b\exp(-\frac{t}{\tau_e})$ (5.71)	N1Shell(r/σ<=1.0), N1Shell(r/σ<=1.3), $r_{sz}(t)$
$Y_3(t) = a\exp(-\frac{1}{2}(\frac{t}{\tau_G})^2) + (1-a)\exp(-\frac{t}{\tau_e})$ (5.72)	S(t)
$Y_4(t) = 1 - a\exp(-\frac{1}{2}(\frac{t}{\tau_G})^2) - (1-a)\exp(-\frac{t}{\tau_e})$ (5.73)	CS(t)
$Y_5(t) = c - b\exp(-\frac{t}{\tau_e})$ (5.74)	$r_{sz}(t)$ when Q is large N1Shell(r/σ<=1.3)
$Y_6(t) = c - a\exp(-\frac{1}{2}(\frac{t}{\tau_G})^2)$ (5.75)	$r_{sz}(t)$ when Q is small
$Y_7(t) = a\exp(-\frac{1}{2}(\frac{t}{\tau_G})^2)$ (5.76)	N1Shell(outer) when Q small

It is also noted that the models may not reflect all the features represented by the data obtained from computer simulation. For example, the second oscillation mode (see in later sections) in the S(t) and CS(t) will not be reflected in the $Y_3(t)$. In some system, the dynamics is biased from the Gaussian and exponential components, which also makes the data-fitting not appropriate. But in general the Gaussian component and the exponential component in the models should approximate data very well. Anyway the parameters obtained here make it easy to observe the trend of the dynamics and to compare the effect of charge, dipole moment, and surface parameters.

The data fit is completed by the evaluation copy of fully featured software called DataFit from Oakdale Engineering [55]. The nonlinear regression (see help file in above software, and chapter 15 of reference [56]) is used to determine the best-fit parameters for a model by minimizing a chosen merit function from Table 5.4. The models in the above table are chosen according to the physical meaning of the dynamics and also from more than 30 candidate models in the DataFit software to allow the best fit. We directly used the data in reduced unit to fit the data and obtain the parameters of the models.

However, the time constants listed in the below tables are not in reduced unit, but in fs to remind the readers about the time range of the dynamics. We have specially converted the time in reduced unit time to time in fs by multiplying 2600, since 1 reduced unit is 2600fs using CHF_3 particles as an example.

5.3 Results And Discussion

5.3.1 Equilibrium Particle Distribution ZD(Z) — Formation Of Adsorption Layers

The equilibrium particle distribution along the direction z perpendicular to the surface, ZD(z) is obtained[(Note 3)] by

$$ZD(z) = \{N(z+dz)-N(z)\}/\rho A dz \qquad (5.77)$$

where N(z) the number of particles in the simulation box from coordinate z=0 to z . The ρA is the density times surface Area, and is used to normalized ZD(z) so that for homogeneous fluids, ZD(z) is 1. If the particles are homogeneously

Table 5.5 The first two of peaks and valleys in ZD for different surface parameters A, B, and C in fluids of dipole moment μ =1.75. P_i=peak position z, pv_i=peak value of ZD; v_i=Valley center position z , and vv_i=Valley value of ZD for i=1, 2 corresponding to the first and second peak (or valley) respectively. Note that the two surfaces are at z=0 and z=6.8σ.

A	B	C	p_1	pv_1	v_1	vv_1	p_2	pv_2	v_2	vv_2
11.5	0.133	1	0.829	7.31	1.33	0.125	1.82	2.63	2.20	0.5
11.5	0.133	2	0.761	17.7	1.26	0	1.72	3.88	2.18	0.125
36	0.01	1	0.556	48.4	0.983	0	1.44	5.59	2.01	0.25
36	0.03	1	0.658	28.9	1.12	0	1.55	5.38	2.02	0.125
36	0.06	1	0.744	21.6	1.24	0	1.63	5	2.16	0.18
36	0.133	1	0.846	16.3	1.34	0	1.77	5	2.23	0.06
36	0.5	1	1.05	9.63	1.55	0	1.96	4	2.47	0.188
11.5	0.133	1	0.829	7.31	1.33	0.125	1.82	2.63	2.20	0.5
36	0.133	1	0.846	16.3	1.34	0	1.77	5	2.23	0.06
36	0.133	4	0.675	61	1.13	0	1.51	12.8	2	0
36	0.133	6	0.648	67.8	1.07	0	1.43	20.8	1.86	0

(Note 3) The adsorption layer of the solvents before the solute is ionized is studied, it is expected the results will apply to the case after the solute ionization since only one solute is ionized.

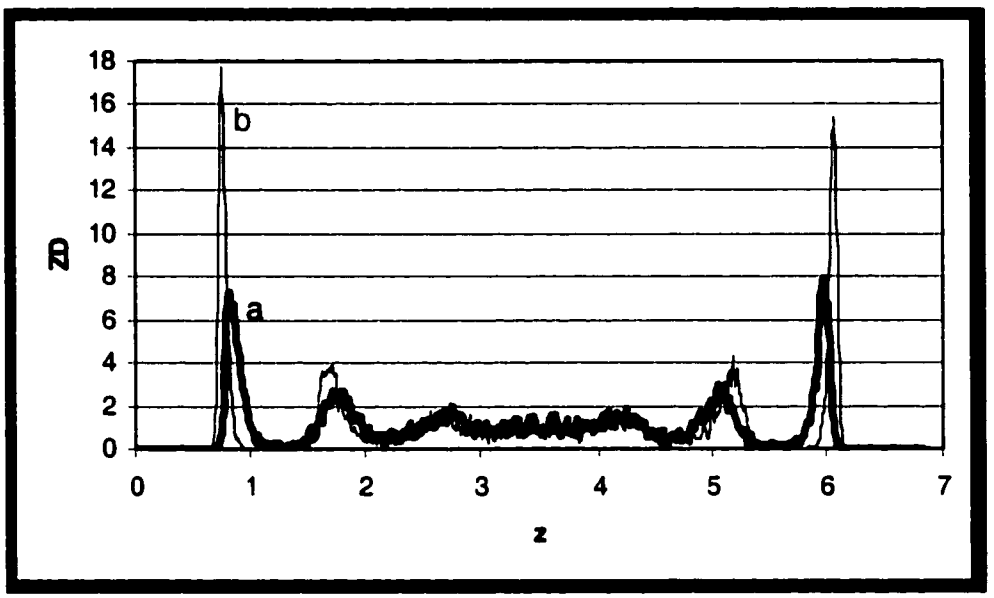

Figure 5.1 Formation of adsorption layers around surfaces with C=1 (thick curve, a) and C=2 (thin curve, b) respectively, A=11.5, and B=0.133 in fluids with dipole moment μ =1.75

distributed, ZD(z) is a constant for all z. However it is shown there are adsorption layers formed close to the surface in addition to fluid bulk region for system with the presence of Stockmayer fluids in between the 2 abstract surfaces from the ZD vs. z diagram. In the Figure 5.1, the peaks are the centers of the adsorption layer with higher solvent density (ZD>1), the valleys are separators of the layers with lower solvent density (ZD<1), compared to the bulk (ZD=1). The peaks and valleys in ZD (z) are affected by the surface parameters A, B, and C as shown in table 5.5.

From the table 5.5, we can see how the adsorption layers are affected by the surface parameters.

As C increases, the first 2 peaks move close to surface, the peak values increase, and the peaks become narrower and the valleys become wider accordingly (Figure 5.1). More solvents are located around the layer center instead of the separation region between adjacent layers. That is to say that the adsorption layers are closer to the surface, and the layer are narrower as the attractive force (or C) increases.

As B increases, the peaks appear at a z value far away from the surface. The first 2 peak's values become smaller, and the peaks become wider. This is because B represents repulsive force; the adsorption layers are formed further away from surface, toward to bulk. Accordingly the adsorption layers are wider due to less attractive force.

Considering B being the counterpart of C, it is understandable that the effects of C are the opposite of B. But the two effects will not counteract each

other completely in quantity. In fact the effect of C is more dominating in all our parameters range. Adjusting parameter A will demonstrate this.

As A changes from 11.5 to 36; the first 2 peaks become narrower and the peak values higher. The parameter A contributes to both repulsive (B) and attractive (C) force. In our study, C effect is larger than B, so increasing A will make the system behave more like increasing C.

In summary, the adsorption layer is narrower in width, closer to the surface, and denser as C increases or B decreases. The A effect is a combination of B and C, which will be similar to C effect due to C dominating B. It is important to note that at certain values of B and C, there are no solvents in the first valley (i.e. vv_1=0 in above Table for C>=2 or A=36.), which separates the first two adsorption layers. That means once the solute goes in the first layer, it may not move to the second layer due to the surface effect upon ionization. This confinement to the translational movement range of the solute plays an important role in the dynamics of the solute-solvents relaxation in the first layer as shown below.

5.3.2 Equilibrium Pair Distribution Function

The pair distribution functions g(r) in surface system before and after solute ionization are shown in Figure 5.2.

After ionization, the first peak of g(r) becomes higher and sharper. This demonstrates a solvent redistribution occurs upon the ionization of the solute.

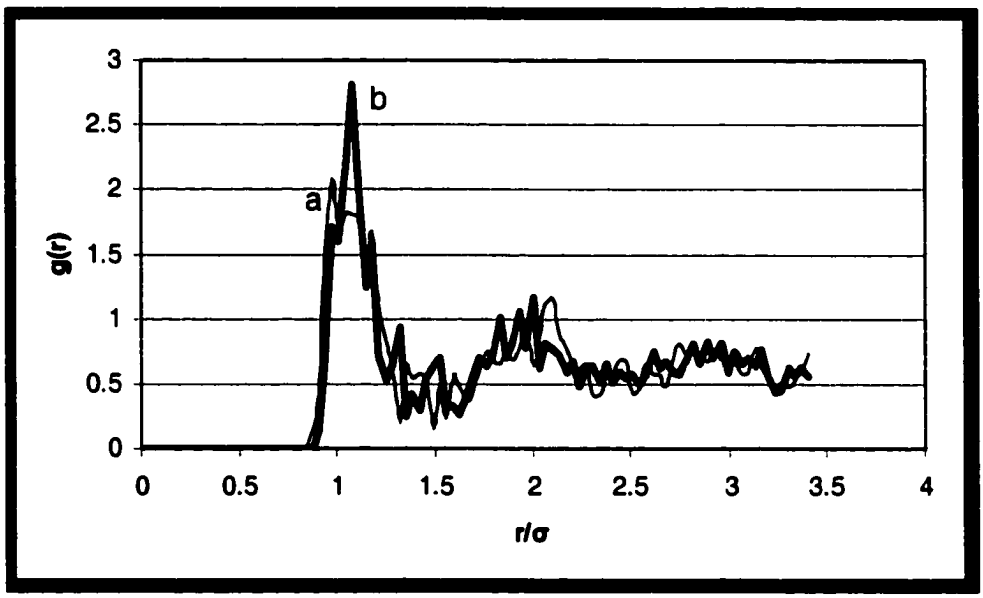

Figure 5.2 Pair distribution functions g(r) in surface system (A=11.5, B=0.133, C=1.0, μ=1.0) before (thin curve, a, Q=0) and after (thick curve, b) onset of charge (Q=20)

The dynamics of this redistribution will be studied in details below. Simply for now it is caused by the solute pulling more solvents into the solute's first shell by charge-dipole interaction.

It is also shown in the figures that it is reasonable to assume the first solvent shell as $r/\sigma <= 1.3$. We will use this concept of first solvent shell extensively later in analysis of the solvent redistribution dynamics (Section 3.5).

5.3.3 Three Modes Dynamics And Two Kinds Of Transient States

5.3.3.1 Solvent Response Function S(t), And Complementary Solvent Response Function CS(t) --- Solvation Dynamics

There are 3 major modes in the relaxation dynamics shown by S(t) in Figure 5.3. It includes a rapid decreases to a (local) minimum (MIN): first mode, then increase from the MIN to cause a local maximum (MAX) that may occur repeatedly (Oscillation, the second mode), and finally a slow decrease to equilibrium (The third mode). We have explicitly identified the oscillation as the 2nd mode in this 3-mode model, compared to the bi-modal model [1, 2] in previous research. In the latter little attention is paid to the second mode / oscillation, but the second and the third modes of our model are simply considered as just one mode.

The CS(t) is also plotted vs. S(t) in the above Figure 5.3. It is obvious the CS(t) behaves opposite to S(t). That is, when S(t) decreases to MIN, the CS(t) will increase to MAX, or verse visa.

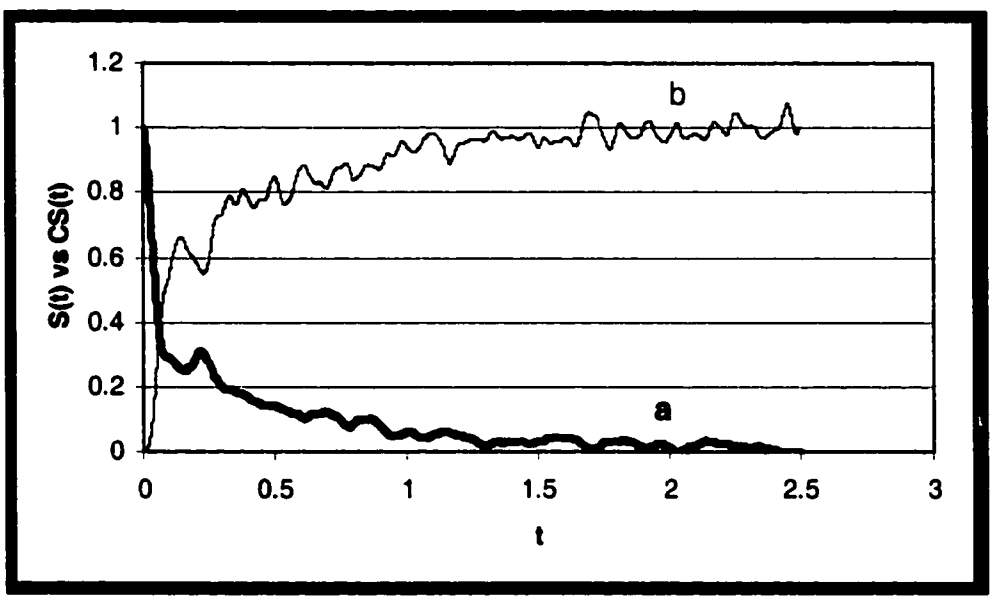

Figure 5.3 The solvation dynamics is typically shown by a three-mode dynamics reflected by S(t) (thick curve, a) and CS(t) (thin curve, b). System (A=11.5, B=0.133, C=1.0, μ=1.75, Q=20)

Table 5.6 The parameters obtained by fitting the data in the Figure 5.3 using models Y_3 (t) and Y_4 (t) of the Table 5.4 for S(t) and CS(t). The time constants are not in reduced unit, but in fs, assuming 2600 fs is a reduced time unit as CHF_3 particles. System (A=11.5, B=0.133, C=1.0, μ=1.75, Q=20)

	a	τ_G (fs)	τ_E (fs)	Model
S(t)	0.654	73.9	1552	$Y_3(t)$
CS(t)	0.484	112	1367	$Y_4(t)$

The dynamics are fitted by using models Y3 (t) and Y4 (t) (see Table 5.4 for models). The Parameters are shown in Table 5.6.

The Gaussian component in S(t) occurs in 73.9 fs responsible for the first mode, while the exponential mode occurs in 1552 fs responsible for the second and third mode (Though the models are not able to model the oscillation behavior explicitly, the oscillation has been combined to the third mode as perturbations and modeled by a single exponential.). Though the CS(t) occurs in a slightly slower Gaussian component (112 fs), and slightly faster exponential component (1367 fs), the opposite behavior in S(t) and CS(t) are still obvious.

The most interesting mode is the second oscillation mode. Most investigators ignored the explanation of the oscillation consisting of decrease to minimum and then increase to a new maximum. We have clarified the dynamics by introducing a new function CS(t), resulting in a mechanism with 2-transient states that clearly explains the oscillation in 5.3.3.2.

The following facts observed in the Figure 5.3 show the solute and its solvent shell are experiencing two kinds transient states:

- The S(t) tracks the solute-solvent interaction potential only, the CS(t) tracts all potential other than the solute-solvent interaction potential.
- The Min and Max in S(t) occur at the same time as the Max and Min in CS(t) respectively.
- The decrease and increase in S(t) occur during the same time range as the increase and decrease in CS(t) respectively.

5.3.3.2 Two Kinds Of Transient States And 3-Mode Solvation Dynamics

It is noted that the solvent-solute interaction potential is minimum at MIN of S(t), so at MIN the solute is at a very favorable state. On the other hand, the other potential including solvent-solvent interaction is at minimum at MIN of CS(t), so at MIN of CS(t) the solvents in the first Shell are in a favorable state. Based on this and the contradicting behavior of the S(t) and CS(t), we proposed the following overall mechanism with two kinds of transient states to interpret the three-mode dynamics of solute-solvent relaxation (Figure 5.4). The first kind consists of the transient states favoring solute, at the minimums (MINs) of S(t) or the corresponding maximums (MAXs) of CS(t). The second kind consists of the transient states favoring solvent shell around the charged solute, at the MAXs of S(t) and the corresponding MINs of CS(t).

The first mode consists of rapid decrease of S(t). The system goes to the transient state favoring to solute, but un-favoring to its solvent shell.

Following the first mode, the second mode occurs, which consists of the increase of S(t) from MIN to MAX to reach a transient state favoring solvent

Shell, but un-favoring to solute. The S(t) may goes from the MAX to another MIN again to cause oscillation in the second mode.

The third mode occurs after the second mode and consists of slow decay in S(t) from the transient state to reach a new equilibrium state favoring both the solute and solvent shell.

At the second mode the oscillation of S(t) may or may not be obvious depending on the coupling of the charged solute and solvents by dipole moment and solute charge.

The two kinds of transient states are supported by the effect of dipole moment (Figure 5.5 (a) and (b)) and charge effects (Figure 5.6 (a) and (b)) in surface and bulk fluids systems. See 5.3.3.3 for details.

In some system the oscillation is not obvious at all, the second mode reduces to the third mode and only the slow decrease to equilibrium is observed, in addition to the first mode of fast decrease. This is especially true when solvent dipole moment (Figure 5.5 (a) and (b)) or solute charge (Figure 5.6 (a) and (b)) are large, which causes strong coupling between solute and solvent. The coupling between solute and solvent is so strong that at the time solute reaches the state favoring itself, the state of favoring the solvent shell is also reached, i.e. no oscillation between the first two kinds of states will develop.

On the other hand in the system of small dipole moment (Figure 5.5 (a) and (b)) and solute charge (Figure 5.6 (a) and (b)), the coupling between solute and solvent is weak; the S(t) will oscillate between MAX and MIN

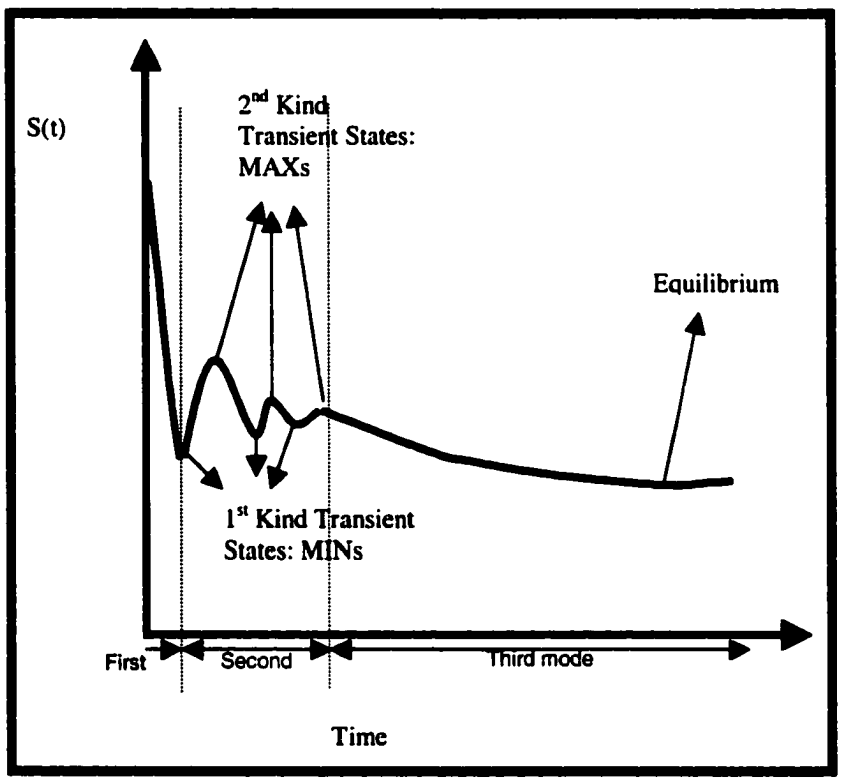

Figure 5.4 Schematic diagram with three mode dynamics of S(t) vs t and two kinds of transient states

several times before equilibrium. That means, when the solute is at a state favoring itself, the solvent shell is not at the corresponding state favoring itself because of the weak coupling. So the oscillation between the first two kinds of states will develop to adjust the solute and its adjacent solvent shell. After the solute and solvent shell experience several states favoring each other, the system will finally reach an equilibrium state favoring both solute and solvent shell. In this case the second mode of S(t) is observed as some oscillations, followed by a final slow decrease to equilibrium in the third mode.

Our mechanism consists of two kinds of transient states, and it is unique in focusing on the states the solute and its adjacent solvent shell will experience. However our mechanism is consistent with the ones by other researchers [1, 2], and in addition it extends to explain the oscillation in S(t), a phenomenon that is usually ignored by other researchers' explanation.

5.3.3.3 Dynamics In AS And Bulk Solution

5.3.3.3.1 Dipole Moment Effect Of AS System And Coupling Among Solvents

The potential between solute and solvents goes down as μ increases because of increasing interaction between solute and solvents (Figure 5.5).

As μ decreases, the oscillation occurs more times before reaching equilibrium. The coupling between solute and solvents is weaker as μ decreases, so the system will experience more than one of each transient states to reach equilibrium. The following table shows the effect of μ on S (t) by data fitting.

Table 5.7 (a) Dipole moment effect μ on S (t) fitted by model Y_3 (t) in AS System (A=11.5, B=0.133, C=1, Q=20)

μ	a	τ_G (fs)	τ_E (fs)
1.75	0.655	73.8	1551
1.4	0.566	74.2	1734
1.0	0.471	84	2000
0.5	0.461	91	2585

As μ decreases, the parameter, a, decreases. That means the proportion of the Gaussian component (first mode) decreases, and the proportion of the exponential component (second and third modes) increases.

Also τ_G slightly increases, but τ_E significantly increases with decrease in μ. That means the first mode occurs slightly slower, but the second and third modes occur much slower at higher μ.

The results are interesting in that the effect of the dipole moment of solvents in pure solvents here is the same as the effect of composition in the binary mixture of solvents having strong dipole and solvents having weak dipole in previous researchers. Thus our results here give new explanations to the components effect of previous researchers [2]. That is, the composition effect of previous researchers is originated from the change in the average dipole moments of the solvent mixture by changing the proportion of solvents with strong dipole and weak dipole.

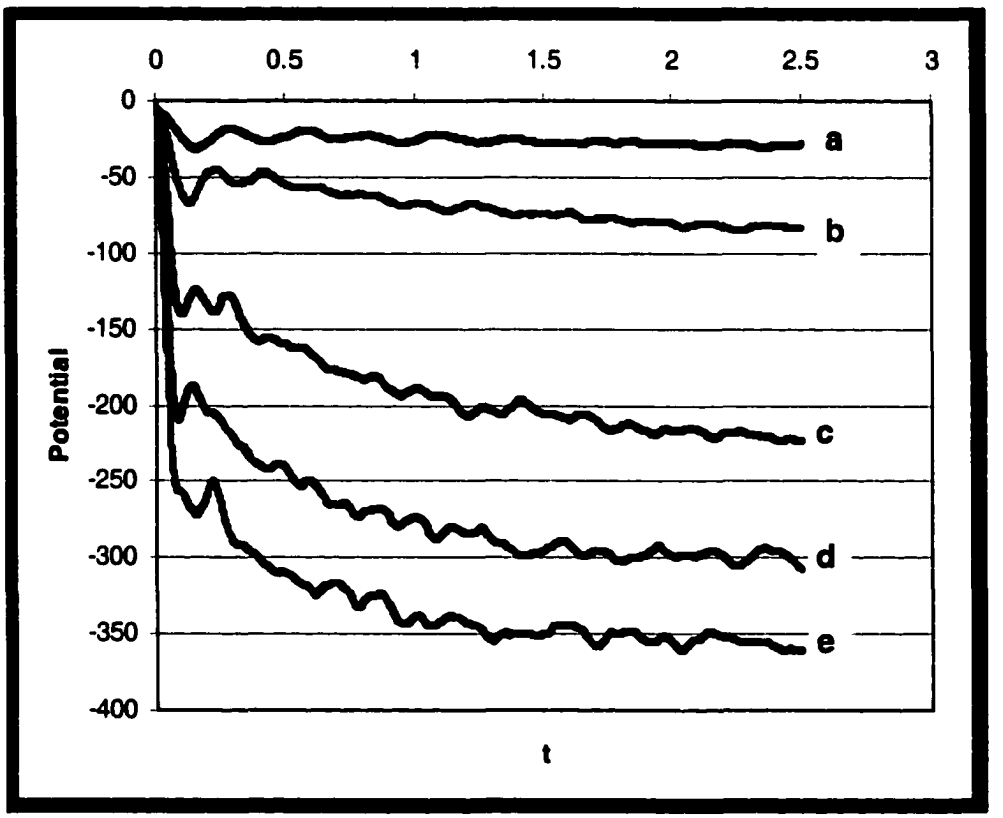

Figure 5.5 (a) The dipole moment μ effect on potential between solute and solvents in surface system (A=11.5, B=0.133, C=1.0). The five curves from top to bottom correspond to: μ=0.25 (a), 0.5 (b), 1.0 (c), 1.4 (d), and 1.75 (e) at Q=20.

5.3.3.3.2 Dipole Moment Effect Of Bulk System And Coupling Among Solvents

As dipole moment decreases (1.75 to 0.25) at Q=20, the rate of the first mode only differs slightly (Figure 5.5 (b)). The 2nd mode is more obvious. This is because the smaller dipole moment makes the reorganization of the solvent shell to equilibrium harder because of weaker coupling by dipole-dipole interaction among solvents. The third slow mode becomes slower as dipole moment decreases.

Table 5.7 (b) The dipole moment μ effect on S(t) for fluids with Q=20 modeled by $Y_3(t)$

μ	a	τ_G(fs)	τ_E(fs)
1.75	0.702	63.8	1444
1.4	0.651	73.9	1302
1.0	0.611	81.5	2297
0.5	0.600	103	3569
0.25	0.565	104	3881

The table 5.7(b) summarized the dipole moment effect on S(t) by fitting data with model. As μ decrease, parameter, a, decreases, that means the Gaussian proportion becomes less. τ_G and τ_E increase, that means both Gaussian and exponential components become slower.

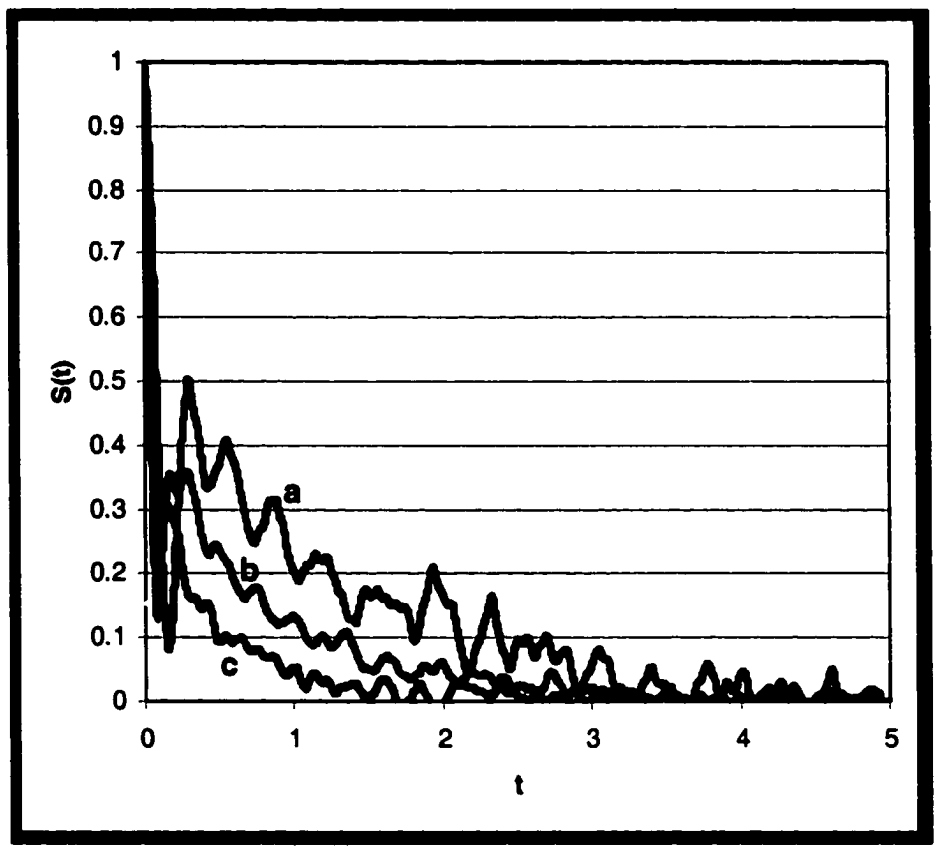

Figure 5.5 (b) Dipole moment effects on S(t) in bulk fluid (Q=20) at μ=0.25 (curve, a), 1.0 (curve, b), and 1.75 (curve, c)

5.3.3.3.3 Charge Effect Of AS System And Coupling Between Solute And Solvent

As Q increases, the first MIN increases, and the 3rd mode becomes more prominent (Figure 5.6).

The table 5.8(a) summarizes the charge effect on S(t) by data fitting.

Table 5.8 (a) The charge Q effect on S(t) for surface system (A=11.5, B=0.133, C=1.0, μ=1.75). The parameters are obtained by fitting data of S(t) using $Y_3(t)$ model.

Q	a	τ_G (fs)	τ_E (fs)
81	0.442	58.3	1296
36	0.503	61.4	1149
20	0.655	73.8	1552
16	0.755	79.0	1640
12	0.872	84.2	2682

Generally speaking, parameters, a, τ_G, and τ_E, decrease as Q increases. That means less proportion of Gaussian or first mode, but more proportion of exponential component or second and third modes at larger Q. Also the first mode is slightly faster, and the exponential mode is fluctuating, though generally faster at larger Q as indicated by the time constants.

The MIN in Figure 5.6 (a) measures the proportion in potential contribution of the first mode over the second and the third mode. The more contribution of the first mode, the lower of the MIN. The more contribution of the third mode, the higher the MIN is. Therefore the MIN increases as charge

increases because more potential decrease occurs in the third mode, which is consistent with the parameter, a, decrease with charge in Table 5.8 (a).

As the charge increases, the potential barrier exerted by the solute charge-solvent dipole interaction to the dipole-dipole interaction among solvents increases. And the solvent reorientation relaxation is more apparent. Therefore the third slow component plays more part.

5.3.3.3.4 Charge Effect Of Bulk System And Coupling Between Solute And Solvent

As charge increases, the interaction potential between solute and solvent becomes lower. Figure 5.6 (b) shows the charge effect on S(t), as Q increases, the 2nd mode gradually disappears, and completely disappear at large charge like Q=48, 81. The 2^{nd} mode begins to appear when the charge decreases to Q=36, and it is very obvious for Q=12, 16, and 20. The 3^{rd} mode of decay to equilibrium becomes more dominating, but is slower as Q increases.

When Q is small (Q=2, 4, 6), the first MIN of S(t) can be lower then the equilibrium value zero of S(t) as in Figure 5.6 (b). This is because coupling between solute-solvents is small at small charge, and the solute gains a transient state favoring to itself easily. The 3^{rd} mode occupies only small proportion. This is because the dipole-dipole interactions among solvents are almost completely used in the third mode with only small counteracting effect (potential barrier due to solute-solvent interaction) by the small charge.

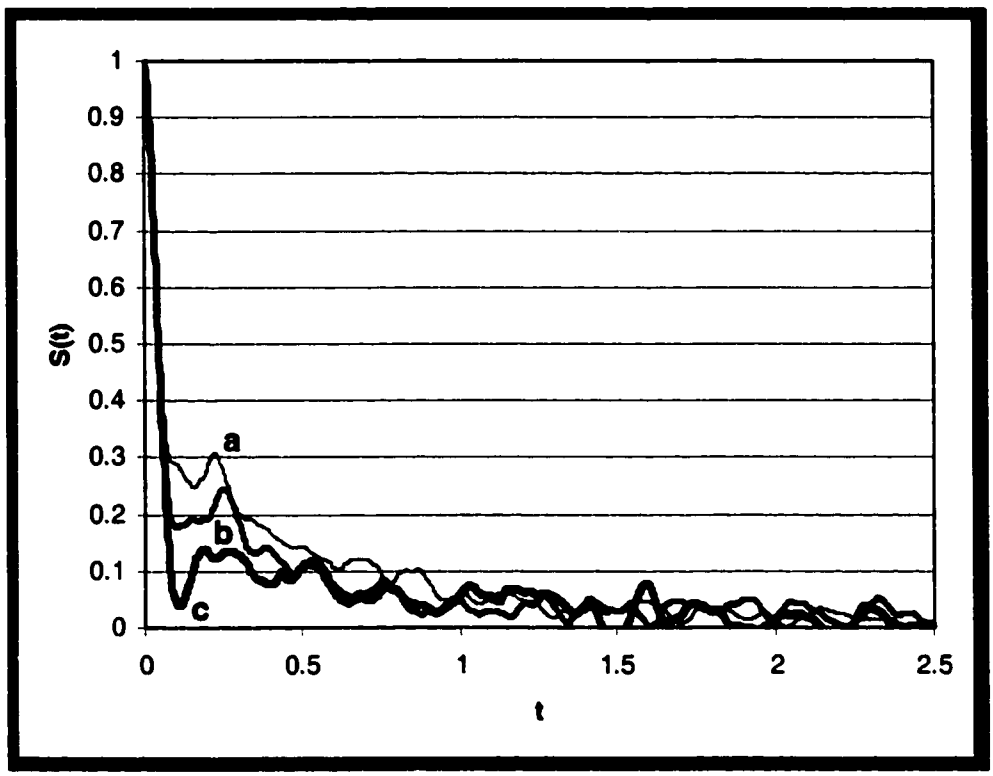

Figure 5.6 (a) The charge Q effect on S(t) for surface system (A=11.5, B=0.133, C=1.0, μ=1.75). The curves from top to bottom correspond to Q=20 (thinnest curve a), 16 (curve, b), and 12 (thickest curve, c)

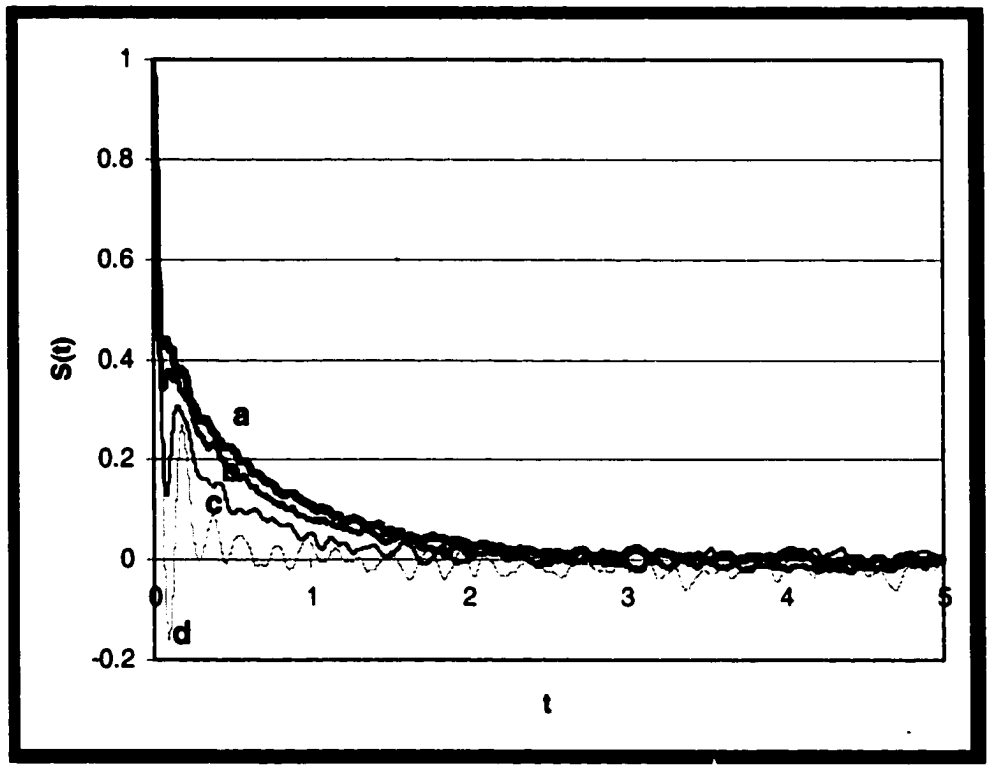

Figure 5.6 (b) The charge Q effect on S(t) for bulk fluids (μ=1.75). The curves from top to bottom correspond to Q=48 (thickest curve, a), 36(curve, b), 20 (curve, c), and 12 (thinnest curve, d)

The three modes are best shown for Q=20. At larger Q=48, the 2nd mode of MIN to MAX disappears, so only the 1st and 3rd modes exist. As Q increases, the rate of the 3rd mode decreases and it is more dominating.

As charge increases, the coupling between the solute and solvents becomes stronger, causing the solvent-solute interaction potential to decrease. It is this stronger coupling that also makes it harder to reach a transient state favoring either to the solute itself or to solvents themselves only. Therefore no MIN/MAX observed when charge is large, and the second mode of oscillation does not occur because it reduces to the third mode. This reduction of the second mode to the third mode is one of the reasons to make it possible that the third mode takes longer time to reach equilibrium because this third mode occupies the time for both the second and the third modes if the charge were small.

Another reason is that the higher charge of the solute cause an orientationally barrier to the solvents, and therefore makes the proportion of the third mode more prominent. This stronger coupling between the charged solute and the polar solvents causes the charge-dipole interaction between the solute and the solvents to be orientationally counteracted by dipole-dipole interaction between the solvents. The solute charge tries to cause the first shell solvents' dipoles aligned to favor the solute by charge-dipole interaction. On the other hand, the dipole-dipole interaction among the solvents causes the solvents to be aligned to favor to the solvents. It takes more time for the

solute and shell solvents to decay to equilibrium simultaneously because of this counteraction. Therefore higher charge slows the third mode.

Table 5.8 (b) Charge Q effect on S(t) in bulk fluids with μ =1.75, modeled by $Y_3(t)$

Q	a	τ_G (fs)	τ_E (fs)
81	0.517	44.9	1876
48	0.545	49.6	1837
36	0.575	52.7	1569
20	0.702	63.8	1444
16	0.796	69.1	1761
12	0.921	73.7	1251

Table 5.8 (b) summarizes the charge effect on S(t) by fitting data as follows: As Q increases, the parameter, a, decreases, that means the Gaussian component become less. The τ_G decreases, that means Guassian component become faster. The τ_E increases/fluctuates, that means exponential part becomes slower (The τ_E at Q=16 is exceptional because the second mode is most obvious in this charge, it interferes the data-fitting for the third mode.)

5.3.3.4 Surface Effect

5.3.3.4.1 MIN of S(t)

As shown below, the surface has only a small effect on the 2nd mode, because doest not change the coupling between solute and the solvents. We are going

to focus on the proportion contributed by the 1st and 2nd as well as 3rd mode together as reflected by the first MIN in S(t).

Though the 3-mode dynamics applies to surface and bulk system, the surface parameters (A, B, and C) do make the dynamics different from the bulk system, especially in the proportion or contribution of each mode in the overall dynamics and the rate of the third mode. The dependence of S(t) in terms of MIN and rate on the surface parameters is discussed below.

As shown in Figure 5.7, the MIN of S(t) goes down as C increases (see also parameter, a, goes up as C increases in Table 5.9). That means the first mode contributes more proportion to the overall dynamics at larger C, and the third mode contributes less proportion accordingly. The reason for this is because the 1st adsorption layer becomes narrower, closer to surface, and locally denser in number of particles than ideal bulk (see 5.3.1). All these cause the first response of the surrounding particles of the ion/solute to be aligned more favorable to solute in potential, so the MIN of S(t) is lower. The surface will influence the S(t) dynamics by changing the properties of the first adsorption layer where the solute is.

As B increases, the MIN of S(t) increase slightly, the trend is opposite to C effect on S(t) as expected (Figure 5.8). The reason is that the proportion of the second and third modes over first mode increases with B. This is consistent with the decease in a, the amplitude of the Gaussian component as B increases in Table 5.9. This is explained also by the adsorption layer effect

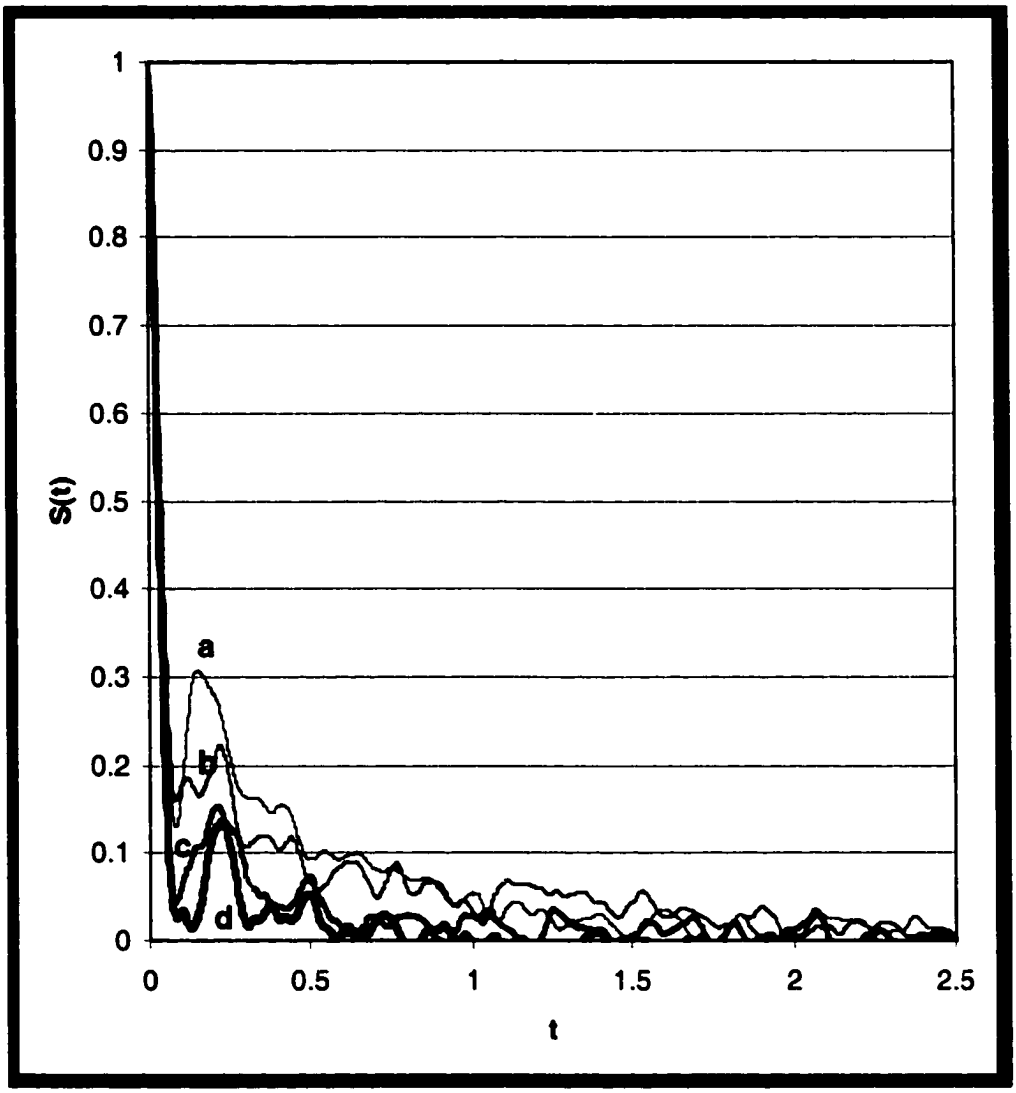

Figure 5.7 Surface effect (C effect) on S(t). The curves a to d from top to bottom (thin to thick) correspond to bulk system (a) and surface system with C=1.0 (b), 4.0 (c) and 6.0 (d) at A=36 and B=0.133 for surface. The fluids have μ=1.75, Q=20.

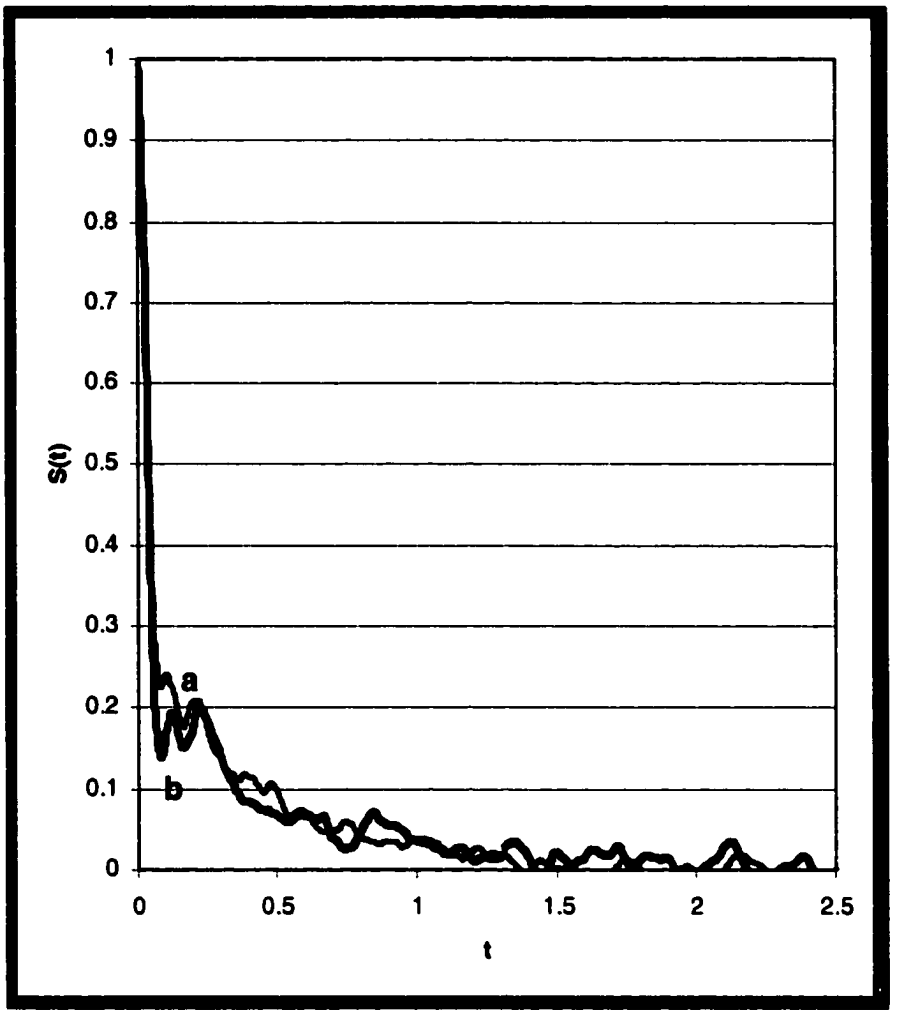

Figure 5.8 Surface effect (B effect B=0.5 and 0.01) on S(t) for system (A=36, C=1, μ=1.75, Q=20). The 2 curves correspond to 0.01 (curve b) and B=0.5 (curve a) respectively.

exerted by the surface. As B increases, the first adsorption layer becomes broader in z and further away from the AS. The local density of the solvents in the immediate surrounding of the solute is smaller; so fewer solvents are aligned to the solute's ionization, and less favorable to the solute potential.

As A increases, the first MIN decreases (Figure 5.9), consistent with the increase in Gaussian amplitude, a, in Table 5.9. This is explained by the fact that A is just a scale factor for the balance of B and C effect. If C dominates, then the S(t) will show the effect of C as A increases. This is exactly the case where C=1 and B=0.133, so first MIN decreases as A increases just as C increases.

In summary, B effect is opposite to C, but A effect follows C effect. This rule will also apply to the effect of rates for different modes of S(t) below. For simplicity, we will only discuss the C effect.

These surface effects are well understood above by the surface effect on the adsorption layers (Section 5.3.1) and by assuming the 1st mode is related to the solvents in the immediate environment of the solute and the 3rd mode to the solvents relatively away from the solutes.

5.3.3.4.2 Rate Of S(t) Modes

The rate of first mode of S(t) seems approximately the same regardless of the C. This is shown in Table 5.9 as about constant τ_G for the Gaussian component.

The rate of the 3rd mode of S(t) is slower as C decrease (Figure 5.7). This is shown in Table 5.9 as increasing τ_E for the exponential component.

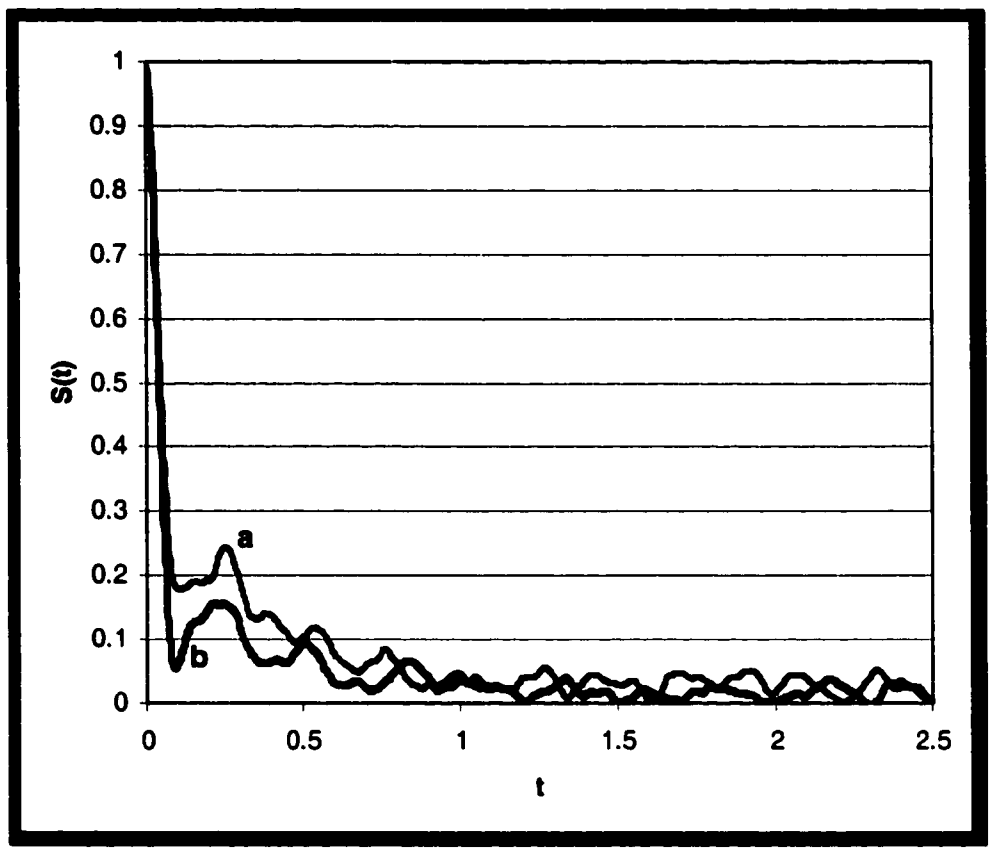

Figure 5.9 Surface effect (A effect) on S(t) for system (B=0.133, C=1.0, μ=1.75, Q=16) at A=11.5 (thin curve, a) and 36 (thick curve, b)

This may be understood by the redistribution of first shell solvents (see also section 5.3.5). The first solvent shell occupies spatially more than one adsorption layer as C decreases, so the redistribution will take more time to corporate the solvents between different layers. For example, at μ=1.75 and Q=12, A=11.5, B=0.133, the first shell will contains solvents from 2 adsorption layers in the case of C=1 instead of just 1 layer as in the case of C=2. When C is as large as 6, the first solvent shell is confined by the surface in z direction to the first adsorption layer, so no solvents cooperation between the first layer and the second layer is needed, and the redistribution goes faster.

5.3.3.4.3 Modeling The Surface Effect On S(t)

The following Table 5.9 summarizes the surface effect on S(t) by fitting data with models.

As shown in the Table 5.9, the parameter, a, increases; but τ_G decreases slightly, and τ_E decreases rapidly with C and A. The effect of A is similar to the effect of C. That is as C and A increases, the proportion of the Gaussian component increase, and all modes goes faster, though the first mode only goes faster a little bit.

The effect of B is complicated. The parameter, a, fluctuates; and τ_E fluctuates with B. The τ_G fluctuates very slightly with B.

5.3.3.5 Comparison Of Surface With Bulk System

The values of MIN in S(t) of surface relative to the bulk depends on A, B, C values. Higher A and C will make the values of MIN lower.

Table 5.9 Effect of surface parameters on S (t) for system with μ=1.75 and (a) Q=20; (b) Q=16

(a) Q=20					
Surface Parameters			Parameters in model Y_3 (t)		
A	B	C	a	τ_G (fs)	τ_E (fs)
36	0.133	1	0.805	72.3	2063
		4	0.873	65.3	1312
		6	0.912	62.5	988
11.53	0.133	1	0.655	73.8	1552
		2	0.781	71.1	1231
36	0.01	1.0	0.782	68.7	1382
	0.03		0.759	63.9	1199
	0.06		0.773	67.8	1696
	0.133		0.805	72.3	2063
	0.5		0.704	71.1	1058
Bulk Fluid With No Surface			0.701	63.7	1433
(b) Q=16					
Surface Parameters			Parameters in model Y_3(t)		
A	B	C	a	τ_G (fs)	τ_E (fs)
11.53	0.133	1	0.755	79.0	1640
36			0.860	75.3	1814

For example: at A=36, the MIN with surface is below that of bulk (see Figure 5.7); while at A=11.5, the MIN with surface is above that of bulk (Figure 5.10). At A=11.5, B=0.133, C=1 and μ=1.75; the S (t) has a higher MIN, lower MAX than Bulk (Figure 5.10).

At large C=6, the third mode disappear due to the first layer is thin, but at smaller C=1.0; the slow decrease shows little difference from that of bulk. This agrees the assumption that the 3rd mode of slow decrease is related to the particles surrounding to the solute at a more extensive space.

At large charge (Q=81), the difference in S(t) between the bulk and surface is very small (Figure 5.11); this is because the charge plays the most part, the surface's effect is not so large any more.

5.3.4 Solute Translational Motion

The overall dynamics are shown above with 3 mode solvent response function S(t) and complimentary solvent response function CS(t). The functions are in terms of energy that is indirectly reflected to translational and rotational motions of the solute and solvents.

In this section, a new function $r_{sz}(t)$, the distance (z-component) of the solute from the surface in the direction perpendicular to the surface, z, is introduced to study the solute translation during the entire process. As shown later, in the first mode time scale of S(t), solute tries to find a favorable position to reduce the potential between solute and solvent. The solute moves away from the surface to a place with higher probability of solvents in its first shell, and then it begins random walk around this favorable position.

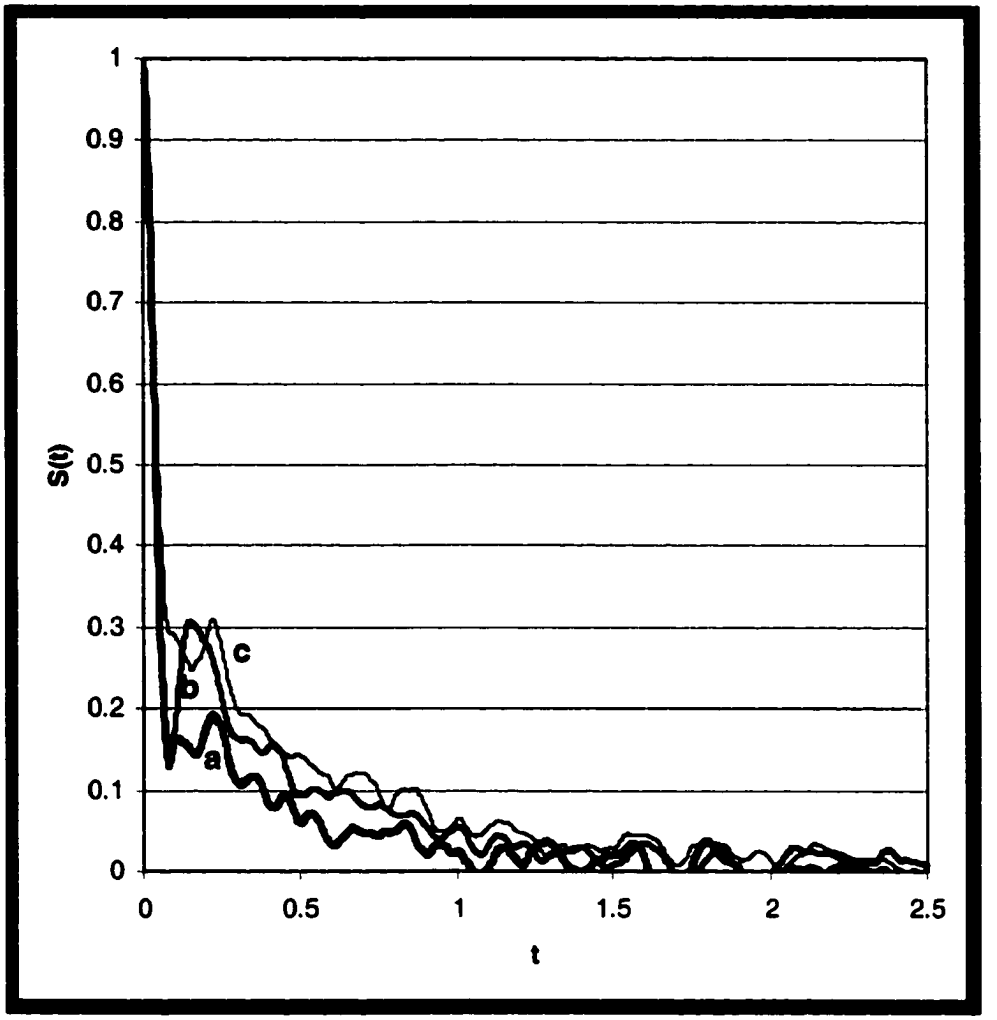

Figure 5.10 The values of MIN/MAX in S(t) of surface compared to the bulk. For surface systems (A=11.5, B=0.133) at C=2 (thickest curve, a) and 1 (thinnest curve, c), as well bulk fluid (Curve, b) with μ=1.75, Q=20.

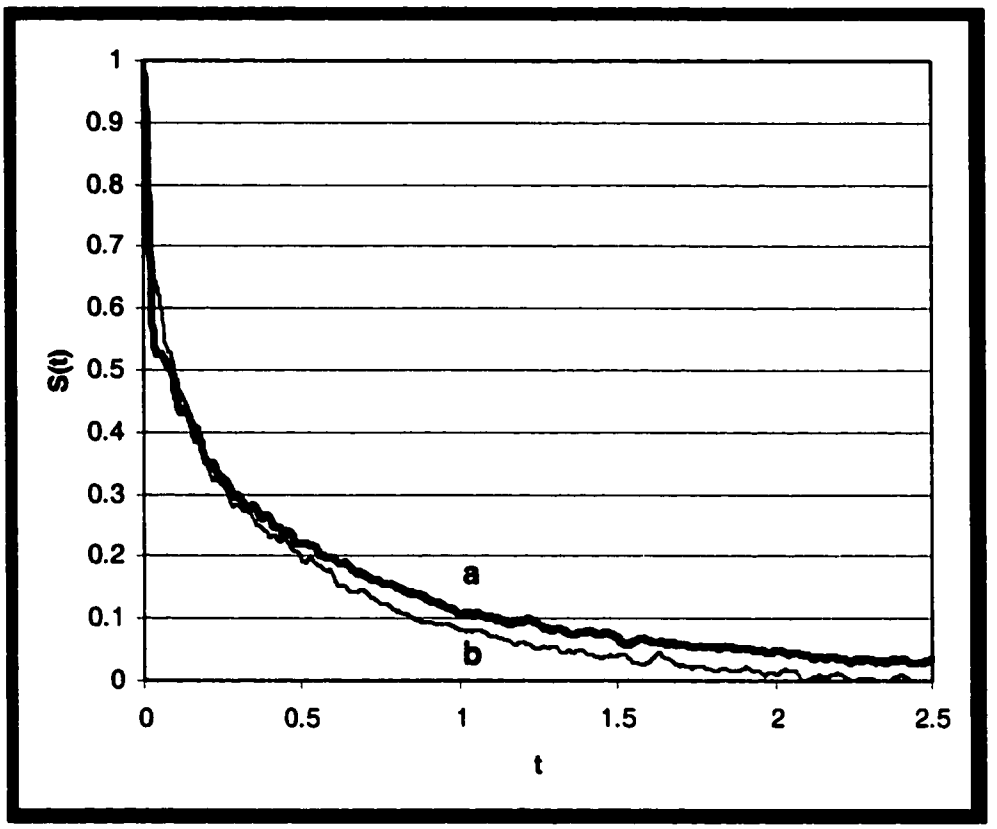

Figure 5.11 Charge effect on MIN/MAX in bulk (thick curve, a) and surface (thin curve, b) systems (A=11.5, B=0.133, C=1) for fluids with (μ=1.75, Q=81).

5.3.4.1 Compare Bulk And Surface System

In bulk fluids, the

$$r_{sz}(t)-r_{sz}(0)=z(t)-z(0), \quad (5.78)$$

always does random walk (Figure 5.12 upper frame), regardless of charge and dipole moment.

In the surface system, the solute will leave the non-polar surface upon ionization to a position depending on the surface (Figure 5.12 lower frame) The charged solute moves away from surface because the polar solvents in the bulk are pulling it due to additional charge-dipole moment interaction upon ionization, while the surface will not have additional interaction.

In the surface system the solute moves away from the surface (z=0) quickly at early stage, then stay around somewhere with a very slight random walk instead of going further away from the surface. The result is surprising because it is expected that the solute should be able to move further along z direction as the case of bulk. After considering the surface effect on the solvents below, it is understandable because the surface has built adsorption layers near the surface by surface-solvents interaction, which limits the translational movement of the solute in z direction.

5.3.4.2 Surface Adsorption Layer Effect

The $r_{sz}(t)$ behaves differently with surface parameters, which shows the adsorption layer effect.

Figure 5.12 Translational movement of the charged solute in bulk fluid and surface system. The upper frame is in bulk fluid system with μ=1.75, Q=20. The lower frame is in surface system with A=11.5, B=0.133, C=1 for fluids with Q=20 and at different μ =0.25 (a) , 0.5(b), 1.0 (c), 1.4(d), and 1.75 (e).

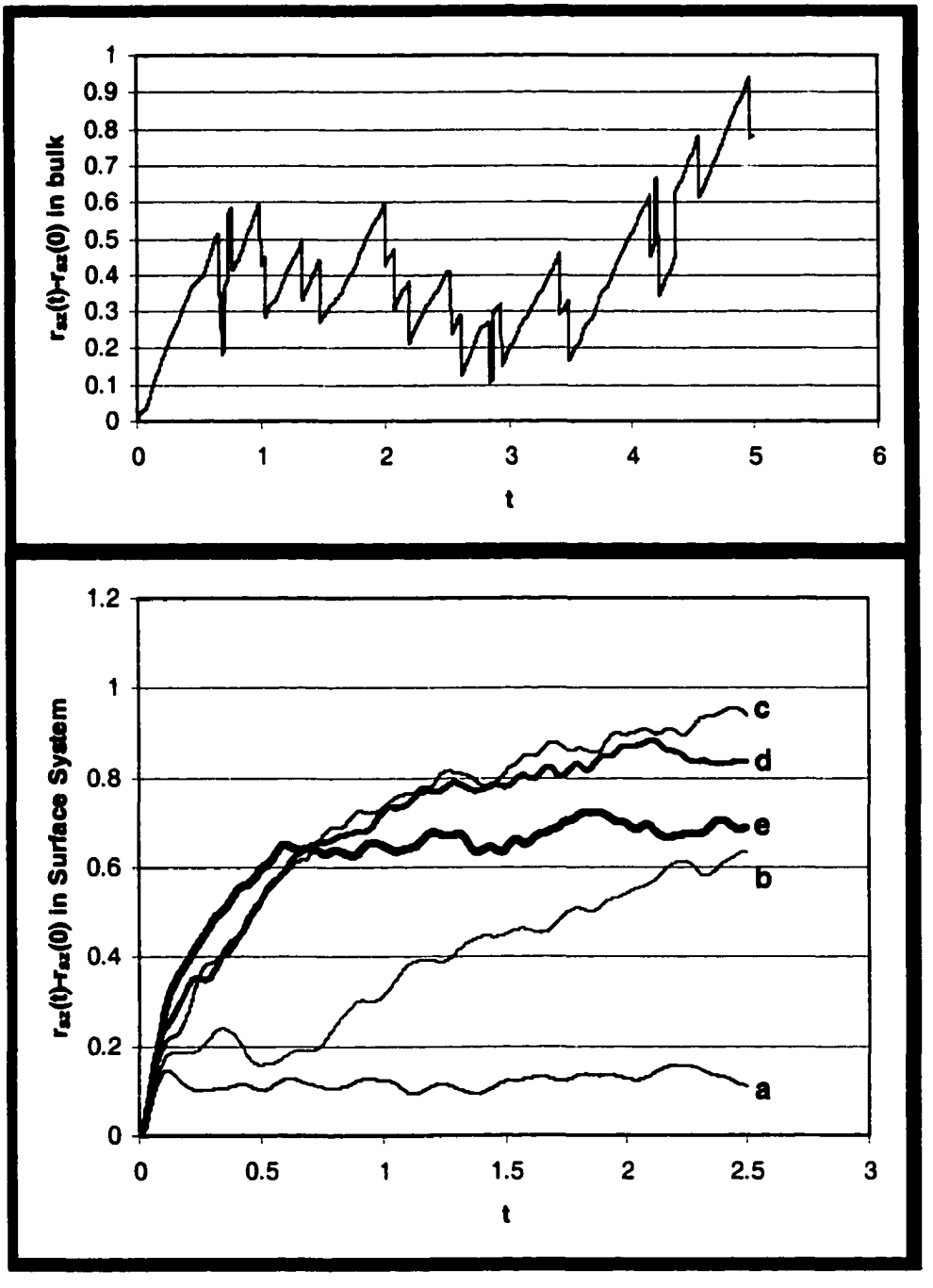

At large C (e.g. 4 and 6), solute will bounce back and fourth along z-direction until it reaches a new equilibrium (Figure 5.13). The r_{sz} vs. t will oscillate around the first peak position.

In this case the first layer is very thin, and the first valley containing no particles separates the first adsorption layer of solvents (vv_1=0, see Table 5.5 in section 5.3.1). The solute is initially in the first layer close to the surface. After ionization, the solute undergoes translational movement to relax. However, the solute is always confined in the first layer by the abstract surface due to the fact that no particles can exist in the first valley. The onset of the charge at the solute will cause the solute to bounce back and fourth around the center of the first layer until it reaches equilibrium. As shown by the r_{sz} changing with t, the r_{sz} always falls within the first peak. At any value of C that will make the first valley zero particles in enough width in z as the cases here, the solute reaches the new equilibrium at a position that is very close to the first peak position.

The extreme case in Figure 5.13 is the surface with large A =36 and C=6 resulting in no solvents in certain spatial area between the first and second layers. The adsorption layers are thin in width, but 1st valley with no particles is wider in width. The solute is confined around z=0.635 (the center of the first layer) after the first rapid movement bouncing fourth and back to surface.

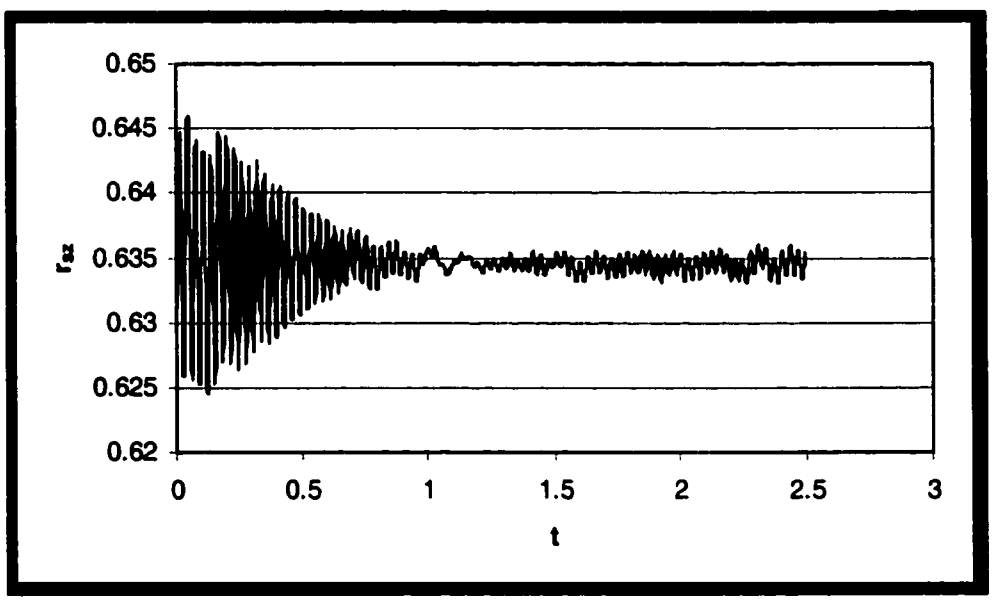

Figure 5.13 Translational movement of charged solute for system with larger C=6 (No particles at first valley) for system with A=36, B=0.133, μ=1.75, and Q=12. The solute will bounce back and fourth along z-direction until it reaches a new equilibrium.

After the adsorbed charged solute moves away from surface to the center of the first layer, the z position is very favorable to the equilibrium. Going further away to cross the first layer to the second will need additional energy, which is not provided simply by the thermodynamic fluctuation (~ k_bT). So the charged solute will stay at the center of the first layer (in terms of z), with very slight random walk due the thermodynamic fluctuation. It is noted that when solvents are not allowed to exist in the valley between the first and second layer, the solute will not cross the first to the second layer (i.e. r_{sz}<= the position where ZD=0).

However, if the C is not large enough to make the valley zero particles like the case of C=1 (Figure 5.14 and Figure 5.12), the particle can establish equilibrium at the new z without oscillating back to the peak position of the first layer. In this case there are particles in the first valley. In addition the first adsorption layer is also thicker, therefore the solute has more space along z to relax without oscillation around the peak position. The solute may relax to a position at the first valley with its solvent shell at the first and the 2nd layer of solvents. The r_{sz} dynamics in Figure 5.13 are different from Figure 5.14, which demonstrate that the solute is NOT confined to the first layer by surface any more if the valley between the two layers can still allow particles to exist.

Therefore the solute will oscillate around the peak position of the first adsorption layer at large C (2, 4, and 6), because no particles existing in the first valley will limit the movement of the solute. However at small (C=1), the

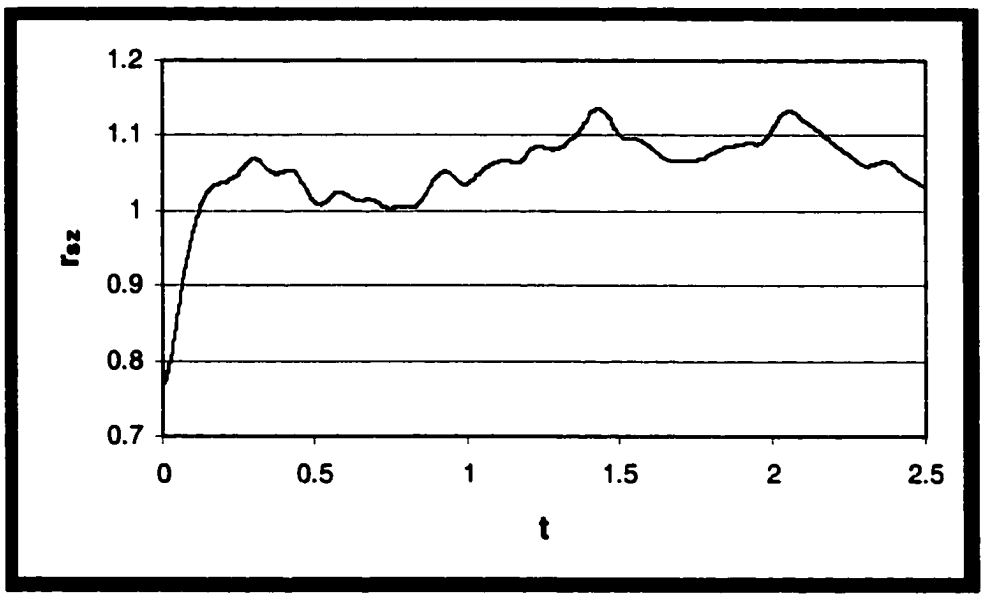

Figure 5.14 Translational movement of charged solute for system with smaller C (particles present in first valley) for system with A=11.5, B=0.133, C=1.0, μ=1.75, and Q=12.

solute will move away from the surface not limited to the first layer. Instead it may move to the 1st valley and form its first solvent shell using particles both in the 1st and 2nd adsorption layers.

5.3.4.3 Dipole And Charge Effect On r_{sz}

To see how r_{sz} changes with dipole and charge, the case where there are particles in the first valley is used (A=11.53807, B=0.133333, C=1.0). As time increases, the $r_{sz}(t)-r_{sz}(t=0)$, the distance of solute from the surface at time t relative the distance at t=0, increases rapidly at early stage, then gradually become random walk (Figure 5.12 lower pane). That means the solute will leave the surface by translation upon the ionization at time 0, until it reaches a new equilibrium state surrounded by more solvents.

As dipole moment decreases, the solute shows fewer tendencies to leave the surface; it tends to be in random walk (Figure 5.12 lower pane). The dipole moment effect is complicated.

Table 5.10 Dipole moment effect on r_{sz}. System with A=11.5, B=0.133, C=1 for fluids with Q=20

Data	μ	c	a	b	a/b	τ_G (fs)	τ_E (fs)	Model
r_{sz}	1.75	0.680	0.141	0.561	0.251	140	744	$Y_2(t)$
	1.4	0.870	0.121	0.767	0.158	91	1610	
	1.0	0.947	0.0962	0.863	0.111	98	1853	

When μ is large (1.0 , 1.4, 1.75), the r_{sz} can be modeled by $Y_2(t)$. As μ increases, the r_{sz} (e.q.) decreases. As μ increases, the Gaussian component grows (the parameter, a, increases), but exponential component dies (the parameter, b, decreases) in model $Y_2(t)$. The Gaussian component fluctuates (τ_G), and exponential component accelerates (τ_E decreases) as μ increases.

As charge Q increases, the solute leaves the surface further (Figure 5.15, Table 5.11), due to the increasing charge-dipole interaction between solute and solvents. This is shown as the fact that the parameter, c, increases as Q increases in Table 5.11.

When Q is small, Q=6, only Gaussian exists, modeled by $Y_6(t)$; When Q is large =81, only exponential exists, modeled by $Y_5(t)$. As Q increases from

Table 5.11 Charge effect on charged solute translation movement in system (A=11.5, B=0.133, C=1, μ=1.75)

Data	Q	c	a	b	a/b	τ_G (fs)	τ_E (fs)	Model
r_{sz}	6	0.169	0.167			108		$Y_6(t)$
	12	0.342	0.238	0.100	2.38	139	4×10^3	$Y_2(t)$
	20	0.680	0.141	0.560	0.252	140	7.4×10^2	
	36	1.28	0.211	1.12	0.188	320	6.48×10^2	
	81	2.53		2.56			799	$Y_5(t)$

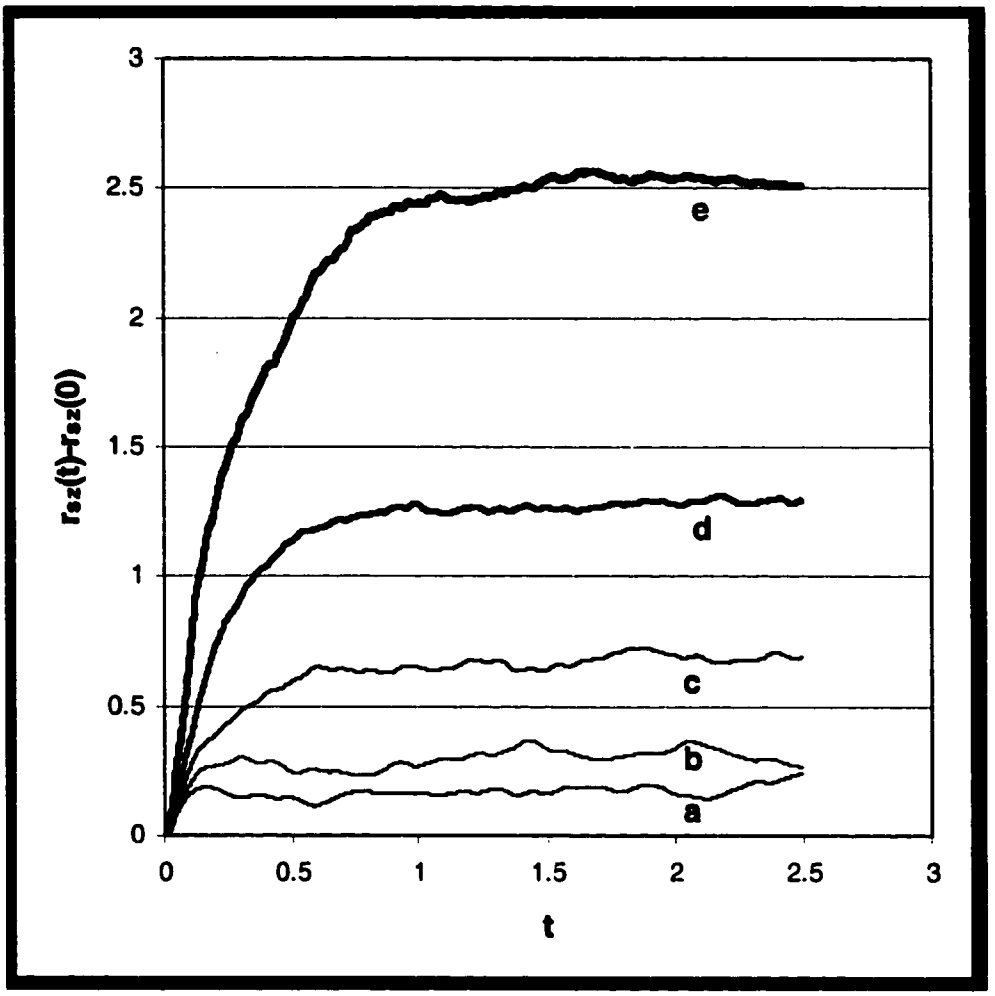

Figure 5.15 Charge effect on charged solute translation movement in system (A=11.5, B=0.133, C=1, μ=1.75) at Q=6 (curve a), 12 (curve b), 20 (curve c), 36 (curve d), and 81(curve e) for the 5 curves from bottom to top respectively.

12 to 36, the r_{sz}(e.q.)=c increase. As Q increases, the Gaussian component dies (the parameter, a, decreases), but exponential component grows the parameter, b, and increases. In model $Y_2(t)$ the Gaussian component slow down (τ_G increases), and exponential component accelerates (τ_E decreases) as Q increases.

5.3.5 Redistribution Of Solvents In The First Shell--- (N1Shell)

The pair distribution function at equilibrium changes before and after onset of charge (Figure 5.2), which means the solvents in the first shell are redistributed. The new function N1Shell explores the details of this redistribution by dividing the first shell into parts including inner and outer shell as shown in the schematic diagram below (Figure 5.16).

5.3.5.1 Solvent Number Dynamics --- Solvent Number Redistribution

Upon solute ionization, it is shown that the number of solvents in the first shell will keep constant if dipole & charge is low. However it generally increases with time until equilibrium if the dipole moment >=0.5 or charge >=20. The results are specially interesting here because the previous researchers only noticed the fact that the solvent number keeps constant with time, since their charge and dipole moment happens to fall within the range of dipole moment <0.5 and charge <20 [(2)]. We have extended their study to a broad range of charge and dipole moment to show the effect of dipole moment and charge to the solvent number. Figure 5.17 shows that the first shell of the solute gains solvents in total from outside in the bulk.

However this is not always true for different parts of the first shell at different time ranges. It is interesting to look at the redistribution of the number of solvents at different parts of the first shell (inner and outer shells). From the Figure 5.17, it is obvious that the inner part gains solvents. This is shown by the fact that N1Shell (r/σ=1) will increase. Correspondingly the outer part of the first shell will lose solvents. This is shown by the fact that the N1Shell (outer) will decrease.

It is also interesting to observe the correspondence between the solvent dynamics and the S(t) dynamics. In the first mode of S(t), the inner shell gains solvents suddenly, while the outer shell loses solvents suddenly. The change in solvent number occurs by translational motion. Thus it is reasonable to predicate that the translation (for both solute and solvents) plays an important part in the first mode.

Subsequently, in the second and third mode of S(t), the inner and outer shell continues to gain and lose solvents respectively, but in a significantly slow speed. So the translational motion plays less important part in $2^{nd}/3^{rd}$ mode than in 1^{st} mode. In other words the rotational motions of the solvents play a more important part. The redistribution goes until equilibrium where there are no net changes in the solvent number.

The rapid decrease in the solvents of outer part demonstrates that at first mode, the solvents outside the first shell failed to respond so quickly to move solvents into the outer part of the shell to compensate its loss of solvents due to moving to the inner part. In the first mode of S(t), the solvents

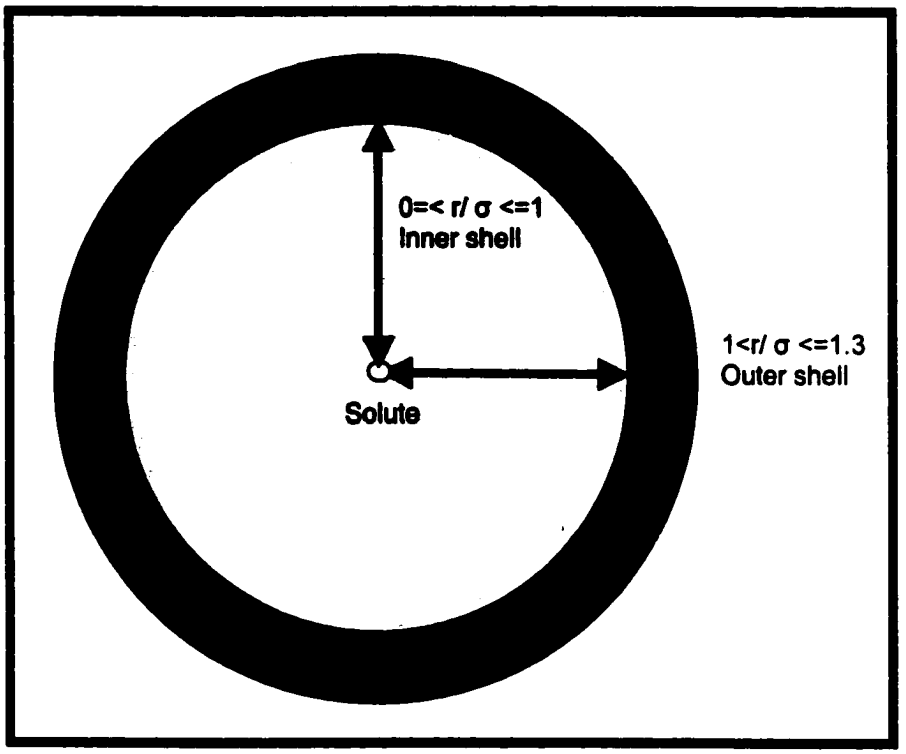

Figure 5.16 First shell = Inner shell + outer shell, and N1Shell=N1Shell (inner)+N1Shell (outer), where N1Shell (inner)=N1Shell (0=< r/ σ <=1.0), and N1Shell (outer)=N1(Shell(1< r/ σ <=1.3). The first shell of the solute at r=0 is defined here as all the solvents located in a distance r <=1.3σ from the solute, or simply r/ σ <=1.3. It is important to divide the shell into parts by r/ σ to understand the solvent shell relaxation. Here this shell is divided into inner part (e.g. 0=< r/ σ <=1.0) and outer part (e.g. 1.0=< r/ σ <=1.3). Simply the outer part is relatively away from the solute, but the inner part is closer to the solute. The division of inner and outer part of the first shell is rough in that the r/ σ range will change with the solute and solvent properties. However the concept of inner ad outer parts are very useful in understanding the 3-mode S(t) dynamics.

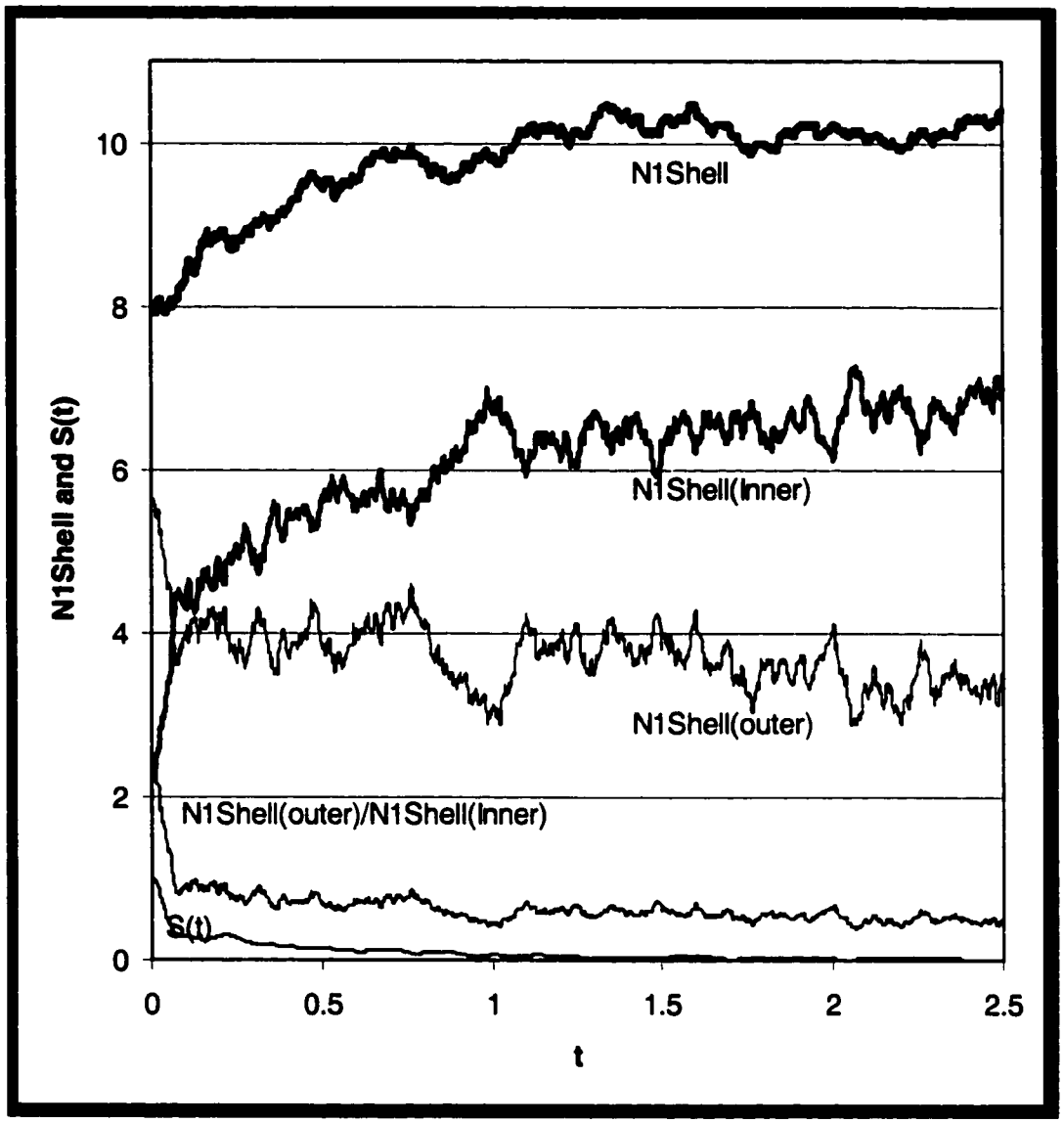

Figure 5.17 Dynamics of solvent number redistribution for system (A=11.5, B=0.133, C=1, μ=1.75, Q=20). The five curves from top to bottom are N1Shell , N1Shell (inner), N1Shell(outer), N1Shell (outer) / N1Shell (inner), and S(t).

in the first shell will be "pulled" from the outer part to the inner part, starting from the onset of charge for the solute. It is concluded that the decrease in S(t) at first mode accompanies the translational movement of solvents to the immediate environment of the solvents, the inner part. So this gives evidence that the first mode is closely relative to the solvents in its immediate environments instead of solvents far away outside the first shell.

If the solvents outside the first shell ($r/\sigma > 1.3$) may not be pulled to the first shell in the limited early time enough to compensate the loss of solvents in the outer part of first shell, the number of the solvents in the outer part of the first shell will certainly decrease. The pulling solvents from outer to inner parts, and the failure of response of the solvents outside the first shell during the first mode time scale is to favor the suddenly ionized solute, but it causes the energy of the solvents to increases, resulting in the subsequent second mode when the solvents try to decrease the energy, and finally the third mode dynamics.

The Table 5.12 shows the amplitudes (a, b) and time constants (τ_G, τ_E) of the dynamics of shell redistribution by data modeling of Figure 5.17.

In Table 5.12, it is obvious that the outer shell is losing solvents ($Y_1(t)$) while the inner shell is gaining solvents ($Y_2(t)$), just like the solvents shell is being compressed. The N1Shell(inner) increases from initial value 2.26=c-a-b=(6.81-1.82-2.73) to c=6.81 with two distinct component: τ_G =92 (fs) and τ_E =1.75 x 10^3 (fs) respectively.

Table 5.12 Dynamics of solvent number redistribution for system (A=11.5, B=0.133, C=1, μ=1.75, Q=20). The eq means the same data in equilibrium.

Data	c	a	b	τ_G (fs)	τ_E (fs)	Mode I
S(t)		0.655	0.345	73.8	1.55×10^3	$Y_3(t)$
$\frac{N1Shell(outer)}{N1Shell(inner)} - eq$		1.46	0.436	78	2.1×10^3	$Y_1(t)$
N1Shell(outer)-eq		1.6	0.74	73	3.3×10^3	$Y_1(t)$
N1Shell(inner)	6.81	1.82	2.73	92	1.75×10^3	$Y_2(t)$
N1Shell	10.8		2.34		1.11×10^3	$Y_5(t)$

The time scale of S(t) and N1Shell(inner) are very close. The inner shell is gaining solvents with τ_G =92 (fs), and τ_E =1.75 x 10^3 (fs) corresponding to the first mode, and second as well as third mode of S(t) respectively.

5.3.5.2 Dipole Moment Effect

At charge Q =20, the N1Shell keeps roughly constant with time when dipole moment is as small as 0.25. When μ becomes as large as 0.5 to 1.75; the N1Shell will increase with time until equilibrium, because the increasing interaction between solute and solvents by charge-dipole moment interaction (Figure 5.18)

It is also shown in the above Figure 5.18, the N1Shell(r/σ=1.3) at equilibrium of solvation (t>=2.5) increases from μ=0.25, 0.5 up to 1.0, and then roughly keep constant.

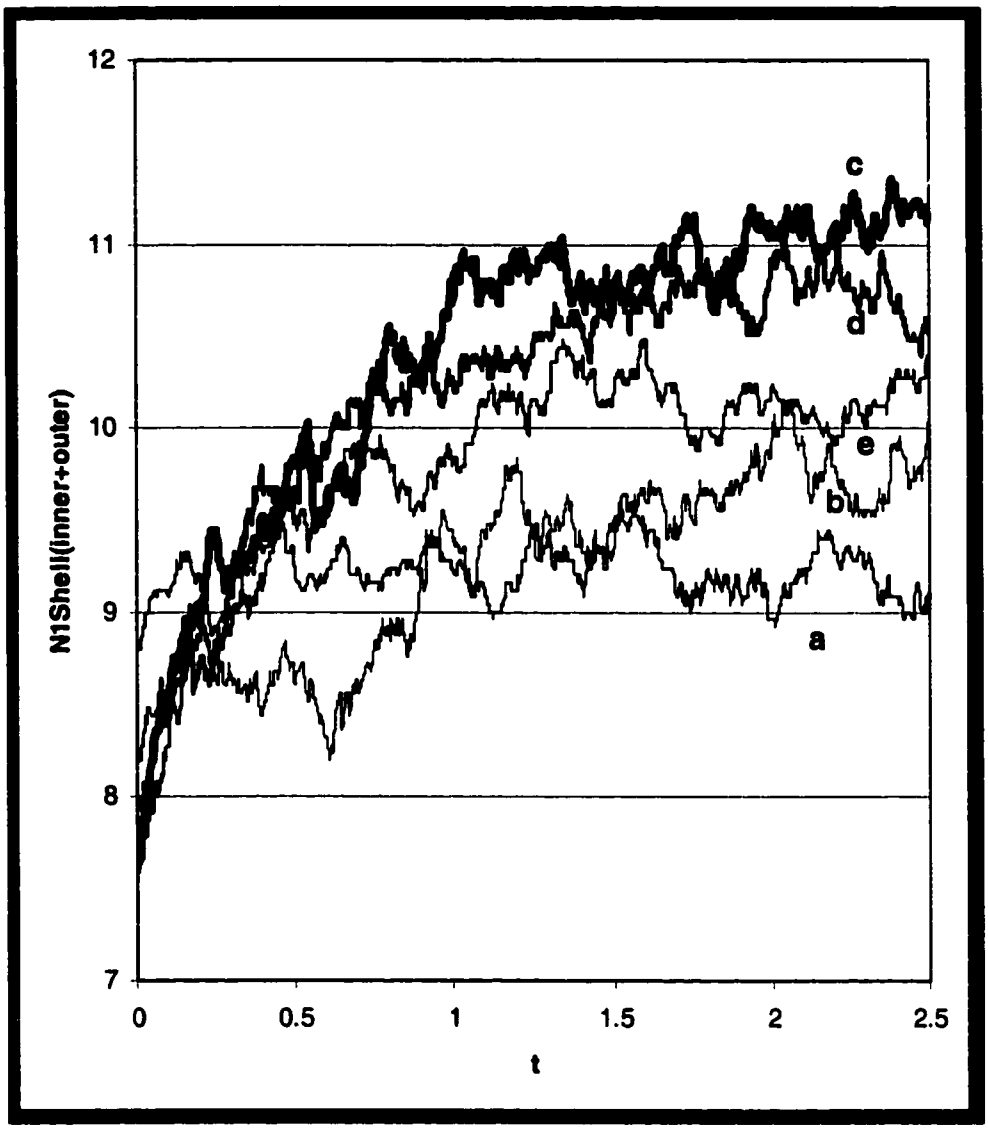

Figure 5.18 Dipole moment effect on the dynamics of solvent number N1Shell redistribution (A=11.5, B=0.133, C=1, Q=20) at μ=0.25(curve, a), 0.5(curve, b), 1.0 (curve, c), 1.4 (curve, d), and 1.75 (curve, e)

Table 5.13 Dipole moment effect on the dynamics of solvent number N1Shell(r/σ=1.3) redistribution (A=11.5, B=0.133, C=1, Q=20). The eq means the same data in equilibrium.

Data	μ	c	a	b	a/b	τ_G (fs)	τ_E (fs)	$Y_i(t)$
N1Shell(inner +outer)	1.75	10.2		2.34	c-b=7.86		1.11×10^3	$Y_5(t)$
	1.4	10.8		2.82	c-b=7.98		1.33×10^3	
	1.0	11.2		3.15	c-b=8.05		1.68×10^3	
	0.5	10.6		2.32	c-b=8.28		5.8×10^3	
N1Shell(inner)	1.75	6.81	1.83	2.72	0.673	92	1.8×10^3	$Y_2(t)$
	1.4	5.87	1.69	2.48	0.681	75	1.2×10^3	
	1.0	4.83	1.53	1.54	0.993	76	1.7×10^3	
	0.5	3.27	0.808	0.589	1.37	56	2.5×10^3	
N1Shell(outer, t)-eq	1.75		1.6	0.74	2.16	73	3.3×10^3	$Y_1(t)$
	1.4		1.37	0.813	1.68	78	-1.99×10^4	
	1.0		1.56	-1.42	-1.10	83	3.1×10^2	
	0.5		0.767	-1.20	-0.639	80	3.3×10^3	
	0.25		1.30	-1.53	-0.85	74	1.1×10^2	
$\frac{N1Shell(outer,t)}{N1Shell(inner,t)} - eq$	1.75		1.46	0.436	3.35	78	2.1×10^3	$Y_1(t)$
	1.4		2.10	0.470	4.47	80	7.9×10^3	
	1.0		1.76	0.384	4.58	70	2.1×10^4	
	0.5		1.26	0.019	66.3	58	6.4×10^4	
	0.25		3.07	-2.9	-1.05	73	120.6	

As shown in Table 5.13, though the N1Shell(inner) and N1Shell(outer) are well modeled Gaussian and exponential components as $Y_2(t)$ increase with time and $Y_1(t)$ decreases with time respectively. The N1Shell(inner + outer) is modeled by a single exponential component as $Y_5(t)$ at this special Q (see charge effect, and how it changes the type of modeling. This may be due to the effect of inner shell cancels the effect of outer shell in the Gaussian component.).

The following dipole moment effects are observed:

- Dynamics of N1Shell(inner + outer): If μ is 0.25, the solvent number in the first shell keeps constant. When is larger than 0.5, and as μ increases, the τ_E decreases, which means the number of solvents in the solvent shell increase more quickly. The solvent number at equilibrium is c and that at start is b, and the change in solvent number is c-b, which nearly constant with slight increases with dipole moment only.
- Dynamics of N1Shell(inner): The solvent number in the inner shell (c) increases as μ increases. The amplitude of both the Gaussian and exponential components (a and b) increases as μ increases. But exponential component increase/dominates more than Gaussian as a/b decreases with μ. The Gaussian becomes faster (τ_G), while exponential (τ_E) become faster/ fluctuates with μ.
- Dynamics of N1Shell(outer): The dynamics are different for large (μ=1.4, 1.75) and small (μ=0.5 to 1.0). When μ is large, the amplitude of both the Gaussian increases (a increases) with μ; but the exponential

components (b) decrease as μ increases. When μ is small, the dynamics decreases with a minimum, and then increases with μ.

- Dynamics of N1Shell (outer)/N1Shell (inner): The Gaussian becomes slower/fluctuates (τ_G), while exponential (τ_E) become faster with μ.

5.3.5.3 Charge Effect On N1Shell

As shown in the Figure 5.19, the N1Shell will keep constant at small charge, but it will increase with time when charge >= 20. The larger the charge, the

Table 5.14 Charge Q effect on the dynamics of solvent number redistribution for system with A=11.5, B=0.133, C=1, μ=1.75 at Q=6, 12, 20, 36 and 81

Data	Q	c	a	b	a/b	τ_G (fs)	τ_E (fs)	Model
N1Shell(inner)	12	4.38	1.52	0.547	2.78	90	2.1×10^3	$Y_2(t)$
	20	6.81	1.83	2.72	0.623	92	1.75×10^3	
	36	9.42	2.08	5.17	0.402	82	1.78×10^3	
	81	11.5	2.61	6.69	0.390	69	1.61×10^3	
N1Shell(outer, t)-eq	20		1.6	0.74	2.16	73	3.3×10^3	$Y_1(t)$
	36		1.0	2.93	0.341	45	2.5×10^3	
	81		0.71	3.81	0.186	25	1.5×10^3	
N1Shell(outer)/N1Shell(inner)-eq	12		1.29	0.262	4.92	78	1.2×10^3	$Y_1(t)$
	20		1.46	0.436	3.35	78	2.1×10^3	
	36		1.48	0.767	1.92	62	1.61×10^3	
	81		1.55	0.807	1.92	42	1.08×10^3	
N1Shell(inner + outer)	20	10.2		2.34			1.1×10^3	$Y_5(t)$
	36	11.3	2.06	1.55	1.33	248	2.1×10^3	$Y_2(t)$
	81	12.9	3.10	2.21	1.40	169	3.3×10^3	

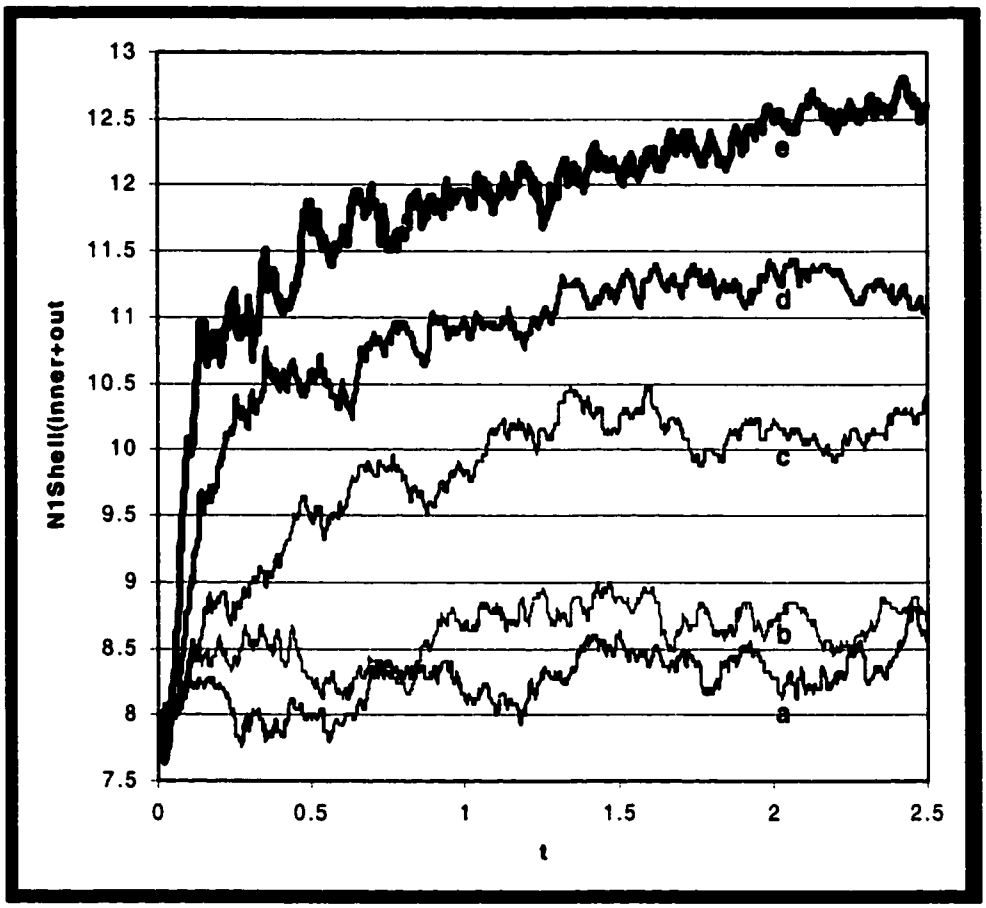

Figure 5.19 Charge effect on the dynamics of solvent number redistribution for system with A=11.5, B=0.133, C=1, μ=1.75 at Q=6 (curve, a), 12 (curve, b), 20 (curve, c), 36 (curve, d) and 81 (curve, e) for curves from bottom to top respectively.

faster and larger the increase, because the larger interaction between solute and solvents by charge-dipole moment interaction.

The Table 5.14 shows the effect of charge on the dynamic parameters of shell redistribution by fitting the data as follows.

- The dynamics of N1Shell(inner): The dynamics of time- increases are modeled by two components: Gaussian and exponential in $Y_2(t)$. As Q increases, c increases or the number of solvents at equilibrium in the inner shell increases. The amplitudes of both components increase with charge (a, b increases). But the proportion of the Gaussian over exponential component decreases as shown by the decrease in a/b. The Gaussian component is slightly faster/fluctuates, and the exponential component is faster as Q increases/fluctuates.
- The dynamics of N1Shell(outer): The dynamics of time-decreases are modeled by two components: Gaussian and exponential in $Y_1(t)$. The amplitudes of Gaussian components decrease, while the amplitudes of exponential components increases with charge (a decreases, b increases). The proportion of the Gaussian over exponential component decreases as shown by the decrease in a/b. The Gaussian component is slightly faster, and the exponential component is faster as Q increases.
- The dynamics of N1Shell(outer)/N1Shell(inner): The dynamics of time-decreases are modeled by two components: Gaussian and exponential in $Y_1(t)$. The amplitudes of both components increase with charge (a, b

increases). But the proportion of the Gaussian over exponential component decreases as shown by the decrease in a/b. The Gaussian component is slightly faster, but the exponential component is faster/fluctuating as Q increases

- N1Shell(outer)/ N1Shell(inner): The N1Shell shows different types of dynamics depending on charge. When Q is small (6, 12), the total solvent number in first shell N1Shell will keep unobservable tendency of increases, nearly constant. When Q is 20, the N1Shell increases exponentially until equilibrium (modeled well $Y_5(t)$). When Q=36, 81, the N1Shell have both Gaussian and exponential components modeled by ($Y_2(t)$). As Q increases, the Gaussian proportion (a) increases and faster (τ_G), but the exponential part increases (b) and slow down (τ_E). The Gaussian proportion increases more than exponential, as shown by increases in (a/b) with Q. The number of solvents at equilibrium (parameters c) increases with Q.

5.3.5.4 Surface Effect On N1Shell And S(t)

As shown in Figure 5.20, the N1Shell (inner) at given time will increases as C increases.

At larger C, N1Shell(inner) will keep constant. At lower C=1.0, N1Shell will increase with t. As C increases, the rate of N1Shell increase with time decays, because the N1Shell starts with a higher number (Figure 5.20). It is this initial higher solvent number that makes more solvents already in the inner shell without the necessity to gain solvents from outer shell.

As B increases, the N1Shell(inner) starts with a lower number of solvents, and increase faster.

The total number of the solvent number in the first shell at this small charge will keep constant.

The surface effect on solvent shell redistribution is summarized in Table 5.15.

Table 5.15 Surface effects on the dynamics of solvent number redistribution for system (A=36, B=0.133, μ=1.75, Q=12)

Data	C	c	a	b	a/b	τ_G (fs)	τ_E (fs)	Model
N1Shell(inner)	1	5.18	0.823	0.60	1.37	68	1.1×10^3	$Y_2(t)$
N1Shell(outer, t)-eq	1		0.27	0.62	0.44	81	4×10^2	$Y_1(t)$
	4		0.35	0.214	1.6	187	4.1×10^3	
	6		0.36	-0.24	-1.5	170	6.6×10^3	
$\frac{N1Shell(outer)}{N1Shell(inner)} - eq$	1		0.27	0.216	1.25	70.7	5.1×10^2	$Y_1(t)$
	4		0.067	0.0388	1.72	194	5.3×10^3	
	6		0.0037	-0.00346	-1.1	377	4.6×10^3	

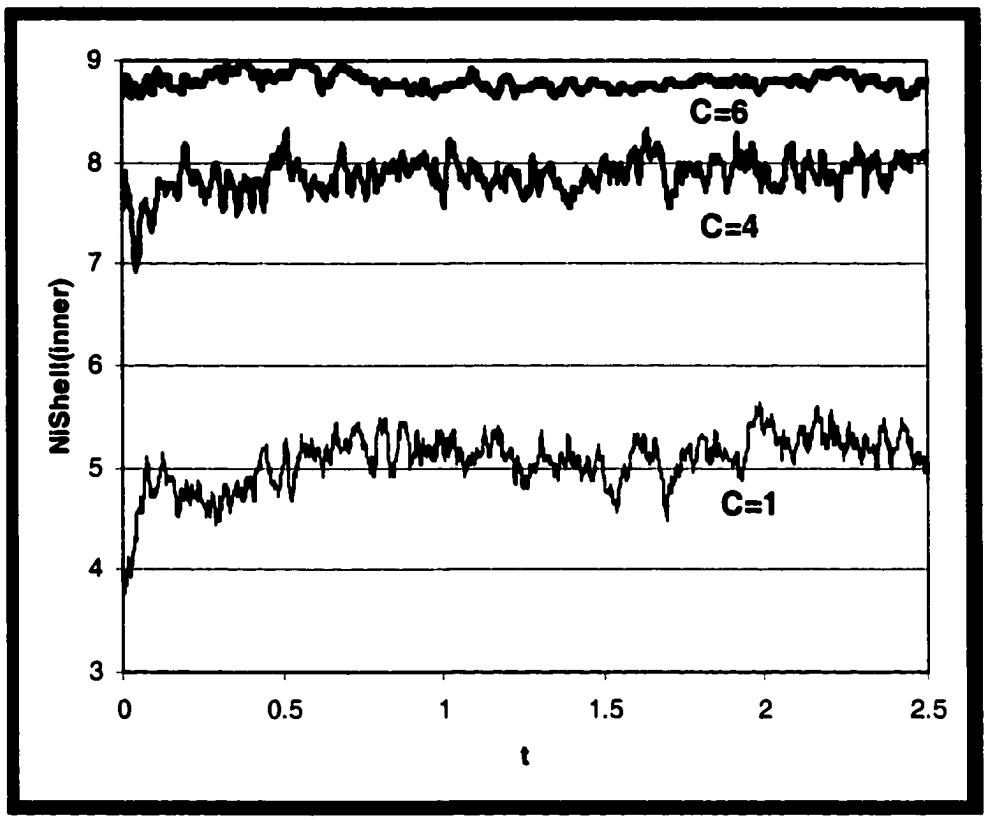

Figure 5.20 Surface effects on the dynamics of solvent number redistribution for system (A=36, B=0.133, μ=1.75, Q=12) at C=1, 4, and 6 from bottom to top curves

The following surface effects on solvent shell redistribution are observed from Table 5.5 and Figure 5.20:

- Dynamics of N1Shell (inner): For C=1 the N1Shell (inner) increases with time modeled by $Y_2(t)$ with c=5.18, a=0.823, b=0.60, τ_G =68 fs, and τ_E =1122 fs. For C=4, 6, the N1Shell (inner) is constant. This may be because the first valley in the adsorption layer prevents the solvents in other solvent layers from coming to the first shell. Also the initial number of solvents is already high.
- Dynamics of N1Shell (outer) modeled by Y_1 (t): As C increase, both Gaussian and exponential components slow down as shown by (τ_G, τ_E) increase. The amplitude of Gaussian increases, but that of exponential decreases, as C increases.
- Dynamics of N1Shell (outer)/N1Shell(inner) $Y_1(t)$: As C increase, both Gaussian and exponential components slow down as shown by (τ_G, τ_E) increase. The amplitude of Gaussian and exponential decreases, as C increases. But b dies faster than a as C increases.

5.4 Conclusion

Using the model of a charged solute in polar Stockmayer solvent fluids between two abstract surfaces, the dependence of the solvation dynamics on dipole moment, solute charge and surface parameters is investigated. The parameters for the solvation dynamics modeled by Gaussian and exponential components are obtained by fitting the data of S(t), CS(t), r_{sz}, and N1Shell.

Compared with previous researchers, the results in our study are unique in the interfacial effect in addition to the more extensive range of the solute charge and system dipole moment effects on the non-equilibrium dynamics.

5.4.1 Overall Picture Obtained By S(t), CS(t), r_{sz} And N1Shell

After obtaining the equilibrium pair distribution ZD and pair distribution g(r) functions, the solvation dynamics are studied.

The overall 3 mode dynamics are shown by the solvent response function S(t) and complimentary solvent response function CS(t). The functions show how the energy relaxes. On the other hand, the translational motion of solute and the spatial redistribution of the first shell solvents are demonstrated by two new functions, the r_{sz} and N1Shell respectively.

The function r_{sz}, is introduced to study the solute translation during the entire solvation. It is found that the solute tries to find a favorable position to reduce the potential between solute and solvent in the first mode time scale of S(t). The solute moves away from the surface to a place with higher probability of solvents in its first shell, and then it begins random walk around this favorable position.

The function N1Shell reflects solvents translation and solvent shell redistribution. It is found that more solvents are moving closer to the solute as shown by the inner shell gaining solvents from the outer shell in the time scale of first mode of S(t).

The solute reaching its favorable transient state in the first mode time scale is shown as follows. The solute translationally moves away from the surface to reach a place in z where more solvents can be found in the solvent adsorption layer. At the same time, more solvents are translationally moving toward the solute from the outer shell to the inner shell. The solute moving toward more solvents combined with the more solvents moving toward the charged solute results in the solute reaching its favorable state.

In return, the relocation of the solute and the redistribution of the solvents happening in the first mode time scale has put the solvents themselves in a very unfavorable state where the interaction between the solvents themselves is in a higher energy state (CS(t) maximum at S(t) minimum); so subsequent second mode is about to occur to reduce the potential of solvents interaction, until the system reaches equilibrium by experience the third mode.

The first rapid decrease, the first mode, of the S(t) is related to N1Shell (inner) of inner shell rapid increases. The suddenly added electrostatic attraction to the polar solvents will pull the solvents closest to the ion itself. This is shown in the increase of N1Shell (inner). This will certainly cause the destruction of the solvent shell, the shell's potential will increase accordingly (CS(t) will increase), and the solvent layer will need to be re-constructed in the subsequent modes.

It is assumed that all these dynamics are caused by translational and rotational movement: the solute moving away from surface and solvents

moving close to solute; the solvents' dipole aligned to the newly created charge, and the solute dipole aligned to solvents' dipole moment. The first mode of dynamics of S(t) is resulted mainly from the fast shrinking of the solvent shell by translation in addition to the re-orientational motion. The subsequent 2nd mode and 3rd mode are primary attributed to the spatial redistribution of the solvents farther away from the solute in the outer shell.

5.4.2 The 3-Mode Dynamics And Two Kinds Of Transient States

It is observed the solvent response function S (t) (the relaxation of the solvents surrounding to the solute) is characterized typically by 3-mode using MD simulation. The 3-mode S(t) consists of a first rapid decrease to a MIN (first mode), then increase to a MAX, and then repeatedly goes from a new MIN to a new MAX to generate oscillation (second Mode), with a final slower decrease to equilibrium state (third Mode). The oscillation behavior is consistent with the observation of the previous research, but is normally ignored in their explanations. We have proposed a new mechanism with 2 kinds of transient states to explain the overall process of the solvation dynamics with the help of the CS(t) function.

During the overall solvation upon ionization of the solute, the system first goes to a state favorable to the solute, but unfavorable to its surrounding the solvents (one of the states in the first kind). Then the system goes to a state unfavorable to the charged solute, but favorable to its surrounding solvents (one of the states in the second kind). The system may further goes to a new

state of the first kind, then to another new state of the second kind repeatedly to cause oscillation in the relaxation of the potential energy of the solute reflected by S(t) and CS(t). So the oscillation in S(t) is explained by the oscillation of the system experiencing the transient states between the first kind and the second kind, which is adjusted by the translational and orientational movement of the solute and its surrounding solvents. The oscillation gradually reduces with time and the system finally reaches a new equilibrium state favoring both the charged solute and its surrounding solvents.

5.4.3 Translational Motion Of Solute

Adsorption layers are formed around surface as shown by equilibrium ZD, under different surface parameters A, B, and C. Based on this, the translation dynamics r_{sz} vs t is understood. It is found that the translational movement away from surface is confined by the surface, i.e. At small C where the first valley permits particles, the solute can move away from first layer; otherwise, the solute is limited to the first layer.

5.4.4 Redistribution Of Solvent Shell

By dividing the first shell into inner and outer parts as well as by correlating dynamics of the N1Shell(t) with that of S(t) , the redistribution is studied. It is found that the first shell gains solvents in total upon ionization. However there is a sudden gain and loss of the solvents in the inner and outer part of the first shell respectively during the first mode. In the second mode, the same trend remains, but occurs significantly slowly, and reaches equilibrium finally in the

third mode. The opposite behavior of the solvent number dynamics for the inner and outer shell indicates that the redistribution of solvents occurs in the solvent relaxation dynamics. The number of solvents in the inner shell increases, while the number of solvents in the outer shell decreases. The net decreases in solvent number of the outer shell means more solvents pulled away to inner shell and fewer solvents gained from outside the shell.

5.4.5 Surface, Charge And Dipole Moment Effects

The solvation dynamics including solute translational motion and solvent shell redistribution is studied under various surface parameters, solute charge, and fluid dipole moments. The dynamic parameters including the amplitudes and time constants are obtained by fitting the data for S(t), $r_{sz}(t)$, N1Shell(t) with Gaussian and exponential components as shown in Table 5.6 to 5.15.

It is also pointed out that the component effect in previous paper [2] may be actually caused by decreasing dipole moment of the mixed fluid by increasing the component of the weak fluid.

5.5 References

(1) Graf, P.; Nitzan, A.; Chem. Phys. 1998, 235, 297-312

(2) Day, T. J. F.; Patey, G. N.; J. Chem. Phys. 1997, 106, 2782-2791

(3) (a) Maroncelli, M. J. Mol. Liq. 1993, 57, 1; (b) Maroncelli, M.; Kumar, V. P.; Papazyan, A.; J. Phys. Chem. 1993, 97, 13

(4) Ultrafast reaction dynamics and solvent effects, AIP conference Proceedings, Gauduel, Y.; Rossky, P. J. (Eds), vol. 298, AIP, New York, 1994

(5) Structure fluctuation, and relaxation in solutions, thematic issue of J. Mol. Liq., vol. 65-66, 1995

(6) Stratt, R. M.; Maroncelli, M. J. Phys. Chem. 1996,100,12981

(7) Jarzeba, W; Walker, G. C; Johnson, A. E.; Barbara, P. F. Chem. Phys. 1991, 152, 57

(8) Hallidy, L. A.; Topp, M. R.; J. Phys. Chem. 1978, 82, 2415

(9) Robinson, G. W.; Robbins, R. J.; Fleming, G. R.; Morris, J. M.; Knight, A. E. W.; Morrison, R. J. S. J. Am. Chem. Soc. 1978, 100, 7145

(10) Perera, L.; Berkowitz, M. L.; J. Chem. Phys. 1992, 96, 3092

(11) Neria, E.; Nitzan, A.; J. Chem. Phys. 1992, 96, 5433

(12) Chandra, A; Wei, D.; Patey, G. N.; J. Chem. Phys. 1993, 99, 4926

(13) Maronecelli, M.; J. Chem. Phys. 1991, 94, 2084

(14) Maroncelli, M; MacInnis J.: Fleming, G. R.; Science, 1989, 243, 1674

(15) Fleming, G. R.; Wolynes, P. G.; Phys. Today, 1990, 43, 36

(16) Phelps, D. K.; Weaver, M. J.; Ladanyi, B. M.; Chem. Phys. 1993, 176, 575

(17) Fonseca, T.; Ladanyi, B. M.; J. Mol. Liq. 1994, 60, 1

(18) Skaf, M. S.; Landanyi, B. M.; J. Mol. Structure 1995, 335, 181

(19) Ladanyi, B. M.; Stratt, R. M.; J. Phys. Chem. 1996, 100, 1266

(20) Horng, M. L.; Gardecki, J. A.; Papazyan, A.; Maroncelli, M. J. Phys. Chem. 1995, 99, 17311

(21) Cho, M.; Rosenthal, S. J., Scherer, N. F.; Ziegler, L. D., Fleming, G. R. J. Chem. Phys. 1992, 96, 5033

(22) Chandra, A.; Chem. Phys. Lett. 1995, 235, 133

(23) Van Leeuwen, M. E.; Fluid Phase Equilibra 1994, 99, 1

(24) Stockmayer, W. H.; (a) J. Chem. Phys. 1941, 9, 398; (b) J. Chem. Phys. 1941, 9, 863

(25) Winkler, R. G.; Hentschke, R.; J. Chem. Phys. 1994, 100, 3930-3939

(26) Hentschke, R.; Winkler,R. G.; J. Chem. Phys. 1993, 99, 5528-5534

(27) Hentschke, R.; Schurmann, B. L.; Rabe, J. P.; J. Chem. Phys. 1992, 96, 6213-6221

(28) Steele, W. A.; Vernov, A. V.; Tildesley, D. J. Carbon, 1987, 25, 7-17

(29) Nicholson, D.; Parsonage, N. G. J. Chem. Soc., Faraday Trans. 1986, 82, 1657-1667

(30) Josh, Y. P.; Tildesley, D. J. Mol. Phys.; 1985, 55, 999-1016

(31) Severin, E. s.; Tildesley, D. J. Mol. Phys. 1980, 41, 1401

(32) Tironi, I. G.; Luty, B. A.; van Gunsteren, W. F. J. Chem. Phys.; 1997, 106, 6068-6075

(33) Allen, M. P.; Tildesley, D. J. Computer Simulation of Liquids, Clarendon Press, Oxford, 1987

(34) Steele, W. A.; The interaction of gases with solid surfaces; in The international encyclopedia of physical chemistry and chemical physics Topic 14: Properties of interfaces Edited by Everett, D. H.; vol 3; Pergamon Press, New York: 1974

(35) Steele, W. A. Surface Science 1973, 36, 317-352

(36) Ryckaert, J.P.; Ciccotti, G.; Berendsen, H.J. C. J. Computational Physics; 1977, 23, 327-341

(37) Pollock, E.L.; Alder, B. J. Physica, 1980, 102A, 1-21

(38) Jaffe, J. E.; Hess, A. C.J. Chem. Phys. 1996, 105, 10983-10988

(39) Smith, P. E.; Blatt, H. D. Pettitt, B. M.; J. Phys. Chem. B. 1997, 101, 3886-3890

(40) Deem, M. W.; Newsam, J. M.; Sinha, S. K. J. Phys. Chem. 1990, 94, 8356-8359

(41) A re-draft of paper: Smith, W. CCP5 Information Quarterly, 1982, 4, 13

(42) Adams, D. J.; Dubey, G. S. J. Computational Physics; 1987, 72, 156-176

(43) Adams, D. J.; Chem. Phys. Lett.; 1979, 62, 1979

(44) Nijboer, B. R. A.; De Wette, F. W. Physica 1957, XXIII, 309-321

(45) Din, X., Michaelides, E. E. J. Phys. Chem. A 1997, 101, 4322-4331

(46) Figueirido, F.; Levy, R. M.; Zhou, R.; Berne, B. J. J Chem. Phys. 1997, 106, 9835-9849

(47) Heyes, D. M. J. Chem. Phys. 1981, 74, 1924-1929

(48) Ladd, A. J. C. Mol. Phys. 1978, 36, 463-474

(49) Ladd, A. J. C. Mol. Phys. 1977, 33, 1039-1050

(50) Gao, G. T.; Zeng, X. C. J. Chem. Phys. 1997, 106, 3311-3316

(51) Hautman, J.; Michael, L. K. Mol. Phys. 1992, 75, 379-395

(52) Parry, D. E. Surface Science; 1975, 49, 433-440

(53) Heyes, D. M.; Barber, M.; Clarke, J. H. R. J. Chem. Soc. Faraday Trans. 2, 1977, 73, 1485

(54) Rhee, Y.J.; Halley, J. W.; Hautman, J.; Rahman, A. Phys. Rev. B. 1989, 40, 36-42

(55) http://www.curvefitting.com

(56) (a) http://www.nr.com; (b) Press, W. H.; Teukolsky, S. A.; Vetterling, W. T.; Flannery, B. P; Numerical Recipes In C: The Art of Scientific Computing; Cambridge University Press 1988-1992

CHAPTER 6 CONCLUSION

In this dissertation, the super-fast dynamics of solutes in polar solution and at interface is studied. These include the dynamics of four bypiridinium ions (MV^+, BV^+, and $BPDPS^-$, and EB^+) in bulk aqueous solution, interfacial electron transfer between MV^+ and CdS, and solvation dynamics upon electron transfer to a solute in Stockmayer (SM) fluids and at SM fluid-abstract surface interface. The first two are mainly studied by time-resolved femtosecond RRS experimentally for specific ions, solvents and CdS surface, while the latter one is studied by computer experiments with MD simulation using simplified general model for solute, solvents and surface. The experimental RRS and the MD simulation compliment each other in resolving the dynamics. The RRS reveals vibrational relaxation dynamics, while the MD simulation reveals translational and rotational dynamics. The following interesting results are obtained.

6.1 Study Of Four Bipyridinium Ions In Bulk Aqueous Solution

Femtosecond time-resolved resonance Raman scattering (RRS) spectroscopy is used to investigate four bipyridinium radicals: methylviologen monocation $MV^{+\cdot}$, benzylviologen monocation $BV^{+\cdot}$, 4,4'-bipyridinium-N,N'-di(propylsulfonate) monoanion $BPDPS^-$, and N,N'-ethylene-2,2'-bipyridinium monocation $EB^{+\cdot}$. Time-resolution of the dynamics of the four radicals using the 379.6 nm laser of 350 fs pulse duration is carried out by a pump and probe technique using the time-dependent transient intensity of Stokes and anti-

Stokes RRS of C-C stretching mode. It is found that the lifetime of the electronic excited state B_{3u} (MO 11, excited) is less than 350 fs and the vibrational relaxation rates in the electronic ground state are some 2-5 ps. The possible vibrational relaxation mechanisms including the radical structure and charge effect on the vibrational relaxation are discussed. Assignments of some in-plane stretching vibration modes for $BV^{+\cdot}$, $BPDPS^{\cdot}$ are tentatively made on the basis of the similarity of their molecular skeletons to those of MV^{+2}, $MV^{+\cdot}$, and BV^{+2}. The shifts in vibrational frequency in the N-R mode are discussed according to the mass and charge effect of the substituted group R, whereas the frequency shifts in the C-C inter-ring stretching vibration upon reduction of BV^{+2} to BV^{+} are interpreted as the increase of interring C-C bond order.

The following results are obtained based on our experimental results and the existing theory about electronic and vibrational relaxation:

1. The measurement of stokes RRS spectra for MV^{+}, BV^{+}, and $BPDPS^{\cdot}$ (Figure 3.3), and the first measurement of anti-stokes RRS spectra for MV^{+}, $BPDPS^{\cdot}$ and EB^{+} (Figure 3.4) are obtained. The tentative assignments of some bands are made (Table 3.1 and 3.2). The wavenumber of the N-R vibration mode for the radicals changing with different R from methyl group, benzyl group to propylsulfonate group are discussed in terms of the mass and charge effect of the substituent groups. It is also found that the increase in wavenumber of the inter-ring C-C mode upon reduction of BV^{+2} to BV^{+} is due to more electron density added to the bond.

2. It is shown that the electronic relaxation from B_{3u} (MO 11, excited) to B_{3u} (MO 7, ground) is much faster than the 350 fs of our pulse duration. The subsequent vibrational relaxation dynamics of the vibrationally-excited B_{3u} (MO 7, ground) population for the C-C stretching mode is found to take place in 2 to 5 ps (Table 3.3 and Figure 3.5).

3. The 2 ps anti -Stokes dynamics is found not to be affected by the N, N'-substituents for the radicals; however the Stokes dynamics does reveal some radical structure affect on the rate of vibrational relaxation (Table 3.3). The 5 ps Stokes dynamics of EB^+ is discussed as the result of the "locking effect" exerted by its 2,2'-ethylene bridge, which limits the twisting of the two rings, decreases the channels to transfer vibrational energy through low frequency modes, and consequently reduces the rate of vibrational relaxation.

4. The charge of the quartnary N^+ structure in the radical has been shown to have little effect on the rate of the vibrational relaxation rate by comparison with neutral molecules of similar size in solution; which is discussed in terms of the delocalization charge density over the 12 ring atoms and confirms the prediction of molecular dynamics simulation.

5. The vibrational energy of the C-C stretching mode may decay via inter- and/or intra-molecular routes, which are not identified at present time due to the limited data. Further work could be done to time-resolve the dynamics of the other modes to determine possible intramolecular decay routes via energy redistribution among the different modes.

6.2 Study Of Interfacial Electron Transfer Between MV^+ And CdS

The first direct femtosecond measurements of the RRS spectrum of photo-induced MV^+ and the dynamics of the photoinduced electron transfer from aqueous colloidal CdS to the adsorbed MV^{+2} have been performed. The RRS spectrum reveals that the part of the electron transfer accompanied by the structure change from aromatic MV^{+2} to a quinoid MV^+ occurs within 350 fs (the pulse width). Time-resolving the dynamics by monitoring the RRS intensity of MV^+ as a function of delay time has been carried out.

The photo-induced MV^+ dynamics in the CdS colloid are quite different from that of the chemically prepared MV^+, the latter is a single-exponential of time constant 3.1ps, however the former is a double-exponential or two components of time constants 270fs and 6.7ps. The fast component 270fs accounts for the part of MV^+ produced within the pulse width by the transfer of very shallowly trapped electrons, and the slow component 6.8ps is assigned as the transfer of relatively deeply trapped electrons. The slower 6.8ps component does not represent the pure electron transfer rate constant because electron hole pair recombination is known to compete on this time scale. This double-exponential behavior for the electron transfer is discussed as the contribution mainly from the distributions in electron trap depths. The calculated relatively deep trap depth 100-300meV is consistent with that given by Weller's group[19,22] as shown in the literatures.

6.3 Solvation Dynamic By MD

The solvation dynamics upon solute ionization in bulk and at surface is studied using molecular dynamics simulation. For 20-40 selected thermodynamics states, the corresponding non-equilibrium solvation, starting from a neutral polar solute in bulk or adsorbed to surface is studied by investigating the solvent response function, the complementary solvent response function, number of solvents in the first solvent shell, solvent distribution along the distance perpendicular to surface, and pair distribution function. The dependence of non-equilibrium solvation dynamics on solute charge, solvent dipole moment, and surface parameters are studied. A mechanism with two kinds of transient states is proposed to explain the 3-mode dynamics, especially the oscillation behavior that is commonly observed, but not well accounted previously. Our study not only extends the previous studies of bulk polar fluids to the surface system, but also applies more extensive range of dipole moments and charge. The dynamic parameters including amplitudes and time constants at various surface, charge, and dipole moments are obtained by fitting the MD data using models consisting of Gaussian and exponential components. Our results are theoretically significant in the study of relaxation of solvents upon interfacial electron transfer to the solute.

6.3.1 Overall Picture Obtained By S(t), CS(t), r_{sz} And N1Shell

The overall 3 mode dynamics are shown by the solvent response function S(t) and complimentary solvent response function CS(t). The functions show how

the energy relaxes. On the other hand, the translational motion of solute and the spatial redistribution of the first shell solvents are demonstrated by two new functions, the r_{sz} and N1Shell respectively.

The function r_{sz}, is introduced to study the solute translation during the entire solvation. It is found that the solute tries to find a favorable position to reduce the potential between solute and solvent in the first mode time scale of S(t). The solute moves away from the surface to a place with higher probability of solvents in its first shell, and then it begins random walk around this favorable position.

The function N1Shell reflects solvents translation and solvent shell redistribution. It is found that more solvents are moving closer to the solute as shown by the inner shell gaining solvents from the outer shell in the time scale of first mode of S(t).

The solute reaching its favorable transient state in the first mode time scale is shown as follows. The solute translationally moves away from the surface to reach a place in z where more solvents can be found in the solvent adsorption layer. At the same time, more solvents are translationally moving toward the solute from the outer shell to the inner shell. The solute moving toward more solvents combined with the more solvents moving toward the charged solute results in the solute reaching its favorable state.

In return, the relocation of the solute and the redistribution of the solvents happening in the first mode time scale has put the solvents themselves in a very unfavorable state where the interaction between the

solvents themselves is in a higher energy state (CS(t) maximum at S(t) minimum); so subsequent second mode is about to occur to reduce the potential of solvents interaction, until the system reaches equilibrium by experience the third mode.

The first rapid decrease, the first mode, of the S(t) is related to N1Shell (inner) of inner shell rapid increases. The suddenly added electrostatic attraction to the polar solvents will pull the solvents closest to the ion itself. This is shown in the increases of N1Shell (inner). This will certainly cause the destruction of the solvent shell, the shell's potential will increases accordingly (CS(t) will increase), and the solvent layer will need to be re-constructed in the subsequent steps.

The subsequent $2^{nd}/3^{rd}$ mode are related to the reorganization of the solvents in the neighbors of the ionized solute, like in 1^{st} shell that are relatively farther away from the solute.

It is assumed that all these dynamics are caused by translational and rotational movement: the solute moving away from surface and solvents moving close to solute; the solvents' dipole aligned to the newly created charge, and the solute dipole aligned to solvents' dipole moment. The first mode of dynamics of S(t) is resulted mainly from and the fast shrinking of the solvent shell by translation in addition to the re-orientational motion. The subsequent 2^{nd} mode and 3^{rd} mode are primary attributed to the spatial redistribution of the solvents farther away from the solute (e.g. $r/\sigma > 1.0$).

6.3.2 The 3-Mode Dynamics And Two Kinds Of Transient States

It is observed the solvent response function S (t) (the relaxation of the solvents surrounding to the solute) is characterized typically by 3-mode using MD simulation. The 3-mode S(t) consists of a first rapid decrease to a MIN (first mode), then increase to a MAX, and then repeatedly goes from a new MIN to a new MAX to generate oscillation (second Mode), with a final slower decrease to equilibrium state (third Mode). The oscillation behavior is consistent with the observation of the previous researchers, but is normally ignored in their explanations. We have proposed a new mechanism with 2 kinds of transient states to explain the overall process of the solvation dynamics with the help of the CS(t) function.

During the overall solvation upon ionization of the solute, the system first goes to a state favorable to the solute, but unfavorable to its surrounding the solvents (one of the states in the first kind). Then the system goes to a state unfavorable to the charged solute, but favorable to its surrounding solvents (one of the states in the second kind). The system may further goes to a new state of the first kind, then to another new state of the second kind repeatedly to cause oscillation in the relaxation of the potential energy of the solute reflected by S(t) and CS(t). So the oscillation in S(t) is explained by the oscillation of the system experiencing the transient states between the first kind and the second kind, which is adjusted by the translational and orientational movement of the solute and its surrounding solvents. The

oscillation gradually reduces with time and the system finally reaches a new equilibrium state favoring both the charged solute and its surrounding solvents.

6.3.3 Translational Motion Of Solute

Adsorption layers are formed around surface as shown by equilibrium ZD, under different A, B, and C. Based on this, the translation dynamics r_{sz} vs t is understood. It is found that the translational movement away from surface is confined by the surface, i.e. At small C where the first valley permits particles, the solute can move away from first layer; otherwise, the solute is limited to the first layer.

6.3.4 Redistribution Of Solvent Shell

By dividing the first shell into inner and outer parts as well as by correlating dynamics of the N1Shell(t) with that of S(t) , the redistribution is studied. It is found that the first shell gains solvents in total upon ionization. However there is a sudden gain and loss of the solvents in the inner and outer part of the first shell respectively during the first mode. In the second mode, the same trend remains, but occurs significantly slowly, and reaches equilibrium finally in the third mode.

The opposite behavior of the solvent number dynamics for the inner and outer shell indicates that the redistribution of solvents occurs in the solvent relaxation dynamics. The inner shell gains solvents from the outer shell, which loses solvents. The net loss in solvent number of the outer shell

means more solvents pulled away to inner shell and fewer solvents gained from outside the shell.

6.3.5 Surface, Charge, And Dipole Moment Effects

The solvation dynamics including solute translational motion and solvent shell redistribution is studied under various surface parameters, solute charge, and fluid dipole moments. The dynamic parameters including the amplitudes and time constants are obtained by fitting the data for S(t), $r_{sz}(t)$, N1Shell(t) with Gaussian and exponential components as shown in Table 5.6 to 5.15.

It is also pointed out that the component effect in previous paper may be actually caused by decreasing dipole moment of the mixed fluid by increasing the component of the weak fluid.

VITA

Yixiang Huang was born in Chen Zhou City, Hunan Province, the People's Republic of China. He entered Hunan University in January 1978 and received his degree of Bachelor of Science, majoring in chemistry, in December 1981. He was then employed by Hunan University until August 1993. In July 1983 he was enrolled in a graduate program of Hunan University, and received his degree of Master of Science in June 1986. From 1986 to 1993 he worked as an instructor in the teaching and research group of physical chemistry of Hunan University. He came to Louisiana State University and A & M College (LSU) to pursue a doctoral program in chemistry at the Department of Chemistry in August 1993. His research interest in the doctoral program focusing on physical chemistry includes ultra-fast phenomena by time-resolved Raman spectroscopy and computer simulation. He was then enrolled in a dual degree program in January 1998. During January 1998 and May 1999, he completed his degree of Master of Science in Systems Science in the Department of Computer Science of LSU. His interest in the master program included high performance computing, database, network, and software design, development and test. Since June 1999 he has been working as a software engineer for Volt Information Science, and then for Microsoft Corporation as a full time employee, while staying as a part-time graduate student in the doctoral program to continue doing research by computer simulation. He will complete his doctoral program and be awarded the degree of Doctor of Philosophy by LSU in May 2001.

DOCTORAL EXAMINATION AND DISSERTATION REPORT

Candidate: Yixiang Huang

Major Field: Chemistry

Title of Dissertation: Superfast Dynamics of Bipyridinium Ions at Interfaces and Polar Solutions

Approved:

Major Professor and Chairman

Dean of the Graduate School

EXAMINING COMMITTEE:

Date of Examination:

April 3, 2001